POLY(IONIC LIQUID) THIN FILMS VIA SURFACE-INITIATED RING-OPENING METATHESIS POLYMERIZATION

By

Ian Gitata Njoroge

Dissertation

Submitted to the Faculty of the

Graduate School of Vanderbilt University

in partial fulfillment of the requirements

for the degree of

DOCTOR OF PHILOSOPHY

in

Chemical Engineering

August 31, 2017

Nashville, Tennessee

Approved:

G. Kane Jennings, Ph.D.

Paul E. Laibinis, Ph.D.

Clare M. M^{c}Cabe, Ph.D.

Douglas E. Adams, Ph.D.

To my extraordinary family, Mary, David, Kevin, Lydiah and Shane, for their countless sacrifices, their unwavering love, and support in my ongoing journey.

To my late uncle, The Reverend Dr. Godfrey Phillip Wa Ngumi, who helped me believe I could achieve the impossible.

and

To my darling Marsha, without you none of this would have been possible.

ACKNOWLEDGMENTS

My journey to obtaining a Ph.D. in Chemical Engineering has been one that has included many winding paths, but I would not have had it any other way. I truly stand on the shoulders of giants that have come before me and that have molded and shaped my abilities. The latest of these giants to play a huge role in my personal and professional development is Professor G. Kane Jennings, without whom I would never have achieved this accomplishment. As such, I would like to thank him for his tireless patience, immense wisdom, pertinent guidance, unrelenting support, and perpetual friendship. I would also like to individually extend my deepest gratitude to the role models that took the form of my committee members, I can only hope to one day achieve the wisdom, intellect and career achievements that you have attained. In particular, I would like to thank Professor Paul E. Laibinis for his thought-provoking questions and insightful input on the manuscript, Professor Clare M. M^{c}Cabe for her insight, foresight and tactful guidance, and last but most certainly not least, Professor Douglas E. Adams for his powerful intellect, infinite curiosity, unbridled optimism and affable personality.

The members of the Jennings lab were integral to the success of the research conducted in this manuscript. In particular, Maxwell T. Robinson has contributed in innumerable ways to this manuscript both intellectually and through his support and friendship. I would like to thank him for the numerous discussions, his brotherly camaraderie, his complex ideas, and his warm friendship. I would like to thank Xuanli Deng and Faustin Mwambutsa for their friendship and support. I would like to thank my fellow members of the "A Team," Cole D. Brubaker and Talitha M. Frecker, our time together solving the deep mysteries of the universe was pleasant and unforgettable. I also would like to thank the enthusiastic, intelligent, insightful,

hardworking undergraduate students that I had the unusual privilege and immense pleasure of working alongside in the research represented here. They include, Paul A. Kempler, Steven T. Arnold, James B. Mansfield, Micheal T. Kosson, Zephyr D. Zink, Maxwell W. Matson, and Brandon W. Bout.

The Chemical and Biomolecular Engineering department provided a collegial community and contributed to my professional development. My time in the department has been characterized by an intellectually stimulating environment and enduring friendships. I would like to thank all the faculty in the department for their constant guidance and judicious advice. I would like to thank all the departmental staff for their invaluable assistance. In particular, I would like to thank Mark Holmes, Mary Gilleran, Rae Uson, Angie Pernell, Julie James, and Robin Midget for their assistance in navigating the Vanderbilt bureaucracy as well as in solving the many administrative and repair challenges that arose over the course of my time in the department. I am grateful for all the ardent friendships that I have had the distinct pleasure to have made in Nashville. In particular, fervent thanks to Dr. Ilknur S. Sevimli, Dr. Joseph W. Webb, Utsav Kumar, Dan Shae, Max Jacobson, Devon Powers, Krysta Waldrop, Francis Knight, Ajay Chhokra, Tim Moore, Andrew Summers, and ValaRae Partee.

I would like to thank the National Science Foundation and the U.S. Office of Naval Research for their financial support of this research through the grants CMMI-1300406 and N00014-10-1-0958 P00012, respectively. I would also like to thank the Vanderbilt Institute of Nanoscale Science and Engineering (VINSE) and the Mass Spectrometry Research Center for their support of this research in the form of instrumentation access.

Finally, and most importantly, I would like to thank the people that motivate me to strive for greater accomplishments and to whom this dissertation is dedicated, my family. Without the love and support of my parents, I would have never made it this far. They sacrificed their happiness and comfort in order for me to accomplish all that

I have in life and for that I will forever be grateful. I thank God each and every day to have blessed me with such industrious, sanguine, generous, and affectionate parents. I would like to thank my brother, Kevin, and his family Lydiah and Shane. Without you my life would be dull and without meaning. You have always managed to inspire the best (and sporadically the worst) in me, you have and continue to always reveal to me new perspectives and approaches to life. Where I seem to languish, you thrive and for that, I will for now and always be forever grateful. I am eternally thankful for your unbridled enthusiasm and joy and for your ability to inject that in the lives of everyone you meet. I would like to thank Jerry Momoh, Kayla Momoh and Jerry Momoh jr. You have adopted me as one of your own and treated me likewise. Ever since we met at St. Andrews Presbyterian college, you have been my home away from home and I am eternally grateful to have known you. My journey would have been infinitely more difficult if I did not have the immense privilege to call you family. I would also like to thank the mentors and giants that I have had the unique privilege of calling family. In particular, the late Reverend Dr. Godfrey Phillip Wa Ngumi, the late Grace Wairimu Wa Mbugua, the late Elijohn Gitata Wa Mbothu, the late Milicah Wanjiku Wa Gitata, the late David Githang'a Wa Njuguna, Virginia Wanjiru Wa Githang'a, and Violet Wandithia Wa Githang'a. Without you, I would not be the person that I am today and I thank God everyday for bringing and keeping you in my life. Last but not least I would like to thank my partner in life (especially these last trying months) Professor Marsha E. Barrett. You are the light of my life and knowing you has been the greatest gift I could have ever asked for. I cannot wait for the adventures that lie ahead, both personally and professionally and I hope that you will always be at my side now and always.

PREFACE

Ionic liquids (ILs) are organic salts that are liquid at or near room temperature (i.e. below 100 °C). They possess unique materials and solvent properties that have led to their use in multiple applications. Poly(ionic liquids) (PILs) refer to a special type of polyelectrolyte that carries an IL species in each of the polymer repeating units. PILs offer advantages over ILs in enhanced mechanical stability, and improved processability, durability and spatial control over the IL moieties. The ability to generate surface-tethered polymer films with IL functionality as side chains can enable coatings with versatile and tailorable properties. This dissertation describes the preparation and characterization of surface-polymerized ILs.

Surface-tethered poly(ionic liquid) (PIL) films were prepared via surface-initiated ring-opening metathesis polymerization (SI-ROMP) of ionic liquid-tethered monomers on gold, silicon, and glass substrates and were shown to be adaptive to their anionic environment. Chapter 4 reports the surface-initiated ring-opening metathesis polymerization (SI-ROMP) of ionic liquid-tethered monomers to grow poly(ionic liquid) (PIL) films on gold and glass substrates. The kinetics of film growth are rapid, with profilometric thicknesses approaching 600 nm within 15 min of polymerization in a 0.1 M monomer solution and substantial film growth observed at monomer concentrations as low as 0.02 M. The ionic liquid (IL) monomer consists of the cation 3-[(bicyclo[2.2.1]hept-5-en-2-yl)ethyl]-1,2-dimethylimidazol-3-ium ($N_1{-}dMIm^+$) with the hexafluorophosphate ($PF_6{}^-$) anion. SI-ROMP of the IL monomer results in a surface-tethered poly(3-[(bicyclo[2.2.1]hept-5-en-2-yl)ethyl]-1,2-dimethylimidazol-3-ium hexafluorophosphate) (p[$N_1{-}dMIm$][PF_6]) film whose $PF_6{}^-$ anion can be easily interchanged to tune the film properties. The p[$N_1{-}dMIm$][PF_6] films are adaptive to their anionic environment with the extent of anion exchange quantified by reflectance-

absorption infrared spectroscopy and ultraviolet-visible spectroscopy. Anionic dyes incorporated into the p[N_1−dMIm] films via anion exchange resulted in a reversible color change in the films. The surface and bulk interaction of the p[N_1−dMIm] films with water was quantified by contact angle goniometry and quartz crystal microbalance with dissipation (QCM-D). The p[N_1−dMIm] film with the perchlorate (ClO_4^-) ion exhibited the lowest advancing contact angle with water of $35 \pm 3°$ compared to the p[N_1−dMIm] film with the bistriflate ($^-NTf_2$) ion which exhibits the highest water contact advancing angle of $65 \pm 3°$. The p[N_1−dMIm][ClO_4] film demonstrated an 8% increase in bulk water content, as determined by QCM-D, compared to the p[N_1−dMIm][PF_6] film. The rate of ion transfer through the film was highly dependent on the anion as characterized by electrochemical impedance spectroscopy (EIS) in different electrolytes. In particular, resistances to ion transfer ranged from 7.90 ± 0.11 kΩ·cm^2 for films containing the PF_6^- anion to $\leq (4.34 \pm 0.04) \times 10^{-3}$ kΩ·cm^2 for films containing the ClO_4^- anion.

For surface-tethered PIL films on gold substrates, anion exchange with certain anions such as triflate, led to the desorption of the PIL films from the surface due to entropic effects and an increase in the glass transition temperature of the films. Chapter 5 explores the fundamental intermolecular forces at play in surface-tethered PILs. I report the preparation of p[N_1−dMIm][PF_6] films on silicon substrates and the incorporation of anions that cause a desorption of the polymer film on gold substrates. I synthesized an IL monomer, 3-[(bicyclo[2.2.1]hept-5-en-2-yl)propyl]-1,2-dimethylimidazol-3-ium hexafluorophosphate ([N_3−dMIm][PF_6]) that incorporates a propyl group between the polymerizable norbornene and the dimethylimidazolium cation. Here, I report the preparation of surface-immobilized PIL films on planar gold substrates via the SI-ROMP of the IL monomer [N_3−dMIm][PF_6]. The increase in repeat unit molecular volume (V_m) for the [N_3−dMIm][PF_6] monomer led to a decrease in the glass transition temperature (T_g) of the surface-tethered film and al-

lowed the incorporation of anions for which anion exchange resulted in a desorption of the p[N_1−dMIm][PF_6] film on gold substrates.

A simple anion exchange of PIL films with aqueous solutions containing a binary mixture anions led to the formation of random copolymer PIL films, that offered a continuous tuning of film properties between the extremes of the two homopolymers incorporating the anions present in the copolymer films. Chapter 6 reports a novel and simple approach to achieve surface-tethered PIL copolymer films via anion exchange. Initially, surface-tethered PIL films were prepared by the SI-ROMP of the ionic liquid monomer [N_1−dMIm][PF_6] whose PF_6^- anion was easily interchanged with aqueous solutions consisting of a binary mixture of anions. The binary mole fraction of each anion in the film was determined by analyzing the infrared spectra of the copolymer films. The thermodynamically driven anion selectivity for exchange from the liquid phase into the PIL copolymer films was determined to follow the order $ClO_4^- > PF_6^- > FSI^-$. The surface wettability of p[N_1−dMIm] copolymer films with the PF_6^- and ClO_4^- anions (p[N_1−dMIm][PF_6][ClO_4]) was quantified by contact angle goniometry with the observation that the surface showed an enrichment in the ClO_4^- anion compared to the average binary anion mole fraction of ClO_4^- in the film (y_{ClO_4}). The rate of ion transport through the p[N_1−dMIm][PF_6][ClO_4] copolymer films linearly depends on the binary anion mole fraction of ClO_4^- in solution (x_{ClO_4}) allowing an extension of the discrete tunability of PIL films to a continuous tunability with the PIL copolymer films to obtain specific properties for any desired application.

Part of the dissertation examines polydicyclopentadiene (pDCPD), which is a rigid, cross-linked polymer with excellent impact strength, high modulus, and high chemical resistance. Commercially used for automotive panels and sporting goods, pDCPD has been experimentally explored for a broad range of applications including ballistic protection. While bulk pDCPD has broad commercial impact, the ability to prepare surface-immobilized polymer films of pDCPD, especially with minimal en-

vironmental impact, could lead to tough, impact-resistant surfaces with numerous applications. In Chapter 7, surface-tethered pDCPD films were prepared on gold and silicon substrates via SI-ROMP of DCPD. The films were grown utilizing monomer in both the vapor phase and the solution phase with the former process exhibiting rapid kinetics producing ∼400 nm thick pDCPD films in less than 1 min of polymerization. No significant differences in thickness were observed for films generated from monomer in the vapor phase with the different isomers (*exo* and *endo*) of DCPD. Decane was used as an inert additive to control the concentration of DCPD monomer in the vapor phase enabling the preparation of pDCPD films with thickness ranging from tens to hundreds of nanometers. The thickness of pDCPD films polymerized using monomer in the vapor phase was enhanced by the presence of a rinsate solvent on the surface of the ROMP-active gold substrates. The choice of ROMP catalyst was an important factor when SI-ROMP was conducted on different substrates. Electrochemical impedance spectroscopy revealed that the films provide effective barriers to the diffusion of aqueous ions in excess of $1 \times 10^6\ \Omega \cdot \mathrm{cm}^2$. The mechanical properties of the surface-tethered pDCPD films were quantified with AFM PeakForce quantitative nanomechanical mapping (QNM) with a measured reduced Young's Modulus (E_r) of 15 GPa. The measured E_r was greater than that of a non cross-linked surface-tethered polymer, pNB, indicating that the pDCPD films are stiffer.

TABLE OF CONTENTS

LIST OF TABLES

LIST OF FIGURES

LIST OF SCHEMES

Chapter 1

INTRODUCTION

Ionic liquids (ILs) are organic salts that are liquid at or near room temperature (i.e. below 100°C) and whose liquid character arises from electrostatic interactions with weakly coordinating ions and large asymmetric chemical structures.[1–6] ILs possess unique physicochemical properties such as negligible vapor pressure, chemical, thermal and electrochemical stability, nonflammability, and relatively high ionic conductivity.[2,3,6,7] Their unique physicochemical properties have led to their use in multiple applications, including as solvents, electrolytes, catalysts, and polymer plasticizers.[8–14] The IL properties are tunable by either the anion or the cation.[2,3,15,16] The anion strongly influences the properties of the IL leading to a gross tuning of IL properties, such as an increase in hydrophobicity by utilizing relatively hydrophobic anions such as bis(trifluoromethanesulfonyl)imide ($^{-}NTf_2$) as compared to hydrophilic anions such as acetate.[2,16] The IL properties can be more finely tuned by varying the cation.[3,15,16]

Poly(Ionic Liquids)

Poly(ionic liquids) (PILs) are permanent polyelectrolytes composed of a polymeric backbone that carries an IL species (cation or anion) in each of its repeating units.[3–5,7] The majority of studies on PILs polymerize an ionic liquid monomer consisting of a polymerizable group tethered to the cation of an IL.[2–5,7] Tethering the cation as opposed to the anion leads to a highly tunable PIL due to the strong influence of the anion on the properties of ILs. PILs differ from classical polyelectrolytes, which are synthesized from solid salt monomers, in that the IL species has a solvent-independent ionization state.[3–5] In addition to retaining the tunable physicochemical properties

of ILs, PILs have additional advantages over ILs such as enhanced mechanical stability, improved processability and durability, and spatial control over the IL species within the polymer structure.[2–5] The solubility of PILs in water can be controlled by exchanging hydrophobic anions into the PIL, resulting in the precipitation of the polymer out of aqueous solution.[3,5,7] The enhanced properties of PILs compared to ILs have led to their incorporation as solid electrolytes in electrochemical devices, sorbents, dispersants, catalysts, separation polymers, and smart materials.[2–5,7] The ionic conductivity in bulk PIL depends on both the anion and cation of the PIL.[2,4] For bulk PIL in which the cation is immobilized on the polymer chain, the PIL becomes a single ion conductor and the choice of anion greatly influences the ionic conduction of the PIL film.[2,4,7] In comparison to ILs, PILs exhibit diminished ionic conductivity due to the immobilization of one of the ions of the IL.

Tethering PILs to surfaces enables the retention of the advantages of PILs in addition to enhancing PIL properties such as thier mechanical stability and processability.[5,6] Surface-initiated polymerization (SIP) can provide improved adhesion of the polymer film, superior control of the film thickness and composition, easy separation of the film from the monomer and exchanged ions, adaptability to multiple substrate compositions, and the ability to prepare uniform films on planar and non-planar geometries.[17,18] Among the various types of SIP, surface-initiated ring-opening metathesis polymerization (SI-ROMP) has emerged over the past decade as a technique for rapid growth that is adaptable to multiple substrates.[17,19,20] The utility and appeal of SI-ROMP has increased with the development of well-defined ROMP catalysts (**1**), leading to rapid initiation and polymerization in comparison to other SIP methodologies such as surface-initiated atom-transfer radical polymerization (SI-ATRP).[21–23]

In Chapter 4, I report the preparation of surface-immobilized PIL films on planar substrates of glass and gold via the SI-ROMP of the IL monomer 3-[(bi-

cyclo[2.2.1]hept-5-en-2-yl)methyl]-1,2-dimethylimidazol-3-ium hexafluorophosphate ([N_1−dMIm][PF_6], **2**). By employing SI-ROMP, I demonstrate the rapid growth of PIL films that are > 500 nm, which is an order of magnitude greater than the thicknesses achieved by other polymerization routes. Thicker films are expected to be more robust as coatings and have greater anion absorption capacity. I investigate the anion exchange of the PIL films with various anions. I report the first incorporation of large anionic dyes into a PIL film, highlighting the ability of the films to behave as anionic chameleons, which means that the films can adapt their appearance to their anionic environment. The anion-dependent surface wettability of the PIL films was characterized by contact angle goniometry. I report the first use of quartz crystal microbalance with dissipation (QCM-D) to determine the bulk interaction of surface-anchored PIL films with water as well as the material properties of the PIL such as dynamic shear modulus and viscosity. The effect of anion on the ion conduction of the surface-anchored PIL films was analyzed using electrochemical impedance spectroscopy (EIS), revealing dramatic differences in the resistance to ion transport between the PIL films with the PF_6^- anion and the ClO_4^- anion. Understanding the ionic conduction of surface-tethered PIL films is important for the use of the films in electrochemical devices

In Chapter 5, I explore the fundamental intermolecular forces at play in surface-tethered PILs. The motivation for this study is the observation that certain anions cause desorption of the surface-tethered p[N_1−dMIm][PF_6] films on gold substrates. The desorption occurred on the same timescale as the anion exchange process. For the anions that caused desorption, the phenomenon was observed for both aqueous solutions prepared with the salts of the offending anions, as well as with ionic liquids whose resident anion was one of the offending anions.

Choi et al.[24] explored the correlation between glass transition temperature (T_g) and repeat unit molecular volume (V_m) for imidazolium ionic liquids, IL monomers,

and PILs. They observed that T_g for the IL monomers and PILs correlated with their V_m.[24] In particular, the IL monomers and PILs containing smaller counter-ions such as Br^- or $BF_4{}^-$ exhibited higher T_g due to a stronger interaction with the imidazolium cation than those with the larger $PF_6{}^-$ or $^-NTf_2$ counter- ions that act as plasticizers.[24] Choi et al.[24] also demonstrated that the imidazolium cation side chain length affected T_g independent of the counter-anion, with a decrease in T_g with increasing V_m approaching a steady value in the large V_m limit.

Ring-opening metathesis polymerization (ROMP) is an equilibrium-controlled reaction that is driven from monomer to polymer by the release of cyclic olefin strain ("ring strain") balanced by entropic penalties.[21] These entropic effects are enhanced when performing ROMP from planar substrates due to a reduction in the degree of freedom for the segmental motion of the polymer chains. SI-ROMP on gold substrates is achieved by the anchoring the catalyst onto a chemisorbed SAM, whereas for SI-ROMP on silicon and glass substrates, the catalyst is anchored onto a covalently bound SAM. A hypothesis is an increase in T_g for a surface-tethered polymer chain via anion exchange with a small counter-ion would lead to an increase in the entropic effects of tethering the chain onto the surface and in the case of chemisorption could lead to detachment of the polymer chain from the interface. I report the preparation of p[N_1−dMIm][PF_6] films on silicon substrates and the incorporation of anions which led to a desorption of the polymer film on gold substrates.

In order to increase the V_m of the IL monomer [N_1−dMIm][PF_6], I synthesized a similar IL monomer 3-[(bicyclo[2.2.1]hept-5-en-2-yl)propyl]-1,2-dimethylimidazol-3-ium hexafluorophosphate ([N_3−dMIm][PF_6]), which incorporates a propyl group between the polymerizable norbornene and the dimethylimidazolium cation. Here, I report the preparation of surface-immobilized PIL films on planar gold substrates via the SI-ROMP of the IL monomer [N_3−dMIm][PF_6]. The increase in V_m led to a decrease in the T_g of the surface-tethered film and allowed the incorporation of anions

for which anion exchange resulted in a desorption of the p[N_1−dMIm][PF_6] film on gold substrates.

Copolymer Poly(Ionic Liquids)

Copolymerization of two different monomers is a general strategy to obtain macromolecules with tuned properties.[3] Random and block copolymers of PILs have been prepared by the copolymerization of ionic monomers with other ionic or nonionic monomers.[3,5,25] Copolymerization of an ionic monomer with a nonionic monomer can lead to random or block copolymers with a dilute charge character due by the reduction of ionic moieties in the polymer backbone.[3,5,25] Crosslinked PILs can also be formed by the copolymerization of ionic monomers with bifunctional crosslinking agents or via the polymerization of bifunctional ionic monomers.[25] Copolymerization can also be done to achieve random or block copolymers with opposite charges on the backbone by the copolymerization of an anionic monomer for which the anion tethered to the polymerizable group with a cationic monomer for which the cation is tethered to the polymerizable group.[3]

Copolymerization of similar ionic (cationic or anionic) monomers having the same polymerizable moieties but different counter-ions can lead to random or block copolymers exhibiting a uniform polymer backbone but different counter-ions.[3,26] In all these approaches, the preparation of two different monomer units is required presenting a synthetic burden to prepare the monomers as well as a challenge to find the optimal polymerization conditions for the formation of the copolymers. A copolymer of PILs, however, can exhibit an increased tunability due to an increase in the number of degrees of freedom for the manipulation of material properties. PILs allow the tuning of the material properties in discrete quantities by anion or cation exchange. An additional tuning knob in the form of a second ionic moiety could provide access to wide array of material properties.

In Chapter 6, I report a novel, simple approach to achieve surface-tethered PIL copolymer films via anion exchange. Initially, surface-immoblized PIL films on gold planar substrates were prepared by the SI-ROMP of $[N_1{-}dMIm][PF_6]$ whose PF_6^- anion can easily be interchanged to tune film properties in discrete quantities. In my approach, anion exchange of the surface-immobilized $p[N_1{-}dMIm][PF_6]$ films with aqueous solutions consisting of a binary mixture of anions provides a novel, rapid route to achieve random surface-tethered PIL copolymers. This route is advantageous compared to traditional PIL copolymerization strategies in that it only requires the synthetic preparation of one monomeric unit to achieve random PIL copolymer films. The preparation of random PIL copolymers via anion exchange is a reversible process providing the capability to reacquire the material properties of the PIL homopolymer prior to the binary anion exchange. In this way the advantages of the PILs are retained and enhanced by the ability to easily prepare PIL copolymer films from the PIL homopolymers.

The binary mole fraction of each anion in the film was determined by analyzing the infrared spectra of the copolymer films. By utilizing a thermodynamic model for the anion exchange equilibrium, I determined the thermodynamically driven anion selectivity for exchange of each anion in the binary mixture from the liquid phase into the PIL copolymer films. I observed that the thermodynamic driving force for anion exchange from the liquid phase to the solid phase follows the order $ClO_4^- > PF_6^- > FSI^-$. The surface wettability of $p[N_1{-}dMIm]$ copolymer films with the PF_6^- and ClO_4^- anions ($p[N_1{-}dMIm][PF_6][ClO_4]$) was quantified by contact angle goniometry with the observation that the surface showed an enrichment in the ClO_4^- anion compared to the average binary anion mole fraction of ClO_4^- in the film (y_{ClO_4}). The rate of ion transport through the $p[N_1{-}dMIm][PF_6][ClO_4]$ copolymer films was shown to be linearly dependent on the binary anion mole fraction of ClO_4^- in solution (x_{ClO_4}) allowing an extension of the discrete tunability of PIL films to a continuous

tunability for obtaining specific properties.

Polydicyclopentadiene

Polydicyclopentadiene (pDCPD) is a rigid, cross-linked polymer with excellent impact strength, high modulus, and high chemical resistance.[27,28] pDCPD is produced commercially via a ring-opening metathesis polymerization (ROMP), reaction injection molding (RIM) process with a variety of metathesis catalysts including the well-defined Grubb's 2nd generation catalyst. Commercially used for automotive panels and sporting goods,[27,28] pDCPD has been experimentally explored for a broad range of applications including ballistic protection.[29] While bulk pDCPD has broad commercial impact, the ability to prepare surface-immobilized polymer films of pDCPD, especially with minimal environmental impact, could lead to tough, impact-resistant surfaces with numerous applications.

SIPs that utilize monomer in the vapor phase allow for a reduction in the consumption of solvent, energy, and monomer and ensure a more environmentally sustainable polymerization process.[30] During ROMP, secondary metathesis reactions such as intermolecular chain-transfer may occur, where one polymer chain containing an active metal alkylidene on its terminus can react with any olefin along the backbone of a different polymer chain, maintaining the total number of polymer chains but increasing or decreasing the molecular weights of the individual polymers accordingly.[21,31] Introduction of the monomer in the vapor phase allows not only for the elimination of the need to find an optimal solvent to solubilize both the monomer and the growing polymer chains, but also reduces polymer chain mobility at the vapor/solid interface, minimizing the occurrence of unwanted secondary metathesis reactions.[30,32]

The majority of studies on surface functionalization using ROMP have been limited to norbornene (NB) and its derivatives due to NB's superior reactivity and ease of derivatization.[33] The ROMP reaction is driven from monomer to polymer by the

release of cyclic olefin strain ("ring strain") balanced by entropic penalties.[21] We have calculated the strain energy of dicyclopentadiene (DCPD) to be 26.7 kcal/mol, which is similar to that of NB (27.2 kcal/mol).[34] Volatile cyclic monomers such as cyclooctatetraene (COT) have been considered for SIP of monomer in the vapor phase. Gu et al.[35] reported the first polymerization of COT in the vapor phase by micro-contact printing and physisorption of catalyst **2** (Scheme 2.3) to prepare highly oriented polyacetylene films. Feng et al.[32] and Lerum and Chen[33] utilized covalently bound catalyst **2** and explored the SI-ROMP of volatile cyclic monomers in the vapor phase.

In Chapter 7, I report the tunable growth of surface-bound pDCPD from the vapor phase. The polymerization of DCPD from the vapor phase is governed by the vapor pressure of DCPD in the polymerization setup. I describe a unique method to control the concentration of DCPD in the vapor phase thereby tuning the resulting polymer film thickness. By utilizing an inert additive during polymerization, I have shown fine control of the pDPCD film thickness from 0 to 400 nm. The ability to tune the pDCPD film thickness in this manner allows the preparation of thin pDCPD films that are difficult to prepare due to the rapid polymerization kinetics of DCPD. I investigate the utility of three catalysts (Scheme 2.3) for the SI-ROMP of DCPD, all known for a high tolerance toward air, moisture, and functional groups.[36–38] I have characterized the material properties of the surface-anchored pDCPD films, including composition, surface wettability, barrier properties to aqueous ion transport, and stiffness. I report the first characterization of pDCPD films as barrier coatings by the use of electrochemical impedance spectroscopy (EIS). The mechanical properties of the pDCPD films were investigated by the use of PeakForce Quantitative Nanomechanical Mapping (QNM) to obtain the reduced Young's modulus (E_r) of the films. Here, I report the first characterization of pDCPD film elastic modulus by PeakForce QNM.

References

[1] Armand, M., Endres, F., MacFarlane, D. R., Ohno, H., and Scrosati, B. (2009) Ionic-Liquid Materials for the Electrochemical Challenges of the Future. *Nature Materials 8*, 621–629.

[2] Green, O., Grubjesic, S., Lee, S., and Firestone, M. A. (2009) The Design of Polymeric Ionic Liquids for the Preparation of Functional Materials. *Polymer Reviews 49*, 339–360.

[3] Mecerreyes, D. (2011) Polymeric Ionic Liquids: Broadening the Properties and Applications of Polyelectrolytes. *Progress in Polymer Science 36*, 1629–1648.

[4] Yuan, J., and Antonietti, M. (2011) Poly(Ionic Liquid)s: Polymers Expanding Classical Property Profiles. *Polymer 52*, 1469–1482.

[5] Yuan, J., Mecerreyes, D., and Antonietti, M. (2013) Poly(Ionic Liquid)s: An Update. *Progress in Polymer Science 38*, 1009–1036.

[6] Xin, B., and Hao, J. (2014) Imidazolium-Based Ionic Liquids Grafted on Solid Surfaces. *Chemical Society Reviews 43*, 7171–7187.

[7] Qian, W., Texter, J., and Yan, F. (2017) Frontiers in Poly(ionic liquid)s: Syntheses and Applications. *Chemical Society Reviews 46*, 1124–1159.

[8] Díaz, M., Ortiz, A., and Ortiz, I. (2014) Progress in the Use of Ionic Liquids as Electrolyte Membranes in Fuel Cells. *Journal of Membrane Science 469*, 379–396.

[9] Gebresilassie Eshetu, G., Armand, M., Scrosati, B., and Passerini, S. (2014) Energy Storage Materials Synthesized from Ionic Liquids. *Angewandte Chemie International Edition 53*, 13342–13359.

[10] Hallett, J. P., and Welton, T. (2011) Room-Temperature Ionic Liquids: Solvents for Synthesis and Catalysis. 2. *Chemical Reviews 111*, 3508–3576.

[11] Kohno, Y., Saita, S., Men, Y., Yuan, J., and Ohno, H. (2015) Thermoresponsive Polyelectrolytes Derived from Ionic Liquids. *Polymer Chemistry 6*, 2163–2178.

[12] Qureshi, Z. S., Deshmukh, K. M., and Bhanage, B. M. (2013) Applications of Ionic Liquids in Organic Synthesis and Catalysis. *Clean Technologies and Environmental Policy* 1–27.

[13] Zhang, S., Sun, J., Zhang, X., Xin, J., Miao, Q., and Wang, J. (2014) Ionic Liquid-Based Green Processes for Energy Production. *Chemical Society Reviews 43*, 7838–7869.

[14] Jiménez, A. E., and Bermúdez, M. D. (2007) Ionic Liquids as Lubricants for Steel-Aluminum Contacts at Low and Elevated Temperatures. *Tribology Letters 26*, 53–60.

[15] Ngo, H. L., LeCompte, K., Hargens, L., and McEwen, A. B. (2000) Thermal Properties of Imidazolium Ionic Liquids. *Thermochimica Acta 357-358*, 97–102.

[16] Zhang, S., Sun, N., He, X., Lu, X., and Zhang, X. (2006) Physical Properties of Ionic Liquids: Database and Evaluation. *Journal of Physical and Chemical Reference Data 35*, 1475–1517.

[17] Olivier, A., Meyer, F., Raquez, J.-M., Damman, P., and Dubois, P. (2012) Surface-Initiated Controlled Polymerization as a Convenient Method for Designing Functional Polymer Brushes: From Self-Assembled Monolayers to Patterned Surfaces. *Progress in Polymer Science 37*, 157–181.

[18] Jennings, G. K., and Brantley, E. L. (2004) Physicochemical Properties of Surface-Initiated Polymer Films in the Modification and Processing of Materials. *Advanced Materials 16*, 1983–1994.

[19] Leitgeb, A., Wappel, J., and Slugovc, C. (2010) The ROMP Toolbox Upgraded. *Polymer 51*, 2927–2946.

[20] Weck, M., Jackiw, J. J., Rossi, R. R., Weiss, P. S., and Grubbs, R. H. (1999) Ring-Opening Metathesis Polymerization from Surfaces. *Journal of the American Chemical Society 121*, 4088–4089.

[21] Bielawski, C. W., and Grubbs, R. H. (2007) Living Ring-Opening Metathesis Polymerization. *Progress in Polymer Science 32*, 1–29.

[22] Love, J. A., Morgan, J. P., Trnka, T. M., and Grubbs, R. H. (2002) A Practical and Highly Active Ruthenium-Based Catalyst that Effects the Cross Metathesis of Acrylonitrile. *Angewandte Chemie International Edition 41*, 4035–4037.

[23] Love, J. A., Sanford, M. S., Day, M. W., and Grubbs, R. H. (2003) Synthesis, Structure, and Activity of Enhanced Initiators for Olefin Metathesis. *Journal of the American Chemical Society 125*, 10103–10109.

[24] Choi, U. H., Mittal, A., Price, T. L., Lee, M., Gibson, H. W., Runt, J., and Colby, R. H. (2015) Molecular Volume Effects on the Dynamics of Polymerized Ionic Liquids and their Monomers. *Electrochimica Acta 175*, 55–61.

[25] Shaplov, A. S., Ponkratov, D. O., and Vygodskii, Y. S. (2016) Poly(ionic liquid)s: Synthesis, properties, and application. *Polymer Science Series B 58*, 73–142.

[26] Jovanovski, V., Marcilla, R., and Mecerreyes, D. (2010) Tuning the Properties of Functional Pyrrolidinium Polymers by (Co)polymerization of Diallyldimethylammonium Ionic Liquids. *Macromolecular Rapid Communications 31*, 1646–1651.

[27] Mol, J. (2004) Industrial Applications of Olefin Metathesis. *Journal of Molecular Catalysis A: Chemical 213*, 39–45.

[28] Simons, R., Guntari, S. N., Goh, T. K., Qiao, G. G., and Bateman, S. A. (2012) Poly(dicyclopentadiene)-Montmorillonite Nanocomposite Formation via Simultaneous Intergallery-Surface Initiation and Chain Crosslinking using ROMP. *Journal of Polymer Science Part A: Polymer Chemistry 50*, 89–97.

[29] Knorr, D. B., Masser, K. A., Elder, R. M., Sirk, T. W., Hindenlang, M. D., Yu, J. H., Richardson, A. D., Boyd, S. E., Spurgeon, W. A., and Lenhart, J. L. (2015) Overcoming the Structural versus Energy Dissipation Trade-Off in Highly Crosslinked Polymer Networks: Ultrahigh Strain Rate Response in Polydicyclopentadiene. *Composites Science and Technology 114*, 17–25.

[30] Fu, D., Weng, L.-T., Du, B., Tsui, O. K. C., and Xu, B. (2002) Solventless Polymerization at the Gas-Solid Interface to Form Polymeric Thin Films. *Advanced Materials 14*, 339–343.

[31] Bielawski, C. W., and Grubbs, R. H. (2000) Highly Efficient Ring-Opening Metathesis Polymerization (ROMP) using New Ruthenium Catalysts Containing N-heterocyclic Carbene Ligands. *Angewandte Chemie - International Edition 39*, 2903–2906.

[32] Feng, J., Stoddart, S. S., Weerakoon, K. A., and Chen, W. (2007) An Efficient Approach to Surface-Initiated Ring-Opening Metathesis Polymerization of Cyclooctadiene. *Langmuir 23*, 1004–1006.

[33] Lerum, M. F. Z., and Chen, W. (2011) Surface-Initiated Ring-Opening Metathesis Polymerization in the Vapor Phase: An Efficient Method for Grafting Cyclic Olefins with Low Strain Energies. *Langmuir 27*, 5403–5409.

[34] Schleyer, P. v. R., Williams, J. E., and Blanchard, K. R. (1970) Evaluation of Strain in Hydrocarbons. The Strain in Adamantane and its Origin. *Journal of the American Chemical Society 92*, 2377–2386.

[35] Gu, H., Zheng, R., Zhang, X., and Xu, B. (2004) Using Soft Lithography to Pattern Highly Oriented Polyacetylene (HOPA) Films via Solventless Polymerization. *Advanced Materials 16*, 1356–1359.

[36] Grubbs, R. H. (2004) Olefin Metathesis. *Tetrahedron 60*, 7117–7140.

[37] Trnka, T. M., and Grubbs, R. H. (2001) The Development of $L_2X_2Ru{=}CHR$ Olefin Metathesis Catalysts: An Organometallic Success Story. *Accounts of Chemical Research 34*, 18–29.

[38] P'Pool, S. J., and Schanz, H. J. (2007) Reversible Inhibition/Activation of Olefin Metathesis: A Kinetic Investigation of ROMP and RCM Reactions with Grubbs' Catalyst. *Journal of the American Chemical Society 129*, 14200–14212.

Chapter 2

BACKGROUND

Surface-Initiated Polymerizations (SIPs)

Surface-immobilized thin polymer films provide a route to alter the surface properties of a material while maintaining the bulk material properties.[1] There are two methods to achieve surface modification with polymer films, "grafting to" and "grafting from" techniques.[1] The "grafting from" approach, also called surface-initiated polymerization (SIP), provides a robust and versatile technique to achieve surface-immobilized films.[1,2] SIP is able to provide improved adhesion of the polymer film via chemisorption, superior control of the polymer film thickness and composition, easy separation of the polymer film from the monomer, tunability to multiple substrate compositions, and the ability to prepare uniform polymer films on planar and non-planar geometries.[1,2] Among the various types of SIP, surface-initiated ring opening metathesis (SI-ROMP) has emerged over the past decade as a rapid and tunable SIP technique.[1,3,4] The utility and appeal of SI-ROMP has increased with the development of well defined SI-ROMP catalysts, leading to rapid initiation and polymerization in comparison to other SIP methodologies such as SI-ATRP.[5]

Surface-Initiated Ring-Opening Metathesis (SI-ROMP)

Olefin metathesis was discovered by accident in the mid-1950s as an outgrowth of the study of Ziegler polymerizations with alternate metal systems.[6,7] The term "olefin metathesis" was coined in 1967 by Calderon and co-workers and is currently understood to mean the metal-catalyzed redistribution of carbon-carbon double bonds, which has a variety of applications including ring-opening metathesis polymerization

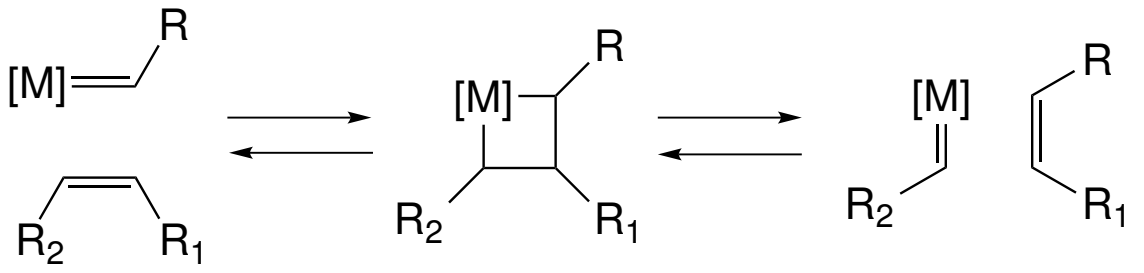

Scheme 2.1: Olefin metathesis mechanism

(ROMP), ring-closing metathesis (RCM), acyclic diene methathesis polymerization (ADMET), ring-opening metathesis (ROM), and cross-metathesis (CM or XMET).[7] Chauvin proposed that olefin metathesis involves the interconversion of an olefin and a metal alkylidene via a metallacylcobutane intermediate by alternating [2 + 2] cycloadditions and cycloreversions (see Scheme 2.1).[5–7] This led to the development of well-defined ROMP catalysts and enabled the synthesis of a wide range of polymers with complex architectures and useful functionality.[5–7]

ROMP is a chain growth polymerization process where a mixture of cyclic olefins is converted to a polymeric material.[5] ROMP reactions are generally reversible, equilibrium-controlled reactions where the position of the equilibrium (monomer vs. polymer) can be predicted by considering the thermodynamics of the polymerization.[5] The reaction is driven by the release of cyclic olefin strain ("ring strain") balanced by entropic penalties.[5] Norbornene (NB) is a cyclic seven-membered ring that exhibits high strain energy (27.2 kcal/mol) and as such exhibits superior reactivity in ROMP.[8] During ROMP it is possible for secondary metathesis reactions such as intermolecular chain-transfer to occur, where one polymer chain containing an active metal alkylidene on its terminus can react with any olefin along the backbone of a different polymer chain maintaining the total number of polymer chains but increasing or decreasing the molecular weights of the individual polymers accordingly.[5,9] ROMP catalyzed by Grubb's catalyst leads to nearly monodisperse polymers and allows the lengths of polymer chains to be controlled by chain termination or adjustment of

the monomer/catalyst ratio.[7] In addition, because the propagating species remain attached at the end of the polymer chain even after the complete consumption of the monomer, block copolymers can be synthesized by this route.[7,10]

SI-ROMP is the implementation of ROMP on surfaces. Among the various types of SIP, SI-ROMP has emerged over the past decade as a rapid and versatile SIP technique.[1,3,4] The utility and appeal of SI-ROMP has increased with the development of well defined SI-ROMP catalysts, leading to rapid initiation and polymerization in comparison to other SIP methodologies such as the more popular SI-ATRP.[5] The key step in SI-ROMP is the immobilization of the initiator/catalyst on the surface. This is usually accomplished by the immobilization of olefin functionality on the substrate either via alkene functional groups or cyclic olefin (i.e. norbornene) functional derivatives (see Scheme 2.2).[2,11,12]

ROMP Catalyst

Early olefin metathesis was accomplished with poorly defined, multicomponent homogenous and heterogenous catalyst systems that consisted of transition metal salts combined with main group alkylating agents, or deposited on solid supports.[6,7] An increased understanding of the olefin metathesis mechanism led to the discovery of the first single-component homogenous catalysts during the late 1970s and early 1980s that included catalysts based on titanium, tungsten and molybdenum that exhibited better initiation and higher activity.[6,7] Functional groups (including oxygen and water) in the substrate or solvent can interfere with catalytic activity by binding competitively to the active metal center and deactivating the catalyst, or by reacting directly with the metal center and destroying the active species.[7] Ruthenium catalysts react preferentially with carbon-carbon double bonds over other species, making catalysts based on ruthenium unusually stable toward alcohols, amides, aldehydes and carboxylic acids when compared to earlier transition metal (Ti, W and Mo), based

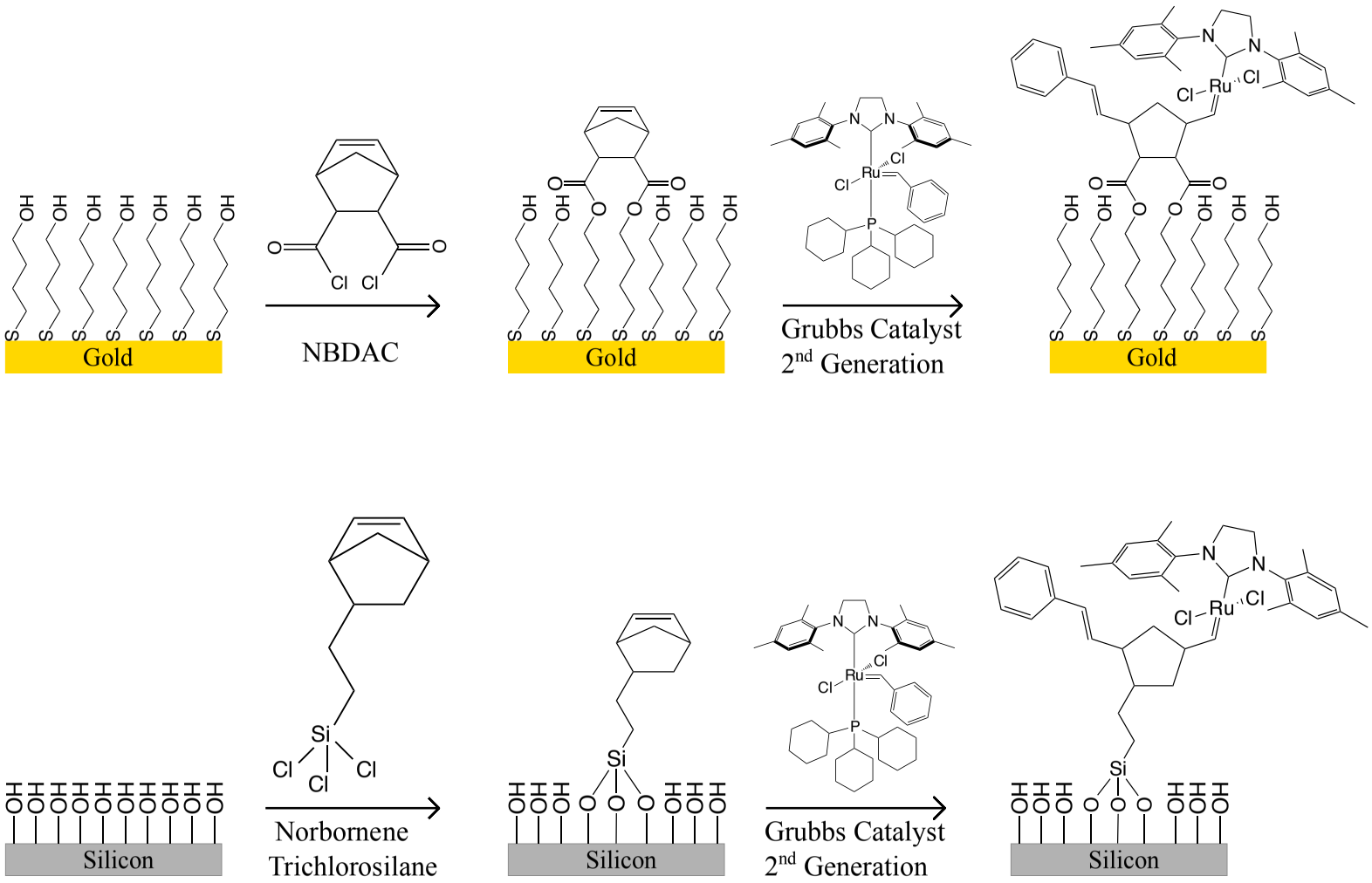

Scheme 2.2: Initiator/catalyst immobilization on gold and silicon substrates.

catalysts.[6,7]

Grubb's catalysts (Scheme 2.3) are homogeneous ruthenium-alkylidene metathesis catalysts that show high tolerance toward air, moisture and functional groups.[6,7,13] Grubb's 1st generation catalyst (**1**), was the first commercially available ruthenium based catalyst, which enabled its widespread use for a variety of applications ranging from the synthesis of pharmaceutical intermediates to the production of a variety of polymer composites.[6,7] The mechanism of metathesis using ruthenium catalysts proceeds by the loss of one of the neutral ligands to produce a 14 e^- species.[14,15] The decomposition of **1** is second order in the 14 e^- species and inversely proportional to phosphine concentration, while productive metathesis is first order in the 14 e^- species.[14,15] Substitution of one of the phosphines in **1** with a N-hetero-cyclic carbene (NHC) was performed in an attempt to increase activity as a result of the NHC ligand ston σ-donating ability and decreased lability, leading to Grubb's 2nd generation catalyst **(2)**.[6,7]

Catalyst **2** exhibited performance that was previously possible only with the most active early metal systems, displayed high rates of ROMP for low-strain substrates, and even accomplished the ROMP of sterically hindered substrates.[6,7,9,14,15] The efficiency of the catalyst depends on the rates of initiation, phosphine rebinding, reaction of the 14 e^- species with olefin and catalyst decomposition.[6,10] While catalyst **2** shows a 2 fold decrease in the rate of formation of the 14 e^- species compared to **1**, it shows an overall catalytic activity that is 2 orders of magnitude higher than that of **1** as the partitioning between the coordination of the alkene substrate and the rebinding of the phosphine ligand is about 4 orders of magnitude greater for **2** relative to **1**.[6,10,16] The high activity of **2** is attributed to its improved selectivity for binding $\pi-$acidic olefinic substrates in the presence of $\sigma-$donating free phosphine and not due to its ability to promote phosphine dissociation.[6,14,16] The activity of **2** has also been shown to be improved at elevated temperatures ($\geq 50\,^{\circ}C$).[9,13] In general, the rate of

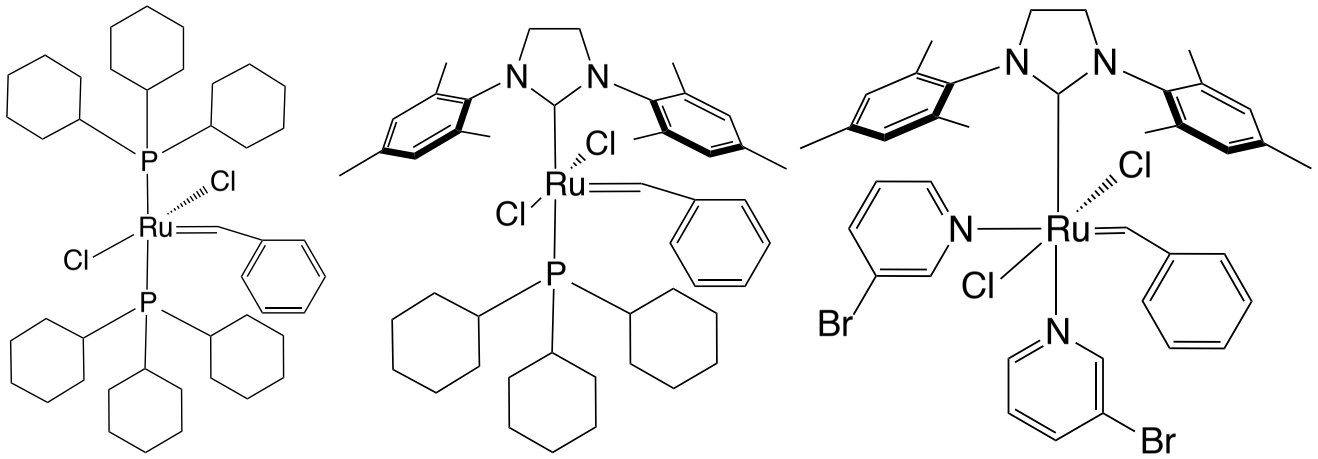

1 **2** **3**

Scheme 2.3: **1**) Grubb's Catalyst 1 st Generation $[(PCy_3)_2(Cl)_2Ru{=}CHPh]$. **2**) Grubb's Catalyst 2 nd Generation $[(H_2IMes)(PCy_3)(Cl)_2Ru{=}CHPh]$. **3**) [1,3-dimesityl-4,5-dihydroimidazol-2-ylidene]bis(3-bromopyridine)dichloro (benzylidene)ruthenium(II) $[(H_2IMes)(3-Br-py)_2(Cl)_2Ru{=}CHPh]$.

catalysis can be improved by increasing the rate of initiation without a substantial increase in the rate of ligand rebinding.[16,17]

The rate of initiation of catalyst **2** can be improved by modifying the ligand environment with bis(pyridine)-coordinated complexes, by taking advantage of the lability of pyridine ligands.[10] Synthesis of bis(pyridine) complexes is easily accomplished by the addition in excess of the appropriate pyridine to **2**.[10,17] Grubb's 3rd generation catalyst **(3)**, can be prepared within minutes via the reaction of **2** (0.59 mmol) with 3-bromopyridine (5.9 mmol).[10,17] The product is isolated in up to 95% yield by simple precipitation with pentane and without further purification.[17] Catalyst **3** has been shown to initiate ROMP at least six orders of magnitude faster than **2**.[10,17]The rapid initiation of catalyst **3** has enabled the production of polymers with very narrow polydispersity and block copolymers.[10]

Poly(Ionic Liquids) (PILs)

Ionic liquids (ILs) are organic salts that are liquid at or near room temperature (i.e. below 100°C).[18,19] Their unique properties have led to their use in multiple applications, including as solvents, electrolytes, catalysts, lubricants, and polymer plasticizers.[20–26] The structure and interaction of ions in the ionic liquids determine their unique physicochemical properties, such as negligible vapor pressure, chemical, thermal and photocatalytic stability, nonflammability, and relatively high ionic conductivity.[18] ILs exhibit lower friction and wear values than traditional liquid lubricants (oils), and their performance depends on the thermal stability, polarity, ability to form ordered adsorbed layers, and the tribocorrosion process at the interface.[26]

pILs are polymers that contain IL groups as side chains.[19] The ability to generate polymer films with IL functionality as side chains can enable coatings with versatile and tailorable properties. He et al.[27] reported the first preparation of pIL brushes by surface-initiated atom transfer radical polymerization (SI-ATRP), where they pre-

pared poly([1-(4-vinylbenzyl)-3-butyl imidazolium] [hexafluorophosphate]) brushes on a flat silicon substrate. They demonstrated the tunable wettability of the pIL brushes by exchanging their counter anions and nanometer-level control over film thickness, using brushes that were $\sim$ 50 nm thick obtained from a 24 h polymerization time.[27] Ye et al.[28] reported the first preparation of pIL brushes via SI-ROMP, where they prepared poly([1-norbornylmethylene-3-methylimidazolium][hexafluorophosphate]) brushes on titanium dioxide (TiO_2) nanowires. They also demonstrated the tunable wettability of the pIL brushes by exchanging their counter anions, using brushes that were $\sim$ 80 nm thick obtained from a 2 h polymerization time.[28]

Ishikawa et al.[29] have performed the only investigation to date of a pIL brush in tribological applications, where they showed that low sliding frictional coefficients (COF $\sim$ 0.01) could be achieved when the substrate and probe both contained a pIL brush and a compatible IL was used as a mobile component. Ishikawa et al. were also able to demonstrate the wear characteristics of the pIL brush, while they were only able to achieve $\sim$ 50 nm thick pIL brushes over a 72 h SI-ATRP process, the pIL brushes were able to withstand up to 800 friction cycles before an increase in the COF in a dry nitrogen atmosphere.

Polydicyclopentadiene (pDCPD)

Dicyclopentadiene (DCPD) is produced in large quantities as a byproduct of petroleum cracking, making DCPD one of the cheapest monomers for ROMP.[30] pDCPD is a tough, rigid, thermoset, industrially important cross-linked polymer with excellent impact strength, high modulus, and high chemical resistance.[31,32] pDCPD is produced commercially via a reaction-injection molding (RIM) process and is commercially used for heavy-truck hoods, tonneau covers for pick-up trucks, snow mobile hoods, tractor fenders, automobile fenders and sporting goods.[31] The polymer is commercially produced with a variety of metathesis catalysts, such as tungsten and

molybdenum complexes combined with alkylaluminums and can be formed via ROMP using a ruthenium catalyst.[6,31,32] Simons et al.[32] reported SI-ROMP of dicyclopentadiene from the surface of clay-based composites utilizing catalyst **3**; however, no other instance of surface polymerization of DCPD has been reported in the literature.

References

[1] Olivier, A., Meyer, F., Raquez, J.-M., Damman, P., and Dubois, P. (2012) Surface-Initiated Controlled Polymerization as a Convenient Method for Designing Functional Polymer Brushes: From Self-Assembled Monolayers to Patterned Surfaces. *Progress in Polymer Science 37*, 157–181.

[2] Jennings, G. K., and Brantley, E. L. (2004) Physicochemical Properties of Surface-Initiated Polymer Films in the Modification and Processing of Materials. *Advanced Materials 16*, 1983–1994.

[3] Leitgeb, A., Wappel, J., and Slugovc, C. (2010) The ROMP Toolbox Upgraded. *Polymer 51*, 2927–2946.

[4] Weck, M., Jackiw, J. J., Rossi, R. R., Weiss, P. S., and Grubbs, R. H. (1999) Ring-Opening Metathesis Polymerization from Surfaces. *Journal of the American Chemical Society 121*, 4088–4089.

[5] Bielawski, C. W., and Grubbs, R. H. (2007) Living Ring-Opening Metathesis Polymerization. *Progress in Polymer Science 32*, 1–29.

[6] Grubbs, R. H. (2004) Olefin Metathesis. *Tetrahedron 60*, 7117–7140.

[7] Trnka, T. M., and Grubbs, R. H. (2001) The Development of $L_2X_2Ru{=}CHR$ Olefin Metathesis Catalysts: An Organometallic Success Story. *Accounts of Chemical Research 34*, 18–29.

[8] Lerum, M. F. Z., and Chen, W. (2011) Surface-Initiated Ring-Opening Metathesis Polymerization in the Vapor Phase: An Efficient Method for Grafting Cyclic Olefins with Low Strain Energies. *Langmuir 27*, 5403–5409.

[9] Bielawski, C. W., and Grubbs, R. H. (2000) Highly Efficient Ring-Opening Metathesis Polymerization (ROMP) using New Ruthenium Catalysts Contain-

ing N-heterocyclic Carbene Ligands. *Angewandte Chemie - International Edition 39*, 2903–2906.

[10] Vougioukalakis, G. C., and Grubbs, R. H. (2010) Ruthenium-Based Heterocyclic Carbene-Coordinated Olefin Metathesis Catalysts. *Chemical Reviews 110*, 1746–1787.

[11] Berron, B. J., Graybill, E. P., and Jennings, G. K. (2007) Growth and Structure of Surface-Initiated Poly(n-alkylnorbornene) Films. *Langmuir 23*, 11651–11655.

[12] Escobar, C. A., Harl, R. R., Maxwell, K. E., Mahfuz, N. N., Rogers, B. R., and Jennings, G. K. (2013) Amplification of Surface-Initiated Ring-Opening Metathesis Polymerization of 5-(Perfluoro-n-alkyl)norbornenes by Macroinitiation. *Langmuir 29*, 12560–12571.

[13] P'Pool, S. J., and Schanz, H. J. (2007) Reversible Inhibition/Activation of Olefin Metathesis: A Kinetic Investigation of ROMP and RCM Reactions with Grubbs' Catalyst. *Journal of the American Chemical Society 129*, 14200–14212.

[14] Love, J. A., Sanford, M. S., Day, M. W., and Grubbs, R. H. (2003) Synthesis, Structure, and Activity of Enhanced Initiators for Olefin Metathesis. *Journal of the American Chemical Society 125*, 10103–10109.

[15] Scholl, M., Ding, S., Lee, C. W., and Grubbs, R. H. (1999) Synthesis and Activity of a New Generation of Ruthenium-Based Olefin Metathesis Catalysts Coordinated with 1,3-Dimesityl-4,5-dihydroimidazol-2-ylidene Ligands. *Organic Letters 1*, 953–956.

[16] Sanford, M. S., Ulman, M., and Grubbs, R. H. (2001) New Insights into the Mechanism of Ruthenium-Catalyzed Olefin Metathesis Reactions. *Journal of the American Chemical Society 123*, 749–750.

[17] Love, J. A., Morgan, J. P., Trnka, T. M., and Grubbs, R. H. (2002) A Practical and Highly Active Ruthenium-Based Catalyst that Effects the Cross Metathesis of Acrylonitrile. *Angewandte Chemie International Edition 41*, 4035–4037.

[18] Xin, B., and Hao, J. (2014) Imidazolium-Based Ionic Liquids Grafted on Solid Surfaces. *Chemical Society Reviews 43*, 7171–7187.

[19] Green, O., Grubjesic, S., Lee, S., and Firestone, M. A. (2009) The Design of Polymeric Ionic Liquids for the Preparation of Functional Materials. *Polymer Reviews 49*, 339–360.

[20] Díaz, M., Ortiz, A., and Ortiz, I. (2014) Progress in the Use of Ionic Liquids as Electrolyte Membranes in Fuel Cells. *Journal of Membrane Science 469*, 379–396.

[21] Gebresilassie Eshetu, G., Armand, M., Scrosati, B., and Passerini, S. (2014) Energy Storage Materials Synthesized from Ionic Liquids. *Angewandte Chemie International Edition 53*, 13342–13359.

[22] Hallett, J. P., and Welton, T. (2011) Room-Temperature Ionic Liquids: Solvents for Synthesis and Catalysis. 2. *Chemical Reviews 111*, 3508–3576.

[23] Kohno, Y., Saita, S., Men, Y., Yuan, J., and Ohno, H. (2015) Thermoresponsive Polyelectrolytes Derived from Ionic Liquids. *Polymer Chemistry 6*, 2163–2178.

[24] Qureshi, Z. S., Deshmukh, K. M., and Bhanage, B. M. (2013) Applications of Ionic Liquids in Organic Synthesis and Catalysis. *Clean Technologies and Environmental Policy* 1–27.

[25] Zhang, S., Sun, J., Zhang, X., Xin, J., Miao, Q., and Wang, J. (2014) Ionic Liquid-Based Green Processes for Energy Production. *Chemical Society Reviews 43*, 7838–7869.

[26] Jiménez, A. E., and Bermúdez, M. D. (2007) Ionic Liquids as Lubricants for Steel-Aluminum Contacts at Low and Elevated Temperatures. *Tribology Letters 26*, 53–60.

[27] He, X., Yang, W., and Pei, X. (2008) Preparation, Characterization, and Tunable Wettability of Poly(ionic liquid) Brushes via Surface-Initiated Atom Transfer Radical Polymerization. *Macromolecules 41*, 4615–4621.

[28] Ye, Q., Gao, T., Wan, F., Yu, B., Pei, X., Zhou, F., and Xue, Q. (2012) Grafting Poly(Ionic Liquid) Brushes for Anti-Bacterial and Anti-Biofouling Applications. *Journal of Materials Chemistry 22*, 13123.

[29] Ishikawa, T., Kobayashi, M., and Takahara, A. (2010) Macroscopic Frictional Properties of Poly(1-(2-methacryloyloxy)ethyl-3-butyl Imidazolium Bis(trifluoromethanesulfonyl)-imide) Brush Surfaces in an Ionic Liquid. *ACS Applied Materials & Interfaces 2*, 1120–1128.

[30] Autenrieth, B., Jeong, H., Forrest, W. P., Axtell, J. C., Ota, A., Lehr, T., Buchmeiser, M. R., and Schrock, R. R. (2015) Stereospecific Ring-Opening Metathesis Polymerization (ROMP) of *endo*-Dicyclopentadiene by Molybdenum and Tungsten Catalysts. *Macromolecules 48*, 2480–2492.

[31] Mol, J. (2004) Industrial Applications of Olefin Metathesis. *Journal of Molecular Catalysis A: Chemical 213*, 39–45.

[32] Simons, R., Guntari, S. N., Goh, T. K., Qiao, G. G., and Bateman, S. A. (2012) Poly(dicyclopentadiene)-Montmorillonite Nanocomposite Formation via Simultaneous Intergallery-Surface Initiation and Chain Crosslinking using ROMP. *Journal of Polymer Science Part A: Polymer Chemistry 50*, 89–97.

Chapter 3

EXPERIMENTAL AND CHARACTERIZATION METHODS

Materials

Gold shot (99.99 %) was obtained from J&J Materials, silicon (100) wafers were purchased from WRS Materials, and chromium-coated tungsten rods were obtained from R.D. Mathis. Deionized water ($\geq$ 2.0 MΩ) was purified using a Millipore Elix filtration system. [(5-bicyclo[2.2.1]hept-2-enyl)ethyl]trichlorosilane ($NBSiCl_3$) was obtained from Gelest, Inc.

The following chemicals were obtained from Sigma-Aldrich and used as received: 4-mercapto-1-butanol (95%), Grubbs catalyst 1 st generation $[(PCy_3)_2(Cl)_2Ru{=}CHPh]$ **(1)**, Grubbs catalyst 2 nd generation $[(H_2IMes)(PCy_3)(Cl)_2Ru{=}CHPh]$ **(2)**, 3-bromopyridine, dicyclopentadiene (98%), trans-3,6-endomethylene-1,2,3,6-tetrahydrophthaloyl chloride (NBDAC), and activated, basic Brockmann I, aluminum oxide (alumina).

The following chemicals were obtained from Fisher Scientific and used as received: allyl bromide (99%), biebrich scarlet, bromocresol green, calcium perchlorate ($Ca(ClO_4)_2$), cesium perchlorate ($CsClO_4$), chloroform, copper foil (0.025 mm thick), cresol red, 1,2-dichloroethane (DCE), 1,2-dimethylimidazole (98%, dMIm), ethanol (200 Proof), eosin Y, fluorescein, hydrogen peroxide (30%, H_2O_2), lithium bis(trifluoromethanesulfonyl)imide ($LiNTf_2$), lithium perchlorate ($LiClO_4$), methyl orange, methylene chloride (DCM), pentane, potassium bis(fluorosulfonyl)imide (KFSI), potassium hexafluorophosphate (KPF_6), potassium perchlorate ($KClO_4$), premium plain microscope slides, sodium perchlorate ($NaClO_4$), sulfuric acid (H_2SO_4), and toluene.

1-Butyl-2,3-dimethylimidazolium bis(trifluoromethylsulfonyl)imide (99%, [BdMIm][NTf_2]) was obtained from IoLiTec Ionic liquids Technologies, Inc. Ag/AgCl reference electrodes were obtained from CH instruments, Inc. Au-coated quartz crystals (4.95 MHz, 14 mm diameter, polished, and AT-cut) were obtained from Biolin Scientific.

Chemical Syntheses

[(H_2IMes)(3 −Br−py)$_2$(Cl)$_2$Ru=CHPh]

[(H_2IMes)(3 −Br−py)$_2$(Cl)$_2$Ru=CHPh] **(3)** was synthesized as described by Love et al.[1] Briefly, 3-bromopyridine (0.94 g, 5.9 mmol) and Grubbs catalyst 2 nd generation **(2)** (0.5 g, 0.59 mmol) were added to a 20 mL vial with a screw cap. The reaction was stirred for 5 min with a color change from red to bright green. Pentane (20 mL) was added into the vial with the precipitation of a green solid. The vial was capped under air and placed in the freezer overnight. The green precipitate was vacuum filtered, washed with pentane (4 x 10 mL), and dried under vacuum to yield **3** as a green powder. (0.51 g, Yield 98%)

5-(bromomethyl)bicyclo[2.2.1]hept-2-ene (N_1−Br)

5-(bromomethyl)bicyclo[2.2.1]hept-2-ene (N_1−Br) was synthesized utilizing a Diels-Alder reaction as described by Ye et al.[2] Briefly, a Parr Instruments high-pressure reaction vessel was charged with dicyclopentadiene (29.7 g, 225 mmol), allyl bromide (47 mL, 544 mmol), and hydroquinone (150 mg). The mixture was held at 170 °C for 24 h. Excess allyl bromide was removed by rotary evaporation and the remaining mixture was purified by vacuum distillation to afford a clear, colorless oil as a mixture of exo and endo isomers. (34 g, Yield 69%)

endo isomer (82%): ^{1}H NMR (400 MHz, $CDCl_3$)(ppm): δ_H 6.21 (1H, dd, J = 5.7, 3.0 Hz, H1), 6.00 (1H, dd, J = 5.7, 2.9 Hz, H2), 3.21 (1H, dd, J = 9.5, 6.8 Hz,

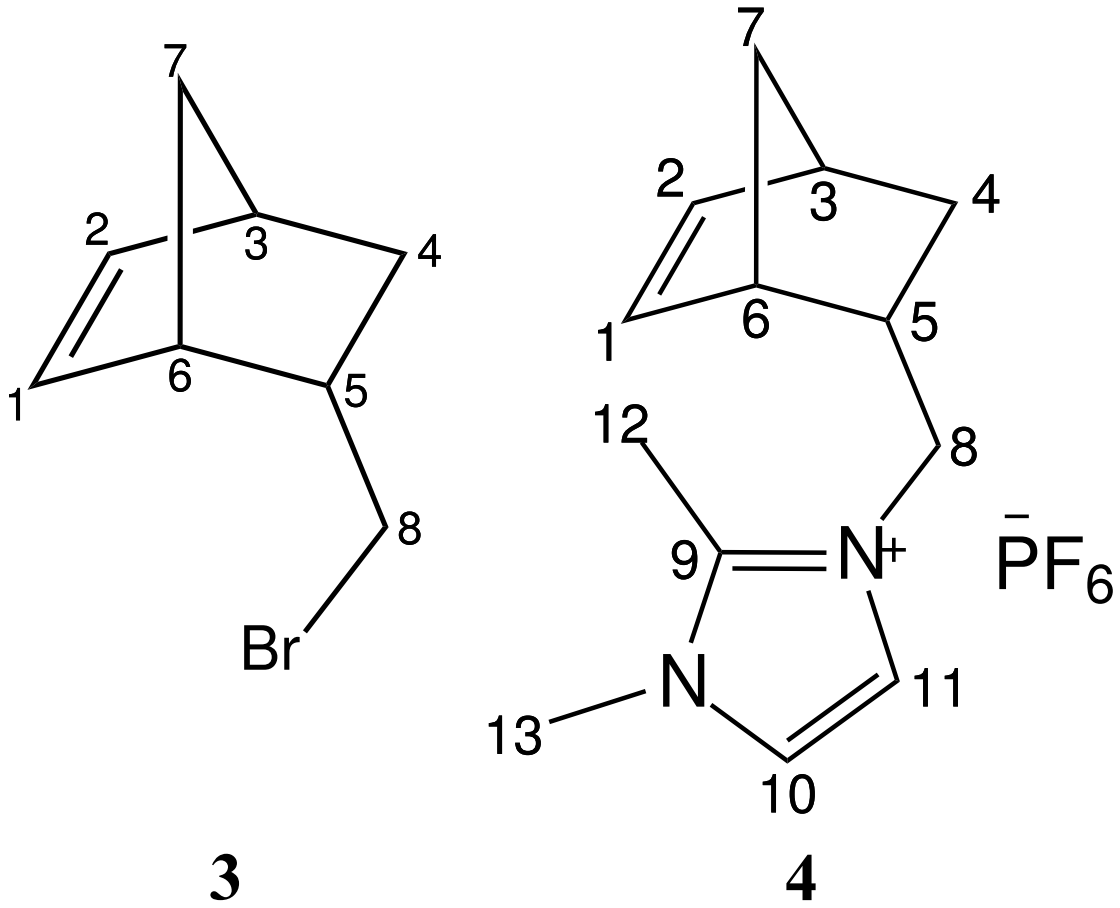

3 **4**

Scheme 3.1: Structures of the ionic liquid monomer precursor and ionic liquid monomer utilized in preparing poly(ionic liquid) films via surface-initiated ring-opening metathesis polymerization (SI-ROMP). **3**) 5-(bromomethyl)bicyclo[2.2.1]hept-2-ene (N_1-Br). **4**) Ionic liquid monomer consisting of the cation 3-[(bicyclo[2.2.1]hept-5-en-2-yl)methyl]-1,2-dimethylimidazol-3-ium (N_1-dMIm^+) and the anion hexafluorophosphate (PF_6^-)

H8), 3.04 (1H, t, $J = 9.6$ Hz, H8), 2.99 (1H, s, H6), 2.88 (1H, s, H3), 2.56 - 2.48 (1H, m, H5), 1.98 - 1.91 (1H, m, $H4_{exo}$), 1.49 (1H, dd, $J = 8.3, 2.1$ Hz, H7), 1.30 (1H, d, $J = 8.4$ Hz, H7), 0.59 (1H, dq, $J = 11.8, 4.4, 2.6$ Hz, $H4_{endo}$)

$^{13}C\{^{1}H\}$ NMR (125 MHz, $CDCl_3$)(ppm): δ_c 138.1 (s, C1), 131.5 (s, C2), 49.6 (s, C7), 45.4 (s, C6), 43.0 (s, C3), 42.0 (s, C5), 38.2 (s, C8), 32.7 (s, C4)

exo isomer (18%): ^{1}H NMR (400 MHz, $CDCl_3$,)(ppm): δ_H 6.12 (1H, dd, $J = 5.6, 3.0$ Hz, H1), 6.09 (1H, dd, $J = 5.6, 2.9$ Hz, H2), 3.48 - 3.38 (2H, m, H8), 2.88 (1H, s, H3), 2.70 (1H, s, H6), 1.90 - 1.83 (1H, m, H5), 1.43 - 1.37 (2H, m, $H4_{exo}$, H7), 1.30 (1H, d, $J = 8.4$ Hz, H7), 1.24 - 1.19 (1H, m, $H4_{endo}$)

$^{13}C\{^{1}H\}$ NMR (125 MHz, $CDCl_3$)(ppm): δ_c 136.9 (s, C1), 136.3 (s, C2), 45.8 (s, C6), 44.9 (s, C7), 42.3 (s, C3), 42.0 (s, C5), 39.2 (s, C8), 33.3 (s, C4)

The ^{1}H and ^{13}C NMR spectra for N_1-Br are shown in Figures 3.1 and 3.2.

3-[(bicyclo[2.2.1]hept-5-en-2-yl)methyl]-1,2-dimethylimidazol-3-ium Hexafluorophosphate

N_1-Br (30 g, 160 mmol) and 1,2-dimethylimidazole (18.5 g, 192 mmol) were added to a 500 mL Schlenk flask. The reaction mixture was placed under nitrogen (N_2) and stirred for $40-50$ h at 60 °C to yield a viscous liquid of 3-[(bicyclo[2.2.1]hept-5-en-2-yl)methyl]-1,2-dimethylimidazol-3-ium bromide ($[N_1-dMIm][Br]$) via the addition of the 1,2-dimethylimidazole across the C−Br bond to form the imidazolium terminus. Ethyl acetate was added to the crude reaction mixture with the precipitation of a solid. The ethyl acetate was decanted and the solid dissolved in water (200 mL). The water fraction was washed with hexanes, ethyl acetate, and DCM (3 x 300 mL). The water fraction was added dropwise with stirring at room temperature to a solution of potassium hexafluorophosphate (35.3 g, 192 mmol) and 600 mL of water with the precipitation of a white solid of 3-[(bicyclo[2.2.1]hept-5-en-2-yl)methyl]-1,2-dimethylimidazol-3-ium hexafluorophosphate ($[N_1-dMIm][PF_6]$). The reaction mixture was extracted with 1200 mL of DCM and the organic extracts were dried over

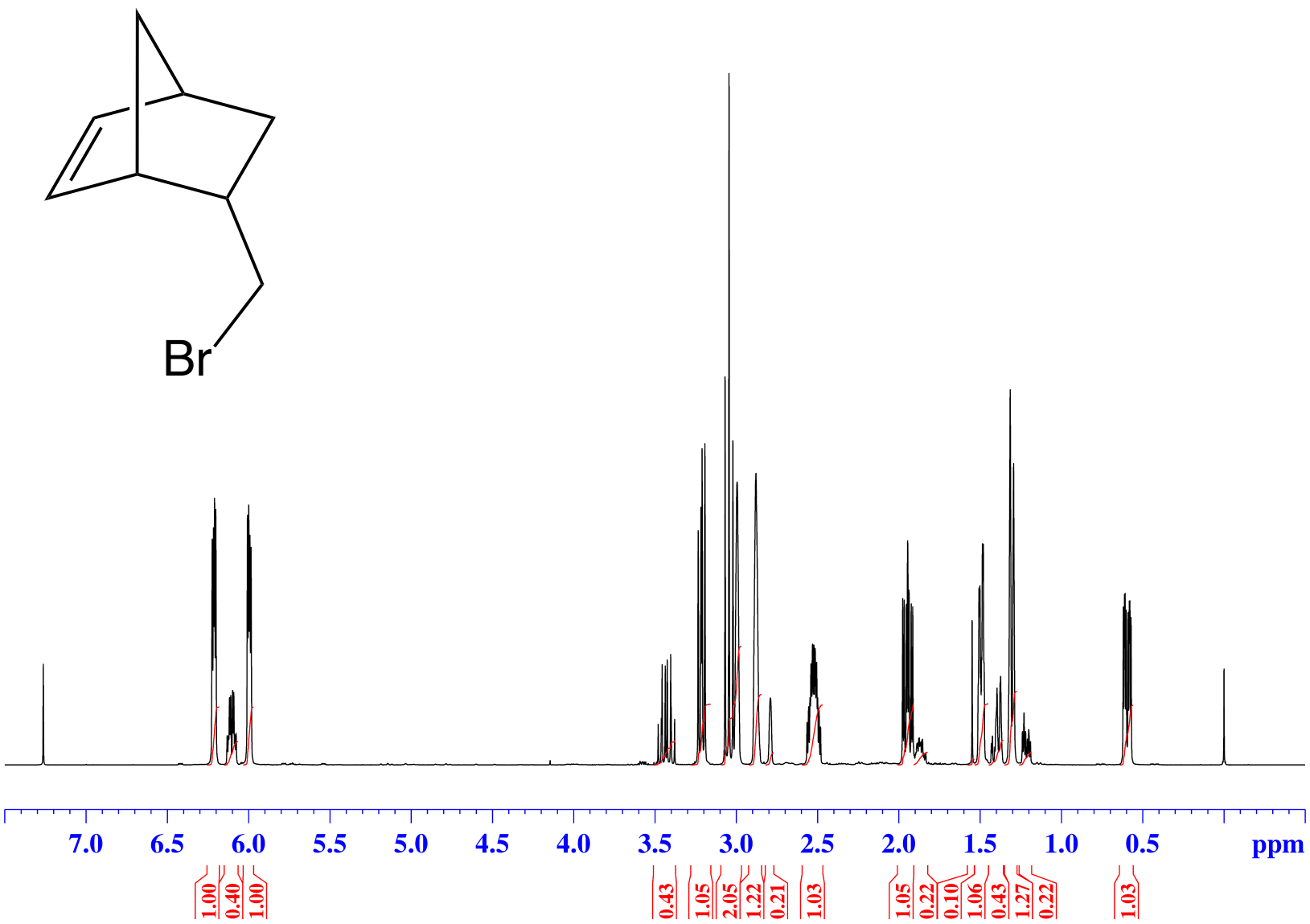

Figure 3.1: ^{1}H NMR spectrum of 5-(bromomethyl)bicyclo[2.2.1]hept-2-ene (N_1−Br) in $CDCl_3$ acquired on a 400 MHz instrument

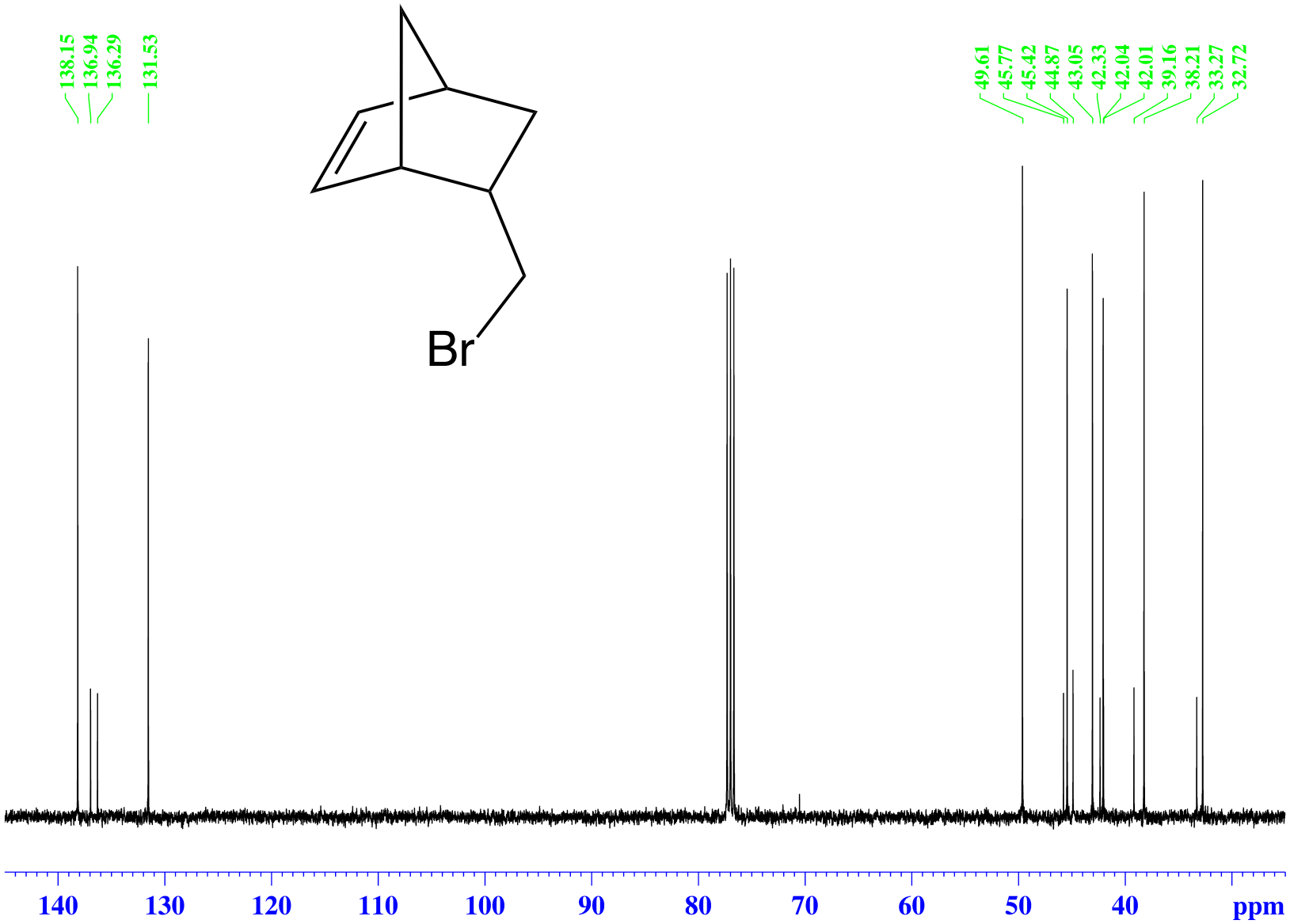

Figure 3.2: $^{13}C\{^{1}H\}$ NMR spectrum of 5-(bromoethyl)bicyclo[2.2.1]hept-2-ene (N_3-Br) in $CDCl_3$ acquired on a 400 MHz instrument

$MgSO_4$. The solvent was removed by rotary evaporation to yield a white solid, which was recrystallized in methanol. (34 g, Yield 60%)

endo isomer (79%): ^{1}H NMR (400 MHz, $(CD_3)_2CO$)(ppm): δ_H 7.59 (1H, d, J = 2.1 Hz, H10), 7.57 (1H, d, J = 2.2, H11), 6.31 (1H, dd, $J = 5.7, 3.1$ Hz, H1), 6.15 (1H, dd, $J = 5.8, 2.8$ Hz, H2), 4.03 - 3.87 (1H, m, H8), 3.94 (3H, s, H13), 3.92 - 3.87 (1H, m, H8), 2.85 (1H, s, H3), 2.79 (1H, s, H6), 2.75 (3H, s, H12), 2.73 - 2.64 (1H, m, H5), 1.99 - 1.93 (1H, m, $H4_{exo}$), 1.43 (1H, dd, $J = 8.3, 2.2$ Hz, H7), 1.31 (1H, d, $J = 8.3$ Hz, H7), 0.71 (1H, dq, $J = 11.8, 4.4, 2.6$ Hz, $H4_{endo}$)

$^{13}C\{^1H\}$ NMR (125 MHz, $(CD_3)_2CO$)(ppm): δ_c 145.5 (s, C9), 139.6 (s, C1), 132.4 (s, C2), 123.3 (s, C11), 121.9 (s, C10), 52.8 (s, C8), 50.1 (s, C7), 44.7 (s, C6), 43.1 (s, C3), 39.8 (s, C5), 35.4 (s, C13), 30.4 (s, C4), 9.8 (s, C12)

exo isomer (21%): ^{1}H NMR (400 MHz, $(CD_3)_2CO$,)(ppm): δ_H 7.65 (1H, d, J = 2.1 Hz, H10), 7.58 (1H, s, H11), 6.11 (1H, dd, $J = 5.7, 2.9$ Hz, H1), 6.05 (1H, dd, $J = 5.6, 3.2$ Hz, H2), 4.39 - 4.24 (2H, m, H8), 3.94 (3H, s, H13), 2.89 (1H, s, H3), 2.83 (1H, s, H6), 2.77 (3H, s, H12), 2.73 - 2.64 (1H, m, H5), 1.99 - 1.93 (1H, m, $H4_{exo}$),1.59 (1H, d, $J = 8.8$ Hz, H7), 1.37 (1H, s, H7), 1.36 - 1.34 (1H, m, $H4_{endo}$)

$^{13}C\{^1H\}$ NMR (125 MHz, $(CD_3)_2CO$)(ppm): δ_c 145.5 (s, C9), 138.0 (s, C1), 136.7 (s, C2), 123.3 (s, C11), 122.0 (s, C10), 53.6 (s, C8), 45.4 (s, C7), 44.5 (s, C6), 42.7 (s, C3), 40.0 (s, C5), 35.4 (s, C13), 31.1 (s, C4), 9.8 (s, C12)

HRMS (ESI) m/z: M^+ Calcd for $C_{13}H_{19}N_2$ 203.1543; Found 203.1541

The ^{1}H and ^{13}C NMR spectrum for $[N_1{-}dMIm][PF_6]$ are shown in Figures 3.3 and 3.4.

5-(bromopropyl)bicyclo[2.2.1]hept-2-ene ($N_3{-}Br$)

5-(bromopropyl)bicyclo[2.2.1]hept-2-ene ($N_3{-}Br$) was synthesized utilizing a Diels-Alder reaction. A Parr Instruments high-pressure reaction vessel was charged with dicyclopentadiene (12.2 g, 92 mmol), bromopentane (25 g, 168 mmol), and

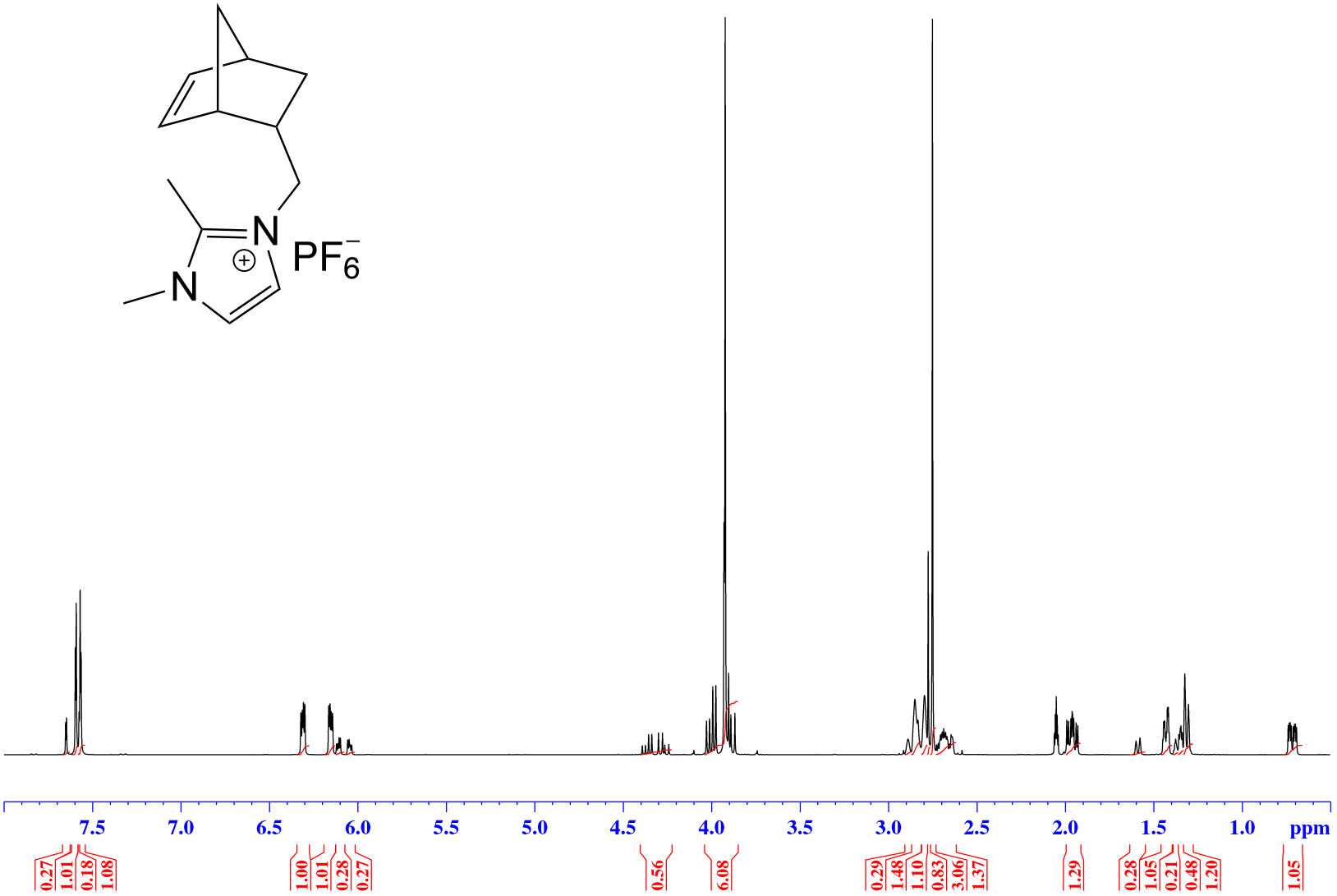

Figure 3.3: ^{1}H NMR spectrum of 3-[(bicyclo[2.2.1]hept-5-en-2-yl)methyl]-1,2-dimethylimidazol-3-ium hexafluorophosphate ($[N_1{-}dMIm][PF_6]$) in $(CD_3)_2CO$ acquired on a 400 MHz instrument.

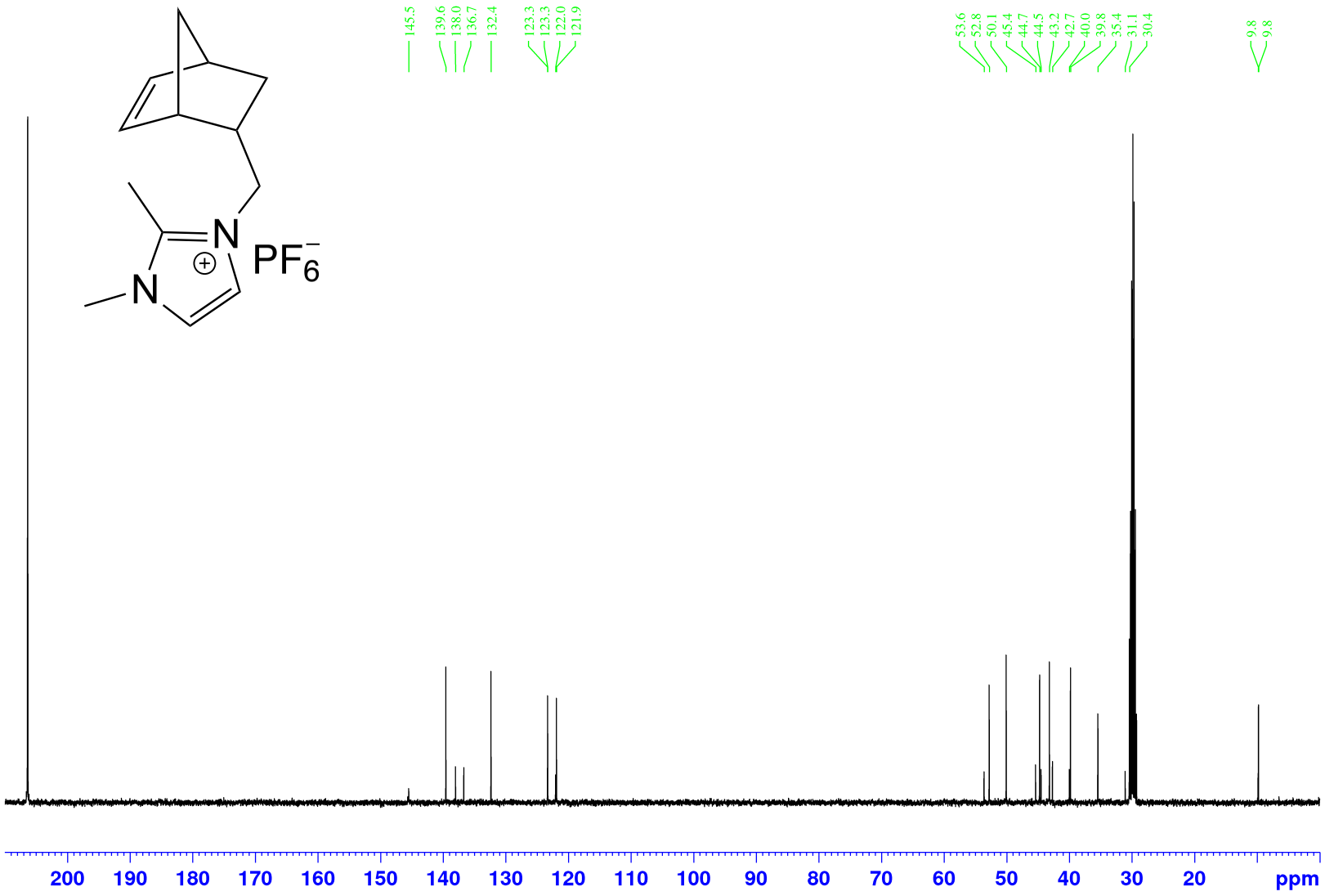

Figure 3.4: $^{13}C\{^{1}H\}$ NMR spectrum of 3-[(bicyclo[2.2.1]hept-5-en-2-yl)methyl]-1,2-dimethylimidazol-3-ium hexafluorophosphate ($[N_1-dMIm][PF_6]$) in $(CD_3)_2CO$ acquired on a 400 MHz instrument

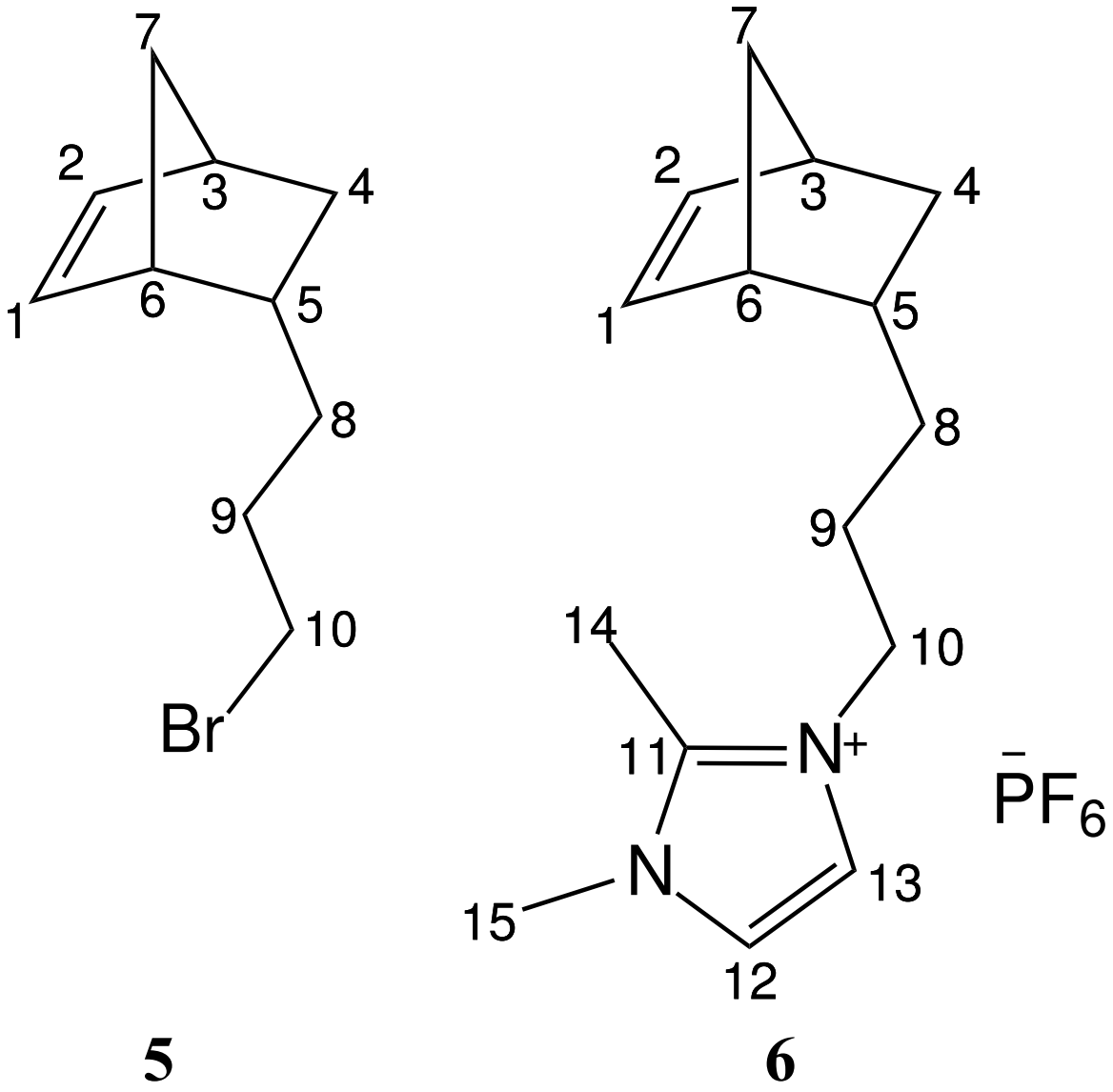

5 **6**

Scheme 3.2: Structures of the ionic liquid monomer precursor and ionic liquid monomer utilized in preparing poly(ionic liquid) films via surface-initiated ring-opening metathesis polymerization (SI-ROMP). **5**) 5-(bromopropyl)bicyclo[2.2.1]hept-2-ene (N_3−Br). **6**) Ionic liquid monomer consisting of the cation 3-[(bicyclo[2.2.1]hept-5-en-2-yl)propyl]-1,2-dimethylimidazol-3-ium (N_3−dMIm$^+$) and the anion hexafluorophosphate (PF_6^-)

hydroquinone (346 mg). The mixture was held at 170 °C for 24 h. The reaction mixture was purified by vacuum distillation to afford a clear, colorless oil as a mixture of exo and endo isomers. (11.25 g, Yield 31%)

endo isomer (82%): ^{1}H NMR (400 MHz, $CDCl_3$)(ppm): δ_H 6.13 (1H, dd, J = 5.6, 3.1 Hz, H1), 5.92 (1H, dd, J = 5.6, 3.0 Hz, H2), 3.43 - 3.34 (2H, m, H10), 2.76 (2H, H6, H3), 2.04 - 1.95 (1H, m, H5), 1.94 - 1.81 (3H, m, $H4_{exo}$, H9), 1.40 (1H, dd, J = 8.0, 2.1 Hz, H7), 1.28 - 1.08 (13H, m, H7, H8), 0.51 (1H, dq, J = 11.2, 4.2, 2.6 Hz, $H4_{endo}$)

$^{13}C\{^{1}H\}$ NMR (125 MHz, $CDCl_3$)(ppm): δ_c 137.2 (s, C1), 132.0 (s, C2), 49.5 (s, C7), 45.3 (s, C6), 42.5 (s, C3), 38.0 (s, C5), 34.0 (s, C10), 33.3 (s, C8), 32.3 (s, C9), 32.0 (s, C4)

exo isomer (18%): ^{1}H NMR (400 MHz, $CDCl_3$)(ppm): δ_H 6.08 (1H, dd, J = 5.6, 3.0 Hz, H1), 6.02 (1H, dd, J = 5.7, 2.9 Hz, H2), 3.43 - 3.34 (2H, m, H10), 2.80 (1H, s, H3), 2.51 (1H, s, H6), 2.04 - 1.95 (1H, m, H5), 1.94 - 1.81 (2H, m, H9), 1.57 - 1.45 (2H, m, H4), 1.33 (2H, s, H7), 1.28 - 1.08 (2H, m, H8)

$^{13}C\{^{1}H\}$ NMR (125 MHz, $CDCl_3$)(ppm): δ_c 136.6 (s, C1), 136.2 (s, C2), 46.3 (s, C6), 45.1 (s, C7), 41.8 (s, C3), 38.0 (s, C5), 35.0 (s, C10), 34.0 (s, C), 32.9 (s, C9), 32.1 (s, C4)

The ^{1}H and ^{13}C NMR spectra for N_3-Br are shown in Figures 3.5 and 3.6.

3-[(bicyclo[2.2.1]hept-5-en-2-yl)propyl]-1,2-dimethylimidazol-3-ium Hexafluorophosphate

N_3-Br (11.5 g, 53.5 mmol) and 1,2-dimethylimidazole (6.10 g, 63.5 mmol) were added to a 250 mL Schlenk flask. The reaction mixture was placed under nitrogen (N_2) and stirred for $60-70$ h at 60 °C to yield a solid of 3-[(bicyclo[2.2.1]hept-5-en-2-yl)propyl]-1,2-dimethylimidazol-3-ium bromide ([N_3-dMIm][Br]). The solid reaction mixture was dissolved in water (250 mL). Ammonium hexafluorophosphate (10.5 g, 64.4 mmol), 250 mL of water and the aqueous reaction mixture were added to a 1

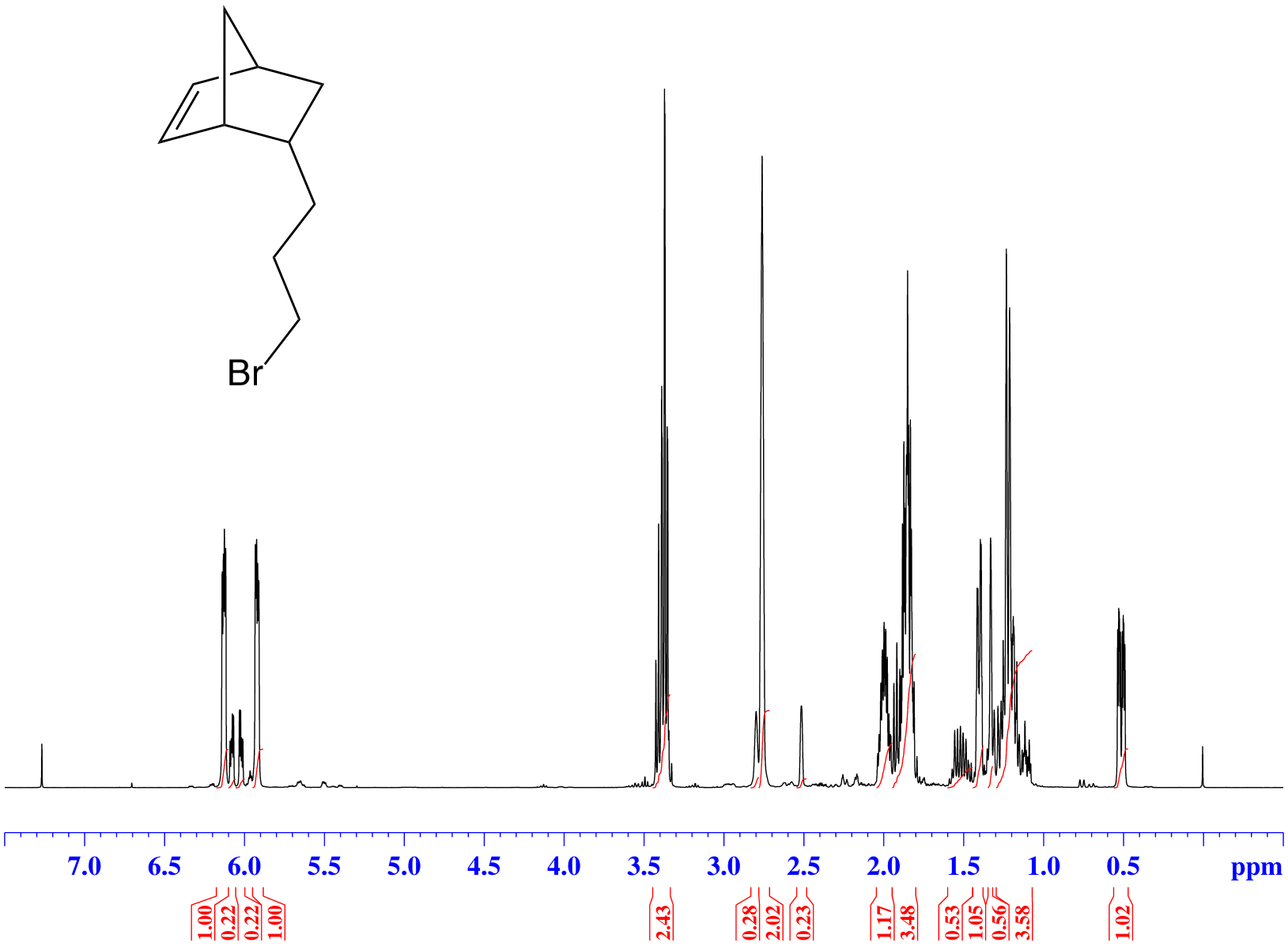

Figure 3.5: ^{1}H NMR spectrum of 5-(bromopropyl)bicyclo[2.2.1]hept-2-ene (N_3-Br) in $CDCl_3$ acquired on a 400 MHz instrument

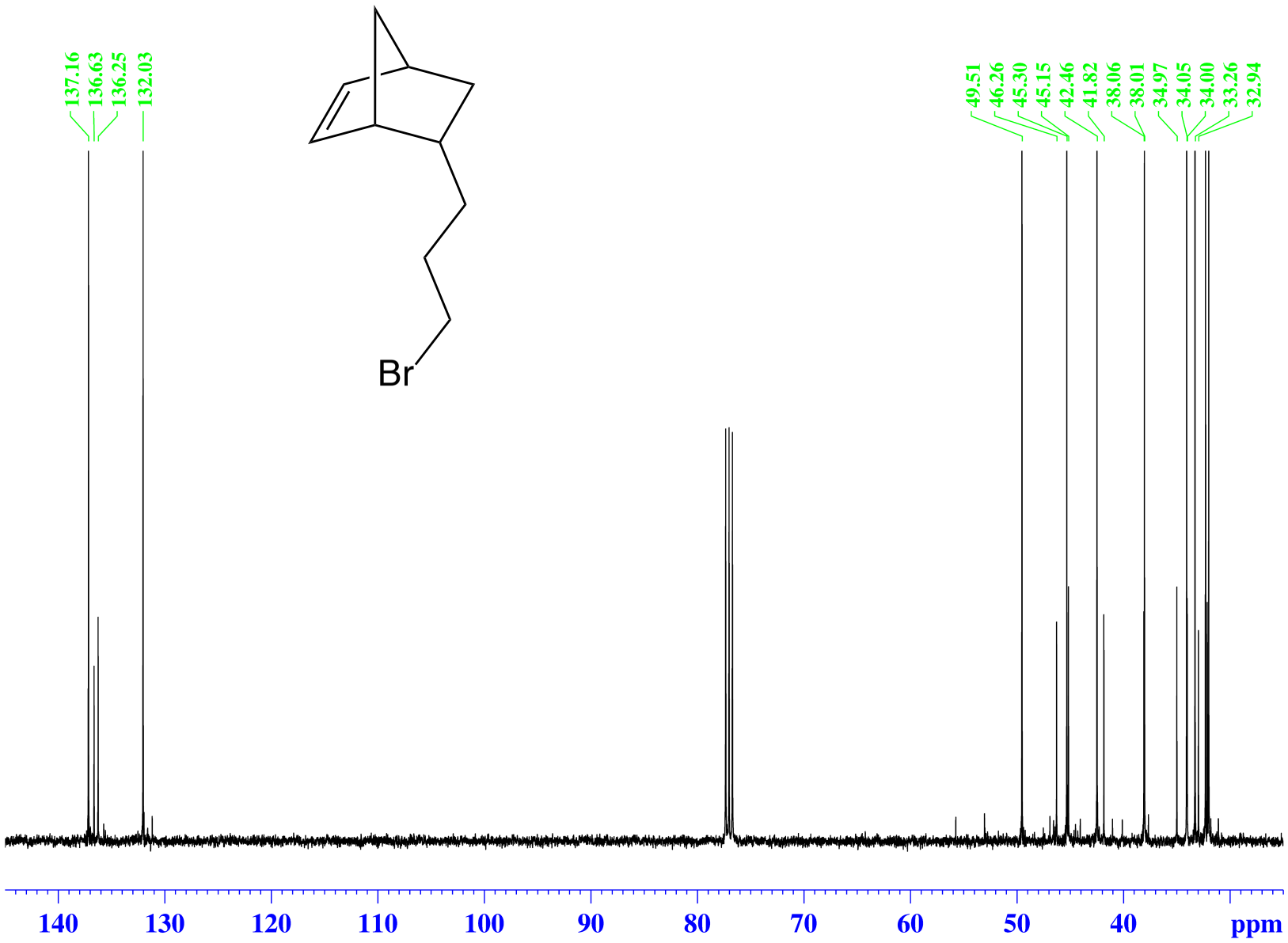

Figure 3.6: $^{13}C\{^{1}H\}$ NMR spectrum of 5-(bromopropyl)bicyclo[2.2.1]hept-2-ene (N_3-Br) in $CDCl_3$ acquired on a 400 MHz instrument

L beaker and stirred at room temperature producing a white precipitate of 3-[(bicyclo[2.2.1]hept-5-en-2-yl)propyl]-1,2-dimethylimidazol-3-ium hexafluorophosphate ($[N_1-dMIm][PF_6]$). The reaction mixture was extracted with 1500 mL of DCM and the organic extracts were dried over $MgSO_4$. The solvent was removed by rotary evaporation to yield a white solid. (17.2 g, Yield 85%)

endo isomer (81%): ^{1}H NMR (400 MHz, $(CD_3)_2CO$)(ppm): δ_H 7.60 (1H, d, J = 2.1 Hz, H12), 7.55 (1H, d, J = 2.2, H13), 6.11 (1H, q, J = 2.9 Hz, H1), 5.92 (1H, q, J = 2.9 Hz, H2), 4.3 - 4.2 (2H, m, H10), 3.92 (3H, s, H15), 2.78 (1H, s, H6), 2.76 (3H, s, H14), 2.73 (1H, s, H3), 1.98 - 1.82 (3H, m, $H4_{exo}$, H9),1.36 - 1.32 (1H, m, H5), 1.29 - 1.11 (4H, m, H7, H8) 0.71 (1H, dq, $J = 11.3, 4.2, 2.6$ Hz, $H4_{endo}$).

$^{13}C\{^1H\}$ NMR (125 MHz, $(CD_3)_2CO$)(ppm): δ_c 144.6 (s, C11), 136.9 (s, C1), 131.9 (s, C2), 122.4 (s, C13), 120.9 (s, C12), 49.1 (s, C7), 48.2 (s, C10), 45.0 (s, C6), 42.3 (s, C3), 38.0 (s, C5), 34.5 (s, C15), 31.9 (s, C4), 30.9 (s, C8), 29.0 (s, C9), 8.7 (s, C14)

exo isomer (19%): ^{1}H NMR (400 MHz, $(CD_3)_2CO$)(ppm): δ_H 7.61 (1H, d, J = 2.1 Hz, H12), 7.56 (1H, s, H13), 6.06 (1H, q, J = 2.9 Hz, H1), 6.00 (1H, q, J = 2.9 Hz, H2), 4.3 - 4.2 (2H, m, H10), 3.92 (3H, s, H15), 2.77 (3H, s, H14), 2.77 (1H, s, H3), 2.52 (1H, d, J = 1.4 Hz, H6), 1.98 - 1.82 (3H, m, H5, H9), 1.54 - 1.42 (2H, m, H4), 1.36 - 1.32 (2H, m, H7), 1.29 - 1.11 (2H, m, H8)

$^{13}C\{^1H\}$ NMR (125 MHz, $(CD_3)_2CO$)(ppm): δ_c 144.6 (s, C11), 136.5 (s, C1), 136.0 (s, C2), 122.4 (s, C13), 120.9 (s, C12), 48.2 (s, C10), 46.1 (s, C6), 44.7 (s, C7), 41.6 (s, C3), 38.2 (s, C5), 34.5 (s, C15), 32.5 (s, C4), 32.5 (s, C8), 29.3 (s, C9), 8.7 (s, C14)

HRMS (ESI) m/z: M^+ Calcd for $C_{15}H_{23}N_2$ 231.1856; Found 231.1854

The ^{1}H and ^{13}C NMR spectra of $[N_3-dMIm][PF_6]$ are shown in Figures 3.7 and 3.8.

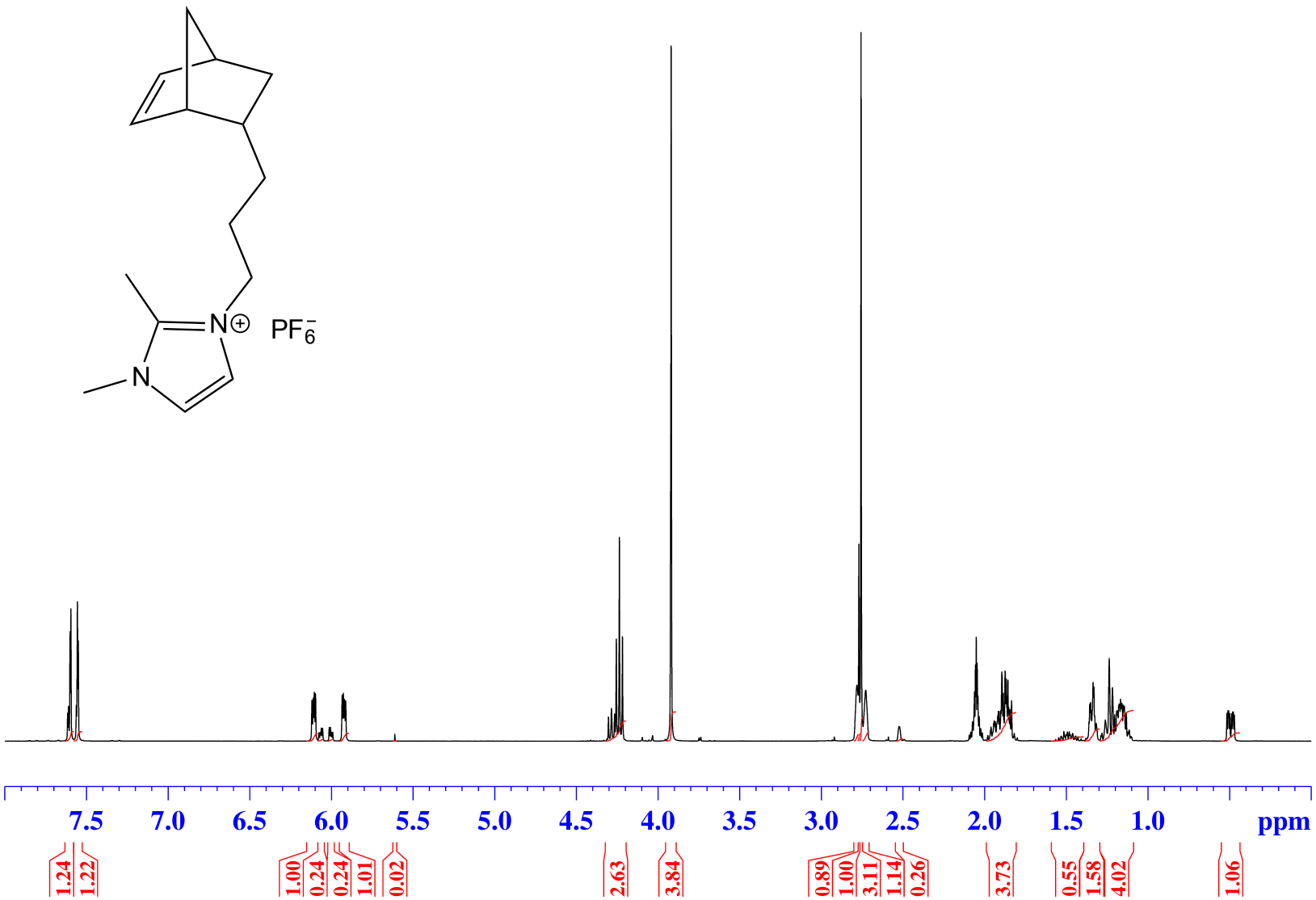

Figure 3.7: ^{1}H NMR spectrum of 3-[(bicyclo[2.2.1]hept-5-en-2-yl)propyl]-1,2-dimethylimidazol-3-ium hexafluorophosphate ([N_3−dMIm][PF_6]) in $(CD_3)_2CO$ acquired on a 400 MHz instrument

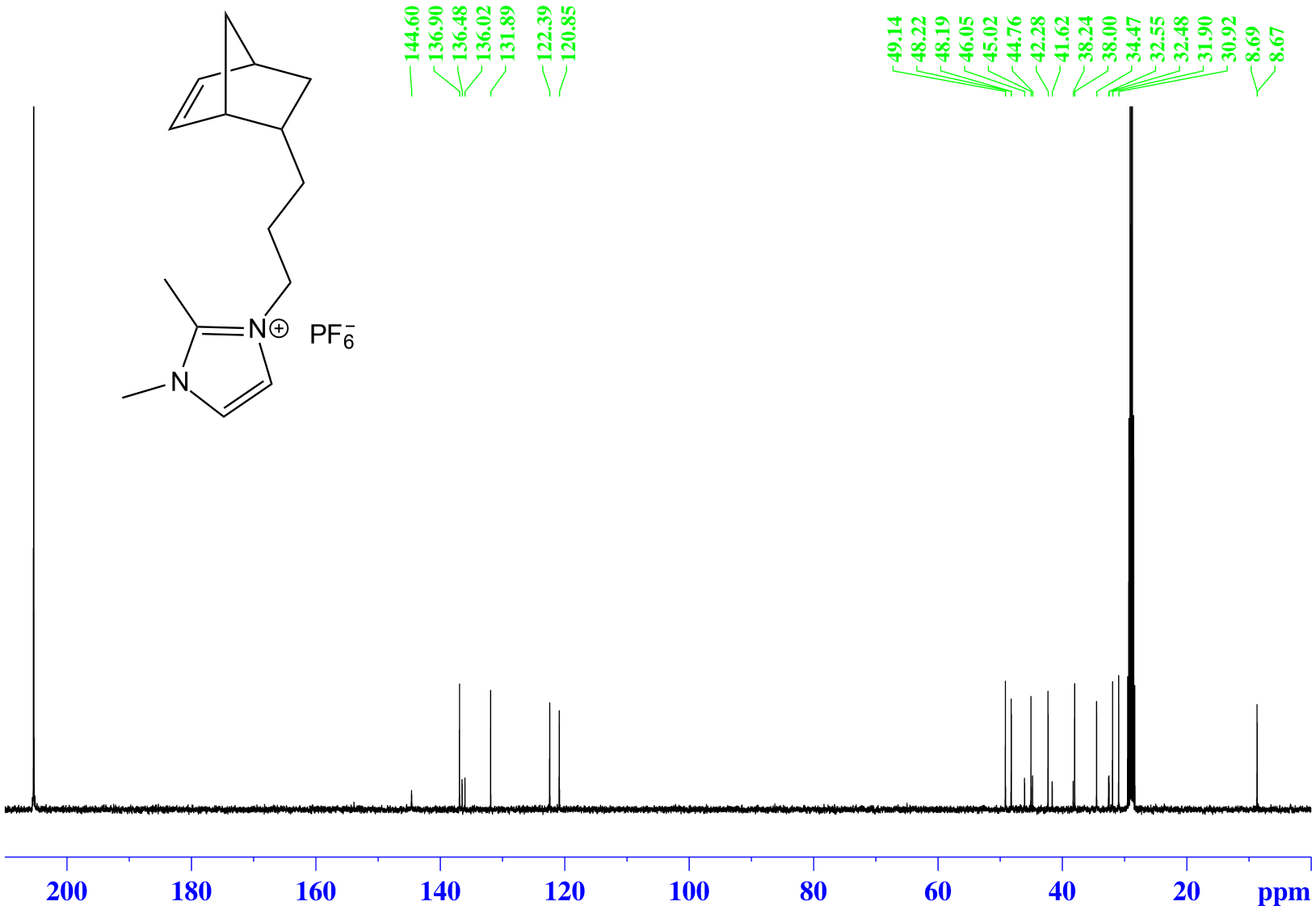

Figure 3.8: $^{13}C\{^{1}H\}$ NMR spectrum of 3-[(bicyclo[2.2.1]hept-5-en-2-yl)propyl]-1,2-dimethylimidazol-3-ium hexafluorophosphate ($[N_3{-}dMIm][PF_6]$) in $(CD_3)_2CO$ acquired on a 400 MHz instrument

Preparation of ROMP-Active Gold Substrates

Gold-coated silicon wafers were prepared by the sequential thermal evaporation of chromium (100 Å) and gold (1250 Å) in a diffusion-pumped chamber (CVC-PSM66 evaporator) at a base pressure of $\leq 4 \times 10^{-6}$ Torr and a rate of $1-2$ Å s^{-1} onto silicon (100) wafers that were pre-rinsed with water and ethanol and dried in a stream of nitrogen. The gold-coated wafers were typically cut into 1.2 cm × 4 cm samples and subsequently placed in a 1 mM ethanolic solution of 4-mercapto-1-butanol for at least 1 h to yield a hydroxyl-terminated self-assembled monolayer (SAM). The films were rinsed with ethanol, water, and ethanol and dried in a stream of nitrogen. The dried substrates were exposed to a 5 mM solution of NBDAC in DCM for 30 min to yield the acylation product of a surface-tethered norbornenyl group.[3] The substrates were rinsed with DCM, ethanol, water, and ethanol and dried in a stream of nitrogen. The norbornenyl-modified substrates were then exposed to a 5 mM solution of Grubbs catalyst in DCM for 12 min, rendering them active for ROMP.

Preparation of ROMP-Active Silicon Substrates

Silicon wafers were typically cut into 1.2 cm × 4 cm samples and sequentially rinsed with ethanol, water, and ethanol and dried in a stream of nitrogen. The substrates were then sonicated in ethanol for 30 min to displace any remaining contaminants and rinsed with water and ethanol and dried in a stream of nitrogen. The silicon substrates were then placed in piranha solution (14 mL H_2SO_4/6 mL H_2O_2) for 30 min to hydroxylate the silicon oxide surface. The substrates were rinsed thrice by submersion in water, rinsed in a stream of water, and ethanol and dried in a stream of nitrogen. The dried substrates were then exposed to a 5 mM solution of $NBSiCl_3$ in toluene for 1 h to yield a surface-tethered norbornenyl-terminated SAM. The substrates were rinsed with toluene, ethanol, water, and ethanol and dried in a stream of nitrogen. The norbornenyl-modified substrates were then exposed to a 5 mM solution

of Grubbs catalyst in DCM for 12 min, rendering them active for ROMP.

Preparation of ROMP-Active Glass Substrates

Microscope glass slides were typically cut into 1.25 cm × 3.8 cm samples and sequentially rinsed with ethanol, water, and ethanol and dried in a stream of nitrogen. The substrates were then sonicated in ethanol for 30 min to displace any remaining contaminants and rinsed with water and ethanol and dried in a stream of nitrogen. The glass substrates were then placed in piranha solution (14 mL H_2SO_4/6 mL 30 % H_2O_{2aq}) for 30 min to hydroxylate the silicon oxide surface. The substrates were rinsed thrice by submersion in water, followed by squeeze bottle rinses of water and ethanol, and dried in a stream of nitrogen. The dried substrates were then exposed to a 5 mM solution of $NBSiCl_3$ in toluene for 1 h to yield a norbornenyl-terminated SAM. The substrates were rinsed with toluene, ethanol, water, and ethanol and dried in a stream of nitrogen. The norbornenyl-modified substrates were then exposed to a 5 mM solution of Grubbs catalyst in DCM for 12 min, rendering them active for ROMP.

Characterization Methods

Polarization Modulation-Infrared Reflection-Absorption Spectroscopy (PM-IRRAS)

Infrared (IR) spectroscopy is a vibrational spectroscopy technique and is able to yield vibrational frequencies and oscillator strengths which can be interpreted in terms of molecular structure and bonding.[4–6] For a molecule to show infrared absorptions, it must possess an electric dipole moment that changes with the vibration of the molecule.[4] Fourier-transform infrared (FTIR) spectroscopy is based on the interference of radiation between two beams of light to yield an interferogram, a signal produced as a function of the change in path length between the two beams, leading

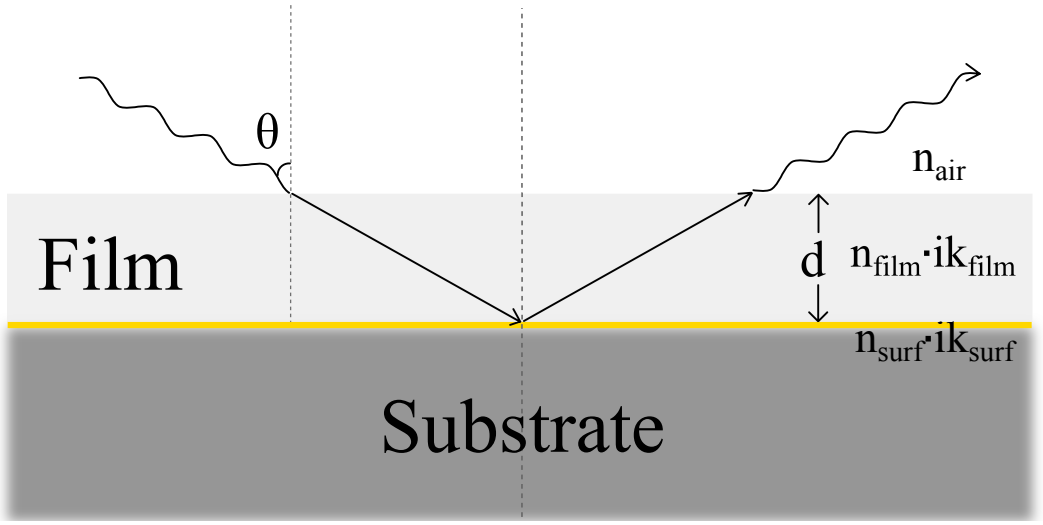

Scheme 3.3: Model of a thin film of thickness d on a metal coated substrate. The radiation is incident at an angle θ and encounters indices of refraction for the film and metal surface, $n \cdot iK$, that are complex and wavelength dependent.

to a greater dynamic range as the two domains of distance and frequency are interconvertible by the use of a Fourier transformation.[4,5] The most common interferometer used in FTIR spectroscopy is a Michelson interferometer.[4,5] Reflectance-absorption infrared spectroscopy (RAIRS) and attenuated total reflectance (ATR) are the two main reflection techniques for the analysis of surfaces.[7]

ATR is an internal reflection technique that uses a crystal (such as ZnSe or Ge) to achieve total internal reflection owing to the fact that the angle of incidence between the sample and the crystal is greater than the critical angle, which is a function of the refractive indices of the two surfaces.[4,7,8] RAIRS is an external reflection technique, as shown in Scheme 3.3, where the incident radiation is focused on the sample and the reflected radiation is measured.[4,5,8] In RAIRS, the reflection spectrum depends strongly on the optical constants of the surface-tethered film/molecules and the substrate.[5–10] When IR light is reflected from a flat metal surface, the electric vector undergoes a phase shift that depends on the polarization of the light.[5,8]

For virtually all incidence angles (θ), IR radiation whose electric field is polarized perpendicular to the plane of reflection (s polarized light) undergoes a phase shift of π

(180°) and the electric vectors at the surface sum to near zero yielding no electric field at the surface.[5–9] For grazing ($80-88°$) incidence angles, IR radiation whose electric field is polarized parallel to the plane of reflection (p polarized light) undergoes a phase shift of approximately $\pi/2$ (90°) and the resulting standing wave at the surface is nonzero and oriented along the surface normal.[5–9] This difference in magnitude for s polarized versus p polarized light at the surface leads to the surface selection rule, which results in the ability to distinguish molecular vibrations which have a transition dipole moment with a large component perpendicular to the substrate from those having a large component parallel to the substrate which show near zero intensity.[5–9]

Typically, in RAIRS experiments, one obtains a p polarized reflectivity of the bare metallic substrate as a background spectra that is used to normalize the p polarized reflectivity of the film on the metallic substrates.[5,11] One can then compute the RAIRS spectrum $\frac{R_p(d)}{R_p(0)}$ and therefore, the absorption spectrum of the form

$$A\left(d\right)=\left(\frac{I_p(0)-I_p(d)}{I_p(0)}\right)=1-\frac{R_p(d)}{R_p(0)} \tag{3.1}$$

where $I_p(0)$ (proportional to $R_p(0)$) and $I_p(d)$ (proportional to $R_p(d)$) are the reflected light intensities in the absence and in the presence of the absorbing film layer (Scheme 3.3).[5,8,11] The absorption intensity observed for a particular electric transition dipole moment is largely dependent on the scalar product of the surface electric field amplitude and the oscillator transition dipole moment, which on metallic substrates leads to

$$A\left(d\right)\propto cos^2\left(\theta_{mz}\right) \tag{3.2}$$

where θ_{mz}, is the average angle between the transition dipole moments (m) and the surface normal (z).[12]

RAIRS, however, has several disadvantages, such as a low signal to noise ratio compensated by long acquisition times resulting in aberrant surface spectra due to minute instabilities in the spectrometer.[5,11] Additionally, changes to the surrounding atmosphere of the sample especially during long acquisition times, lead to surface spectra contaminated with a large amount of background peaks.[11] These disadvantages of RAIRS can be overcome by replacing the absolute reflectivity of the RAIRS measurement with a modulation technique. Polarization modulation-infrared reflection-absorption spectroscopy (PM-IRRAS) is a double modulation technique where FTIR radiation, which is modulated by the interferometer in the frequency range $100 - 20000$ Hz, is passed through a fixed polarizer and then through a photoelastic modulator (PEM), which modulates the radiation in the frequency range $50 - 100$ kHz.[5,13]

In Fourier transform RAIRS, the interferogram is digitally demodulated by the Fourier transform to produce a single-beam spectrum whose amplitude is proportional to $(I_p + I_s)$.[5] In order to demodulate the signal with PEM modulation, a lock-in amplifier set at the frequency of the PEM is utilized and produces and interferogram whose amplitude is proportional to $(I_p - I_s)$.[5,13] This leads to an absorption spectrum of the form[5,8,11,13]

$$A\left(d\right) = \left(\frac{\Delta R}{R}\right) = \frac{I_p - I_s}{I_p + I_s} \tag{3.3}$$

Because a ratio is used for obtaining the absorption spectrum, PM-IRRAS does not require a background correction or a reference material and the effect of water and/or CO_2 vapor is significantly smaller than observed with RAIRS.[5,8,11] A second advantage of PM-IRRAS is that it is able to provide a much higher surface absorption sensitivity since spectrometer and background fluctuations are taken into account during each mirror scan.[5,8,11]

In this thesis, PM-IRRAS is used to study the composition of poly(ionic liquids)

(PILs) (Chapter 4 and 5), to determine the anion concentration in copolymer PILs (Chapter 6), and to study the composition of polydicyclopentadiene (pDCPD) films (Chapter 7). PM-IRRAS) was performed using a Bruker Tensor 27 Fourier transform infrared spectrometer equipped with a PEM-90 photoelastic modulator (Hinds Instruments) and a liquid-nitrogen cooled mercury-cadmium-telluride (MCT) detector with a non-dichroic BaF_2 window. The source beam employed a half-wavelength ($\frac{\lambda}{2}$) retardation modulated at a frequency of 50 kHz and set at 85° incident to the sample surface. Spectra were collected over 5 min (360 scans) at a resolution of 4 cm^{-1}.

Profilometry

Surface topography and film thickness can be determined by a variety of techniques that are broadly categorized into contact and non-contact techniques. Of the contact techniques, the two most common are surface measurements with a stylus profiler (SP) and AFM.[14] While AFM is able to provide fine details of surfaces, the length that the technique is able to survey is on the order of μm and typically takes a large amount of time to capture the data.[14] However, surface measurements with a SP allow for the collection of data on the order of mm.A stylus profiler consists of a tip on the end of a cantilever. In performing surface measurements with a SP, the stylus is placed on the surface to be measured and moved across the surface at a constant velocity to obtain surface height variation due to the deflections of the cantilever.[14] The amount of force applied on the tip, the radius of the tip, and the scanning parameters all affect the sensitivity of the method.

In this thesis, a SP is used to determine the film thickness (Chapter 4, 5, and 7) and roughness (Chapter 7) of the surface-tethered polymer films. The thickness was taken to be the mean height variation for the polymer film from the baseline substrate, while the root mean square roughness (Rq) was taken as the roughness of the polymer films. Profilometric thicknesses were determined using a Veeco Dektak

150 stylus profilometer with a vertical sensitivity of 1 ÅMeasurements were performed using a stylus with a 12.5 μm radius, applying 29.4 μN of force and the hills and valleys detection mode. The scan duration was varied to keep the height data collection rate at 0.028 μm/sample. Film thicknesses were estimated by performing three scans per sample, 1000 μm long, across a hand-made scratch defect used to establish a baseline for polymer growth. The scan results were then plane fitted using the instrument software. Reported values represent the averages and standard deviations of at least three independently prepared films.

Ellipsometry

Ellipsometry is an optical measurement technique that characterizes light reflection (or transmission) from samples by measuring the change in polarized light upon light reflection on a sample.[15–17]

In this thesis, ellipsometry is used to determine film thickness (Chapter 7). Ellipsometric thicknesses were determined with a J.A. Woollam M-2000VI variable angle spectroscopic ellipsometer. Thicknesses and refractive indices were obtained from fits to data taken at 60°, 65°, 70°, and 75° from the surface normal over wavelengths from 371.3 to 1688.7 nm. Optical constants of the gold substrates were taken prior to polymer film growth and used as a baseline for the thickness determinations.

Contact Angle

For a liquid droplet that is adhered to a solid surface as shown in Figure 3.9, the deformation of the water droplet can be described by considering the interfacial free energy between the solid and the air (γ_{SV}), the interfacial free energy between the solid and the liquid (γ_{SL}), and the interfacial free energy between the air and the liquid (γ_{LV}). The contact angle arises from a force balance at the contact line between the three phases.[18] The force balance at the contact line is shown in eq 3.4.

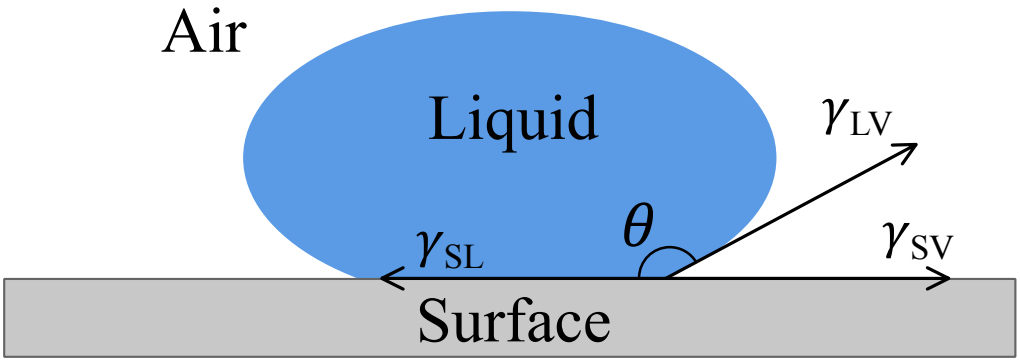

Figure 3.9: Liquid drop on a solid surface in the presence of air. γ_{SV} is the interfacial free energy between the solid and air, γ_{SL} is the interfacial free energy between the solid and the liquid, and γ_{LV} is the interfacial free energy between air and the liquid.

The contact angle is then given by eq 3.5 (Young's equation).

$$\gamma_{SV} = \gamma_{SL} + \gamma_{LV}\, cos\theta \tag{3.4}$$

$$cos\theta = \frac{\gamma_{SV} - \gamma_{SL}}{\gamma_{LV}} \tag{3.5}$$

The Fowkes approximation (eq 3.6) relates γ_{SL} in terms of γ_{SV} and γ_{VL}. The approximation relies on the assumption that the vapor phase (air) provides no stabilizing interactions such that the interfacial free energy for a phase in contact with vapor equals the surface energy of the phase. The third term in the equation, $2\left(\gamma_{SV}\right)^{1/2}\left(\gamma_{VL}\right)^{1/2}$, espresses a stabilization energy for the liquid drop on the surface. Using the Fowkes approximation and the Young equation, the expression in eq 3.7 can be determined.

$$\gamma_{SL} = \gamma_{SV} + \gamma_{VL} - 2\left(\gamma_{SV}\right)^{1/2}\left(\gamma_{VL}\right)^{1/2} \tag{3.6}$$

$$cos\theta = -1 + \frac{2\left(\gamma_{SV}\right)^{1/2}}{\left(\gamma_{VL}\right)^{1/2}} \tag{3.7}$$

For a low energy surface (i.e. $\gamma_{SV} \approx 0$), eq 3.7 reduces to $cos\theta \simeq -1$, meaning that the contact angle is close to 180° and the surface is not wetted by the liquid droplet. For a high energy surface (i.e. $\gamma_{SV} \simeq \gamma_{VL}$), eq 3.7 reduces to $cos\theta \simeq 1$, the contact angle is close to 0°, and the surface is wetted by the liquid droplet. There is also the case for which $\gamma_{SV} \gg \gamma_{VL}$, where eq 3.7 reduces to $cos\theta > 1$ and the surface is fully wetted by the liquid. There are three different types of contact angles, the advancing contact angle (θ_A), the receding contact angle (θ_R) and the equilibrium contact angle (θ_{Eq}). The measurements for for θ_A and θ_R were experimentally collected. For a particular surface, $\theta_A > \theta_{Eq} > \theta_R$. Therefore, measuring θ_A and θ_R determines the range of contact angles possible for a particular liquid on a surface.

Hysteresis is defined as the difference between the θ_A and θ_R, i.e. $H = \theta_A - \theta_R$. Hysteresis is a function of the heterogeneity and the roughness of the surface. For a liquid in contact with a rough surface, the interfacial area is no longer the same as the projected area.[18] For such a surface, the contact angle on the smooth surface can be determined from the measured contact angle using eq 3.8, where ϕ is the fraction by which the interfacial area is greater or less than the projected area and θ_s is the contact angle on a smooth surface.[18]

$$(1 + cos\theta) = \phi(1 + cos\theta_s) \tag{3.8}$$

For a liquid in contact with a surface that is chemically heterogeneous, the contact angle will vary depending on the composition of the surface that it wets and the wetting properties of the homogeneous surfaces that compose the heterogeneous surface. For surfaces with microscopic heterogeneity, the Cassie equation (eq 3.9) relates the measured contact angle and the contact angles of the constituent homogeneous surfaces.[18]

$$cos\theta = \sum_i f_i cos\theta_i \tag{3.9}$$

In this thesis, water contact angles were obtained to determine surface wettability (Chapter 4, 6 and 7). A Rame-Hart manual contact angle goniometer with a micro-liter syringe was used to measure θ_{A} and θ_{R} of static drops of water on the polymer film surfaces. Contact angles were measured on both sides of the image of approximately 5 μL drops with the syringe in the probe droplet during measurements. The reported values and ranges represent the average and standard deviation from three measurements per sample of at least three independently prepared samples.

Electrochemical Impedance Spectroscopy (EIS)

Electrochemical impedance spectroscopy (EIS) is an electrochemical technique that applies an alternating signal of small magnitude to electrochemical cells and observes the systems responses to the perturbation at steady state.[19] Given that the cell is perturbed close to equilibrium, the kinetics and diffusion of ions are greatly simplified.[19] Advantages of EIS include an ability to make high-precision measurements determined by the steadiness of the response leading to long term averaging, an ability to treat the response theoretically by linearized (or otherwise simplified) current-potential characteristics and measurement over a wide time (or frequency) range (10^4 to 10^{-6} s or 10^{-4} to 10^6 Hz).[19] In EIS, a low amplitude sinusoidal potential (E_{ac}) perturbation is applied around the equilibrium potential of the cell or working electrode and depend on the fact that current - overpotential relations are virtually linear at low overpotentials.[19] In a linear system, excitation at frequency ω provides a current also of frequency ω (and only of frequency ω) compared to non-linear current - potential relations that give distorted response behavior.[19]

An electrochemical cell can be considered as an impedance to a small sinusoidal excitation and its response can be represented by an equivalent circuit of resistors

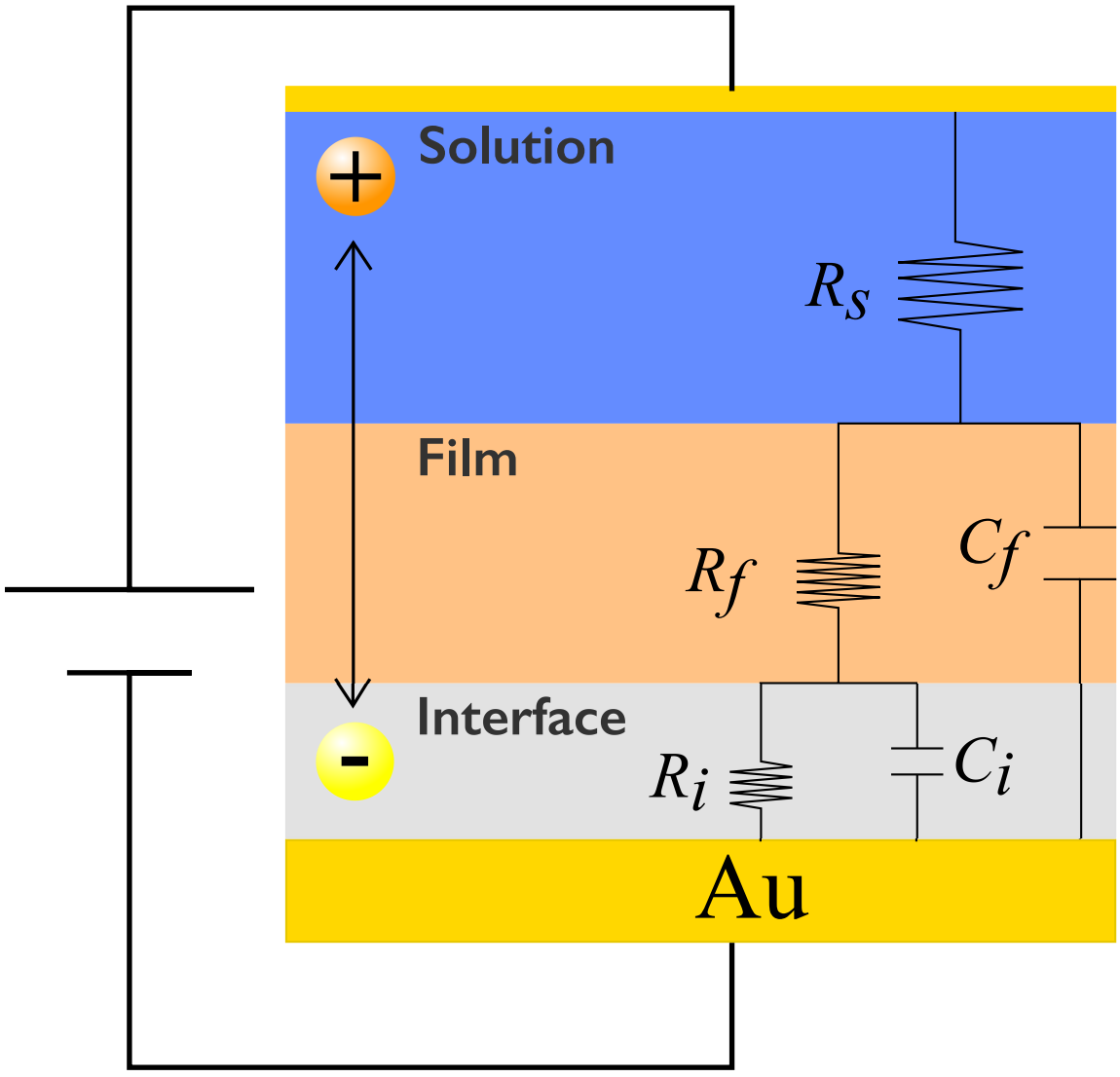

Scheme 3.4: Equivalent circuit model used in the analysis of surface-anchored p[N_1−dMIm] films on gold-coated silicon substrates. The two-time-constant circuit model consists of a solution resistance (R_s) connected in series with a film capacitance (C_f) and resistance (R_f) attached in series with an interfacial capacitance (C_i) and resistance (R_i).

and capacitors that pass current with the same amplitude and phase angle that the real cell does under a given excitation.[19] The electrochemical cells considered in this dissertation were analyzed with the equivalent circuits shown in Schemes 3.4 and 3.5. In both schemes, the current must pass through the solution resistance, an ohmic resistance of the electrolyte solution to ion migration, resulting in the circuit element R_s. Scheme 3.5 represents an equivalent circuit containing redox species that can undergo faradiac processes. The parallel elements are introduced because the total current through the working interface is the sum of distinct contributions from the faradaic process and the double-layer charging.[19] The faradaic processes are represented as a pure resistance,R_i, and a general impedance due to a resistance to mass transfer and Z_w.[19] The double-layer charging is a nearly pure capacitance and is represented in the circuit by the element C_i.

For electrochemical cells that do not contain a redox species, faradaic process only occur at large overpotentials, or at very long measurement times (low frequencies) and as currents are generated by the movement of ions in the cell. Scheme 3.4 represents an equivalent circuit for cells with a film generating an impedance to the migration of ions on the working interface. The film contributions are accounted for by introducing a resistance, R_f, in series with the interfacial response, R_i and C_i, as well as a capacitance C_f.

In Chapters 4 and 6, electrochemical impedance spectroscopy (EIS) was performed with a Gamry Instruments Reference 600 potentiostat. The electrochemical cell consisted of a 0.1 M aqueous solution of the polymer film anion salt with a Ag/AgCl/KCl (3 M) reference electrode, a gold-coated silicon substrate as the counter electrode, and a gold-coated silicon substrate coated with the film to be studied as the working electrode. The film coated substrate was placed in a sample holder of a Flat-Cell (Princeton Applied Research, Model K0235) to limit the testing area to 1 cm^2. The cell was perturbed with a 5 mV rms AC voltage applied around the open circuit po-

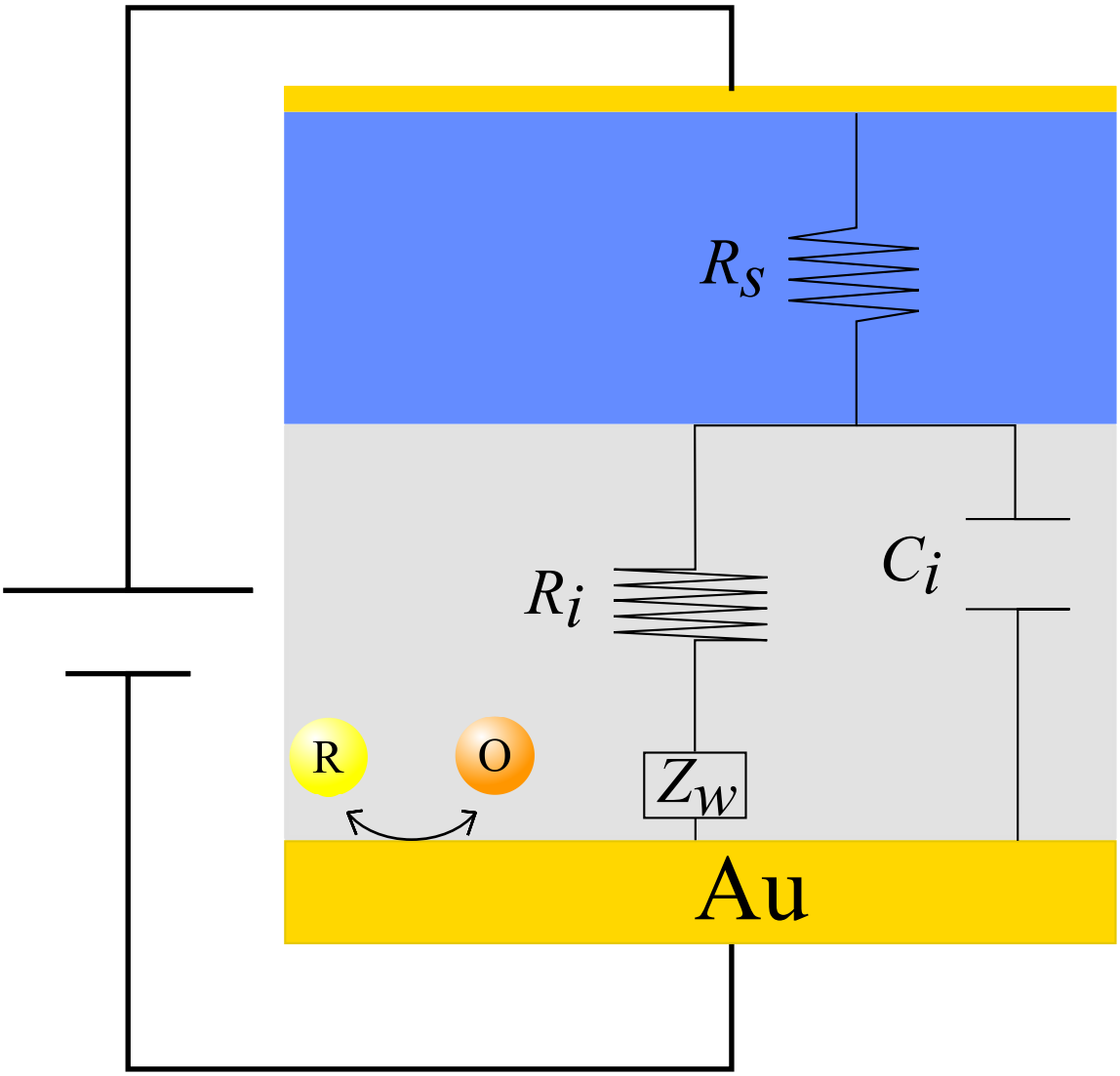

Scheme 3.5: Equivalent circuit model used in the analysis of surface-anchored pDCPD films on gold-coated silicon substrates. The reduced (R) species in the test setup is $K_4Fe(CN)_6$ and the oxidized (O) species is $K_3Fe(CN)_6$. The one-time-constant circuit model consists of a solution resistance (R_s) in series with an interfacial capacitance (C_i), and resistance (R_i), with an additional Warburg impedance (Z_w) to account for a resistance to mass transfer.

tential, which was varied in frequency from 10^5 to 10^{-2} Hz using 10 points per decade. The impedance spectra were fit with the equivalent circuit model shown in Scheme 3.4 using the Gamry E-Chem Analyst software package.

In Chapter 7, the electrochemical cell consisted of an aqueous solution of 1 mM $K_3Fe(CN)_6$, 1 mM $K_4Fe(CN)_6 \cdot 3\,H_2O$, and 0.1 M Na_2SO_4 with a Ag/AgCl/KCl (3 M) reference electrode, a gold-coated silicon substrate as the counter electrode, and a gold-coated silicon substrate coated with the film to be studied as the working electrode. The cell was perturbed with a 5 mV rms AC voltage applied around the open circuit potential, which was varied in frequency from 10^5 to 10^{-2} Hz using 10 points per decade. The impedance spectra were fit with the equivalent circuit model shown in Scheme 3.4 using the Gamry E-Chem Analyst software package.

Quartz Crystal Microbalance with Dissipation (QCM-D)

Quartz crystal microbalance with dissipation (QCM-D) is a technique that allows the precise, time-resolved measurements of the energy dissipation factor of a QCM crystal in conjunction with the commonly measured frequency shift.[20] In a QCM-D measurement the crystal is excited to oscillation in the thickness shear mode at its fundamental (and/or an overtone) resonant frequency, f, by applying an AC voltage across the electrodes as shown in Scheme 3.6 a). f and D measurements are made by periodically disconnecting the oscillating crystal from the AC voltage and performing a fit to the decay of the crystal oscillation where both the frequency and dissipation factor values are obtained simultaneously.[21]

In this thesis, QCM-D was performed in Chapter 4 to determine the water uptake of PIL films. QCM-D was performed with a Biolin Scientific Q-Sense E4 interfaced to a personal computer and an ISMATEC IPC peristaltic pump. The QCM-D sensor crystal consists of a round, AT-cut piezoelectric quartz crystal coated with gold electrodes on their front and back face. f and D measurements were acquired at a rate

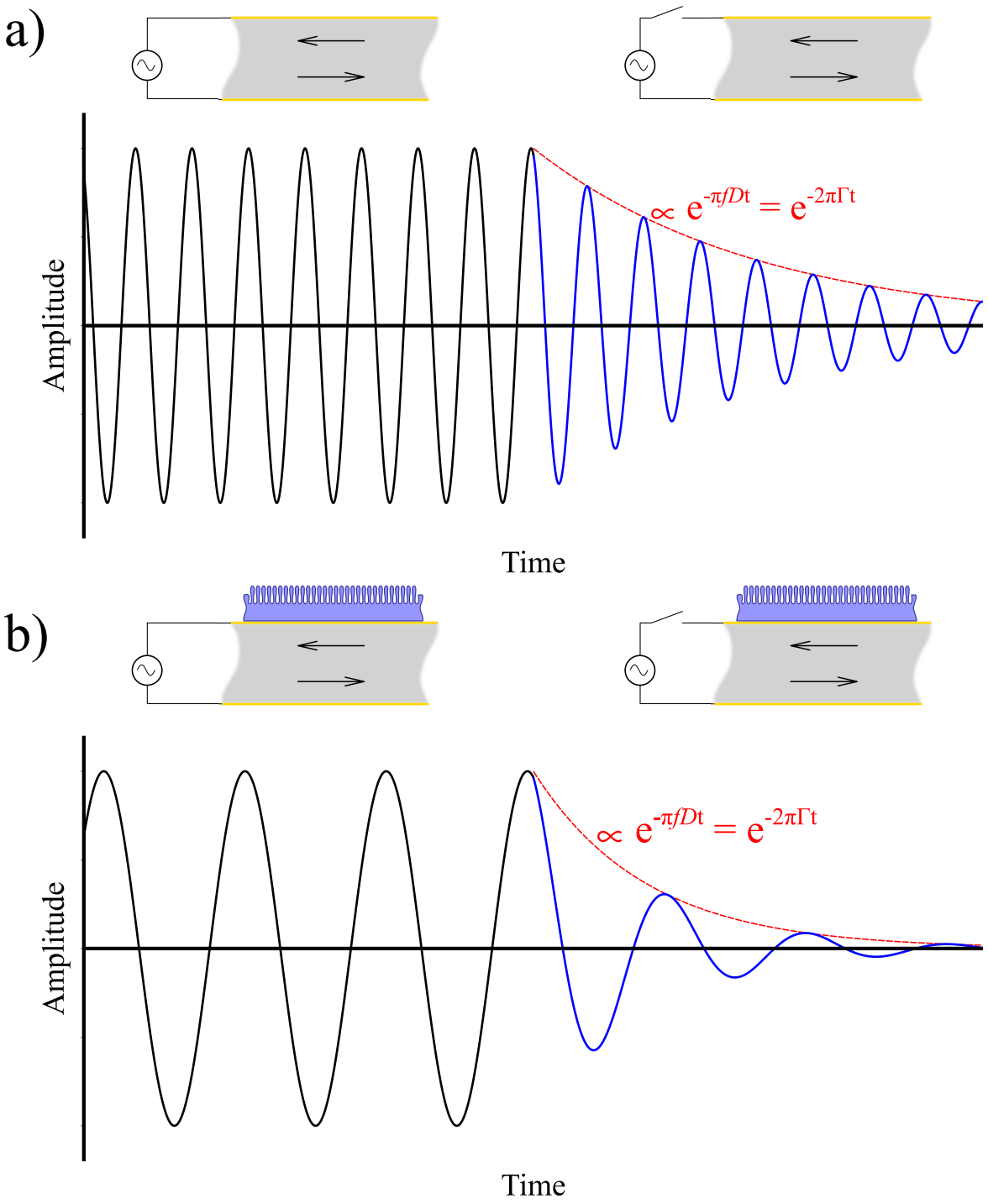

Scheme 3.6: Schematic of QCM-D Operation. a) Amplitude vs. time curves for an unloaded QCM-D sensor as well as a side view of the sensor. Application of an AC voltage on the QCM-D sensor results in a cyclic shear deformation represented by the black curve. Frequency (f) and dissipation factor (D) are determined by intermittent removal of the AC voltage and performing a fit (shown in red) to the decay (shown in blue) of the oscillatory amplitude over time.[22] b) Amplitude vs. time curves for a QCM-D sensor loaded with a viscoelastic film as well as a side view of the sensor. The additional mass from the viscoelastic film induces a decrease in frequency as well as an increase in dissipation due to the viscoelastic nature of the film.

of 200 times per second in ultra pure (18.2 MΩ) water at 20 °C for a period of $15-20$ min. Prior to data collection the sample chamber was flushed with ultra pure (18.2 MΩ) water at a flow rate of 50 μL/min for 2 h in order to ensure temperature stability. Due to the sensitivity of QCM-D to the properties of the bulk fluid, a reference measurement of a pre-treated crystal was collected after a 5 min UVO treatment of the front crystal electrode.

PeakForce Quantitative Nanomechanical Mapping (QNM)

The study of the mechanical properties of soft materials such as thin polymer films is of increasing interest due to their widespread use in modern technologies.[23,24] Indentation is a versatile method for studying local mechanical properties of materials and covers dimensions ranging form the nanoscale to the macroscale.[23,24] Probe indentation, by either nanoindenters or atomic force microscopy (AFM), are the two major techniques available that allow for the collection of force-indentation curves.[24] AFM is more preferable when studying soft materials due to its ability to apply smaller forces and therefore, produce smaller deformations compared to nanoindenters.[24] PeakForce QNM is a recently introduced AFM mode that allows the mapping of the elastic modulus of a sample surface with high spatial resolution at the same rate as regular tapping-mode AFM imaging by the real time calculation of Young's modulus at each surface contact via a fit of the Derjaguin-Muller-Toporov (DMT) model to force-indentation curves.[24,25] Young et al.[25] compared the E_r obtained by PeakForce QNM for polymer films to those obtained via nanoindentation techniques and showed that the technique provided repeatable measurements of polymer elastic moduli when careful calibration procedures were utilized.

In PeakForce quantitative nanomechanical mapping (QNM) the reduced Young's Modulus (E_r) is calculated by fitting the Derjaguin-Muller-Toporov (DMT) model (see eq 3.10) on the unloading (retract) portion of the force-separation curve.

$$E_r = \frac{3\left(F_{\text{tip}} - F_{\text{adh}}\right)}{4\sqrt{Rd^3}} \tag{3.10}$$

In eq 3.10, F_{tip} is the force on the AFM tip, F_{adh} is the adhesive force between the tip and the sample, R is the tip radius and d is the deformation depth. The sample's Young's modulus can be obtained from the measured reduced Young's modulus using eq 3.11 where ν_{t} and E_{t} are the Poisson's ratio and Young's Modulus of the tip and ν_{s} and E_{s} are the Poisson's ratio and Young's Modulus of the sample. Assuming that E_{t} is much greater in magnitude than E_{s} leads to the approximation of E_{t} as infinite and leads to eq 3.12 which can be used to calculate the E_{s}.

$$E_r = \left(\frac{1-\nu_{\text{t}}^2}{E_{\text{t}}} + \frac{1-\nu_{\text{s}}^2}{E_{\text{s}}}\right)^{-1} \tag{3.11}$$

$$E_{\text{s}} = E_r\left(1-\nu_{\text{s}}^2\right) \tag{3.12}$$

In this thesis, PeakForce (QNM) is performed in Chapter 7 to determine the Young's modulus of surface-tethered pDCPD films. PeakForce QNM was performed with a Bruker Dimension Icon® AFM and a RTESPA-300 probe supplied by Bruker. The RTESPA-300 probe has a nominal radius of 8 nm and a nominal spring constant $k = 42$ N/m. The spatial sensitivity of the AFM photodetector (deflection sensitivity) of the RTESPA-300 probe was calibrated using a clean sapphire sample supplied by Bruker. The PeakForce QNM data were collected at an oscillation frequency of 2 kHz with a constant PeakForce amplitude of 150 nm. The sample's Poisson ratio was set to 0 in order to obtain the reduced Young's Modulus. The modulus measurement on each sample corresponds to 512×512 force-separation curves collected over an area of $1\mu\text{m} \times 1\mu\text{m}$ at a scan rate of 1 Hz. The reported values and ranges represent the average and standard deviation from three modulus measurements per sample of at least three independently prepared films.

References

[1] Love, J. A., Morgan, J. P., Trnka, T. M., and Grubbs, R. H. (2002) A Practical and Highly Active Ruthenium-Based Catalyst that Effects the Cross Metathesis of Acrylonitrile. *Angewandte Chemie International Edition 41*, 4035–4037.

[2] Ye, Q., Gao, T., Wan, F., Yu, B., Pei, X., Zhou, F., and Xue, Q. (2012) Grafting Poly(Ionic Liquid) Brushes for Anti-Bacterial and Anti-Biofouling Applications. *Journal of Materials Chemistry 22*, 13123.

[3] Berron, B. J., Payne, P. A., and Jennings, G. K. (2008) Sulfonation of Surface-Initiated Polynorbornene Films. *Industrial & Engineering Chemistry Research 47*, 7707–7714.

[4] Stuart, B. *Infrared Spectroscopy: Fundamentals and Applications*; Wiley: Chichester, England, 2004.

[5] Golden, W. G., Saperstein, D. D., Severson, M. W., and Overend, J. (1984) Infrared Reflection-Absorption Spectroscopy of Surface Species: A Comparison of Fourier Transform and Dispersion Methods. *The Journal of Physical Chemistry 88*, 574–580.

[6] Barner, B. J., Green, M. J., Saez, E. I., and Corn, R. M. (1991) Polarization modulation Fourier transform infrared reflectance measurements of thin films and monolayers at metal surfaces utilizing real-time sampling electronics. *Analytical Chemistry 63*, 55–60.

[7] Yarwood, J. (1993) Surface Analysis. *Analytical Proceedings 30*, 13–18.

[8] Roy, D., and Fendler, J. (2004) Reflection and Absorption Techniques for Optical Characterization of Chemically Assembled Nanomaterials. *Advanced Materials 16*, 479–508.

[9] Greenler, R. G. (1966) Infrared Study of Adsorbed Molecules on Metal Surfaces by Reflection Techniques. *The Journal of Chemical Physics 44*, 310–315.

[10] Greenler, R. G. (1969) Reflection Method for Obtaining the Infrared Spectrum of a Thin Layer on a Metal Surface. *The Journal of Chemical Physics 50*, 1963–1968.

[11] Buffeteau, T., Desbat, B., and Turlet, J. M. (1991) Polarization Modulation FT-IR Spectroscopy of Surfaces and Ultra-Thin Films: Experimental Procedure and Quantitative Analysis. *Applied Spectroscopy 45*, 380–389.

[12] Nuzzo, R. G., Dubois, L. H., and Allara, D. L. (1990) Fundamental studies of microscopic wetting on organic surfaces. 1. Formation and structural characterization of a self-consistent series of polyfunctional organic monolayers. *Journal of the American Chemical Society 112*, 558–569.

[13] Green, M. J., Barner, B. J., and Corn, R. M. (1991) RealâĂŘTime Sampling Electronics for Double Modulation Experiments with Fourier Transform Infrared Spectrometers. *Review of Scientific Instruments 62*, 1426–1430.

[14] Poon, C. Y., and Bhushan, B. (1995) Comparison of Surface Roughness Measurements by Stylus Profiler, AFM and Non-Contact Optical Profiler. *Wear 190*, 76–88.

[15] Fujiwara, H. *Spectroscopic Ellipsometry*; John Wiley & Sons, Ltd, 2007; pp 1–11.

[16] Tompkins, H. G., and Irene, E. A. *Handbook of Ellipsometry*; Springer Berlin Heidelberg, 2005.

[17] Irene, E. A. In *A Brief History and State of the Art of Ellipsometry BT - Ellipsometry at the Nanoscale*; Losurdo, M., and Hingerl, K., Eds.; Springer Berlin Heidelberg: Berlin, Heidelberg, 2013; pp 1–30.

[18] Israelachvili, J. *Academic, New York*, 3rd ed.; Academic Press, 2010; p 704.

[19] Bard, A. J., and Faulkner, L. R. *Fundamentals and Applications*, 2nd ed.; John Wiley & Sons, Inc., 2001.

[20] Höök, F., Rodahl, M., Brzezinski, P., and Kasemo, B. (1998) Energy Dissipation Kinetics for Protein and Antibody-Antigen Adsorption under Shear Oscillation on a Quartz Crystal Microbalance. *Langmuir 14*, 729–734.

[21] Rodahl, M., and Kasemo, B. (1996) A Simple Setup to Simultaneously Measure the Resonant Frequency and the Absolute Dissipation Factor of a Quartz Crystal Microbalance. *Review of Scientific Instruments 67*, 3238–3241.

[22] Reviakine, I., Johannsmann, D., and Richter, R. P. (2011) Hearing What You Cannot See and Visualizing What You Hear: Interpreting Quartz Crystal Microbalance Data from Solvated Interfaces. *Analytical Chemistry 83*, 8838–8848.

[23] Du, B., Tsui, O. K. C., Zhang, Q., and He, T. (2001) Study of Elastic Modulus and Yield Strength of Polymer Thin Films Using Atomic Force Microscopy. *Langmuir 17*, 3286–3291.

[24] Dokukin, M. E., and Sokolov, I. (2012) Quantitative Mapping of the Elastic Modulus of Soft Materials with HarmoniX and PeakForce QNM AFM Modes. *Langmuir 28*, 16060–16071.

[25] Young, T. J., Monclus, M. A., Burnett, T. L., Broughton, W. R., Ogin, S. L., and Smith, P. A. (2011) The Use of the PeakForce Quantitative Nanomechanical Mapping AFM-based Method for High-Resolution Young's Modulus Measurement of Polymers. *Measurement Science and Technology 22*, 125703.

Chapter 4

DYNAMIC ANION-ADAPTIVE POLY(IONIC LIQUID) FILMS VIA SURFACE-INITIATED RING-OPENING METATHESIS POLYMERIZATION

Introduction

The majority of surface-tethered PILs in the literature have been prepared by SI-ATRP. These films have been prepared on both planar substrates[1–4] and nonplanar substrates[5] making it difficult to compare the prepared PIL films solely by film thickness. For the planar substrates, thin polymer films ($\leq$ 50 nm) were formed by very long polymerization times ($\geq$ 24 h).[2,3] For example, He et al.[2] reported the preparation of poly([1-(4-vinylbenzyl)-3-butyl imidazolium][hexafluorophosphate]) brushes by SI-ATRP on a flat silicon substrate. They demonstrated nanometer-level control over film thickness, tunable wettability of the PIL brushes by exchanging their counter anions, and $\sim$ 50 nm thick films for a 24 h polymerization.[2]

The ROMP reaction is driven by the release of ring strain balanced by entropic penalties.[6] Norbornene (NB), a cyclic seven-membered ring, which exhibits a high amount of strain energy (27.2 kcal/mol),[7] is typically chosen as the polymerizable group in ROMP monomers.[8] Ye et al[9] reported the first preparation of PIL films via SI-ROMP on non-planar substrates, where they form poly([3-[(bicyclo[2.2.1]hept-5-en-2-yl)methyl]-1,2-methylimidazol-3-ium][hexafluorophosphate]) films on titanium dioxide (TiO_2) nanowires. They demonstrated the tunable wettability of the PIL films by immersion of the nanowires in aqueous salt solutions with varying anions, and achieved brushes that were $\sim$ 80 nm thick over a 2 h polymerization time.[9] They

investigated the use of the PIL films with anions, such as, [Cl], [BF_4], and $^{-}NTf_2$. The preparation of PIL films via SI-ROMP on planar substrates has not been reported in the literature.

In this chapter, I report the preparation of surface-immobilized PIL films on planar substrates of glass and gold via the SI-ROMP of the IL monomer 3-[(bicyclo[2.2.1]hept-5-en-2-yl)methyl]-1,2-dimethylimidazol-3-ium hexafluorophosphate ([N_1-dMIm][PF_6]). By employing SI-ROMP, I demonstrate the rapid growth of PIL films that are $>$ 500 nm, which is an order of magnitude greater than the thicknesses achieved by other polymerization routes. Thicker films are expected to be more robust as coatings and to have greater anion absorption capacity. I investigated the anion exchange of the PIL films with a variety of anions. I report the first incorporation of large anionic dyes into a PIL film, highlighting the ability of the films to behave as anionic chameleons, which means that the films can adapt to their anionic environment. The anion-dependent surface wettability of the PIL films was characterized by contact angle goniometry. I report the first use of quartz crystal microbalance with dissipation (QCM-D) to determine the bulk interaction of surface-anchored PIL films with water as well as the material properties of the PIL such as dynamic shear modulus and viscosity. The effect of anion on the ion conduction of the surface-anchored PIL films was analyzed using electrochemical impedance spectroscopy (EIS), revealing dramatic differences in the resistance to ion transport between the PIL films with the PF_6^{-} anion and the ClO_4^{-} anion. Understanding the ionic conduction of surface-tethered PIL films is important for the use of the films in electrochemical devices.

Polymerization of [N_1-dMIm][PF_6] on Gold and Glass Substrates

ROMP-active substrates of gold and glass were prepared as described in Chapter 3. Freshly prepared ROMP-active substrates were quickly rinsed with DCE and immediately placed in a 0.1 M [N_1-dMIm][PF_6] solution in DCE for up to 15 min. The substrates were subsequently rinsed with DCM, ethanol, water, and ethanol and dried in a stream of nitrogen.

Polymerization on QCM-D Quartz Sensor

To prevent non-specific growth of the polymer on the quartz surface and the gold electrode on the back of the sensor, the QCM-D sensor was exposed to a 5 mM solution of decyltrichlorosilane in toluene for 1 h to yield a methyl-terminated SAM on the exposed quartz surface and sequentially rinsed with toluene, ethanol, water, and ethanol and dried in a stream of nitrogen. The gold electrode on the back of the sensor was then exposed to decanethiol to yield a methyl-terminated SAM. The sensor was rinsed with ethanol, water, and ethanol and dried in a stream of nitrogen. The active surface of the QCM-D sensor was rendered ROMP-active as described in Chapter 3 for gold substrates. The ROMP-active sensor was quickly rinsed with DCE and immediately placed in a 0.02 M [N_1-dMIm][PF_6] solution in DCE for 15 min. The sensor was subsequently rinsed with DCM, ethanol, water, and ethanol and dried in a stream of nitrogen.

Ionic Polymer Film Anion Exchange

The anion exchange of p[N_1-dMIm] films with resident anion was accomplished by simply immersing the film into an aqueous solution containing 0.2 M of the salt of the desired anion for a minimum of 2 h.[2,10] The chemical structures of the anions

considered in this chapter are shown in Figure 4.1.

Results and Discussion

Polymer Film Growth

Initial attempts at the SI-ROMP of a norbornene-tethered IL focused on the monomers 3-[(bicyclo[2.2.1]hept-5-en-2-yl)methyl]-1-methylimidazol-3-ium bromide and 3-[(bicyclo[2.2.1]hept-5-en-2-yl)methyl]-1-methylimidazol-3-ium hexafluorophosphate. SI-ROMP of both of these monomers was unsuccessful with catalyst **1**. The methyl imidazolium (MIm) functional group of these monomers is known to inhibit ring-opening metathesis polymerization with Grubb's catalyst via the abstraction of the acidic proton on the C_2 carbon of the MIm functional group leading to complexation with the 14 e^- species of the catalyst and competitive inhibition of the reaction of the 14 e^- species with olefin.[11,12] The inhibition of the catalyst can be avoided by utilizing the dimethylimidazolium (dMIm) functional group.[12]

Polymerization of the ionic liquid monomer 3-[(bicyclo[2.2.1]hept-5-en-2-yl)methyl]-1,2-dimethylimidazol-3-ium hexafluorophosphate ([N_1-dMIm][PF_6]) at a concentration of 0.1 M in DCE for 15 min led to a surface-tethered polymer film that exhibited a profilometric thickness of 652 ± 29 nm. Figure 4.2 shows the IR spectrum of a p[N_1-dMIm][PF_6] polymer film grown on a gold substrate. The dominant absorption band is the P−F stretch at 865 cm^{-1}.[13] Weaker absorption bands due to the polymer carbon backbone are also observed, in particular, a C=C stretching absorption band at 1589 cm^{-1}, a symmetric CH_2 in-plane bending (scissoring) absorption band at 1462 and 1423 cm^{-1}, an asymmetric CH_3 absorption band at 1392 cm^{-1}, a symmetric CH_3 absorption band at 1243 cm^{-1}, and a vibrational CH_3 in-plane bending (rocking) absorption band at 742 cm^{-1}.[14]

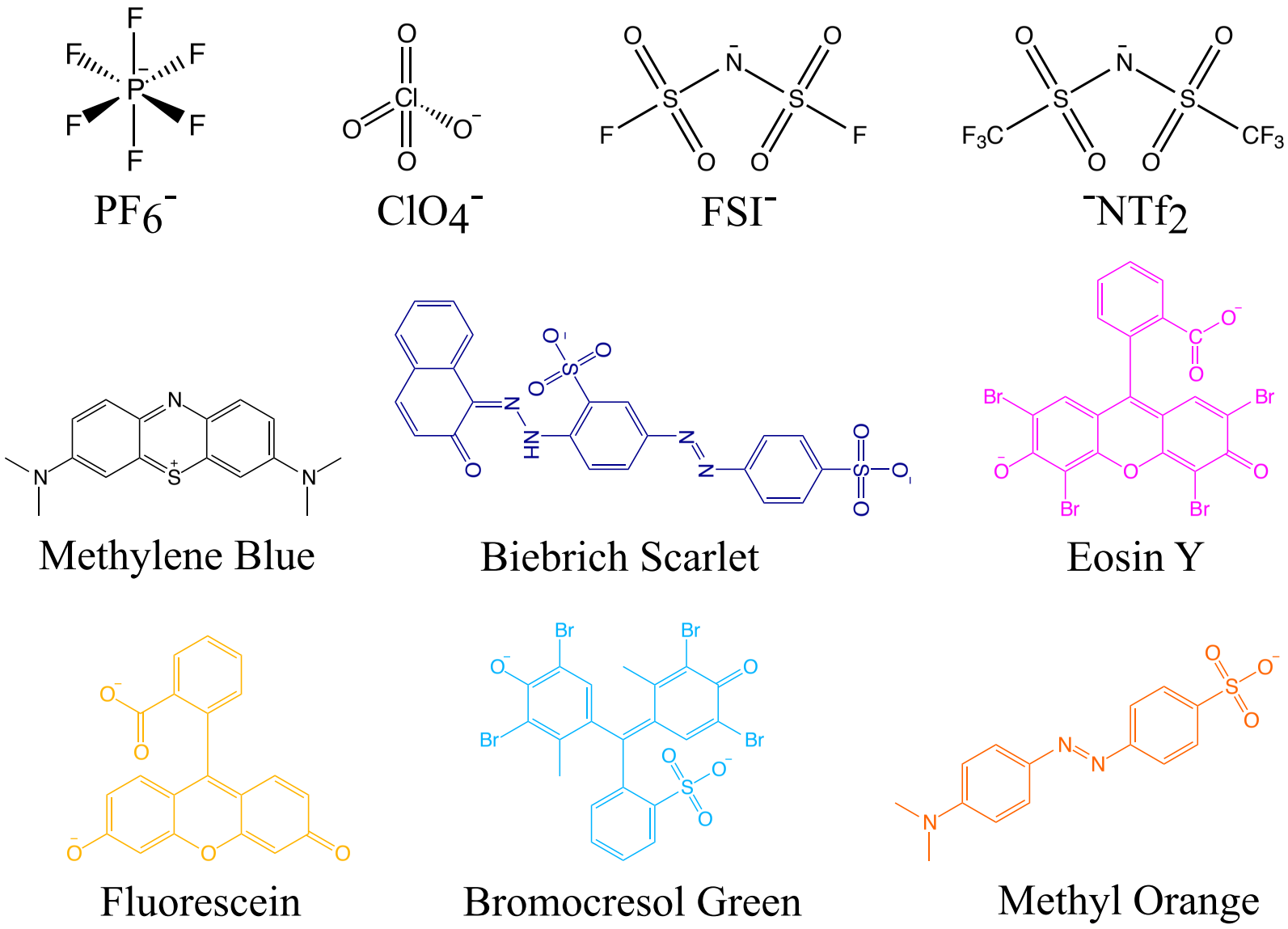

Figure 4.1: Structures of anions considered for exchange into p[N_1-dMIm] films as well as the structure of the cation methylene blue.

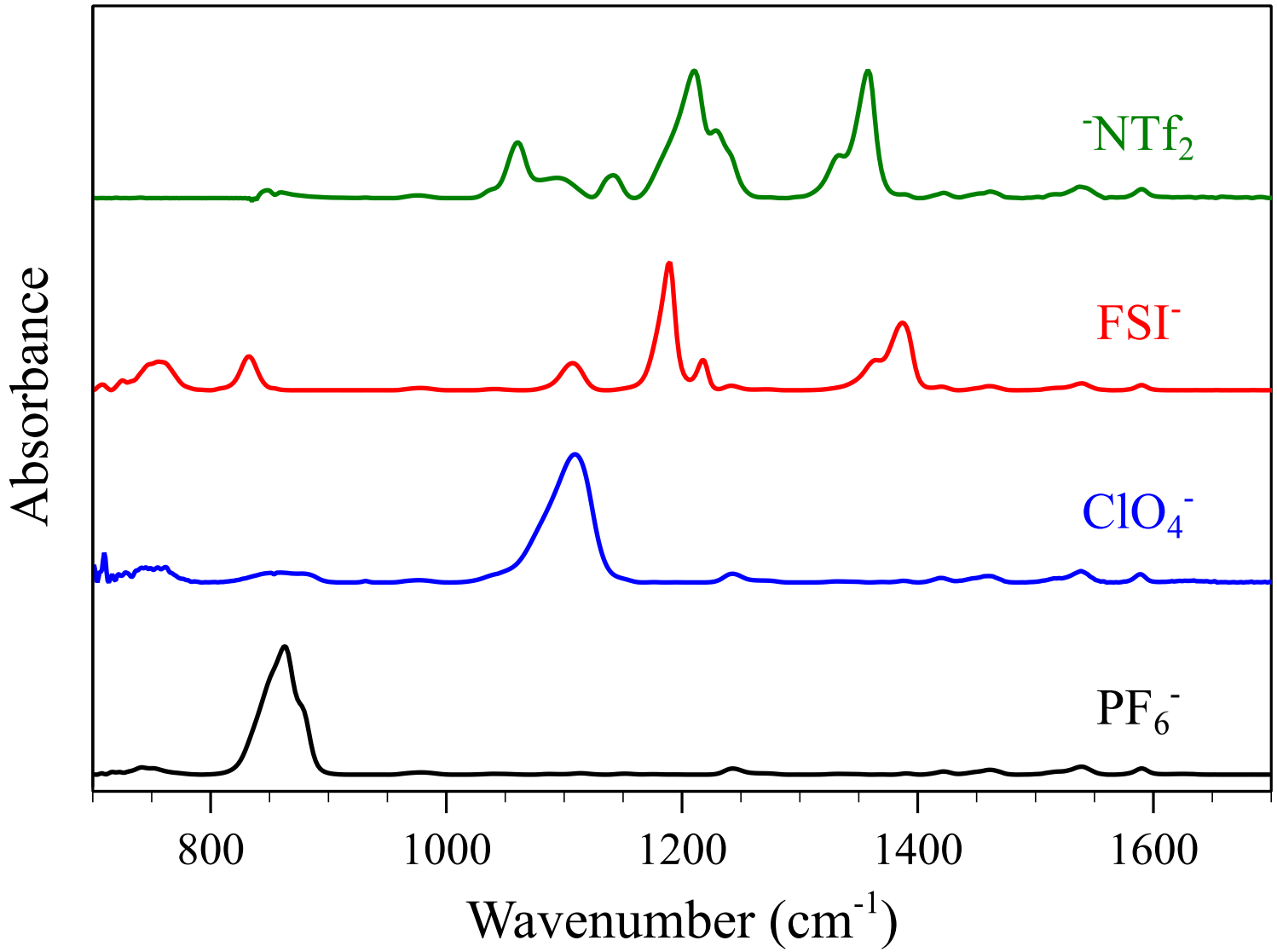

Figure 4.2: Polarization modulation-infrared reflectance-absorption spectra of p[N_1-dMIm] films on gold substrates. The p[N_1-dMIm] films were initially polymerized with the PF_6^- anion, but were successfully exchanged with ClO_4^-, FSI^- and $^-NTf_2$ anions.

p[N_1-dMIm] Film Anion Exchange

Anion exchange of the PF_6^- anion for p[N_1-dMIm][PF_6] films on gold substrates was successfully accomplished with the anions ClO_4^-, FSI^-, and $^-NTf_2$ as evidenced by the IR spectra shown in Figure 4.2. The major absorption bands in the IR spectra for the anions PF_6^-, ClO_4^-, FSI^-, and $^-NTf_2$ are summarized in Table 4.1. The dominant absorption band in the spectrum for the ClO_4^- anion is the Cl−O stretch at 1110 cm^{-1}. For the IR spectra with the FSI^- and $^-NTf_2$ anions, the dominant absorption bands are the SO_2^- and C−F bands between 1100 and 1400 cm^{-1}. The polymer backbone structure for the p[N_1-dMIm] films with the anions PF_6^-, ClO_4^-, FSI^-, and $^-NTf_2$ was characterized by observing the C_{sp2}−H and C_{sp3}−H bands in IR spectra (Figure 4.3.) The retention of the C_{sp2}−H and C_{sp3}−H bands for all the anions studied suggests minimal variation in the polymer backbone structure due to anion exchange.

The major absorbance bands in the IR spectra for the anions PF_6^-, ClO_4^-, FSI^-, and $^-NTf_2$ are summarized in Table 4.2. There are minimal variations in the C_{sp^3}−H stretch vibration band peak positions for the p[N_1−dMIm] polymer film with anion exchange as shown in Figure 4.3 and Table 4.2; however, the peak shapes are similar for the various anions observed in Figure 4.3. There are minimal variations in the peak position and shape for the C_{sp^2}−H stretch vibration bands for p[N_1−dMIm] polymer film with the anions PF_6^-, ClO_4^-, and FSI^-. The p[N_1−dMIm][NTf_2] film, however, does show a change in peak shape and position for the C_{sp^2}−H stretch vibration bands. The C_{sp^2}−H peak shape observed with the anions PF_6^-, ClO_4^-, and FSI^- is recoverable with anion exchange.

Profilometric thicknesses of the p[N_1-dMIm][PF_6] films formed on gold substrates after anion exchange with ClO_4^-, FSI^-, and $^-NTf_2$ are reported in Table 4.1. No statistically significant change in thickness was observed for p[N_1−dMIm][PF_6] films after exchange with the ClO_4^- and $^-NTf_2$ anions. However, p[N_1−dMIm][PF_6] films

Table 4.1: Profilometric Thicknesses and Anion Polarization Modulation-Infrared Reflectance-Absorption Bands for p[N_1-dMIm] Films.[13–19]

Anion	Thickness (nm)	Functional Group	Wavelength (cm^{-1})
PF_6^-	650 ± 30	P−F stretch	865
ClO_4^-	590 ± 30	C−O stretch	1110
FSI^-	530 ± 4	ν_{as} SO_2 in-plane stretch	1384
		ν_{as} SO_2 out-of-plane stretch	1360
		ν_s SO_2 in-plane stretch	1217
		ν_s SO_2 out of plane stretch	1188
		ν_s SO_2out of plane stretch	1188
		ν_{as} S−F/S−N−S stretch	834
$^-NTf_2$	650 ± 50	ν_{as} SO_2 in-plane stretch	1357
		ν_{as} SO_2 out-of-plane stretch	1331
		ν_s SO_2 stretch	1230
		ν_{as} CF_3 stretch	1210
		ν_s SO_2 stretch	1140
		ν_{as} S−N−S stretch	1060

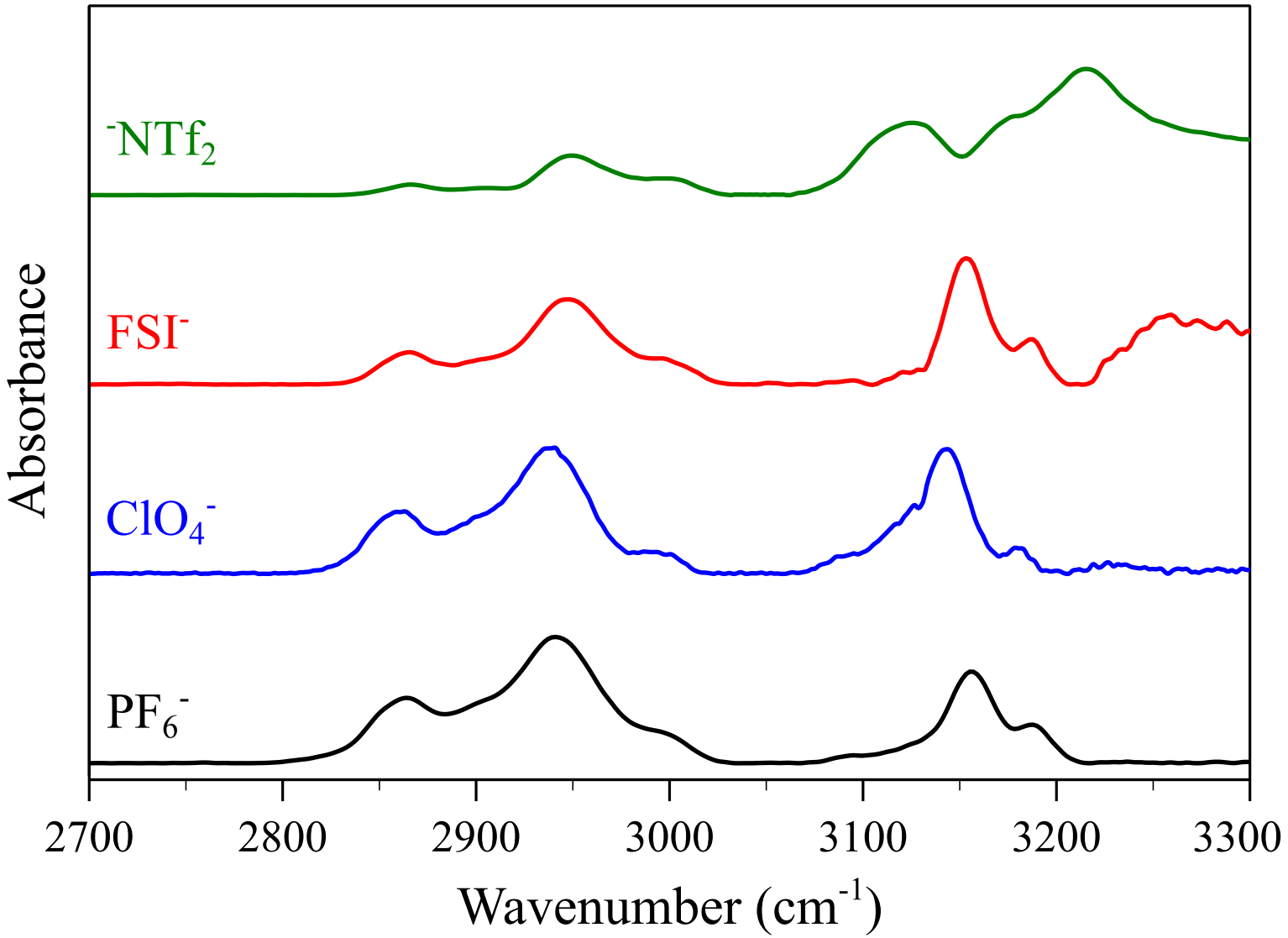

Figure 4.3: Polarization modulation-infrared reflectance-absorption spectra of p[N_1−dMIm] films on gold substrates. The p[N_1−dMIm] films were initially polymerized with the PF_6^- anion, but were successfully exchanged with ClO_4^-, FSI^- and $^-NTf_2$ anions.

Table 4.2: Film Anion Polarization Modulation-Infrared Reflectance-Absorption Bands of p[N_1−dMIm] Films.[14,16–19]

Anion	C_{sp^3}−H Bands (cm^{-1})	C_{sp^2}−H Bands (cm^{-1})
PF_6^-	2865 (ν_s), 2942 (ν_{as})	3157, 3189
ClO_4^-	2861 (ν_s), 2939 (ν_{as})	3143, 3181
FSI^-	2865 (ν_s), 2948 (ν_{as})	3154, 3189
$^-NTf_2$	2866 (ν_s), 2950 (ν_{as})	3177, 3216

after exchange with the FSI^- anion exhibit a lower film thickness. The profilometric thickness of the p[N_1−dMIm][PF_6] films can be recovered by anion exchange of the p[N_1−dMIm][FSI] film with the $PF_6{}^-$ anion as listed in Table 4.1.

Larger anions in the form of anionic dyes were also incorporated into p[N_1−dMIm] films on glass substrates. The anionic dyes, methyl orange, fluorescein, biebrich scarlet, eosin Y, and bromocresol green were exchanged into p[N_1−dMIm][PF_6] films as shown in Figure 4.4 a. The polymer films are reversibly colored by the incorporation of the anionic dyes. Absorption spectra for the p[N_1−dMIm] polymer films with the anionic dyes are shown in Figure 4.4 b. p[N_1−dMIm] polymer films exposed to the anionic dyes show broad absorbance of light in the wavelengths 300 to 800 nm. The p[N_1−dMIm][PF_6] films were also exposed to a 0.2 M aqueous solution of methylene blue as a positively charged control for non-specific staining. p[N_1−dMIm][PF_6] films exposed to methylene blue, however, did not acquire any color as shown in Figure 4.4 a and did not exhibit absorbance over the original p[N_1−dMIm][PF_6] films as shown in Figure 4.4 b. The lack of observable color and absorbance for the polymer films exposed to the cationic dye supports exchange of the anionic dyes into the films. These results demonstrate that the films adapt to the anionic environment that they encounter, thereby functioning as anionic chameleons.

p[N_1−dMIm] Film-Water Interaction

The anion strongly influences the surface wettability of surface-tethered ILs,[20] as well as the solubility of PILs with water.[10,21] The interaction of the p[N_1−dMIm] films with water both at the surface and within the PIL was investigated. The surface wettability of the p[N_1−dMIm] films was assessed by contact angle goniometry with a measured advancing (θ_A) water contact angle of 61±2° for the p[N_1−dMIm][PF_6] film, 65 ± 3° for the p[N_1−dMIm][NTf_2] film, 63 ± 2° for the p[N_1−dMIm][FSI] film, and 35±3° for the p[N_1−dMIm][ClO_4] film. The low advancing contact angle observed for

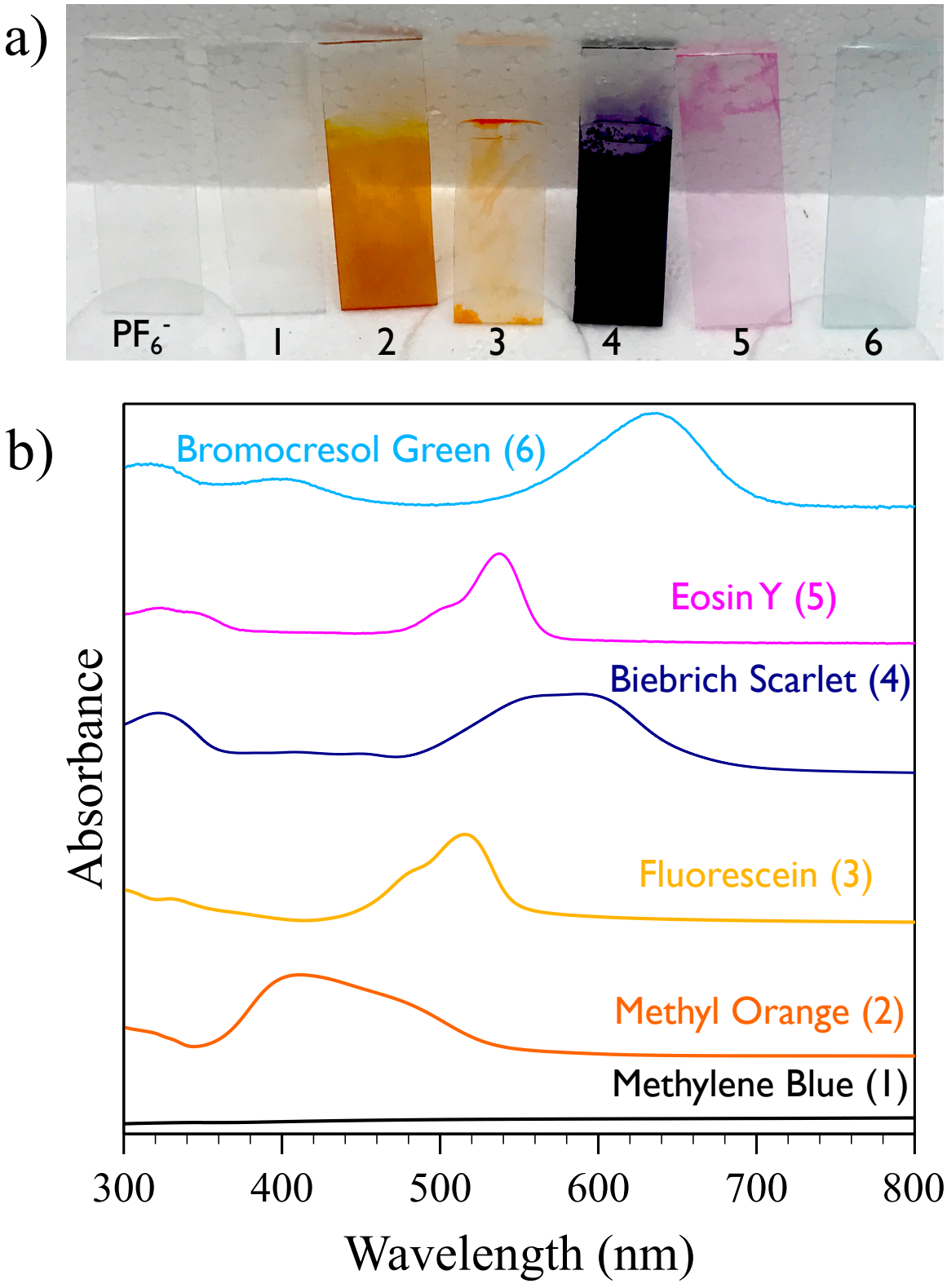

Figure 4.4: a) Images of p[N_1−dMIm] with various anionic dyes on glass slides b) Ultraviolet-Visible absorption spectra of p[N_1−dMIm] films with various anionic dyes. Absorption spectra of the as-polymerized p[N_1−dMIm][PF_6] films were collected and subtracted from the spectra for the p[N_1−dMIm] films with the anionic dyes.

the p[N_1−dMIm][ClO_4] film suggests that the surface wettability is anion-dependent with the ClO_4^- being the most hydrophilic anion. For a surface-tethered methylimidazolium IL, Lee et al.[20] observed the same order of increasing hydrophobicity by contact angle for the $^-NTf_2$, PF_6^-, and ClO_4^- anions.

The interaction of water within the p[N_1−dMIm] films was investigated by performing quartz crystal microbalance with dissipation (QCM-D) in an aqueous environment. In QCM-D, the addition of a mass to the crystal electrodes results in a decrease in frequency.[22,23] Laterally homogeneous films exhibit dissipation related to the viscoelastic properties of the films.[23] Frequency and dissipation data for the pretreated quartz crystal were collected and used as the baseline data. The QCM-D spectra for the p[N_1−dMIm] film showing the changes in frequency (Δf) and dissipation (ΔD) with respect to the film anion are shown in Figure 4.5. Growth of the p[N_1−dMIm][PF_6] film on the sensor crystal results in a large decrease in Δf for both the fundamental frequency and the 3rd overtone frequency, which is consistent with the attachment of a polymer film to the surface. In order to comprehend the changes in mass observed by varying the anions, I utilized the molecular weights, listed in Table 4.3, of the monomeric cation [N_1−dMIm] with the various anions that were investigated. The relative changes in mass arising from anion exchange observed for the films by QCM-D should conform to the relative variation in molecular weight for the monomeric cation with the various anions.

Anion exchange of the p[N_1−dMIm][PF_6] film to a p[N_1−dMIm][ClO_4] film leads to a decrease in Δf for both overtones collected as shown in Figure 4.5, which is consistent with the larger mass of the PF_6^- monomer compared to that of the ClO_4^- monomer. The p[N_1−dMIm][FSI] film and the p[N_1−dMIm][NTf_2] film both show an increase in Δf for both overtones collected as shown in Figure 4.5, which is consistent with the larger mass for both the FSI^- and $^-NTf_2$ monomers compared to that of the PF_6^- monomer. The variations in ΔD can be better understood by performing a

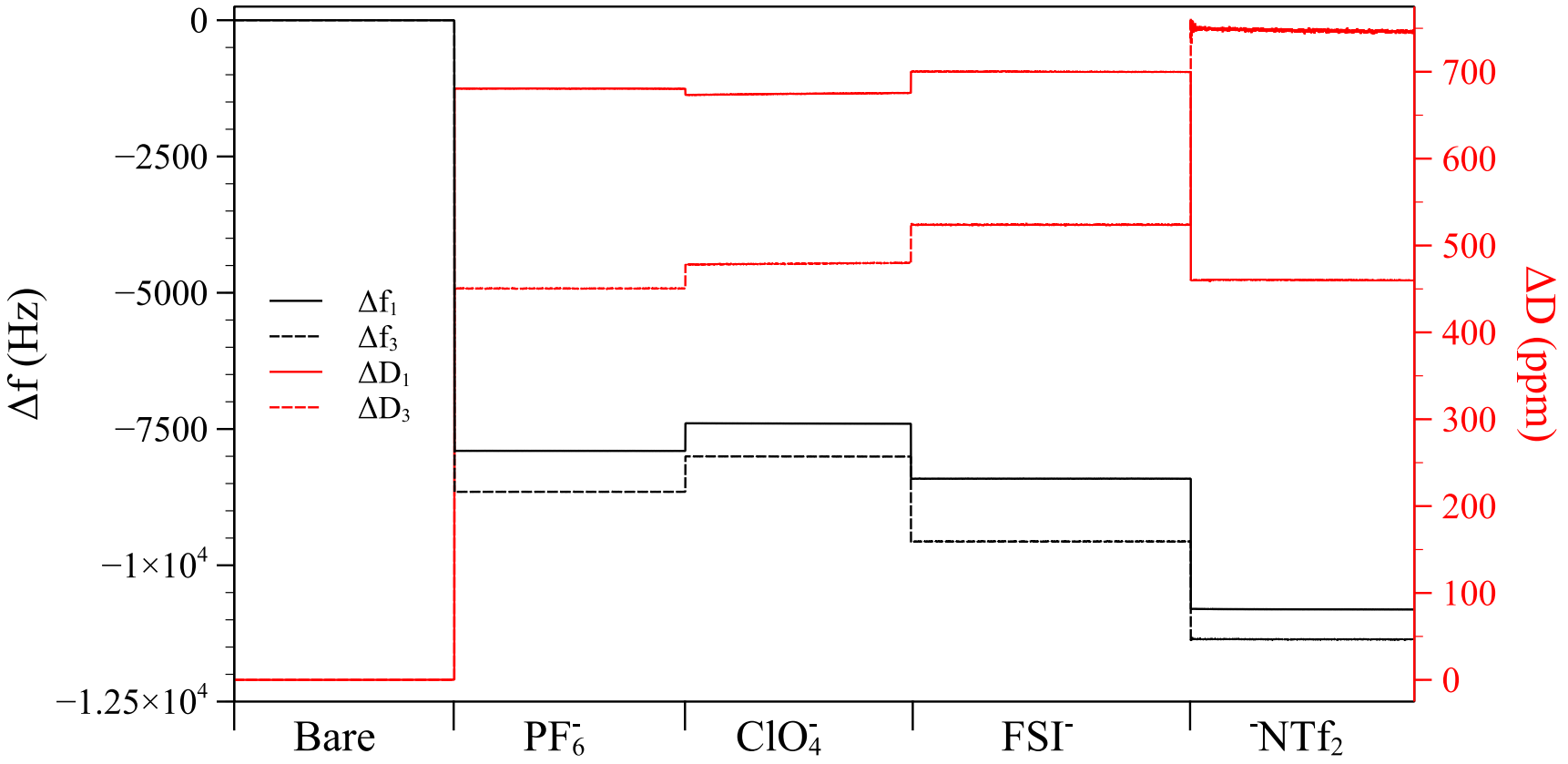

Figure 4.5: QCM-D spectra of p[N_1−dMIm] films. The p[N_1−dMIm] film was polymerized on a Au-coated quartz crystal with the PF_6^- anion, but was successfully exchanged with ClO_4^-, FSI^- and $^-NTf_2$ anions. The spectra were collected for a minimum of 20 min in 18.2 MΩ H_2O at 20 °C and a flow rate of 50 μL/min after a 2 h flush of the chamber. The fundamental (5 MHz) and the third overtone (15 MHz) were recorded. The bare spectrum was collected for the Au-coated quartz crystal after UVO treatment and prior to polymerization.

Table 4.3: p[N_1−dMIm] Mass, Storage Modulus (G'), and Viscosity (η) Values Obtained from a Fit of the QCM-D Spectra in Figure 4.5 with a Kelvin-voigt Model. Fractional Water Uptake (υ) Obtained from Equation 4.1.

Anion	MW[a] (g/mol)	Mass (μg/cm^2)	G' (MPa)	η (mPa·s)	υ
PF_6^-	144.96	138.39 ± 0.01	33.37 ± 0.02	242 ± 0.2	0.00
ClO_4^-	99.45	129.37 ± 0.04	26.31 ± 0.02	225 ± 0.4	0.08
FSI^-	180.12	146.93 ± 0.01	34.22 ± 0.02	191 ± 0.2	−0.04
$^-NTf_2$	280.14	188.54 ± 0.06	43.88 ± 0.12	547 ± 1.6	−0.02

[a] Molecular weight of the monomeric cation N_1−dMIm$^+$ with the listed anion.

quantitative analysis of the QCM-D spectra. In general, an increase in ΔD indicates an increase in the viscoelasticity of the surface-tethered PIL film. Attachment of the p[N_1−dMIm][PF_6] film leads to an increase in ΔD as shown in Figure 4.5 consistent with the attachment of a soft polymeric film on the QCM crystal surface. Anion exchange of the PF_6^- anion with other anions leads to increases or decreases in ΔD, due to the effect of the anion on the viscoelastic properties of the film. Therefore, in order to determine the viscoelastic properties of the surface-tethered PIL film with the various anions, a quantitative analysis of the mass, shear modulus, and viscosity of the p[N_1−dMIm] films was conducted by fitting the spectra in Figure 4.5 using a Voigt-based viscoelastic model included in the Q-Sense software. The Kelvin-voigt model relies on a continuum model where the sample properties are parametrized by a set of one or more slabs with certain thicknesses, densities, and viscoelastic properties.[23] The results of the quantitative analysis are shown in Table 4.3.

The viscoelastic properties of the film in the Kelvin-voigt model are represented by the complex shear modulus, $G = G^{'} + iG^{''}$, where i is the imaginary unit.[23] The storage modulus $G^{'}$ is a measure of the energy stored elastically and is concerned with the extent of deformation due to the applied force. The p[N_1−dMIm] film with the $^-NTf_2$ anion exhibits the least amount of deformation, due to the highest value of storage modulus observed of 43.88 ± 0.12 MPa, as listed in Table 4.3. In comparison the p[N_1−dMIm] film with the ClO_4^- anion shows a greater than a one and a half times increase in deformation with a storage modulus of 26.31 ± 0.02 MPa. The p[N_1−dMIm] film with the PF_6^- and FSI^- anions show similar amounts of deformation that are intermediate to those of the other films. The loss modulus $G^{''} = \omega\eta$ describes the viscous energy dissipation of the material, where the viscosity η can be thought of as a friction coefficient that relates the applied force to the rate of deformation.[23] The p[N_1−dMIm] film with the $^-NTf_2$ anion exhibits the highest amount of viscous energy dissipation due to the highest value of η, 546.8 ± 1.6 mPa·s,

while the p[N_1−dMIm] film with the FSI^- anion shows an almost 3 fold decrease in viscous energy dissipation, 190.6 ± 0.2 mPa·s, for the anions investigated. The p[N_1−dMIm] films with the PF_6^- and the ClO_4^- anions show similar amounts of viscous energy dissipation that are intermediate to those of the other films.

The calculated mass reported for the p[N_1−dMIm] films include absorbed water in the surface-tethered polymer films. In order to determine the amount of water uptake in the p[N_1−dMIm] films, the ratio of the observed mass to the expected mass relative to the p[N_1−dMIm][PF_6] film was calculated as

$$\upsilon = 1 - \frac{M(X^-)MW(PF_6)}{M(PF_6)MW(X^-)} \tag{4.1}$$

where, υ is the fractional uptake of water into the film relative to the p[N_1−dMIm][PF_6] film, $M(X^-)$ is the calculated mass for the film with the X^- anion and $MW(X^-)$ is the molecular weight of the IL monomer with the X^- anion. The calculated values for the fractional uptake, υ, are shown in Table 4.3. Positive values of υ indicate an increase in PIL film water swelling compared to that of the p[N_1−dMIm] film with the PF_6^- anion, while negative values indicate a decrease in PIL film water swelling. As shown in Table 4.3, the p[N_1−dMIm][ClO_4] film shows an 8% increase in υ compared to the film with the PF_6^- anion. The increase in υ is expected due to the hydrophobicity of the PF_6^- anion compared to the ClO_4^- as determined by surface wettability above. However, the magnitude of increase in υ is minimal compared to the differences in θ_A observed for the PF_6^- and ClO_4^- anions. Additionally, the p[N_1−dMIm] films with the FSI^- and the $^-NTf_2$ anions exhibit similar surface wetting behavior to the p[N_1−dMIm][PF_6] film, and they show a 4% and a 2% decrease in υ, respectively, suggesting a minimal effect of the film anion on water uptake for these films with similar surface wetabilities. The surface wettability of the films with water and their viscoelastic properties are highly dependent on the anion present in the film and are tunable via a simple anion exchange mechanism.

Ion Transport in p[N_1−dMIm] Films

Ion transport in bulk PILs has been shown to be a function of polymer properties such as glass transition temperature and the interstitial space or free volume of the polymeric chains which impacts ion mobility.[24] Understanding ion transport in surface-tethered PILs is crucial for the implementation of PIL films in electrochemical devices requiring intimate contact between the PIL film and electrode surface. Ion transport through the p[N_1−dMIm] films with the anions PF_6^-, $^-NTf_2$, FSI^-, and ClO_4^- was investigated by utilizing electrochemical impedance spectroscopy (EIS). The studies were conducted in the presence of a 0.1 M aqueous solution of a salt with the same anion as the polymer film to avoid anion exchange during the collection of the spectra. Representative Bode plots of EIS spectra for p[N_1−dMIm] films on gold substrates with various anions as well as a control film consisting of a hydroxyl-terminated SAM on gold substrates exposed to NBDAC conducted in the presence of a 0.1 M KPF_6 aqueous solution are shown in Figure 4.6. The impedance spectra were fit with the equivalent circuit model shown in Scheme 3.4 to quantify the circuit parameters as shown in Tables 4.4 and 4.5.

Phase angle plots of EIS spectra corresponding to the Bode plots of Figure 4.6 for p[N_1−dMIm] films on gold substrates with various anions, as well as a control film consisting of a hydroxyl-terminated SAM on gold substrates exposed to NBDAC, conducted in the presence of a 0.1 M KPF_6 aqueous solution are shown in Figure 4.7.

In collecting EIS spectra, an electrochemical cell with the modified gold substrates as the working electrode and electrolyte solution is perturbed with a sinusoidal potential of varying frequency (f). Sinusoidal perturbation of the working electrode potential with high frequencies results in the observation of the ohmic resistance of the electrolyte solution to ion migration termed, solution resistance (R_s). The R_s for the control film as well as the p[N_1−dMIm] films with varying anions was observed for high frequencies, $f \geq 10^4$ Hz, as shown in Figure 4.6 and quantified in Table 4.4.

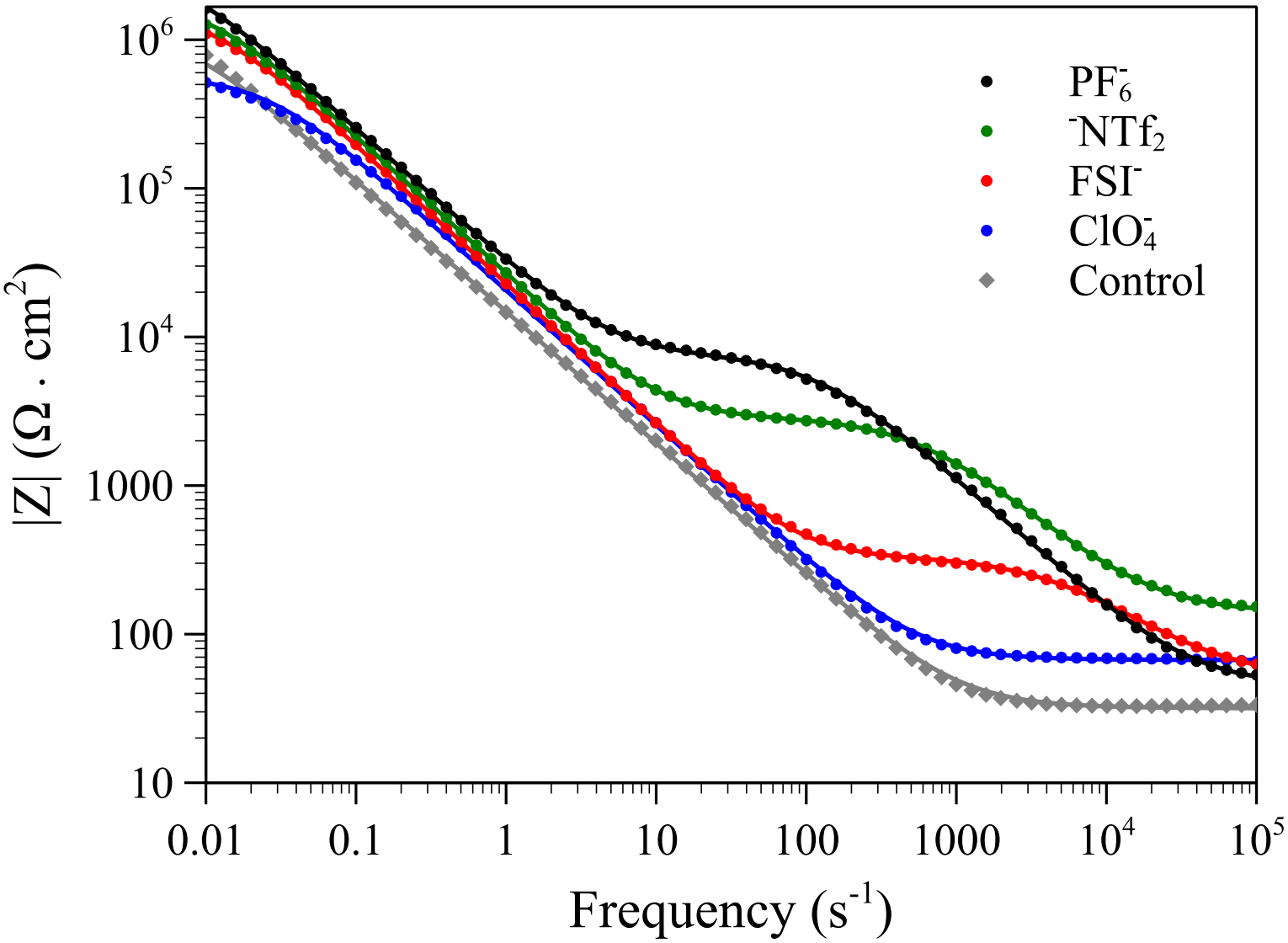

Figure 4.6: Bode plot of EIS spectra for p[N_1−dMIm] films acquired in a 0.1 M aqueous solution of the polymer film anion salt. The salts used were KPF_6, $LiNTf_2$, KFSI, $LiClO_4$. EIS of a film consisting of a hydroxyl-terminated SAM exposed to NBDAC acquired in a 0.1 M KPF_6 aqueous solution is shown as a control. The solid curves represent fits using the equivalent circuit in Scheme 3.4.

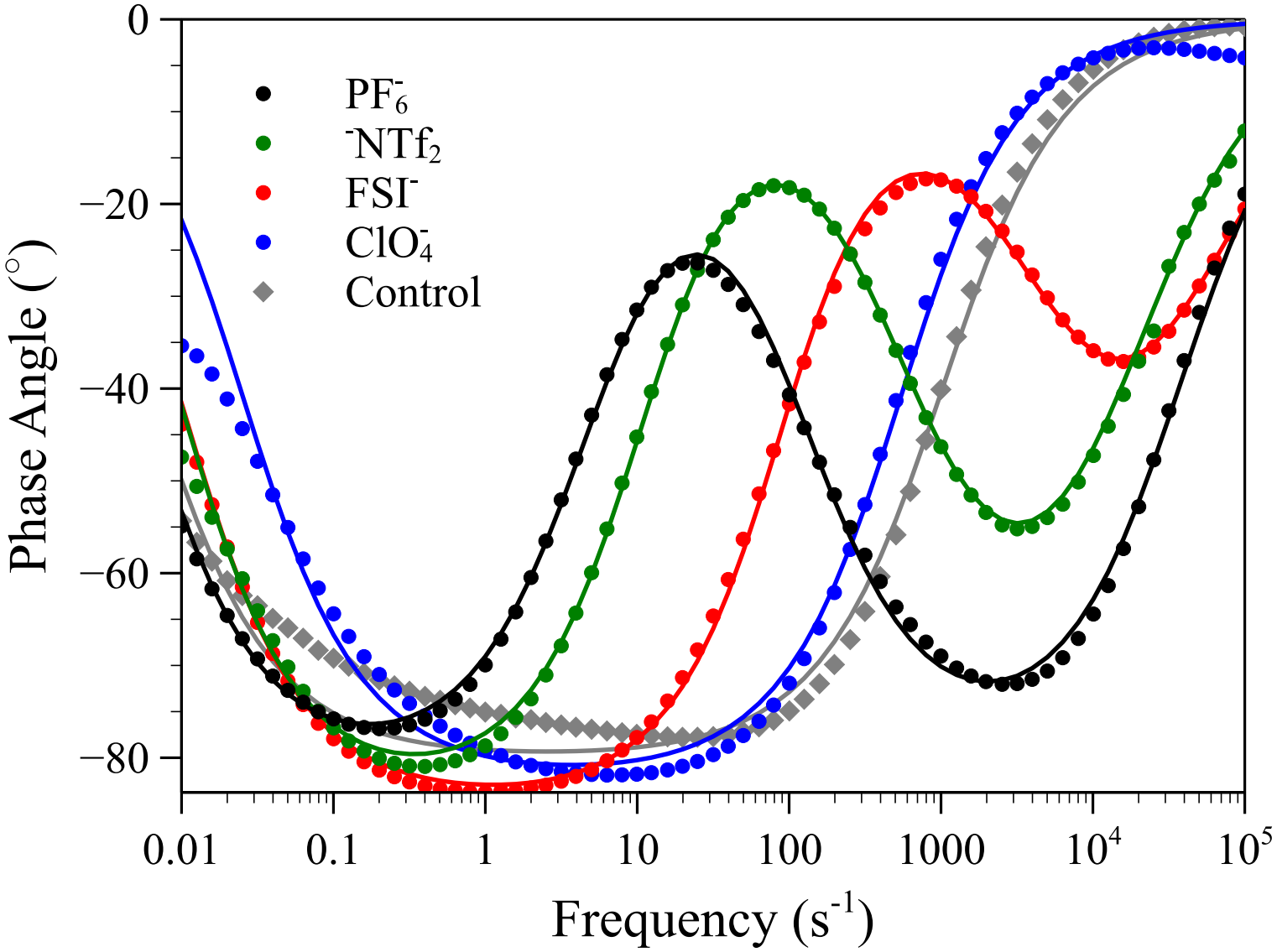

Figure 4.7: Phase angle plot of EIS spectra for p[N_1−dMIm] films acquired in a 0.1 M aqueous solution of the polymer film anion salt. The anion salts used were KPF_6, $LiNTf_2$, KFSI, and $LiClO_4$. EIS of a film consisting of a hydroxyl-terminated SAM exposed to NBDAC acquired in a 0.1 M KPF_6 aqueous solution is shown as a control. The solid curves represent fits to the equivalent circuit in Scheme 3.4.

Variations in R_s are due to the different ionic conductivities of electrolyte solutions arising from the different salts utilized in the collection of the EIS spectra.

Low frequency sinusoidal perturbation of the working electrode potential results in the observation of ion migration occurring at long timescales such as the formation of an electrical double layer at the electrode surface, referred to as interfacial capacitance (C_i), and the resistance to ion transport at the electrode interface, or interfacial resistance (R_i). The C_i for the control film as well as the p[N_1−dMIm] films with varying anions was observed for low frequencies, $f \leq 1$ Hz, as shown in Figure 4.6. The values for the C_i and R_i obtained from a fit of the data are listed in Table 4.4. The C_i for the PF_6^-, $^-NTf_2$, and FSI^- anions are statistically similar and lower than the C_i observed for the ClO_4^- anion. The higher C_i for the p[N_1−dMIm][ClO_4] film is consistent with a wetter interfacial region and/or close approach of the ClO_4^- anion to the metal surface. The interface for the control film is modified when preparing the p[N_1−dMIm] films, which is reflected in the C_i for the control film being greater than that for the p[N_1−dMIm] films with varying anions as shown in Figure 4.6.

Sinusoidal perturbation of the working electrode potential with intermediate frequencies results in the observation of ion migration occurring at intermediate timescales such as a film capacitance (C_f) due to a separation of charge between the metal surface and the bulk solution as well as the resistance, (R_f), that the PIL film provides against ion migration. As shown in Figure 4.6, the EIS spectra for the p[N_1−dMIm] film with the anions PF_6^-, NTf_2^-, and FSI^- are substantially different from that of the p[N_1−dMIm][ClO_4] film and the control film. In particular, I observe a R_f and a C_f for the p[N_1−dMIm] film with the anions PF_6^-, $^-NTf_2$, and FSI^- for intermediate frequencies, $1 \leq f \leq 10^4$ Hz. The film resistance values (R_f) can be used to calculate a film conductivity (κ_f) by using,

$$\kappa_f = \frac{l}{AR} \tag{4.2}$$

Table 4.4: p[N_1−dMIm] Solution Resistance (R_s), Interfacial Resistance (R_i), and Interfacial Capacitance (C_i) Values Obtained from a Fit of the EIS Spectra in Figure 4.6 with the Equivalent Circuit in Scheme 3.4.

Electrolyte	R_s ($\Omega \cdot cm^2$)	R_i ($M\Omega \cdot cm^2$)	C_i ($\mu F/cm^2$)
KPF_6	45 ± 1	3.52 ± 0.2	8.7 ± 0.2
$LiNTf_2$	139 ± 2	1.94 ± 0.05	8.7 ± 0.1
KFSI	50 ± 2	1.68 ± 0.05	8.8 ± 0.2
$LiClO_4$	67 ± 1	0.59 ± 0.01	12.8 ± 0.1
Control[a]	32 ± 1	1.36 ± 0.04	22.1 ± 0.2

[a] The control film is a gold substrate modified with a hydroxyl-terminated SAM exposed to NBDAC with spectra acquired in a 0.1 M KPF_6 aqueous solution.

where l is the film thickness, A is the cross-sectional area of the sample, and R is the measured resistance. The capacitive behavior observed in Figure 4.6, however, is indicative of a leaky capacitor and therefore a constant phase element (CPE) was used in lieu of a capacitor to fit the EIS spectra. The impedance of the CPE is given by,

$$Z_{CPE} = \frac{1}{Y_0(jf)^{\alpha}} \tag{4.3}$$

where Y_0 is a constant with dimensions $s^{\alpha}/\Omega \cdot cm^2$ and α is a dimensionless constant with a value between 0 and 1. The CPE can be converted into an effective capacitance by using,[25]

$$C = Y_0(f_{\mathrm{m}}^{''})^{\alpha-1} \tag{4.4}$$

where $f_{\mathrm{m}}^{''}$ is the frequency at which the imaginary part of the impedance ($Z^{"}$) has a maximum.[25] The numerical values for the film resistance, conductivity, and capacitance obtained from a fit of the data with the equivalent circuit of Scheme 3.4 are shown in Table 4.5.

The p[N_1−dMIm] film anion determines the R_f with the order PF_6^- > $^-NTf_2$ ≫ FSI^- ≫ ClO_4^- and consequently the κ_f with the inverse order of the R_f. The observed order for the R_f does not exhibit a correlation with any of the other measured properties. Therefore, a combination of effects arising from the varying properties of the films with anion exchange, for instance, the glass transition temperature, ion dissociation, and water content, lead to the differences in ion transport observed for the different films.

The lack of a film impedance to the migration of ions in the p[N_1−dMIm][ClO_4] films could potentially be attributed to an effect of the cation as opposed to the anion. The effect of the electrolyte cation on the ion transport properties of the p[N_1−dMIm]

Table 4.5: p[N_1−dMIm] Film Resistance (R_f), Conductivity (κ_f), and Capacitance (C_f) Values Obtained from a Fit of the EIS Spectra in Figure 4.6 with the Equivalent Circuit in Scheme 3.4.

Electrolyte	R_f ($K\Omega \cdot cm^2$)	κ_f ($\mu S/cm$)	C_f ($\mu F/cm^2$)
KPF_6	7.90 ± 0.11	0.008 ± 0.001	0.23 ± 0.01
$LiNTf_2$	2.82 ± 0.04	0.013 ± 0.001	0.14 ± 0.01
KFSI	0.29 ± 0.01	0.180 ± 0.004	0.16 ± 0.03
$LiClO_4$[a]	$\leq (4.34 \pm 0.04) \times 10^{-3}$	$\geq 13.6 \pm 0.8$	-

[a] Values calculated for a p[N_1−dMIm][ClO_4] film EIS spectra collected in a 0.5M $CaClO_4$ solution exhibiting an R_s of $4.34 \pm 0.04\ \Omega \cdot cm^2$. The film resistance for the film is theoretically lower than the R_s observed.

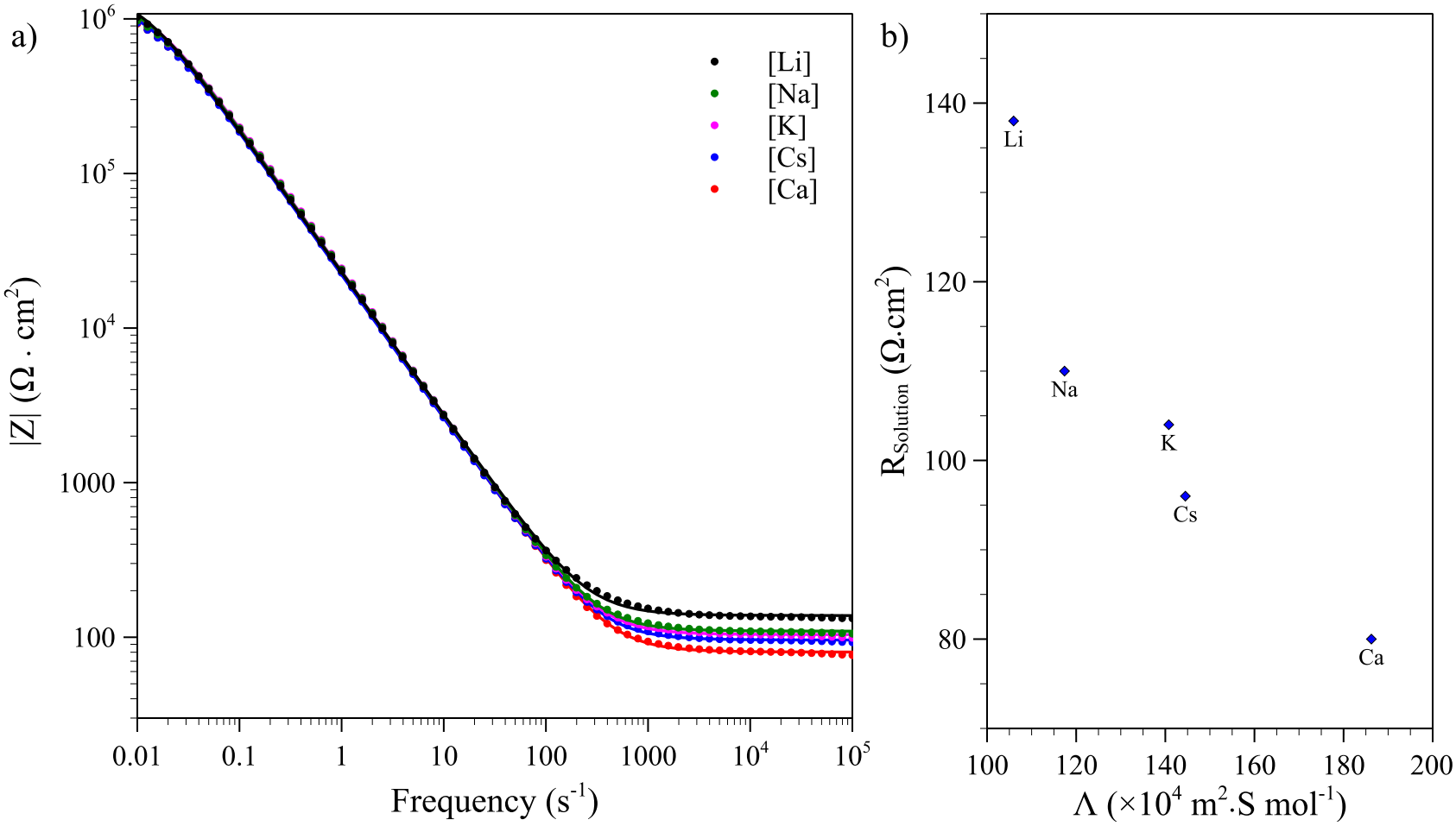

Figure 4.8: Effect of the electrolyte cation on the ion transport properties of p[N_1-dMIm] films. a) Bode plot of EIS spectra of p[N_1−dMIm][ClO_4] films acquired in 0.05 M aqueous solutions of ClO_4^- salts with varying cations. The solid curves represent fits using the equivalent circuit in Scheme 3.4. b) Solution resistance versus salt limiting molar conductivity.

films was investigated using EIS of p[N_1−dMIm][ClO_4] films shown in Figure 4.8 in the form of Bode plots. The corresponding phase angle plots are included in Figure 4.9. The studies were conducted in the presence of 0.05 M aqueous solutions of ClO_4^- salts with varying cations. The spectra for the p[N_1−dMIm][ClO_4] films do not show an obvious film resistance to ion migration for the cations investigated. The p[N_1−dMIm][ClO_4] films show almost identical impedance behavior in the low and intermediate frequency regions, $f \leq 100$ Hz. However, for the high frequency region, one can observe that the solution resistance, R_s, is a function of the cation present in the electrolyte. In particular, the solution resistance decreases with increasing equivalent ionic conductivity (Λ°) at infinite dilution of the various salts considered. Therefore, the electrolyte cation impacts the EIS spectrum by changing the R_s due to a change in the characteristic molar conductivity of the salt.

The R_s of the electrolyte salt determines the lowest resistance that can be observed in a particular EIS measurement. The film resistance to ion migration in the p[N_1−dMIm][ClO_4] films can possibly be measured by lowering the R_s of the electrolyte salt. $Ca(ClO_4)_2$ exhibits the highest Λ° of the salts investigated and the R_s of spectra collected in $Ca(ClO_4)_2$ can be lowered by increasing the molarity of the aqueous electrolyte used in the EIS measurement. EIS spectra of p[N_1−dMIm][ClO_4] films collected in a 0.5 M aqueous solution of $Ca(ClO_4)_2$ exhibited R_s of 4.34 ± 0.04 $\Omega \cdot cm^2$. However, these spectra did not show a film resistance to ion migration. Thus, for the p[N_1−dMIm][ClO_4] films, using the lowest R_s measured, one can conclude that $R_f \leq 4.34 \pm 0.04\ \Omega \cdot cm^2$ and subsequently $\kappa_f \geq 13.6 \pm 0.8\ \mu S/cm$.

As noted earlier, the water content in the films plays a role in the variation in R_f observed for the different films. The effect of the aqueous environment on the ion transport properties of the p[N_1−dMIm] films was investigated by conducting EIS in an ionic liquid. The studies were conducted with p[N_1−dMIm][NTf_2] films in the presence of 1-butyl-2,3-dimethyl imidazolium bis(trifluoromethylsulfonyl)imide

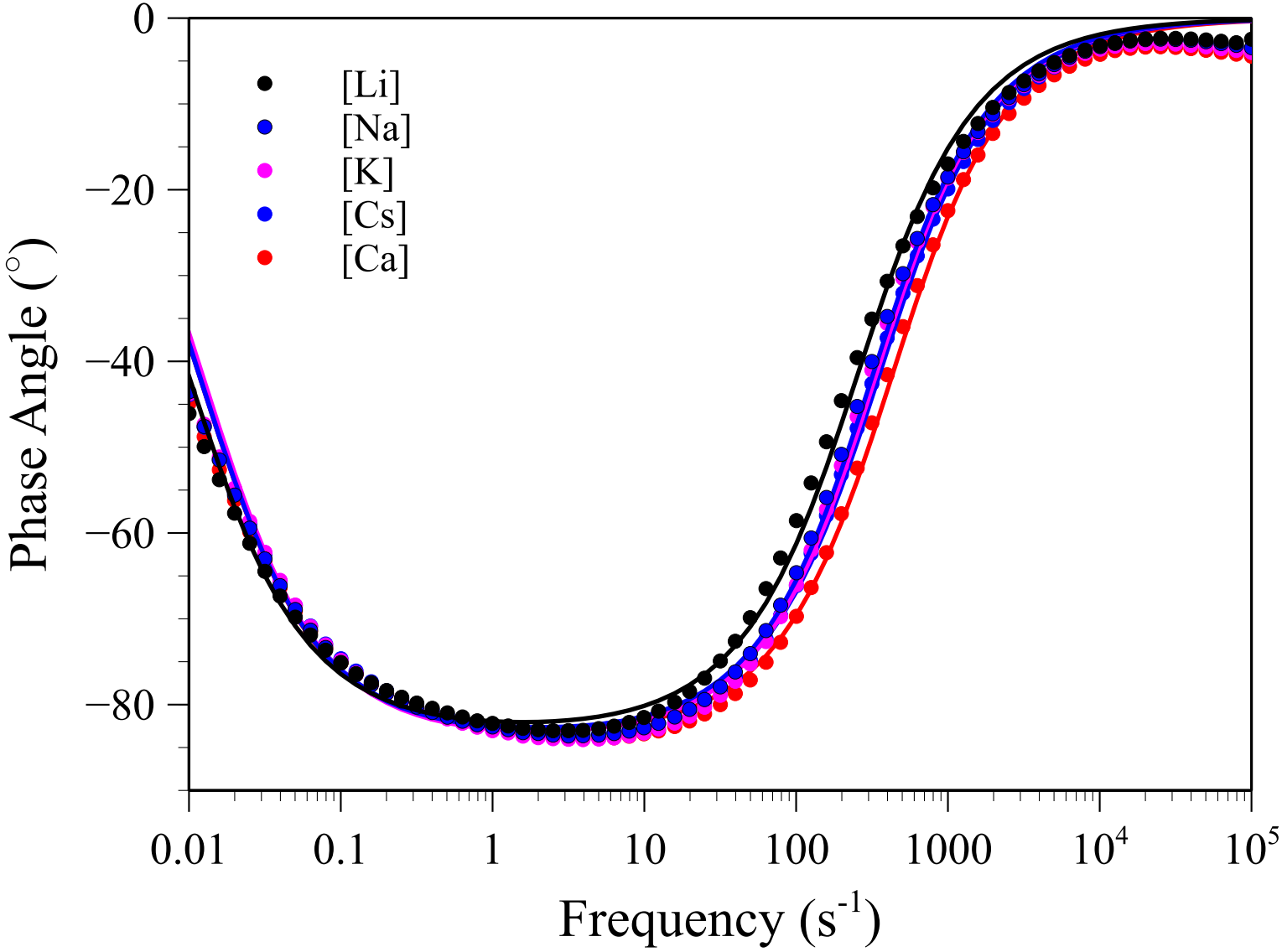

Figure 4.9: Phase angle plot of EIS spectra for p[N_1−dMIm][ClO_4] films acquired in 0.05 M aqueous solutions of ClO_4^- salts with varying cations. The solid curves represent fits to the equivalent circuit in Scheme 3.4.

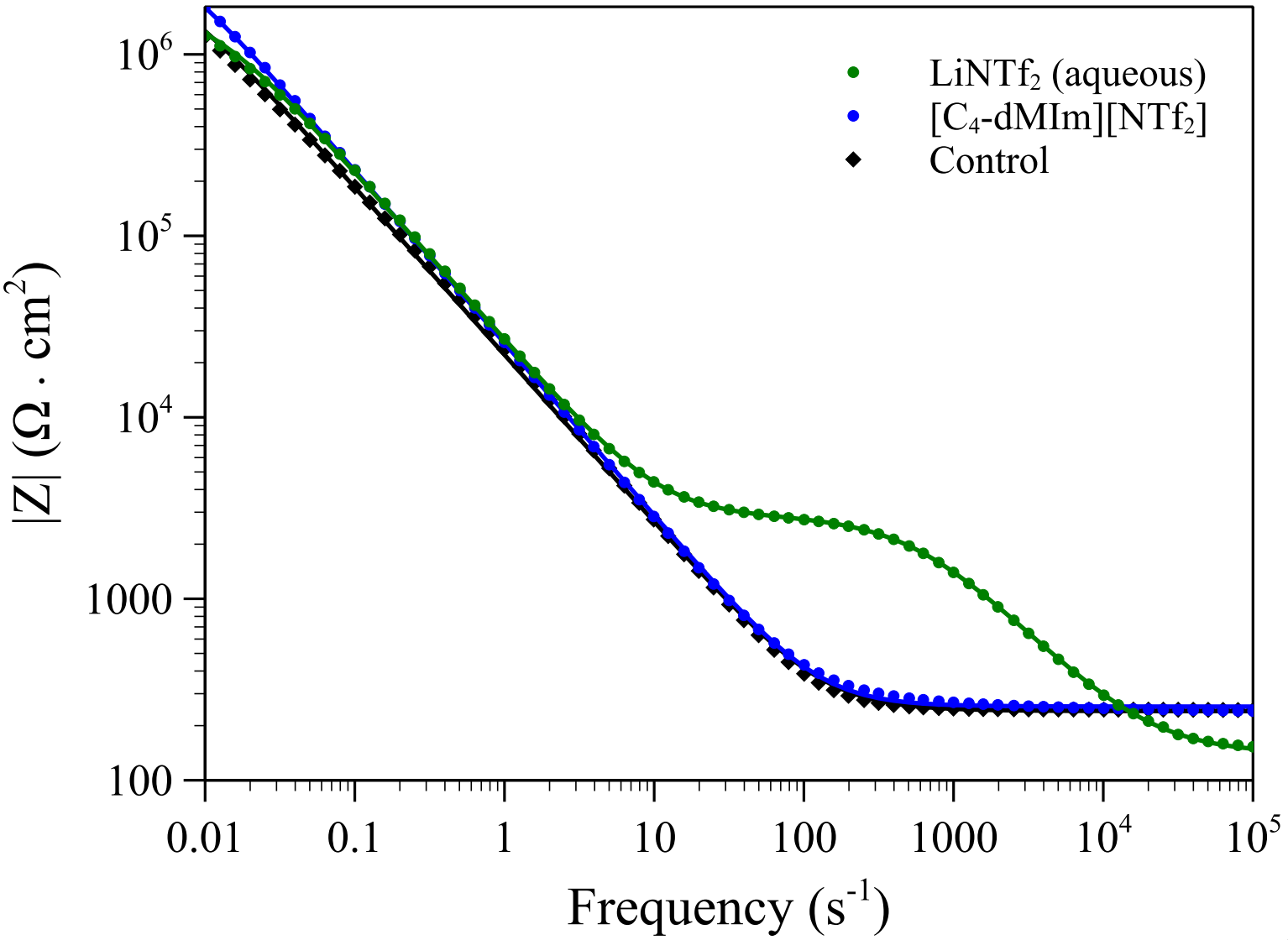

Figure 4.10: Solvation effect on the ion transport properties of p[N_1−dMIm] films. Bode plot of EIS spectra of p[N_1−dMIm][NTf_2] films conducted in a 0.1 M $LiNTf_2$ aqueous solution as well as in [C_4−dMIm][NTf_2]. Data from a hydroxyl-terminated SAM exposed to NBDAC acquired in [C_4−dMIm][NTf_2] is shown as a control. The solid curves represent fits using the equivalent circuit shown in Scheme 3.4.

Table 4.6: p[N_1−dMIm][NT_2f] Solution Resistance (R_s), Film Resistance (R_f), Conductivity (κ_f), and Capacitance (C_f) Values Obtained from a Fit of the EIS Spectra in Figure 4.10 with the Equivalent Circuit in Scheme 3.4.

Cation	R_s ($\Omega \cdot cm^2$)	R_f ($K\Omega \cdot cm^2$)	κ_f (μS/cm)	C_f (μF/cm^2)
Li^+	139 ± 2	2.82 ± 0.04	0.013 ± 0.001	0.14 ± 0.01
C_4−dMIm^{+a}	255 ± 1	-	$\geq 0.257 \pm 0.020^a$	-
Control^b	241 ± 1	-	-	-

[a] The film resistance for the film is theoretically lower than the R_s observed. [b] The control film is a gold substrate modified with a hydroxyl-terminated SAM exposed to NBDAC with spectra acquired in [C_4−dMIm][NTf_2].

Table 4.7: p[N_1−dMIm][NTf_2] Interfacial Resistance (R_i) and Capacitance (C_i) Values Obtained from a Fit of the EIS Spectra in Figure 4.10 with the Equivalent Circuit in Scheme 2.

Cation	R_i ($M\Omega \cdot cm^2$)	C_i ($\mu F/cm^2$)
Li^+	1.94 ± 0.05	8.7 ± 0.1
C_4−dMIm$^+$	4.43 ± 0.18	8.4 ± 0.1
Control[1]	3.12 ± 0.11	11.6 ± 0.10

[a] The control film is a gold substrate modified with a hydroxyl-terminated SAM exposed to NBDAC with Spectra acquired in [C_4−dMIm][NTf_2].

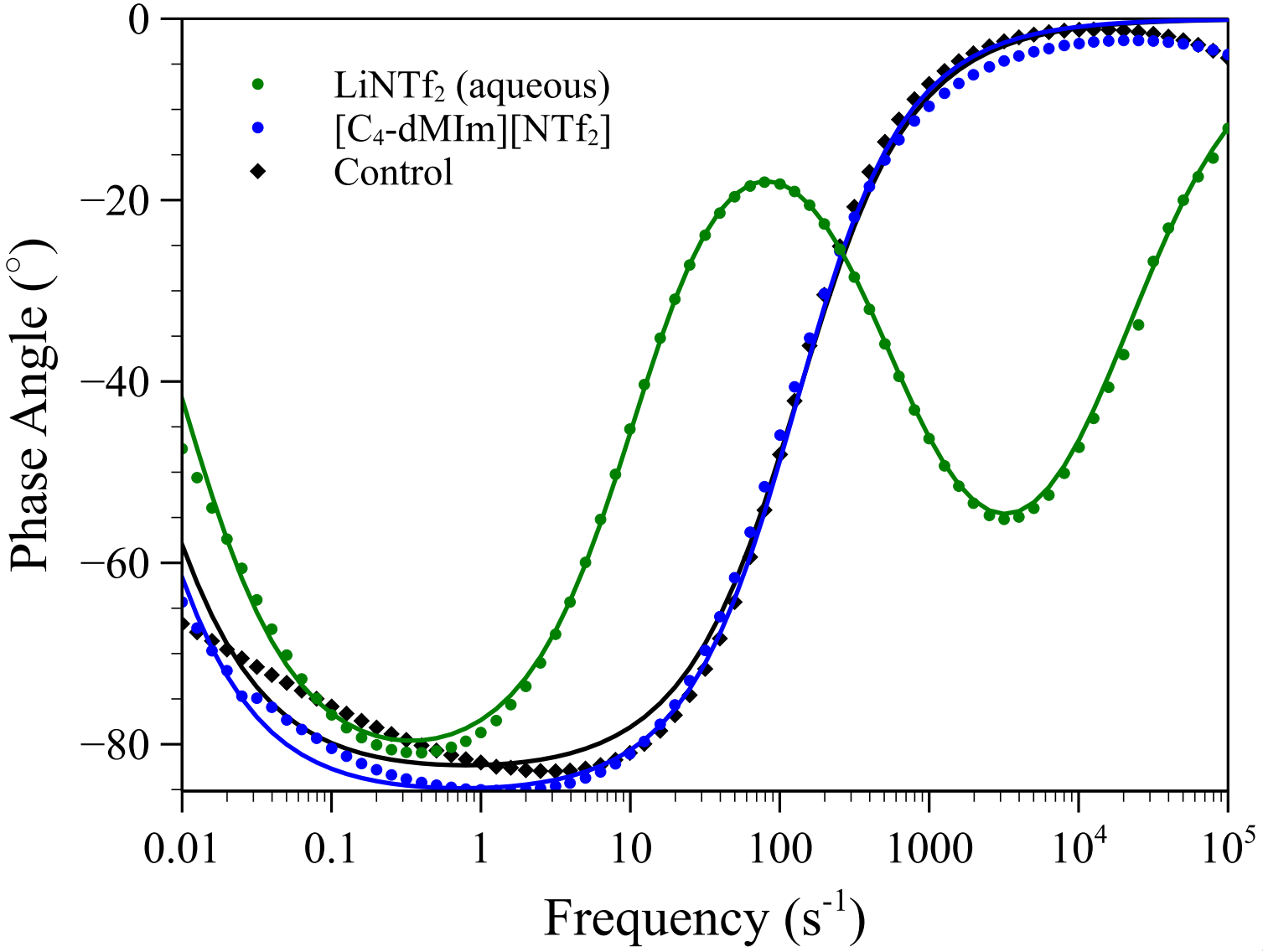

Figure 4.11: Phase angle plot of EIS spectra of p[N_1−dMIm][NTf_2] films conducted in a 0.1M $LiNTf_2$ aqueous solution as well as in [C_4−dMIm][NTf_2]. Data from a hydroxyl-terminated SAM exposed to NBDAC acquired in [C_4−dMIm][NTf_2] is shown as a control. The solid curves represent fits to the equivalent circuit in Scheme 3.4.

([C_4−dMIm][NTf_2]). Representative Bode plots for the p[N_1−dMIm][NTf_2] films in both the IL and aqueous solution as well as a control film consisting of a hydroxyl-terminated SAM exposed to NBDAC conducted in the presence of [C_4−dMIm][NTf_2] are shown in Figure 4.10. The corresponding phase angle plots are included in Figure 4.11. The values for the circuit parameters obtained from a fit of the data with the equivalent circuit shown in Scheme 3.4 are listed in Table 4.6. A higher solution resistance, $\sim 250\ \Omega \cdot cm^2$, is observed in the spectrum of both the control film and the p[N_1−dMIm][NTf_2] film solvated by the ionic liquid. The higher solution resistance is attributed to a decreased molar conductivity for the ionic liquid as compared to that of the aqueous salt solution. The spectrum for the p[N_1−dMIm][NTf_2] film obtained in [C_4−dMIm][NTf_2] does not show a film resistance but rather shows an interfacial capacitance regime from high to low frequencies. The utilization of the IL, [C_4−dMIm][NTf_2], results in over an order of magnitude increase in κ_f as compared to the aqueous electrolyte. The improved solvation of the PIL film with the IL results in the minimization of the impedance to ion transport. The reduction in the impedance to ion transport in the film arises due to a combined phase similar to the IL resulting in improved migration of the $^{-}NTf_2$ ion.

The values for the C_i and R_i obtained from the fit of the EIS Spectra in Figure 4.10 with the Equivalent Circuit shown in Scheme 3.4 are shown in Table 4.7. Phase angle plots of EIS spectra corresponding to the Bode plots of Figure 4.10 for p[N_1−dMIm][NTf_2] films on gold substrates, as well as a control film consisting of a hydroxyl-terminated SAM on gold substrates exposed to NBDAC, conducted in the presence of [C_4−dMIm][NTf_2] are shown in Figure 4.11.

Conclusions

The synthesis and subsequent SI-ROMP of an IL monomer to form dynamic, anion-adaptive PIL films with thicknesses greater than 500 nm was achieved.

p[N_1−dMIm][PF_6] films undergo anion exchange with traditional anions, such as ClO_4^-, FSI^-, and $^-NTf_2$], as well as larger anions in the form of dyes to alter properties, including ion conduction, mechanical properties, surface wettability, and color. The p[N_1−dMIm] films behave as anionic chameleons and as such, adapt to their anionic environment where dynamic environmental response is critical. The surface wettability and viscoelastic properties, i.e. storage and loss modulus, of the p[N_1−dMIm] films are highly dependent on the film anion and are tunable via a simple anion exchange mechanism. The electrolyte cation does not impact ion conduction in p[N_1−dMIm] films when performed in aqueous electrolytes, while the film anion determines the resistance of the p[N_1−dMIm] film to ion conduction with the order, $PF_6^- > {}^-NTf_2 \gg FSI^- \gg ClO_4^-$. In particular, the film resistance to ion conduction for the p[N_1−dMIm] with the ClO_4^- anion is estimated to be orders of magnitude lower despite the film being only slightly more solvated, suggesting that the ClO_4^- anion behaves differently than the other ions investigated. The film resistance in aqueous electrolytes can be eliminated by employing an ionic liquid as the electrolyte, improving the solvation of the p[N_1−dMIm] films. The adaptability and tunability of these surface-tethered films enable their use for multiple applications.

References

[1] Yu, B., Zhou, F., Hu, H., Wang, C., and Liu, W. (2007) Synthesis and Properties of Polymer Brushes Bearing Ionic Liquid Moieties. *Electrochimica Acta 53*, 487–494.

[2] He, X., Yang, W., and Pei, X. (2008) Preparation, Characterization, and Tunable Wettability of Poly(ionic liquid) Brushes via Surface-Initiated Atom Transfer Radical Polymerization. *Macromolecules 41*, 4615–4621.

[3] Ishikawa, T., Kobayashi, M., and Takahara, A. (2010) Macroscopic Frictional Properties of Poly(1-(2-methacryloyloxy)ethyl-3-butyl Imidazolium Bis(trifluoromethanesulfonyl)-imide) Brush Surfaces in an Ionic Liquid. *ACS Applied Materials & Interfaces 2*, 1120–1128.

[4] Bui-Thi-Tuyet, V., Trippé-Allard, G., Ghilane, J., and Randriamahazaka, H. (2016) Surface and Electrochemical Properties of Polymer Brush-Based Redox Poly(Ionic Liquid). *ACS Applied Materials & Interfaces 8*, 28316–28324.

[5] Wang, P., Zhou, Y.-N., Luo, J.-S., and Luo, Z.-H. (2014) Poly(Ionic Liquid)s-Based Nanocomposite Polyelectrolytes with Tunable Ionic Conductivity Prepared via SI-ATRP. *Polymer Chemistry 5*, 882–891.

[6] Bielawski, C. W., and Grubbs, R. H. (2007) Living Ring-Opening Metathesis Polymerization. *Progress in Polymer Science 32*, 1–29.

[7] Schleyer, P. v. R., Williams, J. E., and Blanchard, K. R. (1970) Evaluation of Strain in Hydrocarbons. The Strain in Adamantane and its Origin. *Journal of the American Chemical Society 92*, 2377–2386.

[8] Lerum, M. F. Z., and Chen, W. (2011) Surface-Initiated Ring-Opening Metathe-

sis Polymerization in the Vapor Phase: An Efficient Method for Grafting Cyclic Olefins with Low Strain Energies. *Langmuir 27*, 5403–5409.

[9] Ye, Q., Gao, T., Wan, F., Yu, B., Pei, X., Zhou, F., and Xue, Q. (2012) Grafting Poly(Ionic Liquid) Brushes for Anti-Bacterial and Anti-Biofouling Applications. *Journal of Materials Chemistry 22*, 13123.

[10] Mecerreyes, D. (2011) Polymeric Ionic Liquids: Broadening the Properties and Applications of Polyelectrolytes. *Progress in Polymer Science 36*, 1629–1648.

[11] P'Pool, S. J., and Schanz, H. J. (2007) Reversible Inhibition/Activation of Olefin Metathesis: A Kinetic Investigation of ROMP and RCM Reactions with Grubbs' Catalyst. *Journal of the American Chemical Society 129*, 14200–14212.

[12] Vygodskii, Y. S., Shaplov, A. S., Lozinskaya, E. I., Filippov, O. A., Shubina, E. S., Bandari, R., and Buchmeiser, M. R. (2006) Ring-Opening Metathesis Polymerization (ROMP) in Ionic Liquids: Scope and Limitations. *Macromolecules 39*, 7821–7830.

[13] Heyns, A., and van Schalkwyk, G. (1973) A Study of the Infrared and Raman Spectra of Ammonium Hexafluorophosphate NH4PF6 over a Wide Range of Temperatures. *Spectrochimica Acta Part A: Molecular Spectroscopy 29*, 1163–1175.

[14] Silverstein, R. M., Webster, F. X., and Kiemle, D. J. *Spectrometric Identification of Organic Compounds*, seventh ed.; Wiley: New York, 2005.

[15] Hathaway, B. J., and Underhill, A. E. (1961) 592. The Infrared Spectra of some Transition-Metal Perchlorates. *Journal of the Chemical Society (Resumed)* 3091–3096.

[16] Hardwick, L. J., Saint, J. A., Lucas, I. T., Doeff, M. M., and Kostecki, R. (2009) FTIR and Raman Study of the $Li_xTi_yMn_{1-y}O_2$(y = 0, 0.11) Cathodes in Methylpropyl Pyrrolidinium Bis(fluoro-sulfonyl)imide, LiTFSI Electrolyte. *Journal of The Electrochemical Society 156*, A120–A127.

[17] Yoon, H., Best, A. S., Forsyth, M., MacFarlane, D. R., and Howlett, P. C. (2015) Physical Properties of High Li-ion Content N-propyl-N-methylpyrrolidinium Bis(fluorosulfonyl)imide Based Ionic Liquid Electrolytes. *Physical Chemistry Chemical Physics 17*, 4656–4663.

[18] Kiefer, J., Fries, J., and Leipertz, A. (2007) Experimental Vibrational Study of Imidazolium-Based Ionic Liquids: Raman and Infrared Spectra of 1-ethyl-3-methylimidazolium Bis(trifluoromethylsulfonyl)imide and 1-ethyl-3-methylimidazolium Ethylsulfate. *Applied Spectroscopy 61*, 1306–1311.

[19] Shkrob, I. A., Marin, T. W., Zhu, Y., and Abraham, D. P. (2014) Why Bis(fluorosulfonyl)imide Is a "Magic Anion" for Electrochemistry. *The Journal of Physical Chemistry C 118*, 19661–19671.

[20] Lee, B. S., Chi, Y. S., Lee, J. K., Choi, I. S., Song, C. E., Namgoong, S. K., and Lee, S.-g. (2004) Imidazolium Ion-Terminated Self-Assembled Monolayers on Au: Effects of Counteranions on Surface Wettability. *Journal of the American Chemical Society 126*, 480–481.

[21] Qian, W., Texter, J., and Yan, F. (2017) Frontiers in Poly(ionic liquid)s: Syntheses and Applications. *Chemical Society Reviews 46*, 1124–1159.

[22] Höök, F., Rodahl, M., Brzezinski, P., and Kasemo, B. (1998) Energy Dissipation Kinetics for Protein and Antibody-Antigen Adsorption under Shear Oscillation on a Quartz Crystal Microbalance. *Langmuir 14*, 729–734.

[23] Reviakine, I., Johannsmann, D., and Richter, R. P. (2011) Hearing What You Cannot See and Visualizing What You Hear: Interpreting Quartz Crystal Microbalance Data from Solvated Interfaces. *Analytical Chemistry 83*, 8838–8848.

[24] Yuan, J., Mecerreyes, D., and Antonietti, M. (2013) Poly(Ionic Liquid)s: An Update. *Progress in Polymer Science 38*, 1009–1036.

[25] Hsu, C. H., and Mansfeld, F. (2001) Technical Note: Concerning the Conversion of the Constant Phase Element Parameter Y0 into a Capacitance. *Corrosion 57*, 747–748.

Chapter 5

STABILITY OF SURFACE-TETHERED POLY(IONIC LIQUID) FILMS TO ION EXCHANGE

Introduction

Ionic liquid (IL) properties are highly dependent on the coulombic interactions between their constituent ions.[1] The modification of the IL chemical structure such as that introduced by tethering ILs to polymerizable monomers or subsequent polymerization of the IL monomers into polymers (PILs) leads to a significant alteration of their physical properties due to the introduction of large intra- and inter-molecular Coulombic interactions.[1] A molecular-level understanding between the chemical structure and ion dynamics is required in order to fully understand the intermolecular forces at play in the ILs and PILs.

In Chapter 4, I reported the preparation of surface-immobilized PIL films on planar substrates of glass and gold via the SI-ROMP of the IL monomer [N_1−dMIm][PF_6]. In this chapter, I explore the fundamental intermolecular forces at play in surface-tethered PILs. The motivation for this study is the observation that certain anions lead to the desorption of the surface-tethered p[N_1−dMIm][PF_6] films on gold substrates. The desorption occurs on the same timescale as the anion exchange process. For the anions that cause desorption, the phenomenon was observed for both aqueous solutions prepared with the salts of the offending anions, as well as with ionic liquids whose resident anion was one of the offending anions.

Choi et al.[1] explored the correlation between glass transition temperature (T_g) and repeat unit molecular volume (V_m) for imidazolium ionic liquids, IL monomers and PILs. They observed that the T_g for the IL monomers and PILs are correlated

with their V_m.[1] In particular, the IL monomers and PILs containing counter-ions such as Br^- or BF_4^- exhibited higher T_g due to a stronger interaction with the imidazolium cation than those with the PF_6^- or $^-NTf_2$ counter-ions that act as plasticizers.[1] Choi et al.[1] also demonstrated that the imidazolium cation side chain length affected T_g independent of the counter-anion, with a decrease in T_g with increasing V_m approaching a steady value in the limit of large V_m.

Ring-opening metathesis polymerization (ROMP) is an equilibrium-controlled reaction that is driven from monomer to polymer by the release of cyclic olefin strain ("ring strain") balanced by entropic penalties.[2] These entropic effects are enhanced when performing ROMP from planar substrates due to a reduction in the degree of freedom for the segmental motion of the polymer chains. SI-ROMP on gold substrates is achieved by anchoring the catalyst onto a chemisorbed SAM, whereas for SI-ROMP on silicon and glass substrates, the catalyst is anchored onto a covalently bound SAM. One can then hypothesize that an increase in T_g for a surface-tethered polymer chain via anion exchange with a small counter-ion would lead to an increase in the entropic effects of tethering the chain onto the surface and, in the case of weaker sufrace attachment, could lead to detachment of the polymer chain from the interface. I report the preparation of p[N_1−dMIm][PF_6] films on gold and silicon substrates and the incorporation of anions that lead to a desorption of the polymer film on gold substrates.

In order to increase the V_m of the IL monomer [N_1−dMIm][PF_6], I synthesized a similar IL monomer [N_3−dMIm][PF_6], which incorporates a propyl group between the polymerizable norbornene and the dimethylimidazolium cation. Here, I report the preparation of surface-immobilized PIL films on planar gold substrates via the SI-ROMP of the IL monomer [N_3−dMIm][PF_6]. The increase in V_m led to a decrease in the T_g of the surface-tethered film and allowed the successful incorporation of anions that would have led to desorption of the p[N_1−dMIm][PF_6] film on gold substrates.

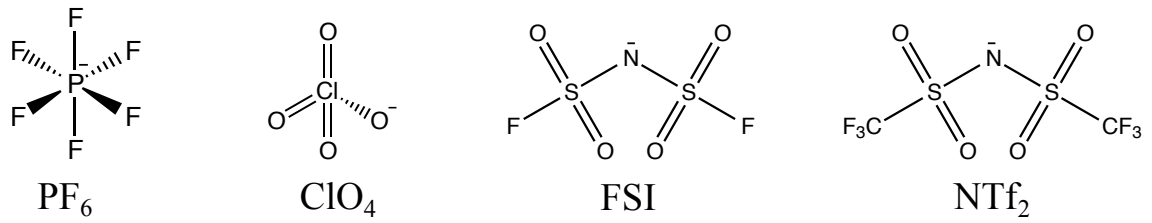

Figure 5.1: Structures of anions successfully exchanged into p[N_1−dMIm] films on gold substrates.

Experimental

Polymerization of [N_1−dMIm][PF_6] on Gold and Glass Substrates

ROMP-active substrates of gold and glass were prepared as described in Chapter 3. The ROMP-active substrates were quickly rinsed with DCE and immediately placed in a 0.1 M [N_1−dMIm][PF_6] solution in DCE for up to 15 min. The substrates were subsequently rinsed with DCM, ethanol, water, and ethanol and dried in a stream of nitrogen.

Ionic Polymer Film Anion Exchange

The anion exchange of p[N_1−dMIm] and p[N_3−dMIm] films with resident anion was accomplished by simply immersing the film into an aqueous solution containing 0.2 M of the salt of the desired anion for a minimum of 2 h.[3,4] The chemical structure of the anions considered in this chapter that successfully exchanged into p[N_1−dMIm][PF_6] films on gold substrates are shown in Figure 5.1. Larger anions in the form of anionic dyes were also successfully exchanged into p[N_1−dMIm][PF_6] films on glass substrates (Figure 4.4).

The chemical structures of the anions considered in this chapter that resulted in p[N_1−dMIm][PF_6] film desorption from gold substrates are shown in Figure 5.2.

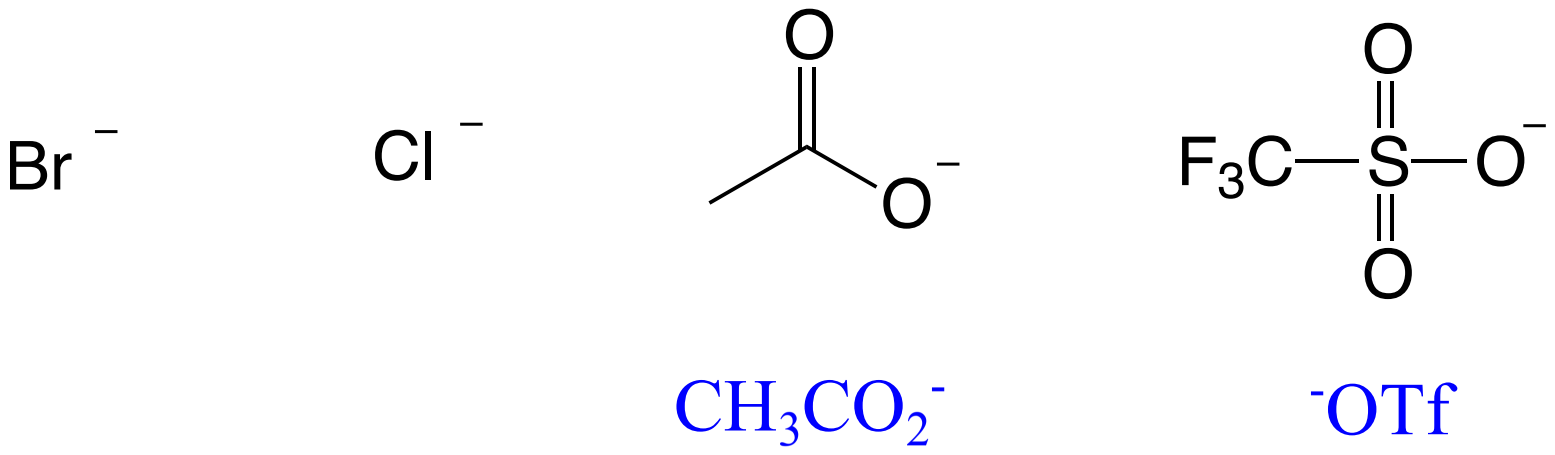

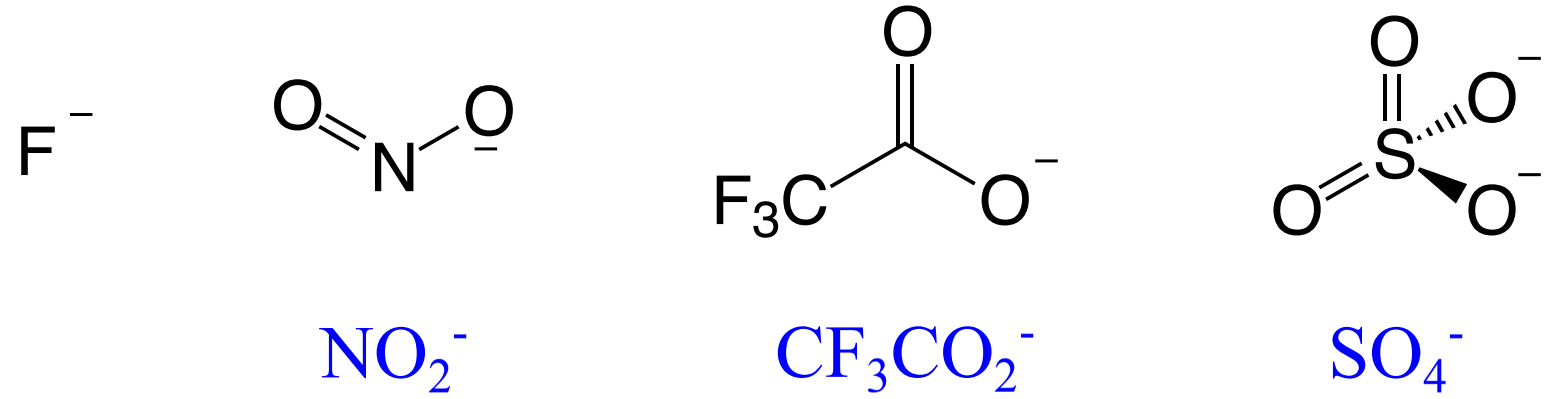

Figure 5.2: Anions that resulted in p[N_1−dMIm][PF_6] film desorption from gold substrates.

Results and Discussion

Polymerization of the ionic liquid monomer [N_1−dMIm][PF_6] at a concentration of 0.1 M in DCE for 15 min on gold substrates led to a surface-tethered polymer film that exhibited a profilometric thickness of 650 ± 30 nm. The IR spectrum of p[N_1−dMIm][PF_6] was consistent with that reported in Figure 4.2. Anion exchange of the p[N_1−dMIm][PF_6] films was successfully accomplished with the anions ClO_4^-, FSI^-, and $^-NTf_2$ and was consistent with the spectra reported in Figure 4.2. Anion exchange of the p[N_1−dMIm][PF_6] films with large anionic dyes was also successfully accomplished (Figure 4.4). Anion exchange of the p[N_1−dMIm][PF_6] films with the anions shown in Figure 5.2, resulted in p[N_1−dMIm][PF_6] film desorption from gold substrates.

The desorption of the p[N_1−dMIm] film with the anions shown in Figure 5.2 was hypothesized to be caused by an increase in the entropy for the chains to remain immobilized at the surface induced by an increase in the polymer T_g. This increase in entropic energy leads to a cleaveage of the gold-thiol interaction and subsequent desorption of the polymer chains into the aqueous phase during anion exchange. In order to determine the mechanism of desorption, we prepared p[N_1−dMIm] films on silicon which utilizes a more robust attachment scheme of the polymer chains to the interface. A more robust attachment should be able to accommodate the increase in entropic energy arising from an increase in T_g. Additionally, the polymerization of a monomer [N_3−dMIm][PF_6] with a greater V_m on gold substrates would lead to a decrease in T_g for the polymer film and subsequently decrease the entropic energy for the polymer film with the anions shown in Figure 5.2.

p[N_1−dMIm] Films Prepared on Silicon Substrates

Polymerization of [N_1−dMIm][PF_6] at a concentration of 0.1 M in DCE for 15 min on silicon substrates led to a surface-tethered polymer film that exhibited a pro-

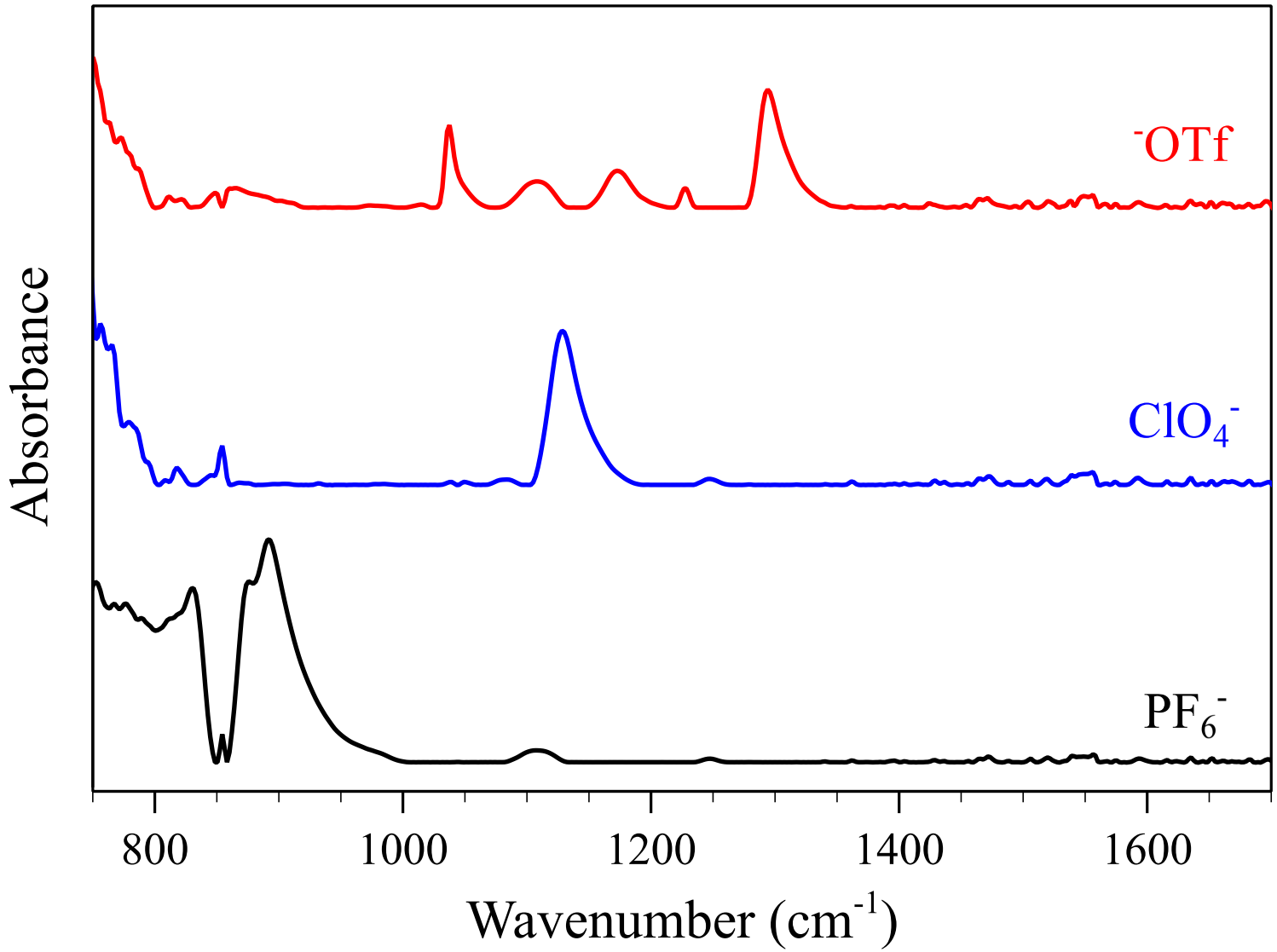

Figure 5.3: Polarization modulation-infrared reflectance-absorption spectrum of p[N_1−dMIm] films on silicon substrates. The p[N_1−dMIm] films were initially polymerized with the PF_6^- anion, but were successfully exchanged with ClO_4^- and $^-$OTf anions.

filometric thickness of 519 ± 52 nm. Figure 5.3 shows the IR spectrum, centered at 1200 cm^{-1}, of a p[N_1−dMIm][PF_6] polymer film grown on a gold substrate. The dominant absorption band is the P−F stretch at 895 cm^{-1}.[5] Weaker absorption bands due to the polymer carbon backbone are also observed, in particular, a C=C stretching absorption band at 1589 cm^{-1}, a symmetric CH_2 in-plane bending (scissoring) absorption band at 1462 and 1423 cm^{-1}, an asymmetric CH_3 absorption band at 1392 cm^{-1}, a symmetric CH_3 absorption band at 1243 cm^{-1}, and a vibrational CH_3 in-plane bending (rocking) absorption band at 742 cm^{-1}.[6]

Anion exchange of the resident anion for p[N_1−dMIm][PF_6] films on silicon substrates was successfully accomplished with the anions ClO_4 and $^-$OTf as evidenced by the IR spectra shown in Figure 5.3. The major absorption bands in the IR spectra for the anions PF_6^-, ClO_4^-, and $^-$OTf are summarized in Table 5.1. The dominant absorption band in the spectrum for the ClO_4^- anion is the Cl−O stretch at 1110 cm^{-1}. For the IR spectra with the $^-$OTf anion, the dominant absorption bands are the SO_3^- and C−F bands between 1000 and 1300 cm^{-1}.

Profilometric thicknesses of the p[N_1−dMIm][PF_6] films grown on silicon substrates after anion exchange with ClO_4^-, and $^-$OTf are reported in Table 5.1. There was no statistically significant change in thickness observed for p[N_1−dMIm][PF_6] films after exchange with the ClO_4^- and $^-$OTf anions. The ability to incorporate the $^-$OTf anion via anion exchange in p[N_1−dMIm][PF_6] films on silicon substrates and not in p[N_1−dMIm][PF_6] films on gold substrates suggests that the surface attachment route utilized for SI-ROMP on gold substrates is unable to withstand the increased entropic effects arising from an increase in the T_g with the smaller $^-$OTf anion.

Figure 5.4 shows IR spectra for the C−H stretching region of p[N_1−dMIm] polymer films on silicon substrates with various anions. The major absorbance bands in the IR spectra for the anions PF_6^-, ClO_4^-, and $^-$OTf are summarized in Table 5.2.

Table 5.1: Profilometric Thicknesses and Anion Polarization Modulation-Infrared Reflectance-Absorption Bands for p[N_1−dMIm] Films Prepared on Silicon Substrates.[5–12]

Anion	Thickness (nm)	Functional Group	Wavelength (cm^{-1})
PF_6^-	519 ± 52	P−F stretch	891
ClO_4^-	457 ± 41	C−O stretch	1128
$^-$OTf	505 ± 29	$\nu_{as}SO_3$ stretch	1295
		ν_s CF_3 stretch	1228
		ν_{as} CF_3 stretch	1173
		ν_s SO_3 stretch	1038

There are minimal variations in the $C_{sp^3}-H$ stretch vibration band peak positions for the p[N_1−dMIm] polymer film with anion exchange as shown in Figure 5.4 and Table 5.2; however, the peak shapes are similar for the various anions observed in Figure 5.4. There are minimal variations in the peak position and shape for the $C_{sp^2}-H$ stretch vibration bands for p[N_1−dMIm] polymer film with the anions PF_6^-, ClO_4^-, and $^-$OTf. The retention of the $C_{sp2}-H$ and $C_{sp3}-H$ bands for all the anions studied suggests minimal variation in the polymer backbone structure due to anion exchange.

Polymerization of [N_3−dMIm][PF_6] on Gold Substrates

Polymerization of the ionic liquid monomer [N_3−dMIm][PF_6] at a concentration of 0.1 M in DCE for 15 min on gold substrates led to a surface-tethered polymer film that exhibited a profilometric thickness of 301 ± 198 nm. Figure 5.5 shows the IR spectrum, centered at 1200 cm^{-1}, of a p[N_3−dMIm][PF_6] polymer film grown on a gold substrate. The dominant absorption band is the P−F stretch at 862 cm^{-1}.[5] Weaker absorption bands due to the polymer carbon backbone are also observed, in particular, a C=C stretching absorption band at 1591 cm^{-1}, a symmetric CH_2 in-plane bending (scissoring) absorption band at 1462 and 1423 cm^{-1} and a symmetric CH_3 absorption band at 1246 cm^{-1}.[6]

Anion exchange of the PF_6^- anion for p[N_3−dMIm][PF_6] films on gold substrates was successfully accomplished with the anions ClO_4^-, $^-$OTf, and $CF_3CO_2^-$ as evidenced by the IR spectra shown in Figure 5.5. The major absorption bands in the IR spectra for the anions PF_6^-, ClO_4^-, $^-$OTf, and $CF_3CO_2^-$ are summarized in Table 5.3. The dominant absorption band in the spectrum for the ClO_4^- anion is the Cl−O stretch at 1113 cm^{-1}. For the IR spectra with the $^-$OTf anion, the dominant absorption bands are the SO_3 and C−F bands between 1000 and 1300 cm^{-1}. For the IR spectra with the $CF_3CO_2^-$ anion, the dominant absorption bands are the C=O and C−F bands between 1100 and 1700 cm^{-1}.

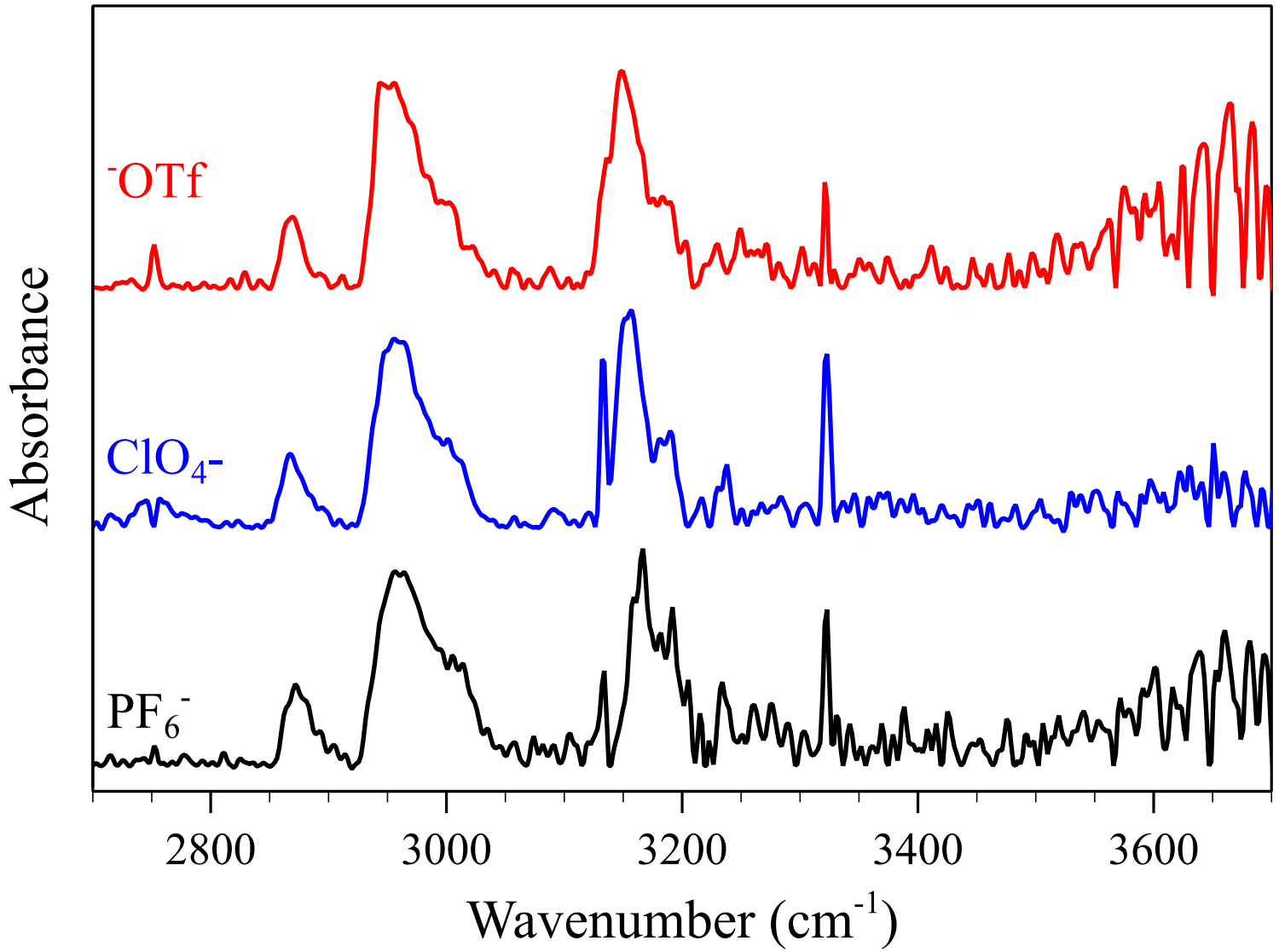

Figure 5.4: Polarization modulation-infrared reflectance-absorption spectrum of p[N_1−dMIm] films on silicon substrates. The p[N_1−dMIm] films were initially polymerized with the PF_6^- anion, but were successfully exchanged with ClO_4^- and $^-$OTf anions. The spectra present the C−H stretching region of the p[N_1−dMIm] films.

Table 5.2: Film Anion Polarization Modulation-Infrared Reflectance-Absorption Bands of p[N_1−dMIm] Films.[6,8–11]

Anion	C_{sp^3}−H Bands (cm^{-1})	C_{sp^2}−H Bands (cm^{-1})
PF_6^-	2873 (ν_s), 2961 (ν_{as})	3168, 3193
ClO_4^-	2869 (ν_s), 2959 (ν_{as})	3158, 3191
^-OTf	2870 (ν_s), 2950 (ν_{as})	3150, 3188

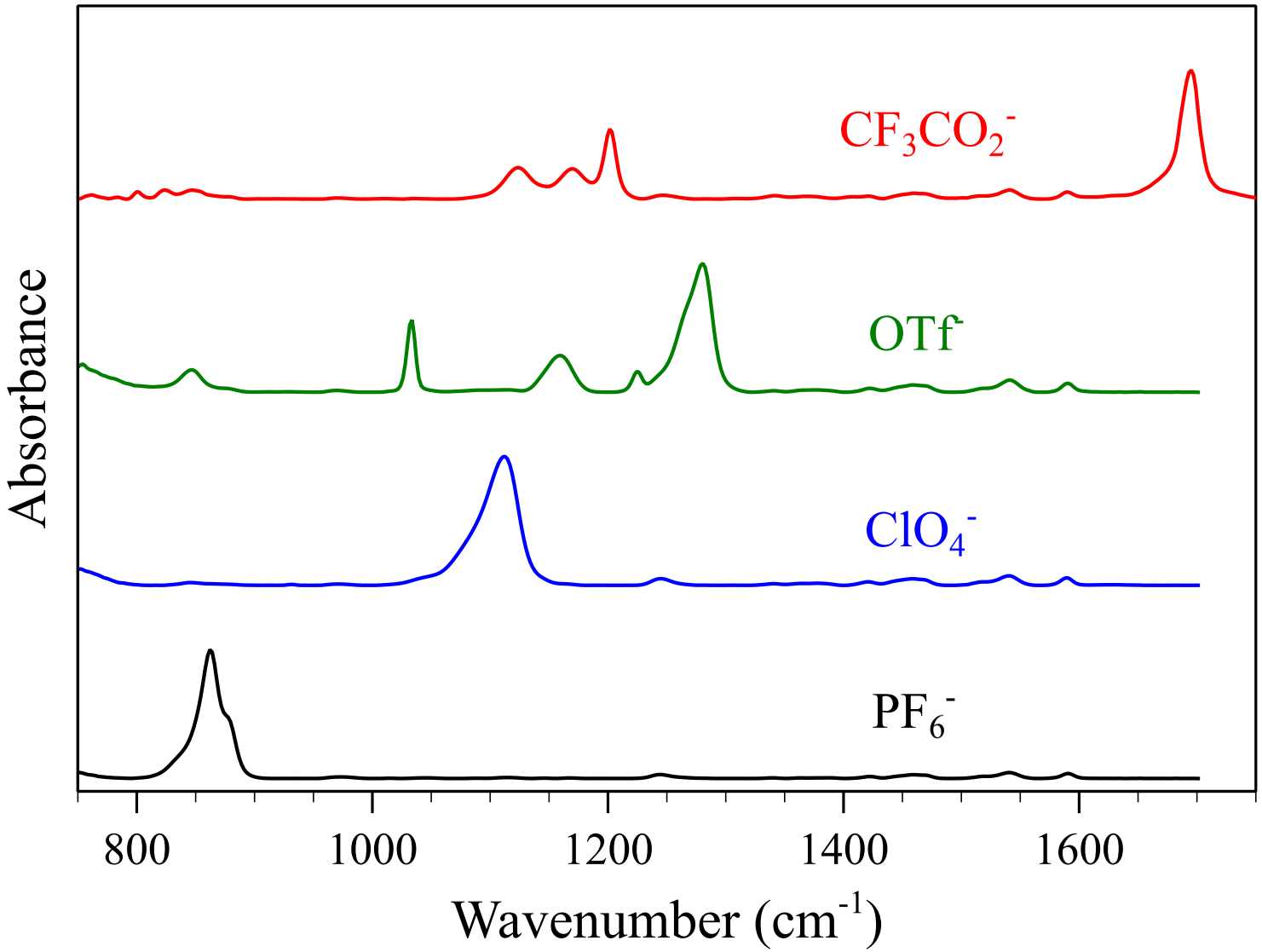

Figure 5.5: Polarization modulation-infrared reflectance-absorption spectrum of p[N_3−dMIm] films on gold substrates. The p[N_3−dMIm] films were initially polymerized with the PF_6^- anion, but were successfully exchanged with ClO_4^-, $^-$OTf and $CF_3CO_2^-$ anions.

Table 5.3: Anion Polarization Modulation-Infrared Reflectance-Absorption Bands for p[N_3−dMIm] Films.[5–11]

Anion	Functional Group	Wavelength (cm^{-1})
PF_6^-	P−F stretch	862
ClO_4^-	C−O stretch	1113
$^-$OTf	$\nu_{as}SO_3$ stretch	1281
	ν_s CF_3 stretch	1226
	ν_{as} CF_3 stretch	1161
	ν_s SO_3 stretch	1034
$CF_3CO_2^-$	ν_{as} C=O stretch	1695
	ν_{as} CF_3 stretch	1201
	ν_{as} CF_3 stretch	1170
	ν_s CF_3 stretch	1124

Figure 5.6 shows IR spectra for the C−H stretching region of p[N_3−dMIm] polymer films on gold substrates with various anions. The major absorbance bands in the IR spectra for the anions PF_6^-, ClO_4^-, $^-$OTf, and $CF_3CO_2^-$ are summarized in Table 5.4. There are minimal variations in the C_{sp^3}−H stretch vibration band peak positions for the p[N_1−dMIm] polymer film with anion exchange as shown in Figure 5.6 and Table 5.4; however, the peak shapes are similar for the various anions observed in Figure 5.6. There are minimal variations in the peak position and shape for the C_{sp^2}−H stretch vibration bands for p[N_3−dMIm] polymer films with the anions PF_6^-, ClO_4^-, and $^-$OTf. The p[N_3−dMIm][CF_3CO_2] film, however, does show a change in peak shape and position for the C_{sp^2}−H stretch vibration bands. The C_{sp^2}−H peak shape observed with the anions PF_6^-, ClO_4^-, and $^-$OTf is recoverable with anion exchange. The retention of the C_{sp2}−H and C_{sp3}−H bands for all the anions studied suggests minimal variation in the polymer backbone structure due to anion exchange.

The p[N_3−dMIm][PF_6] films on gold substrates were able to undergo anion exchange with the $^-$OTf and $CF_3CO_2^-$ anion while remaining tethered to the gold substrate. In preparing surface-tethered p[N_3−dMIm][PF_6] films we were able to increase the V_m of the surface-tethered PIL films while maintaining the chemical structure of the polymer. As expected an increase in the V_m led to a lowering in T_g thereby allowing the incorporation of anions in the p[N_3−dMIm][PF_6] films without surface detachment as was observed for p[N_1−dMIm][PF_6] films.

Conclusions

p[N_1−dMIm][PF_6] films polymerized on gold substrates undergo anion exchange with traditional anions, such as ClO_4^-, FSI^-, and $^-NTf_2$, as well as large anionic dyes, but are unable to incorporate anions such as Br^-, Cl^-, $^-$OTf, and $CF_3CO_2^-$ without detachment from the gold surface. This behavior is attributed to an increase in the glass transition temperature T_g, where the incorporation of certain

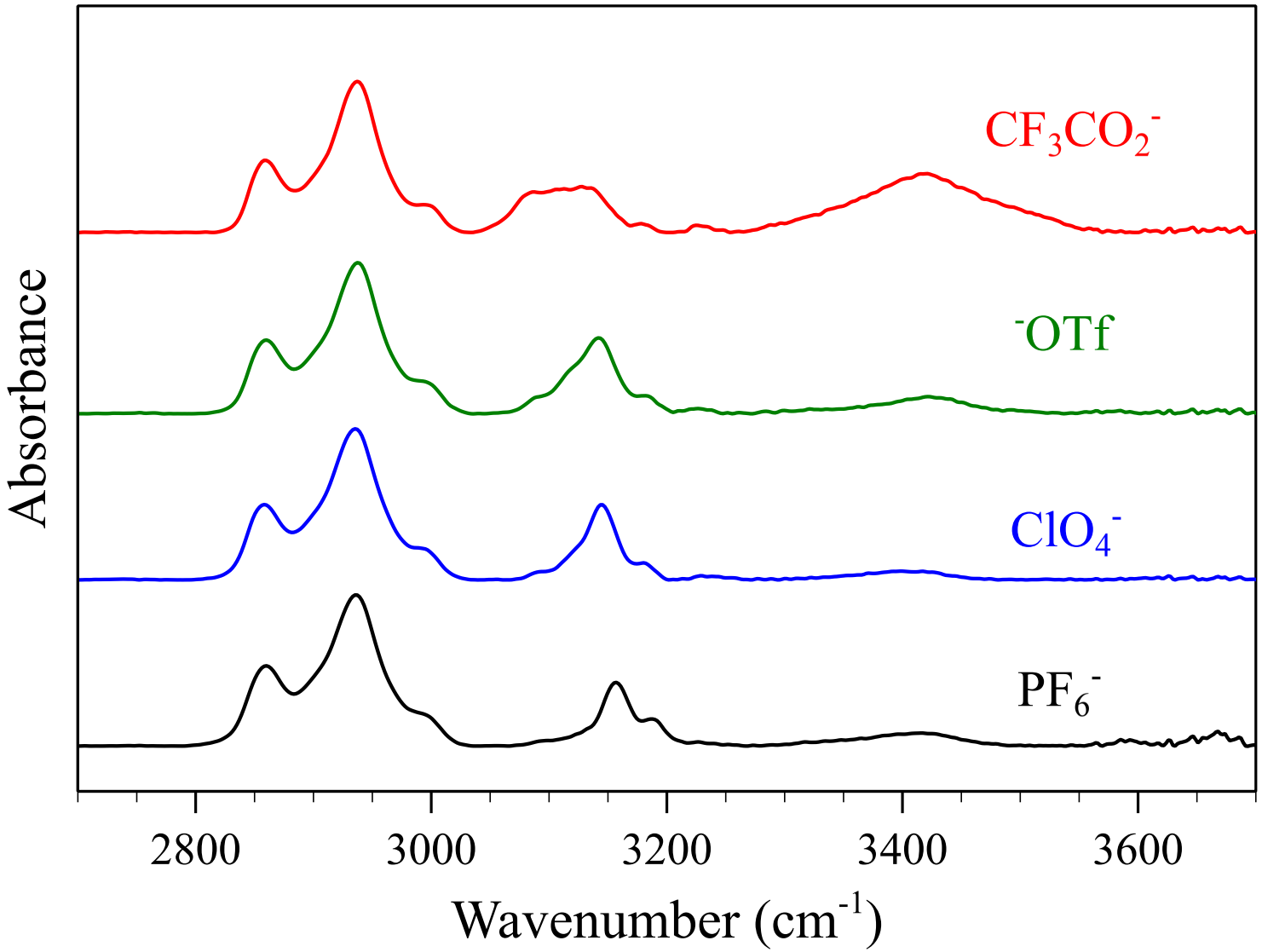

Figure 5.6: Polarization modulation-infrared reflectance-absorption spectrum of p[N_3−dMIm] films on silicon substrates. The p[N_3−dMIm] films were initially polymerized with the PF_6^- anion, but were successfully exchanged with ClO_4^-, $^-$OTf, and $CF_3CO_2^-$ anions. The spectra present the C−H stretching region of the p[N_1−dMIm] films.

Table 5.4: Film Anion Polarization Modulation-Infrared Reflectance-Absorption Bands of p[N_1−dMIm] Films.[6,8–11]

Anion	C_{sp^3}−H Bands (cm^{-1})	C_{sp^2}−H Bands (cm^{-1})
PF_6^-	2861 (ν_s), 2937 (ν_{as})	3158, 3188
ClO_4^-	2859 (ν_s), 2936 (ν_{as})	3146, 3183
^-OTf	2861 (ν_s), 2939 (ν_{as})	3144, 3185
$CF_3CO_2^-$	2861 (ν_s), 2939 (ν_{as})	3128, 3180

anions leads to a stronger coupling of the film. This increase in T_g results in an increase in the entropic penalties for the film to remain tethered to the surface via a chemisorbed gold-thiol bond and results in the detachment of the polymer film with anion exchange. The incorporation of the disruptive anions was accomplished by the preparation of p[N_1−dMIm][PF_6] films on silicon substrates to exploit a covalent attachment to ensure a more robust tethering of the polymer films against film desorption. p[N_1−dMIm][PF_6] films prepared on silicon substrates were able to incorporate disruptive anions in the form of triflate ($^-$OTf), which could not be incorporated for the p[N_1−dMIm][PF_6] films on gold substrates. The film thickness of these films remained constant throughout the anion exchange process with minimal variation in the polymer carbon backbone as observed by the retention of the C_{sp2}−H and C_{sp3}−H infrared absorption bands.

The synthesis and subsequent SI-ROMP of an IL monomer ([N_3−dMIm][PF_6]) exhibiting a larger repeat unit molecular volume (V_m) to form dynamic, anion-adaptive PIL films on gold substrates was achieved. An increase in V_m leads to a decrease in T_g and subsequently in the entropic penalties for a surface-tethered PIL film to remain tethered to the surface while incorporating small anions. The p[N_3−dMIm][PF_6] films on gold substrates were shown to undergo anion exchange with anions, such as ClO_4^-, as well as disruptive anions in the form of $^-$OTf and trifluoroacetate $CF_3CO_2^-$.

References

[1] Choi, U. H., Mittal, A., Price, T. L., Lee, M., Gibson, H. W., Runt, J., and Colby, R. H. (2015) Molecular Volume Effects on the Dynamics of Polymerized Ionic Liquids and their Monomers. *Electrochimica Acta 175*, 55–61.

[2] Bielawski, C. W., and Grubbs, R. H. (2007) Living Ring-Opening Metathesis Polymerization. *Progress in Polymer Science 32*, 1–29.

[3] He, X., Yang, W., and Pei, X. (2008) Preparation, Characterization, and Tunable Wettability of Poly(ionic liquid) Brushes via Surface-Initiated Atom Transfer Radical Polymerization. *Macromolecules 41*, 4615–4621.

[4] Mecerreyes, D. (2011) Polymeric Ionic Liquids: Broadening the Properties and Applications of Polyelectrolytes. *Progress in Polymer Science 36*, 1629–1648.

[5] Heyns, A., and van Schalkwyk, G. (1973) A Study of the Infrared and Raman Spectra of Ammonium Hexafluorophosphate NH4PF6 over a Wide Range of Temperatures. *Spectrochimica Acta Part A: Molecular Spectroscopy 29*, 1163–1175.

[6] Silverstein, R. M., Webster, F. X., and Kiemle, D. J. *Spectrometric Identification of Organic Compounds*, seventh ed.; Wiley: New York, 2005.

[7] Hathaway, B. J., and Underhill, A. E. (1961) 592. The Infrared Spectra of some Transition-Metal Perchlorates. *Journal of the Chemical Society (Resumed)* 3091–3096.

[8] Hardwick, L. J., Saint, J. A., Lucas, I. T., Doeff, M. M., and Kostecki, R. (2009) FTIR and Raman Study of the $Li_xTi_yMn_{1-y}O_2$(y = 0, 0.11) Cathodes in Methyl-propyl Pyrrolidinium Bis(fluoro-sulfonyl)imide, LiTFSI Electrolyte. *Journal of The Electrochemical Society 156*, A120–A127.

[9] Yoon, H., Best, A. S., Forsyth, M., MacFarlane, D. R., and Howlett, P. C. (2015) Physical Properties of High Li-ion Content N-propyl-N-methylpyrrolidinium Bis(fluorosulfonyl)imide Based Ionic Liquid Electrolytes. *Physical Chemistry Chemical Physics 17*, 4656–4663.

[10] Kiefer, J., Fries, J., and Leipertz, A. (2007) Experimental Vibrational Study of Imidazolium-Based Ionic Liquids: Raman and Infrared Spectra of 1-ethyl-3-methylimidazolium Bis(trifluoromethylsulfonyl)imide and 1-ethyl-3-methylimidazolium Ethylsulfate. *Applied Spectroscopy 61*, 1306–1311.

[11] Shkrob, I. A., Marin, T. W., Zhu, Y., and Abraham, D. P. (2014) Why Bis(fluorosulfonyl)imide Is a "Magic Anion" for Electrochemistry. *The Journal of Physical Chemistry C 118*, 19661–19671.

[12] Johnston, D. H., and Shriver, D. F. (1993) Vibrational Study of the Trifluoromethanesulfonate Anion: Unambiguous Assignment of the Asymmetric Stretching Modes. *Inorganic Chemistry 32*, 1045–1047.

Chapter 6

SURFACE-TETHERED POLY(IONIC LIQUID) COPOLYMER FILMS VIA ANION EXCHANGE

Introduction

Copolymerization of two different monomers is a general strategy to obtain macromolecules with tuned properties.[1] Random and block copolymers of PILs have been prepared by the copolymerization of ionic monomers with other ionic or nonionic monomers.[1–3] Copolymerization of an ionic monomer with a nonionic monomer can lead to random or block copolymers with a dilute charge character due by the reduction of ionic moieties in the polymer backbone.[1–3] Crosslinked PILs can also be formed by the copolymerization of ionic monomers with bifunctional crosslinking agents or via the polymerization of bifunctional ionic monomers.[2] Copolymerization can also be carried out to achieve random or block copolymers with opposite charges on the backbone by the copolymerization of an anionic monomer with a cationic monomer.[1] Copolymerization of similar ionic (cationic or anionic) monomers possessing the same polymerizable moieties but different counter ions can lead to random or block copolymers exhibiting a uniform polymer backbone but different counter ions.[1,4] In all the above approaches, the preparation of two different monomer units was necessary in order to achieve the copolymers, which presents a synthetic burden in the preparation of the monomers as well as a challenge to find the optimal polymerization conditions for the formation of the copolymers.

In this chapter, I report a novel and simple approach to achieve surface-tethered coPIL films via anion exchange. Initially, surface-immoblized PIL films on planar substrates of gold were prepared by the SI-ROMP of the ionic liquid monomer

[N_1−dMIm][PF_6] whose PF_6^- anion can easily be interchanged to tune film properties in a discrete manner. In my approach, anion exchange of the surface-immobilized p[N_1−dMIm][PF_6] films with aqueous solutions consisting of a binary mixture of anions provides a novel and rapid route to achieve random surface-tethered coPIL films. This route is advantageous compared to traditional PIL copolymerization strategies in that it only requires the synthetic preparation of one monomeric unit to achieve random coPIL films. The composition of the random coPIL films can easily be controlled in a continuous manner by varying the binary mole fraction of each anion in solution prior to anion exchange. The preparation of random coPIL films via anion exchange is a reversible process providing the capability to reacquire the material properties of the PIL homopolymer . In this way the advantages of the PILs are retained and enhanced by the ability to easily prepare coPIL films from the PIL homopolymers. Further, use of surface-tethered films allows for the ease of separation of the coPIL films from the anion exchange solution.

By utilizing a thermodynamic model for the anion exchange equilibrium, I was able to determine the thermodynamically driven anion selectivity for exchange of each anion in the binary mixture from the liquid phase into the coPIL films. I observed that the thermodynamic driving force for anion exchange from the liquid phase to the solid phase follows the order $ClO_4^- > PF_6^- > FSI^-$. The surface wettability of p[N_1−dMIm] copolymer films with the PF_6^- and ClO_4^- anions (p[N_1−dMIm][PF_6][ClO_4]) was quantified by contact angle goniometry with the observation that the surface showed an enrichment in the ClO_4^- anion compared to the average binary anion mole fraction of ClO_4^- in the film (y_{ClO_4}). The rate of ion transport through the p[N_1−dMIm][PF_6][ClO_4] copolymer films was shown to be linearly dependent on the binary anion mole fraction of ClO_4^- in solution (x_{ClO_4}) allowing for an extension of the discrete tunability of PIL films to a continuous tunability with the coPIL films to obtain specific properties for any desired application.

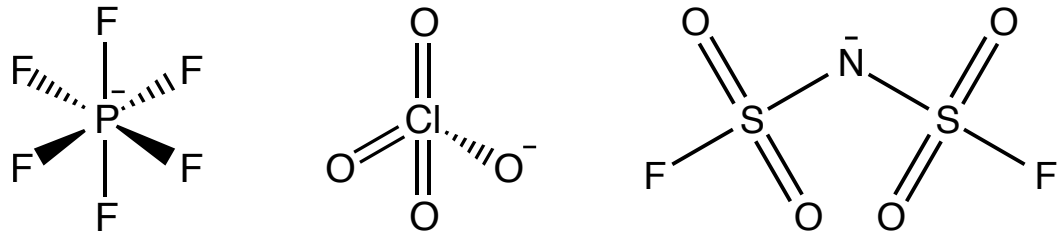

Figure 6.1: Structures of anions exchanged into p[N_1−dMIm] films.

Experimental Methods

Polymerization of [N_1−dMIm][PF_6] on Gold and Glass Substrates

ROMP-active substrates of gold and glass were prepared as described in Chapter 3. The ROMP-active substrates were quickly rinsed with DCE and immediately placed in a 0.1 M [N_1−dMIm][PF_6] solution in DCE for up to 15 min. The substrates were subsequently rinsed with DCM, ethanol, water, and ethanol and dried in a stream of nitrogen.

Ionic Polymer Film Anion Exchange

The anion exchange of p[N_1−dMIm] films with resident anion was accomplished in a reversible manner by simply immersing the film in an aqueous solution containing 0.2 M of the salt of the desired anion for a minimum of 2 h.[1,5] The substrates were subsequently rinsed with water and ethanol and dried in a stream of nitrogen. The chemical structure of the anions considered in this chapter are shown in Figure 6.1.

The anion exchange of p[N_1−dMIm] films containing a resident anion with a mixture of anions was accomplished in a reversible manner by immersing the film in an aqueous solution containing 0.2 M of the salts of the desired anions for a minimum of 2 h. Initially, 0.2 M aqueous solutions containing the pure salt of the desired anions were prepared and then combined volumetrically to achieve the desired mole fraction in the exchange solution. The substrates were subsequently rinsed with water and

ethanol and dried in a stream of nitrogen.

Results and Discussion

Polymerization of the ionic liquid monomer $[N_1-dMIm][PF_6]$ at a concentration of 0.1 M in DCE for 15 min led to a surface-tethered polymer film that exhibited a profilometric thickness of 650 ± 30 nm. The IR spectrum of $p[N_1-dMIm][PF_6]$ was consistent with that reported in Figure 4.2.

Copolymer

Anion exchange of the $p[N_1-dMIm][PF_6]$ films was successfully accomplished with the anions ClO_4^-, FSI^-, and $^-NTf_2$ and was consistent with the spectra reported in Figure 4.2. Anion exchange of the PF_6^- anion with a solution consisting of salts of both a PF_6^- anion as well as ClO_4^- anion was successfully accomplished as evidenced by the IR spectra shown in Figure 6.2. The IR spectrum for the $[PF_6]/[ClO_4]$ copolymer sample exhibits both the P−F stretch peak at 855 cm^{-1} and the Cl−O stretch peak at 1106 cm^{-1} and retains the absorption bands due to the polymer carbon backbone.

The intensity of the absorbance peaks in Figure 6.2 depends on the anion concentration and the chemical structure of the anion in the film. In particular the $p[N_1-dMIm]$ film with the PF_6^- anion exhibits a more intense peak compared to the ClO_4^- anion. In order to determine the relative concentrations of each anion in the film, I considered two regions of the spectra to represent contributions from the PF_6^- anion and the ClO_4^- anion. The absorbance bands in the spectra that are due to the PF_6^- anion occur in the region $800-950$ cm^{-1} (Region A) and the absorbance bands in the spectra that are due to the ClO_4^- anions occur in the region $1000-1500$ cm^{-1} (Region B). For $p[N_1-dMIm]$ film spectra, I summed the absorbance in regions A and B and normalized the total absorbance in each region to the total absorbance

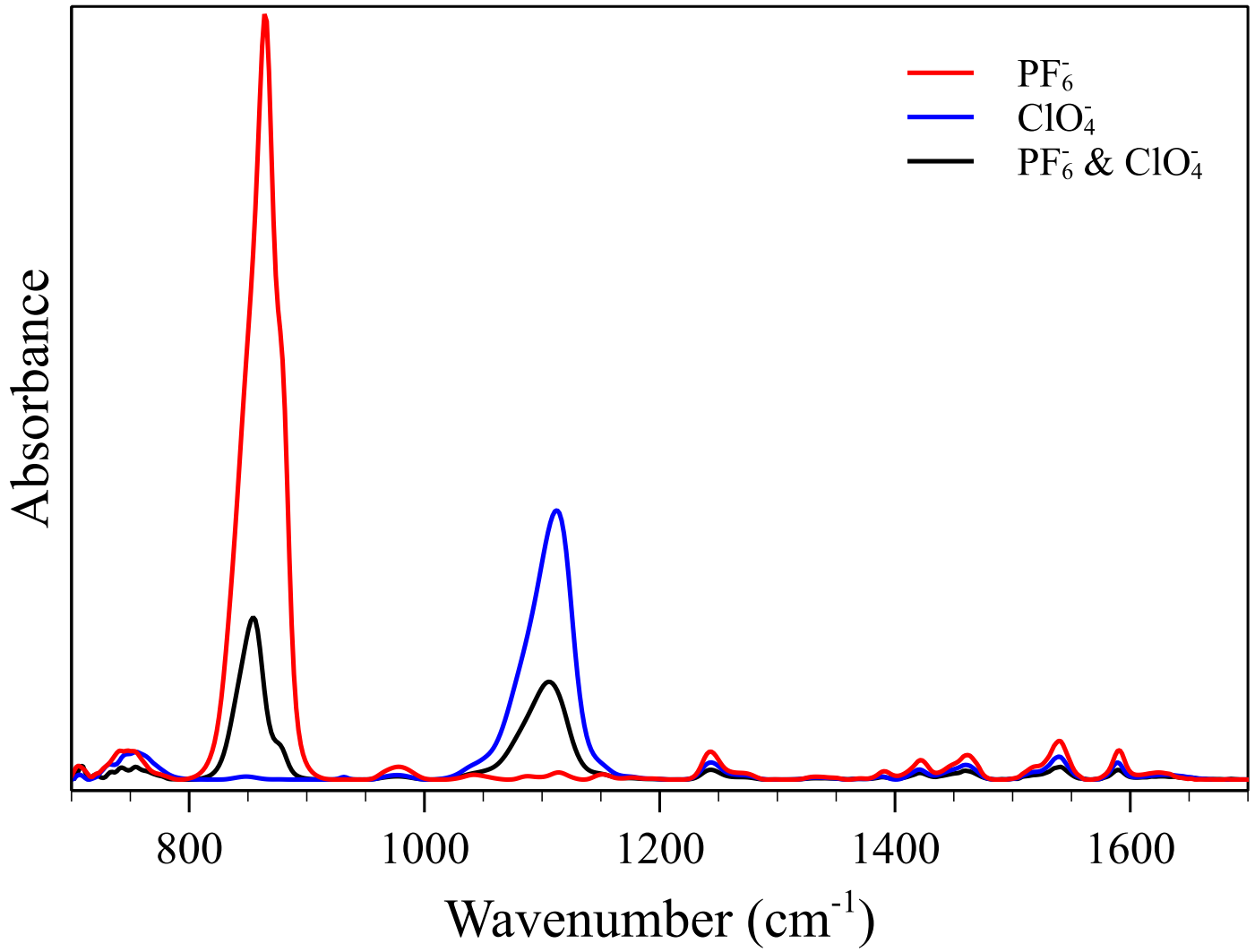

Figure 6.2: Polarization modulation-infrared reflectance-absorption spectrum of p[N_1−dMIm] films on gold substrates. Representative IR spectra of a p[N_1−dMIm] film with the PF_6^-, ClO_4^-, and a copolymer consisting of both the PF_6^- and ClO_4^- anion.

for the region $800 - 1500$ cm^{-1}, thereby estimating the fractional contribution to the spectral intensity arising from each anion in the copolymer film. In order to determine the mole fraction of each anion in the copolymer film, I solved the following set of equations for y_{PF_6}, the binary anion mole fraction of PF_6^- in the film and y_{ClO_4}, the binary anion mole fraction of ClO_4^- in the film.

$$Co(A) = y_{PF_6} PF_6^-(A) + y_{ClO_4} ClO_4^-(A) \tag{6.1}$$

$$Co(B) = y_{PF_6} PF_6^-(B) + y_{ClO_4} ClO_4^-(B) \tag{6.2}$$

In eq 6.1 and 6.2, $PF_6^-(A)$ corresponds to the normalized absorbance for region A for a p[N_1−dMIm][PF_6] film, $PF_6^-(B)$ corresponds to the normalized absorbance for region B for a p[N_1−dMIm][PF_6] film. Similarly, $ClO_4^-(A)$ and $ClO_4^-(B)$ correspond to the normalized absorbance for regions A and B for a p[N_1−dMIm][ClO_4] film, and $Co(A)$ and $Co(B)$ correspond to the normalized absorbance for regions A and B for a p[N_1−dMIm] film with both the PF_6^- and ClO_4^- anions (p[N_1−dMIm][PF_6][ClO_4].

Figure 6.3 shows y_{ClO_4} as a function of the binary anion mole fraction of ClO_4^- in solution(x_{ClO_4}) used in the exchange of p[N_1−dMIm] films prepared. The anion exchange was performed starting with p[N_1−dMIm][PF_6] and p[N_1−dMIm][ClO_4] films using 0.2 M aqueous solutions with varying x_{ClO_4} and consequently x_{PF_6}. The p[N_1−dMIm] films exhibit a high selectivity for PF_6^- in the film, as evidenced by the fact that all the data lie below the $x = y$ line. For example, anion exchange of p[N_1−dMIm][PF_6] films with a 0.2 M aqueous solution with $x_{ClO_4} = 0.5$ leads to a p[N_1−dMIm][PF_6][ClO_4] copolymer film with $y_{ClO_4} = 0.09 \pm 0.02$. The data for the anion exchange from p[N_1−dMIm][PF_6] films is not statistically different from that for the anion exchange from p[N_1−dMIm][ClO_4] films, indicating that the anion exchange conditions were sufficient to achieve equilibrium.

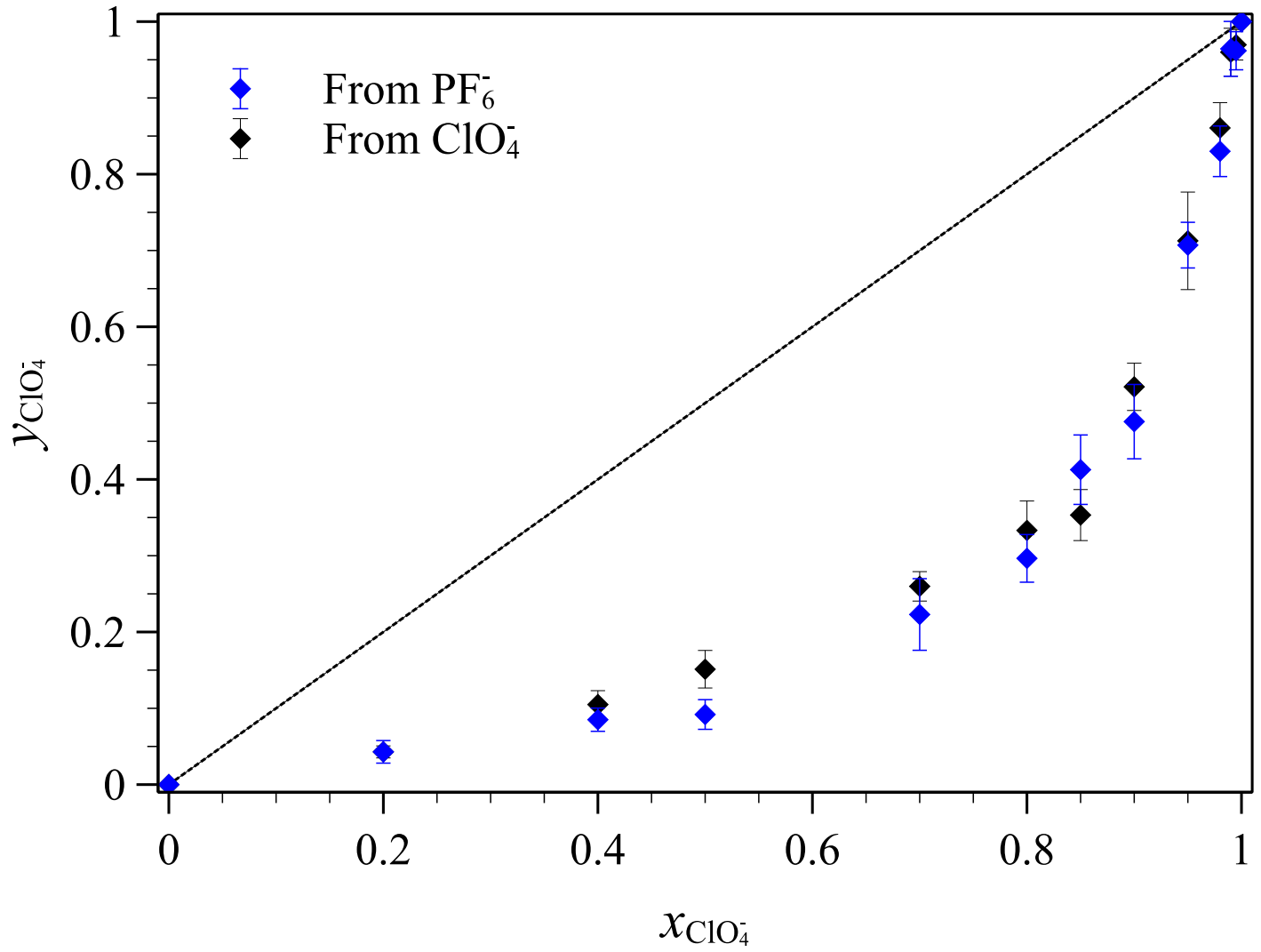

Figure 6.3: Binary anion mole fraction of ClO_4^- in the film (y_{ClO_4}) as a function of the binary anion mole fraction of ClO_4^- in solution (x_{ClO_4}) for p[N_1−dMIm][PF_6][ClO_4] copolymer films prepared by anion exchange. Anion exchange was performed from p[N_1−dMIm][PF_6] and p[N_1−dMIm][ClO_4] films with 0.2 M aqueous solutions containing both PF_6^- and ClO_4^- anions. Reported values represent the averages and standard deviations of at least three independently prepared films.

In order to determine the partitioning of the PF_6^- and ClO_4^- anions from the liquid into the solid phase, I determined an equilibrium constant using the chemical potential of each anion in the liquid and solid phase. Assuming ideal behavior, one can obtain

$$\mu_a^l = \mu_a^\circ + RTln(x_a) \tag{6.3}$$

$$\mu_a^s = \mu_a^\circ + RTln(y_a) \tag{6.4}$$

$$K_a = \frac{y_a}{x_a} = e^{-\frac{\Delta\mu_a}{RT}} \tag{6.5}$$

where x_a is the mole fraction of anion a in the solution phase, y_a is the mole fraction of anion a in the solid phase, and K_a is the equilibrium constant for anion a. Considering that

$$x_a K_a + x_b K_b = y_a + y_b = 1 \tag{6.6}$$

which leads to

$$y_a = \frac{x_a}{x_a + x_b\left(\frac{K_b}{K_a}\right)} \tag{6.7}$$

for which one can define $\alpha = \frac{K_b}{K_a}$, the selectivity of the anion b for the solid phase compared to that for anion a. One can rewrite eq 6.7 in terms of the anion a as follows

$$y_a = \frac{x_a}{x_a + (1 - x_a)\,\alpha} \tag{6.8}$$

Eq 6.8 was used to fit the data shown in Figure 6.3, with $\alpha = 9 \pm 1$ for the film composition data acquired from a p[N_1−dMIm][PF_6] film and $\alpha = 8 \pm 1$ for the film composition data acquired from a p[N_1−dMIm][ClO_4] film, as shown in Figure 6.4.

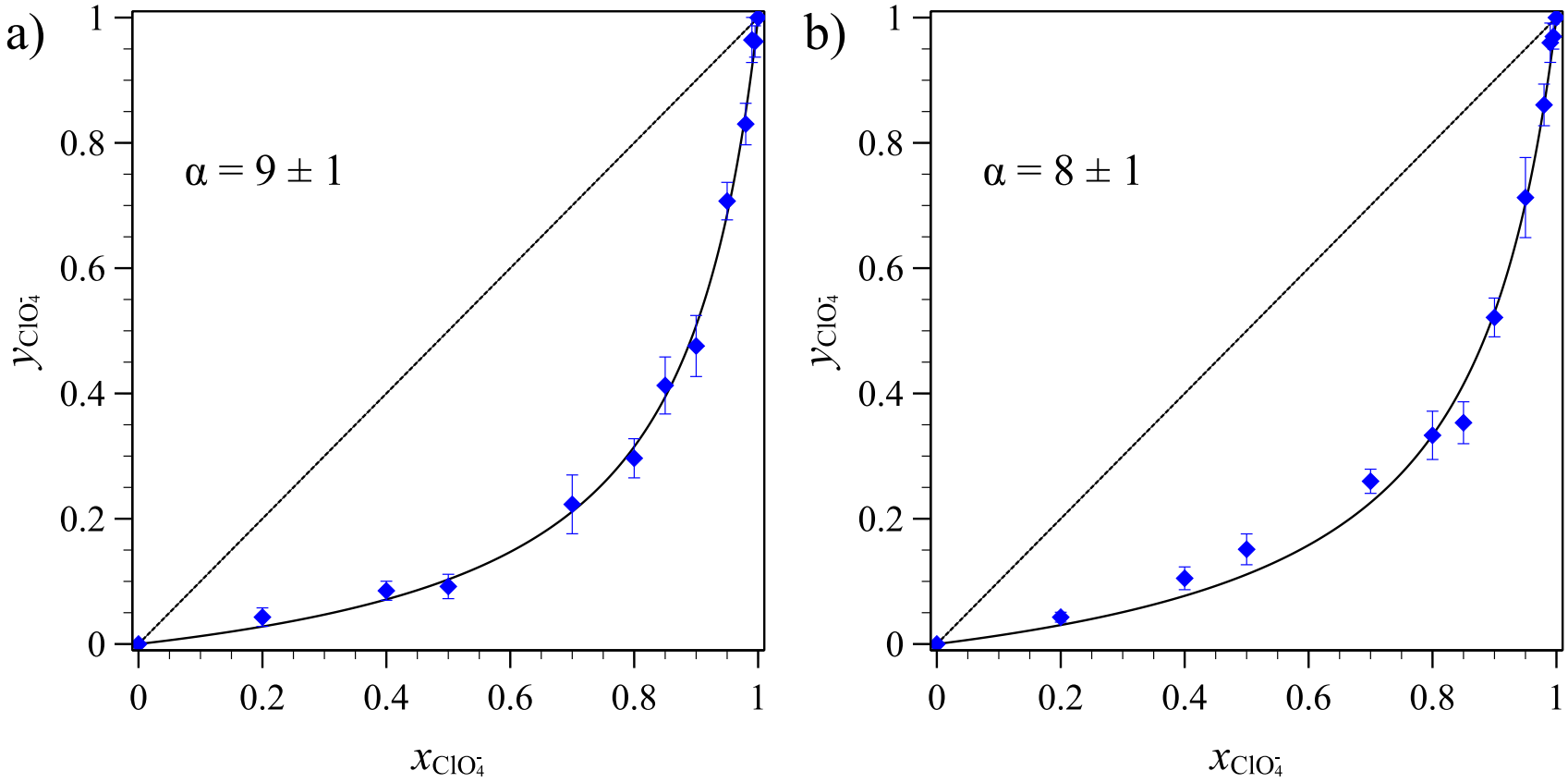

Figure 6.4: Binary anion mole fraction of ClO_4^- in the film (y_{ClO_4}) as a function of the binary anion mole fraction of ClO_4^- in solution (x_{ClO_4}) for p[N_1−dMIm][PF_6][ClO_4] copolymer films prepared by anion exchange. a) Anion exchange from p[N_1−dMIm][PF_6] films with 0.2 M aqueous solutions containing both PF_6^- and ClO_4^- anions. b) Anion exchange from p[N_1−dMIm][ClO_4] films with 0.2 M aqueous solutions containing both PF_6^- and ClO_4^- anions. Values represent the averages and standard deviations of at least three independently prepared films. Solid lines are fits of the data with eq 6.8.

The binary anion mole fraction of FSI^- in the film (y_{FSI}) as a function of the binary anion mole fraction of FSI^- in solution (x_{FSI}) for p[N_1−dMIm][PF_6][FSI] copolymer films is shown in Figure 6.5. The relative concentrations of each anion in the film were determined by considering two regions of the spectra representing contributions from the PF_6^- anion and the FSI^- anion. I summed the absorbance in the spectra arising from the PF_6^- anion in the region $800 - 950$ cm^{-1} (Region A), as well as the absorbance in the spectra arising from the FSI^- anion in the region $1000 - 1500$ cm^{-1} (Region B), and normalized it to the total absorbance for the region $800 - 1500$ cm^{-1}, thereby estimating the fractional contribution to the spectral intensity arising from each anion in the copolymer film. The mole fraction of each anion in the copolymer film was determined as described above for the exchange involving the PF_6^- and ClO_4^- anions (eqs 6.1 and 6.2). The p[N_1−dMIm] films exhibit a high selectivity for FSI^- as compared to PF_6^- in the film, as evidenced by the fact that the data lie above the $x = y$ line. For example, anion exchange of p[N_1−dMIm][PF_6] films with a 0.2 M aqueous solution with $x_{FSI} = 0.5$ leads to a p[N_1−dMIm][PF_6][FSI] copolymer film with $y_{FSI} = 0.79 \pm 0.05$.

The selectivity of copolymer films with the PF_6 and FSI^- anions exhibits a stark difference as compared to that of the PF_6^- and ClO_4^- anions. In particular, the copolymer with the FSI^- anion exhibits the opposite selectivity of the copolymer with the ClO_4^- anion. The anion exchange between the liquid phase and the solid phase is an equilibrium process with constant exchange of anions between the two phases and the difference in selectivity can be related to the thermodynamic driving force present in the formation of the copolymer films. For the anion exchange, the partitioning in the liquid and solid phases is determined both by the mole fraction and the thermodynamic driving force of the anions in either phase. For a particular ionic composition, an anion that has a smaller thermodynamic driving force for exchange from the liquid phase to solid phase will exhibit a selectivity for the liquid phase, while

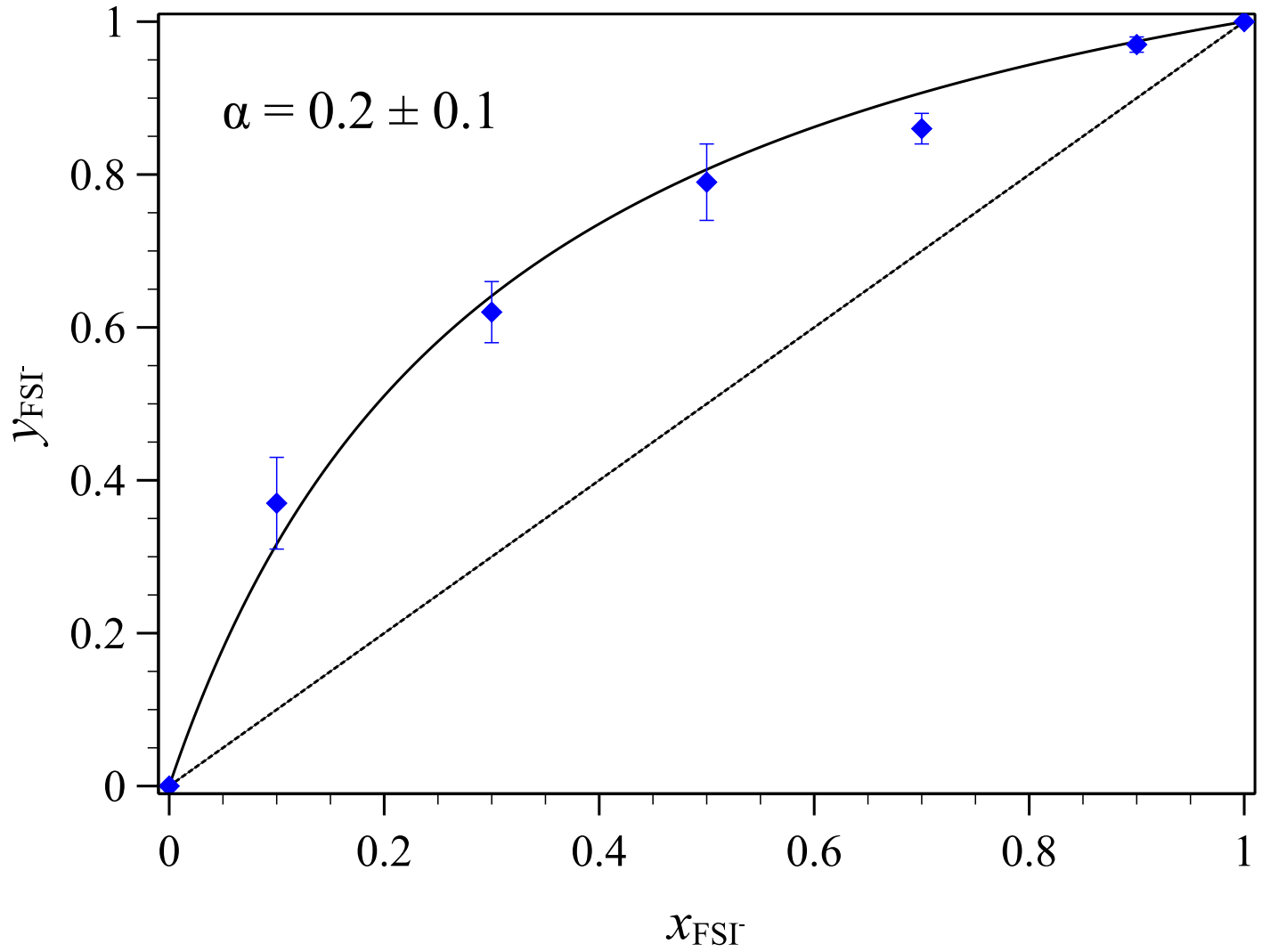

Figure 6.5: Binary anion mole fraction of FSI^- in the film (y_{FSI}) as a function of the binary anion mole fraction of FSI^- in solution (x_{FSI}) for p[N_1−dMIm][PF_6][FSI] copolymer films prepared by anion exchange. Anion exchange was performed from p[N_1−dMIm][PF_6] films with 0.2 M aqueous solutions containing both PF_6^- and FSI^- anions. Values represent the averages and standard deviations of at least three independently prepared films. The solid line is a fit of the data with eq 6.8.

one that exhibits a larger thermodynamic driving force for exchange from the liquid phase to the solid phase will exhibit a selectivity for the solid phase. Subsequently, for a given binary system and thermodynamic driving forces, a large mole fraction in the liquid phase of the anion with a smaller thermodynamic driving force is required to obtain a large mole fraction in the solid phase. In that way, we can rank the thermodynamic driving forces for exchange from the liquid phase to the solid phase for the anions considered as $ClO_4^- < PF_6^- < FSI^-$. Conversely, the thermodynamic driving forces for exchange from the solid to the liquid phase for the anions considered would follow the inverse order.

Contact Angle

Considering that the anion strongly influences the surface wettability of surface-tethered ILs[6] as well as the solubility of PILs with water,[1,7] the surface wettability of the p[N_1−dMIm][PF_6][ClO_4] copolymer films was assessed by contact angle goniometry as shown in Figure 6.6. I have previously shown, in Chapter 4, that the advancing water contact angle (θ_A) of a p[N_1−dMIm][PF_6] film ($61 \pm 2°$) is greater than that of a p[N_1−dMIm][PF_6] film ($35 \pm 3°$),[8] which I attribute to the stronger interaction of ClO_4^- with water, as compared to PF_6^-, to stabilize the water /polymer interface. For surfaces with microscopic heterogeneity, the Cassie equation (eq 6.9) gives the relationship between the measured contact angle and the contact angle of the homogenous surfaces[9]

$$cos\theta = \sum_i f_i cos\theta_i \tag{6.9}$$

where, f_i is the fraction of the surface covered by component i. In Figure 6.6, the solid line represents the Cassie relationship for a p[N_1−dMIm][PF_6][ClO_4] copolymer film. The advancing water contact angles for the p[N_1−dMIm][PF_6][ClO_4] film, however, lie below the Cassie line, indicating an enrichment of the surface in ClO_4^- anion,

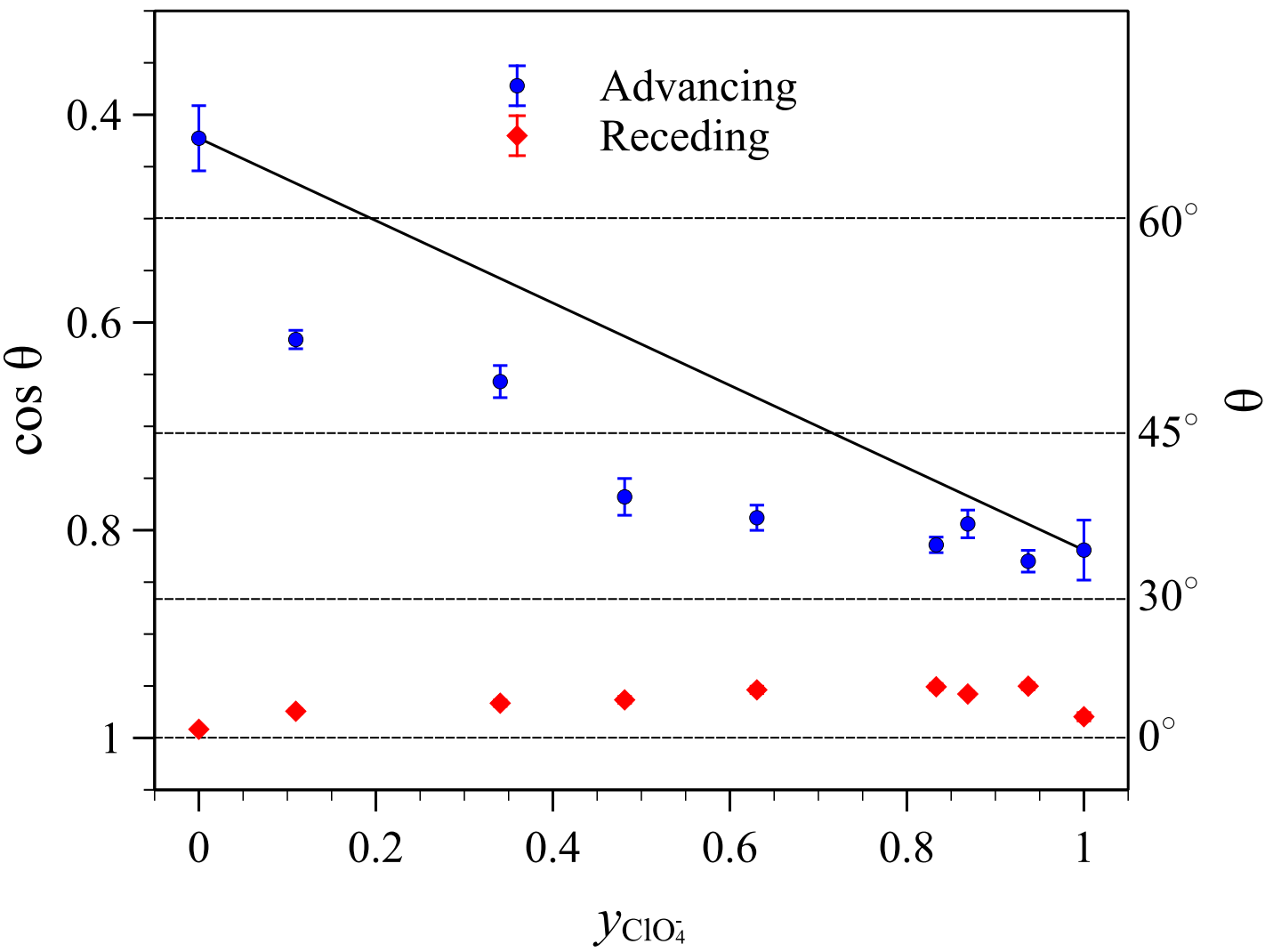

Figure 6.6: p[N_1−dMIm][PF_6][ClO_4] surface wettability with water as a function of the binary anion mole fraction of ClO_4^- in the film (y_{ClO_4}). The solid line is a representation of the Cassie equation for a film combining the PF_6^- and the ClO_4^- anions.

compared to the average binary anion mole fraction of ClO_4^- in the film (y_{ClO_4}). For example, $y_{ClO_4} = 0.5$ leads to a θ_A that is statistically the same as that for a pure ClO_4^- film. This enrichment in the surface concentration of ClO_4^- compared to PF_6^- can be related to the thermodynamic driving forces as discussed above. We note that anion exchange is a thermodynamically driven process and as such there is constant exchange of anions between the solid and the liquid phase. However, when we remove the sample from solution we interrupt that exchange and essentially entrap the anions in the film. The receding water contact angles for the p[N_1−dMIm][PF_6], p[N_1−dMIm][ClO_4], and p[N_1−dMIm][PF_6][ClO_4] films did not show any significant differences and were actually quite hydrophillic, as shown in Figure 6.6. During removal of the sample from the exchange solution, the minimization of interfacial energy between the polymer film and the aqueous phase results in a surface enrichment of the ClO_4^- anion compared to the bulk y_{ClO_4}.

Ion Transport in p[N_1−dMIm][PF_6][ClO_4] Copolymer films

I have previously shown, in Chapter 4, that the film anion determines the resistance of the p[N_1−dMIm] film to ion conduction with the order, $PF_6^- > {}^-[NTf_2 \gg FSI^- \gg ClO_4^-$, while the electrolyte cation does not impact ion conduction in p[N_1−dMIm] films when performed in aqueous electrolytes.[8] Ion transport through the p[N_1−dMIm][PF_6][ClO_4] films was investigated by utilizing electrochemical impedance spectroscopy (EIS). The studies were conducted in the presence of a 0.1 M aqueous solution of salts with the same binary anion mole fraction of ClO_4^- in solution (x_{ClO_4}) used in the anion exchange of the polymer film in order to avoid anion exchange during collection of the spectra. Representative Bode plots of EIS spectra for p[N_1−dMIm][PF_6][ClO_4] films prepared by anion exchange from a p[N_1−dMIm][PF_6] film with 0.2 M aqueous solutions of varying x_{ClO_4}, as well as a pure p[N_1−dMIm][PF_6] film ($y_{ClO_4} = 0$), and a pure p[N_1−dMIm][ClO_4] film

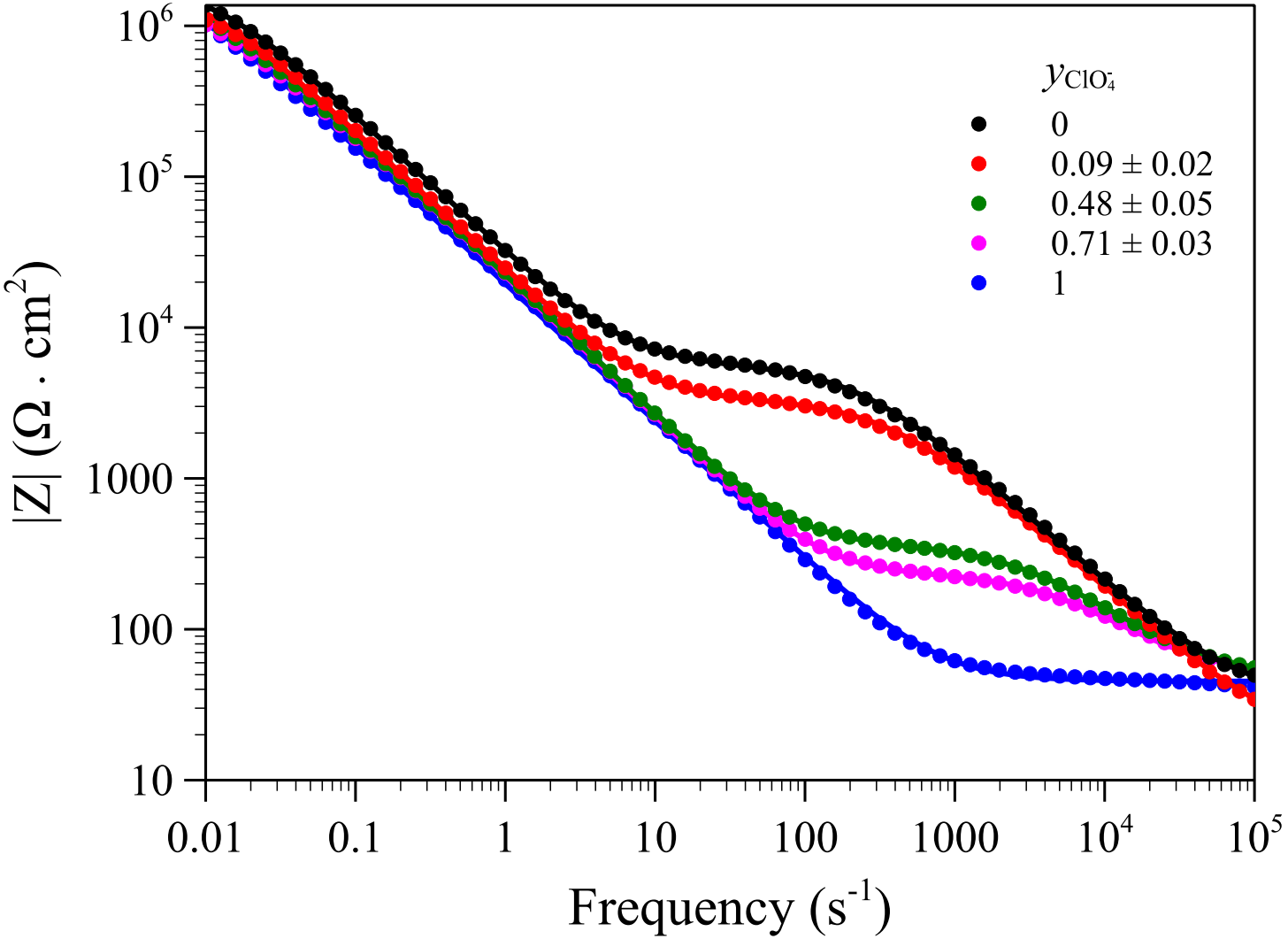

Figure 6.7: Bode plot of EIS spectra for a pure p[N_1−dMIm][PF_6] film (y_{ClO_4} = 0), a pure p[N_1−dMIm][ClO_4] film (y_{ClO_4} = 1), and p[N_1−dMIm][PF_6][ClO_4] films with varying binary anion mole fraction of ClO_4^- in solution (x_{ClO_4}). The spectra were acquired in a 0.1 M aqueous solution consisting of the same x_{ClO_4} used to prepare the CoPIL film. The salts used were KPF_6 and $KClO_4$. Solid curves represent fits to the equivalent circuit in Scheme 3.4.

($y_{ClO_4} = 1$), are shown in Figure 6.7. The corresponding phase angle plots are included in Figure 6.8. The impedance spectra were fit using the equivalent circuit model in Scheme 3.4 to quantify the circuit parameters as shown in Tables 6.1 and 6.2.

The R_s for the pure p[N_1−dMIm][PF_6] film ($y_{ClO_4} = 0$), as well as the pure p[N_1−dMIm][ClO_4] film ($y_{ClO_4} = 1$), and the p[N_1−dMIm][PF_6][ClO_4] films with varying y_{ClO_4} was observed for high frequencies, $f \geq 10^4$ Hz, as shown in Figure 6.7 and quantified in Table 6.1. Variations in R_s are due to the different ionic conductivities of electrolyte solutions arising from the different salts utilized in the collection of the EIS spectra.[8] The C_i for the pure p[N_1−dMIm][PF_6] film ($y_{ClO_4} = 0$), as well as the pure p[N_1−dMIm][ClO_4] film ($y_{ClO_4} = 1$), and the p[N_1−dMIm][PF_6][ClO_4] films with varying y_{ClO_4} was observed for low frequencies, $f \leq 1$ Hz, as shown in Figure 6.7. The values for the C_i and R_i obtained from fits to the equivalent circuit in Scheme 3.4 are listed in Table 6.1. The C_i for the p[N_1−dMIm][PF_6][ClO_4] films varies between the values observed for the pure p[N_1−dMIm][PF_6] film and the pure p[N_1−dMIm][ClO_4] film.

The film capacitance (C_f) due to a separation of charge between the metal surface and the bulk solution as well as the resistance (R_f) that the PIL film provides against ion migration are parameters derived for phenomena that happen at intermediate time scales, which are typically observed in the intermediate frequency sinusoidal perturbation of the working electrode potential. As shown in Figure 6.7, the EIS spectra for the pure p[N_1−dMIm][PF_6] film ($y_{ClO_4} = 0$) is dramatically different from that of the pure p[N_1−dMIm][ClO_4] film ($y_{ClO_4} = 1$). In particular, one can observe a R_f and a C_f for the pure p[N_1−dMIm][PF_6] film for the intermediate frequency range, $1 \leq f \leq 10^4$ Hz. The conversion of the film resistance values (R_f) to a film conductivity (κ_f) is accomplished by using eq 4.2. The capacitive behavior observed in Figure 6.7, however, is indicative of a leaky capacitor and therefore a constant

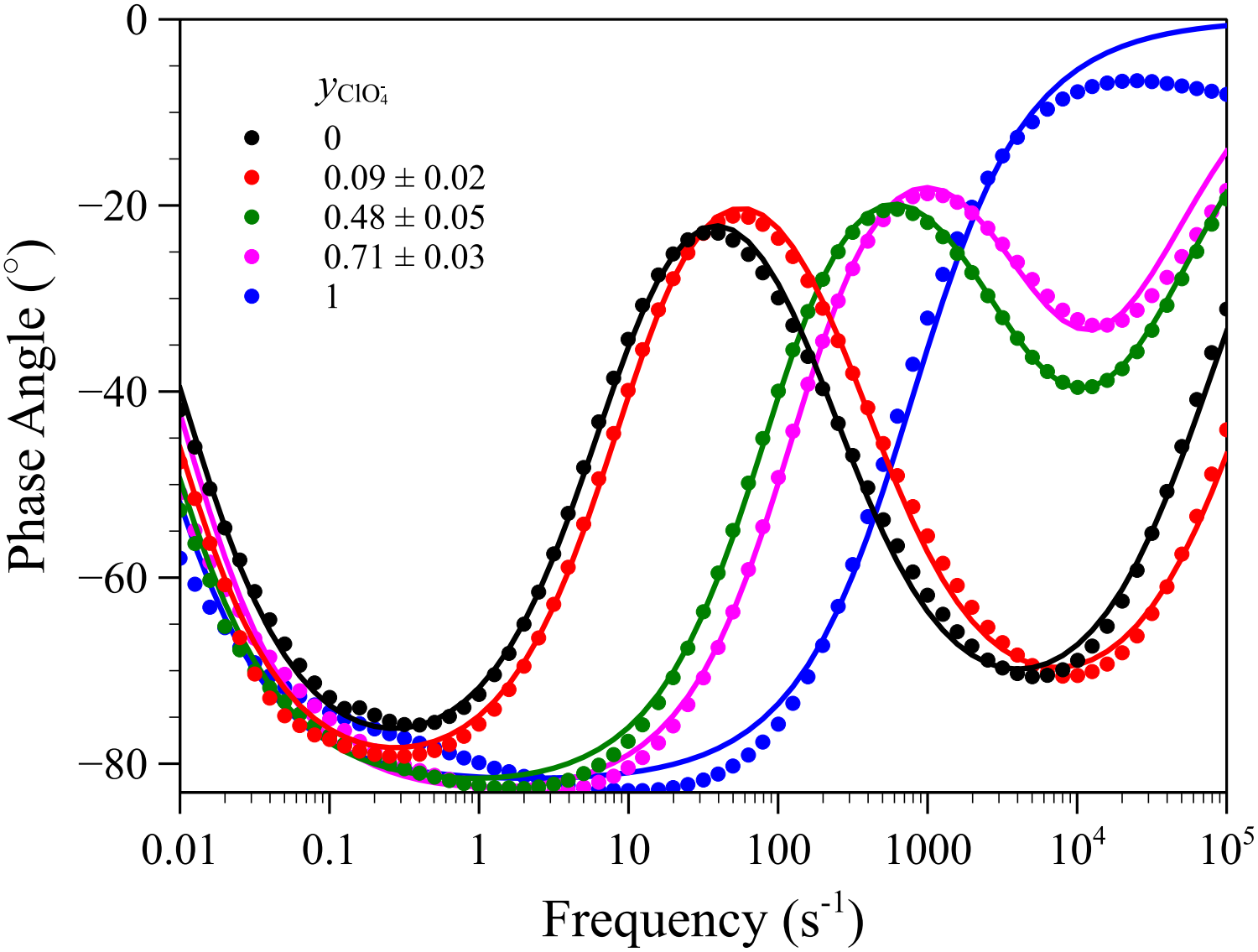

Figure 6.8: Phase angle plot of EIS spectra for a pure p[N_1−dMIm][PF_6] film ($y_{ClO_4} = 0$), a pure p[N_1−dMIm][ClO_4] film ($y_{ClO_4} = 1$), and p[N_1−dMIm][PF_6][ClO_4] films with varying binary anion mole fraction of ClO_4^- in solution (x_{ClO_4}). The spectra were acquired in a 0.1 M aqueous solution consisting of the same x_{ClO_4} used to prepare the polymer film. The salts used were KPF_6 and $KClO_4$. The solid curves represent fits of the data with the equivalent circuit in Scheme 3.4.

Table 6.1: p[N_1−dMIm] Solution Resistance (R_s), Interfacial Resistance (R_i), and Interfacial Capacitance (C_i) Values Obtained from Fits of the EIS Spectra in Figure 6.7 to the Equivalent Circuit in Scheme 3.4.

y_{ClO_4}	R_s ($\Omega \cdot cm^2$)	R_i ($M\Omega \cdot cm^2$)	C_i ($\mu F/cm^2$)
0	35 ± 1	1.99 ± 0.06	8.4 ± 0.2
0.09 ± 0.02	18 ± 1	2.02 ± 0.06	8.7 ± 0.1
0.48 ± 0.05	47 ± 1	2.15 ± 0.08	10.4 ± 0.2
0.71 ± 0.03	50 ± 1	1.62 ± 0.04	9.9 ± 0.3
1	45.1 ± 0.3	2.05 ± 0.06	14.3 ± 0.1

Table 6.2: p[N_1−dMIm] Film Resistance (R_f), Conductivity (κ_f), and Capacitance (C_f) Values Obtained from Fits of the EIS Spectra in Figure 6.7 using the Equivalent Circuit in Scheme 3.4.

y_{ClO_4}	R_f ($K\Omega \cdot cm^2$)	κ_f ($\mu S/cm$)	C_f ($\mu F/cm^2$)
0	5.89 ± 0.07	0.011 ± 0.001	0.17 ± 0.01
0.09 ± 0.02	3.43 ± 0.04	0.019 ± 0.001	0.18 ± 0.01
0.48 ± 0.05	0.43 ± 0.01	0.193 ± 0.010	0.23 ± 0.04
0.71 ± 0.03	0.19 ± 0.01	0.335 ± 0.017	0.23 ± 0.06
1^a	$\leq (4.34 \pm 0.04) \times 10^{-3}$	$\geq 13.6 \pm 0.8$	-

[a] Values calculated for a p[N_1−dMIm][ClO_4] film EIS spectra collected in a 0.5M $CaClO_4$ solution exhibiting an R_s of $4.34 \pm 0.04\ \Omega \cdot cm^2$.[8] The film resistance for the film is theoretically lower than the R_s observed.[8]

phase element (CPE) was used in lieu of a capacitor to fit the EIS spectra. The CPE can be converted into an effective capacitance by using eq 4.4.[10] The numerical values for the film resistance, conductivity, and capacitance obtained from a fit of the data with the equivalent circuit of Scheme 3.4 are shown in Table 6.2.

The R_f of the copolymer films decreases with an increase in the binary anion mole fraction of ClO_4^- in solution (x_{ClO_4}). The increase in x_{ClO_4} also results in a thermodynamically determined change in film composition as observed before, and therefore, the R_f of the copolymer film shows a trend with an increase in y_{ClO_4}. However, this is a secondary effect arising from the fact that x_{ClO_4} and y_{ClO_4} are related via eq 6.8. Consequently, the κ_f of the copolymer films increase with an increase in x_{ClO_4}. In order to determine the effect of x_{ClO_4} on the R_f, I normalized the R_f to the value obtained for the pure p[N_1−dMIm][PF_6] film. Figure 6.9 is a plot of the normalized film resistance obtained from a fit of the EIS spectra with the equivalent circuit of Scheme 3.4 as a function of x_{ClO_4}. The R_f was shown to vary linearly with x_{ClO_4} from the value obtained for the p[N_1−dMIm][PF_6] film to that obtained for the p[N_1−dMIm][ClO_4] film.

This linear dependence of R_f on x_{ClO_4} is expected if one considers the thermodynamic driving forces of anion exchange. As mentioned before, the anion exchange process is an equilibrium process with the constant exchange of anions between the solid and the liquid phase. Our electrochemical cell is composed of a solution of the same composition as that used in the anion exchange of the copolymer films and as such there is a constant exchange of anions between the solid phase (film) and the liquid phase. In EIS, a low amplitude sinusoidal potential (E_{ac}) perturbation is applied around the equilibrium potential of the working electrode and depends on the fact that current-overpotential relations are virtually linear at low overpotentials.[11] Given that there are no redox species present in the electrochemical cell, the E_{ac} drives the motion of ions (ionic conductivity) through the film as mediated by the

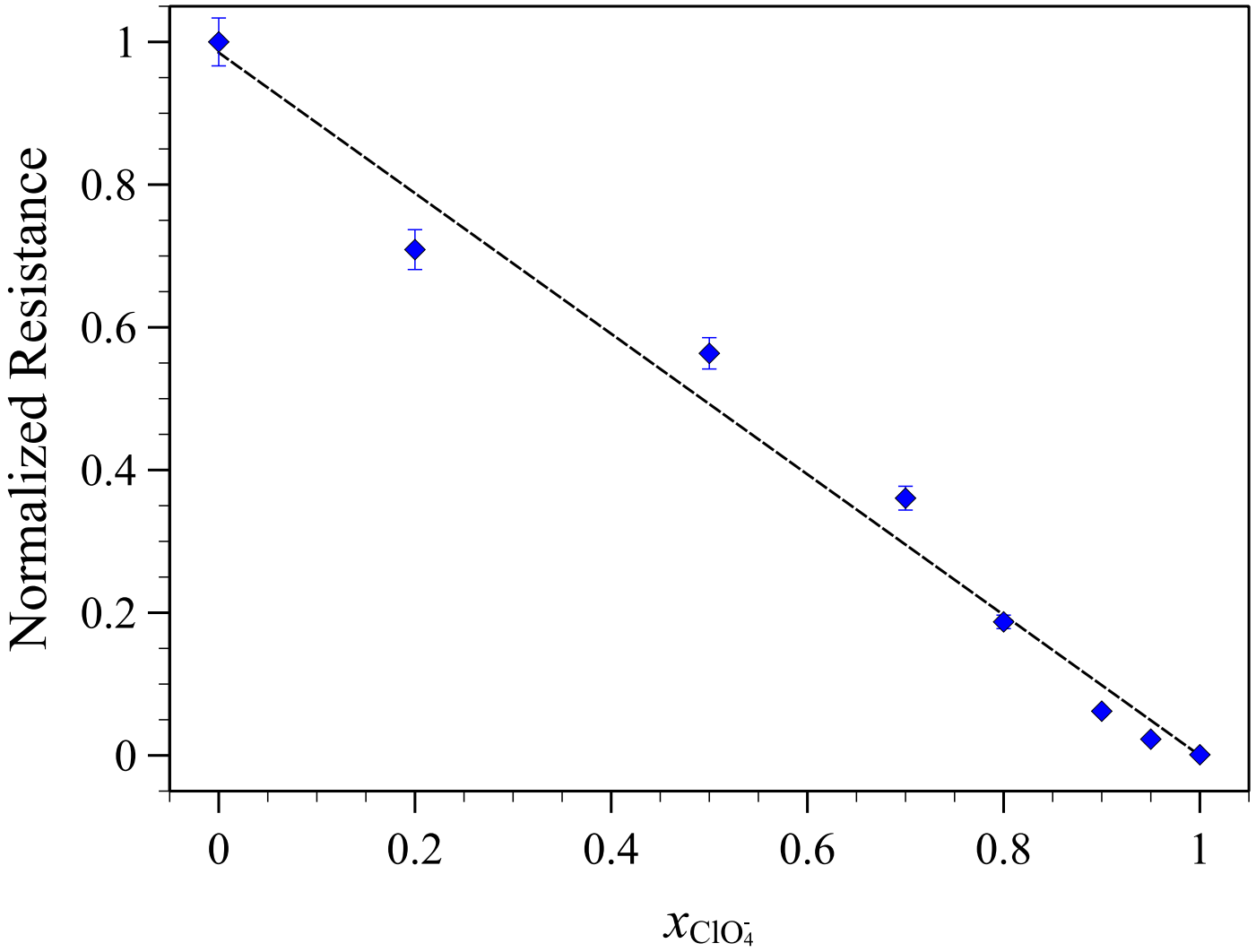

Figure 6.9: Normalized film resistance as a function of the binary anion mole fraction of ClO_4^- in solution (x_{ClO_4}) for p[N_1−dMIm][PF_6][ClO_4] copolymer films prepared by anion exchange from p[N_1−dMIm][PF_6] films with 0.2 M aqueous solutions containing both PF_6^- and ClO_4^- anions. Values represent the averages and standard deviations of at least three independently prepared films. The solid line is a linear fit of the data ($R^2 = 0.98$).

exchange of ions between the liquid and solid phases. Therefore, the R_f is an indirect measure of both the thermodynamic driving force for anion exchange as well as the ionic mobility of the anion. The ionic mobility of PF_6^- is 5.6×10^4 $m^2 \cdot S$ mol^{-1}, while that of ClO_4^- is 6.7×10^4 $m^2 \cdot S$ mol^{-1}.[12] However, the similarity in mobility does not explain the fact that the R_f for thep[N_1−dMIm][ClO_4] film is at least 3 orders of magnitude lower than that of the p[N_1−dMIm][PF_6] film as shown in Table 6.2, therefore the difference in R_f is largely due to the differences in the thermodynamic driving force rather than ion mobility

For the p[N_1−dMIm][PF_6][ClO_4] copolymer films, the y_{ClO_4} depends on the x_{ClO_4} and as such the R_f of the p[N_1−dMIm][PF_6][ClO_4] copolymer films is linearly dependent on the x_{ClO_4} due to the sensitivity of EIS to the motions of the PF_6^- compared to the ClO_4^- anion. For example, for a film prepared from a solution with $x_{ClO_4} = 0.5$, the solution solution contains equal mole fractions of ClO_4^- and PF_6^- anions. However, since the ClO_4^- anions contribute very little to the R_f but yet still participate in anion exchange with the film, the R_f is determined by the continuous anion exchange of the PF_6^- anions with the film, resulting in half the value of the R_f observed for a PF_6^- solution ($x_{ClO_4} = 0$).

Conclusions

Poly(ionic liquid) (PIL) random co-polymer films were prepared by the simple anion exchange of p[N_1−dMIm] films with 0.2 M aqueous solutions consisting of the PF_6^- anion with either the ClO_4^- or the FSI^- anions. The composition of the random co-polymer PIL films was determined using infrared spectroscopy (PM-IRRAS) and a linear system of equations. The p[N_1−dMIm] films exhibit a thermodynamically driven selectivity, with the PF_6^- anion selective for the film for p[N_1−dMIm][PF_6][ClO_4] co-polymer films and the FSI^- anion selective for the film for p[N_1−dMIm][PF_6][FSI] co-polymer films. The surface wettability for

p[N_1−dMIm][PF_6][ClO_4] films is dependent on the film composition, continuously tunable with film composition, and shows that the concentration of the ClO_4^- anion on the surface is higher than that determined for the p[N_1−dMIm][PF_6][ClO_4] film. The resistance of the p[N_1−dMIm][PF_6][ClO_4] film to ion conduction is linearly dependent on the binary anion mole fraction of ClO_4^- in solution(x_{ClO_4}), which is thermodynamically related to the binary anion mole fraction of ClO_4^- in the film (y_{ClO_4}). In this way a key characteristic of the film, film resistance, can be continuously tuned between the extremes of the two homopolymers. The ability to easily form random co-polymer films that exhibit a continuum of properties between the properties of the homopolymers greatly increases the utility of PIL films. PIL films already exhibit tremendous discrete tunability in their properties via anion exchange, which can now be extended to a continuous tunability to obtain specific properties for any desired application.

References

[1] Mecerreyes, D. (2011) Polymeric Ionic Liquids: Broadening the Properties and Applications of Polyelectrolytes. *Progress in Polymer Science 36*, 1629–1648.

[2] Shaplov, A. S., Ponkratov, D. O., and Vygodskii, Y. S. (2016) Poly(ionic liquid)s: Synthesis, properties, and application. *Polymer Science Series B 58*, 73–142.

[3] Yuan, J., Mecerreyes, D., and Antonietti, M. (2013) Poly(Ionic Liquid)s: An Update. *Progress in Polymer Science 38*, 1009–1036.

[4] Jovanovski, V., Marcilla, R., and Mecerreyes, D. (2010) Tuning the Properties of Functional Pyrrolidinium Polymers by (Co)polymerization of Diallyldimethylammonium Ionic Liquids. *Macromolecular Rapid Communications 31*, 1646–1651.

[5] He, X., Yang, W., and Pei, X. (2008) Preparation, Characterization, and Tunable Wettability of Poly(ionic liquid) Brushes via Surface-Initiated Atom Transfer Radical Polymerization. *Macromolecules 41*, 4615–4621.

[6] Lee, B. S., Chi, Y. S., Lee, J. K., Choi, I. S., Song, C. E., Namgoong, S. K., and Lee, S.-g. (2004) Imidazolium Ion-Terminated Self-Assembled Monolayers on Au: Effects of Counteranions on Surface Wettability. *Journal of the American Chemical Society 126*, 480–481.

[7] Qian, W., Texter, J., and Yan, F. (2017) Frontiers in Poly(ionic liquid)s: Syntheses and Applications. *Chemical Society Reviews 46*, 1124–1159.

[8] Njoroge, I., Matson, M. W., and Jennings, G. K. K. (2017) Dynamic Anion-Adaptive Poly(Ionic Liquid) Films via Surface-Initiated Ring-Opening Metathesis Polymerization. *The Journal of Physical Chemistry C*

[9] Israelachvili, J. *Academic, New York*, 3rd ed.; Academic Press, 2010; p 704.

[10] Hsu, C. H., and Mansfeld, F. (2001) Technical Note: Concerning the Conversion of the Constant Phase Element Parameter Y0 into a Capacitance. *Corrosion 57*, 747–748.

[11] Bard, A. J., and Faulkner, L. R. *Fundamentals and Applications*, 2nd ed.; John Wiley & Sons, Inc., 2001.

[12] Rumble, J. R., Ed. *Chemical Rubber Company handbook of chemistry and physics*, 98th ed.; CRC Press/Taylor & Francis: Boca Raton, Fla., 2018.

Chapter 7

SURFACE-INITIATED RING-OPENING METATHESIS POLYMERIZATION OF DICYCLOPENTADIENE FROM THE VAPOR PHASE

Introduction

In this chapter, I report the preparation of surface-immobilized pDCPD films on gold and silicon substrates by the surface-initiated ring-opening metathesis polymerization (SI-ROMP) of dicyclopentadiene (DCPD) from the vapor phase and compare it to that in the liquid phase by the characterization of polymerization kinetics, pDCPD film composition, barrier properties, and mechanical properties. SIPs that utilize monomer in the vapor phase allow for a reduction in the consumption of solvent, energy, and monomer and ensure a more environmentally sustainable polymerization process.[1] During ROMP, secondary metathesis reactions such as intermolecular chain-transfer may occur, where one polymer chain containing an active metal alkylidene on its terminus can react with any olefin along the backbone of a different polymer chain, maintaining the total number of polymer chains but increasing or decreasing the molecular weights of the individual polymers accordingly.[2,3] Introduction of the monomer in the vapor phase allows not only for the elimination of the need to find an optimal solvent to solubilize both the monomer and the growing polymer chains, but also reduces polymer chain mobility at the vapor/solid interface, minimizing the occurrence of unwanted secondary metathesis reactions.[1,4]

Here, I report the tunable growth of surface-bound pDCPD from the vapor phase. The polymerization of DCPD in the vapor phase is governed by the vapor pressure of DCPD in the polymerization setup. I describe a unique method to control the concentration of DCPD in the vapor phase thereby tuning the resulting polymer film

thickness. By utilizing an inert additive during polymerization, I have shown fine control of the pDPCD film thickness from 0 to 400 nm. The ability to tune the pDCPD film thickness in this manner allows the preparation of thin pDCPD films that are difficult to prepare due to the rapid polymerization kinetics of DCPD.

The first successful instance of SIP employing the introduction of monomer in the vapor phase was reported by Fu et al.[1] The authors performed SI-ROMP, surface-initiated cationic living polymerization, and surface-initiated oxidative polymerization to achieve micro-contact printed polymeric thin films. In the case of SI-ROMP, the authors utilized a physisorption process to anchor the ROMP catalyst on the surface. However, deposition methods based on physisoprtion give rise to weak interactions that undermine the adhesion between the film and the solid surface.[5,6] Fu et al.[1] were able to achieve polynorbornene (pNB) films that exhibited a maximum growth rate of 4 μm/h by SI-ROMP of norbornene (NB) using catalyst **1** (Scheme 2.3). pNB films polymerized utilizing monomer in the vapor phase have also been achieved using micro-contact printing and physisorption of catalyst **1** at room temperature and pressure by Gu et al.[7] The authors were able to observe a maximum thickness of 18 μm for pNB films polymerized for 4 h, with a loss of thickness for films grown for longer than 4 h.[7]

The majority of studies on surface functionalization using ROMP have been limited to norbornene (NB) and its derivatives due to NB's superior reactivity and ease of derivatization.[8] The ROMP reaction is driven from monomer to polymer by the release of cyclic olefin strain ("ring strain") balanced by entropic penalties.[2] I have calculated the strain energy of DCPD to be 26.7 kcal/mol, which is similar to that of NB (27.2 kcal/mol).[9] Volatile cyclic monomers such as cylooctateraene (COT) have been considered for SIP of monomer in the vapor phase. Gu et al.[10] reported the first polymerization of COT in the vapor phase by micro-contact printing and physisorption of catalyst **2** (Scheme 2.3) to prepare highly oriented polyacetylene films. Feng

et al.[4] and Lerum and Chen[8] utilized covalently bound catalyst **2** and explored the SI-ROMP of volatile cyclic monomers in the vapor phase. Surface-tethered films of pDCPD prepared by the SI-ROMP of DCPD from the vapor phase and employing micro-contact printing and physisorption of catalyst **2** were reported by Fu et al.[1] The authors, however, did not report any pDCPD film growth kinetics nor characterize the pDCPD film properties. To advance pDCPD films toward applications, a thorough understanding of their growth kinetics, composition, and properties is needed.

I investigate the utility of three catalysts (Scheme 2.3) for the SI-ROMP of DCPD, all known for a high tolerance toward air, moisture, and functional groups.[11–13] Catalyst **1** was the first commercially available ruthenium-based catalyst, which enabled its widespread use for a variety of applications ranging from the synthesis of pharmaceutical intermediates to the production of a variety of polymer composites.[11,12] Catalyst **2** exhibits high rates of ROMP for low-strain substrates and can even accomplish the ROMP of sterically hindered substrates.[3,11,12,14,15] The activity of **2** is improved at elevated temperatures ($\geq 50\,^{\circ}\mathrm{C}$) due to an increased rate of initiation.[3,13] Catalyst **3** initiates ROMP at least six orders of magnitude faster than **2**.[16,17] The rapid initiation of catalyst **3** has enabled the production of polymers with very narrow polydispersity and block copolymers.[16] Catalyst **3** has been utilized in the preparation of highly cross-linked thermoset nanocomposites by the SI-ROMP of DCPD from the surface of clay-based composites using monomer in the liquid phase.[18]

I have characterized the material properties of the surface-anchored pDCPD films, including composition, surface wettability, barrier properties to aqueous ion transport, and stiffness. I report the first characterization of pDCPD films as barrier coatings by the use of electrochemical impedance spectroscopy (EIS). The barrier properties of surface-tethered hydrocarbon films have been extensively studied and the films show excellent resistance to water and ion transport.[19–23] The highly cross-linked nature of the pDCPD films should enable these films to exhibit comparable performance as

barrier coatings. The mechanical properties of the pDCPD films were investigated by the use of PeakForce Quantitative Nanomechanical Mapping (QNM) to obtain the reduced Young's modulus (E_r) of the films. The study of the mechanical properties of soft materials such as thin polymer films is of increasing interest due to their widespread use in modern technologies.[24,25] Indentation is a versatile method for studying local mechanical properties of materials and covers dimensions ranging form the nanoscale to the macroscale.[24,25] Probe indentation, by either nanoindenters or atomic force microscopy (AFM), are the two major techniques available that allow for the collection of force-indentation curves.[25] However, AFM is more preferable when studying soft materials due to its ability to apply smaller forces and therefore, produce smaller deformations compared to nanoindenters.[25] PeakForce QNM is a recently introduced AFM mode that allows for the mapping of the elastic modulus of a sample surface with high spatial resolution at the same rate as regular tapping-mode AFM imaging by the real time calculation of Young's modulus at each surface contact via a fit of the Derjaguin-Muller-Toporov (DMT) model to force-indentation curves.[25,26] Young et al.[26] compared the E_r obtained by PeakForce QNM for polymer films to those obtained via nanoindentation techniques and showed that the technique provided repeatable measurements of polymer elastic moduli when careful calibration procedures were utilized. Here I report the first characterization of pDCPD film elastic modulus by PeakForce QNM.

Experimental Methods

Polymerization

Polymerization was accomplished either in the solution or the vapor phase. For solution-phase polymerization, the ROMP-active substrates were quickly rinsed with DCE and immediately placed in a monomer solution of dicyclopentadiene in DCE for up to 15 min. The substrates were subsequently rinsed with DCM, ethanol, water,

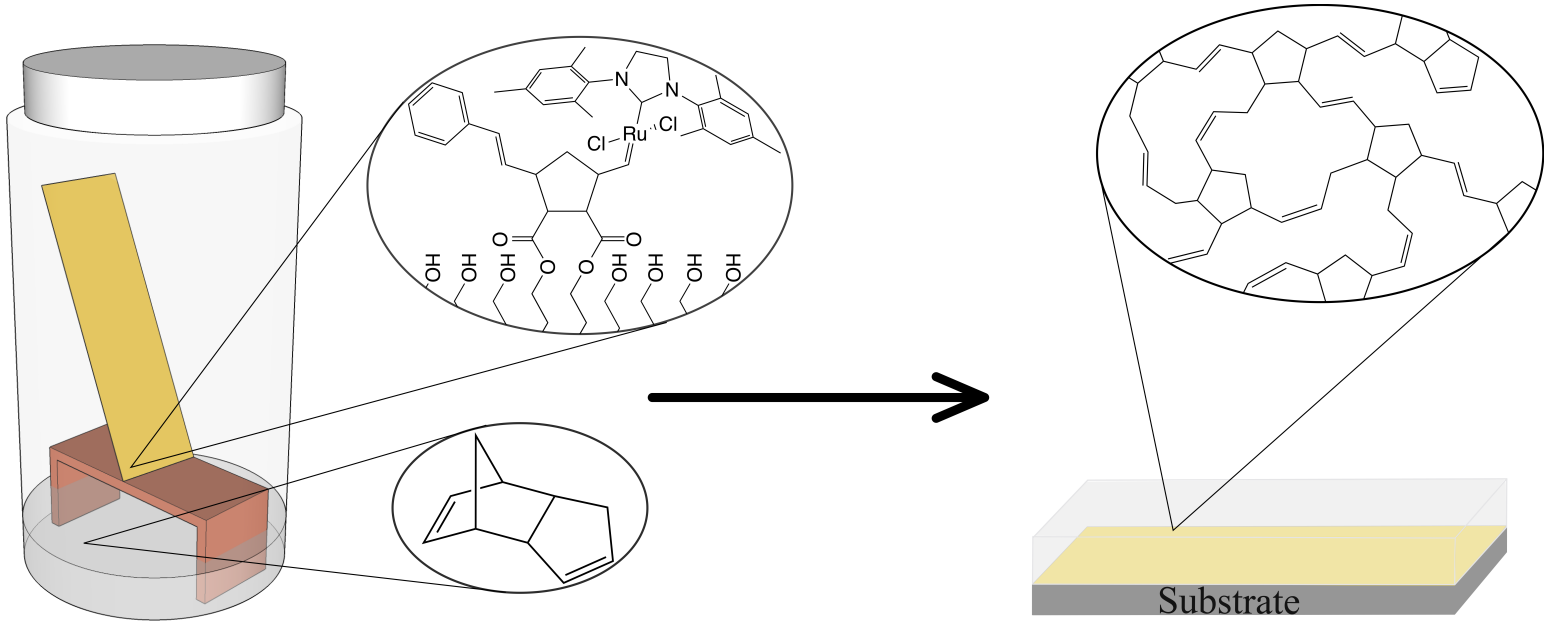

Scheme 7.1: Reaction scheme for the SI-ROMP of DCPD from the vapor phase. ROMP-active substrates, modified with catalyst **2** or **3**, were added to the reaction vial consisting of a 20 mL scintillation vial, equipped with a copper stage and filled with $\geq$ 2.0 g of DCPD monomer. The neat DCPD monomer was heated to and maintained at 55 °C for the duration of the polymerization.

and ethanol and dried in a stream of nitrogen.

For vapor-phase polymerization, the ROMP-active substrates were quickly rinsed with DCM, dried in a stream of nitrogen, and immediately placed in a pre-heated (55 °C) reaction vial containing a shallow pool of DCPD and a sample stage extending into the vapor space as shown in Scheme 7.1 for up to 15 min. The substrates were subsequently rinsed with DCM, ethanol, water, and ethanol and dried in a stream of nitrogen.

Determination of Polydicyclopentadiene Vapor Pressure: US Coast Guard Data

The US Coast Guard reports data on the saturated vapor density of dicyclopentadiene in their Chemical Hazard Response Information (CHRIS).[27]

Saturated Vapor Pressure - The value is the pressure (in pounds per square inch absolute) of the vapor in equilibrium with the liquid form at the specified temperature. Vapor pressure values can be used to estimate the relative volatility of chemicals at a given temperature, and to calculate the pressure over a liquid that is shipped in a closed container. The vapor pressure increases as temperature increases; a table is given to show this effect. Note that the vapor pressure scale is logarithmic.

Saturated Vapor Density - The value is the weight (in pounds) of one cubic foot of vapor that is in equilibrium with the liquid form. If it is assumed that the vapor behaves as an ideal gas, the relation $\frac{\mathrm{pM}}{\mathrm{RT}}$ holds, where p is the vapor pressure, M is the molecular weight, R is the gas constant, and T is the temperature (in absolute units). Since the vapor pressure varies with temperature, the saturated vapor density also varies with temperature, as shown on the table.

The saturated vapor density reported for dicyclopentadiene at 130 °F (54.44 °C) is 0.00728 lbs/ft^3. This value can be converted to an effective molar concentration C_{vap} in the vapor phase by

$$\mathrm{C}_{vap} = \left(\frac{0.00728 \, \frac{\mathrm{lb}}{\mathrm{ft}^3} \times 453.5924 \, \frac{\mathrm{g}}{\mathrm{lb}}}{28.31685 \, \frac{\mathrm{L}}{\mathrm{ft}^3} \times 132.31 \, \frac{\mathrm{g}}{\mathrm{mol}}} \right) = 8.82 \times 10^{-4} \, \mathrm{M} = 0.882 \, \mathrm{mM} \tag{7.1}$$

Determination of Polydicyclopentadiene Vapor Pressure: Vapor Pressure Determination

Burchfield[28] reports the following constants for the Clausius Clapeyron equation (eq 7.2) for estimating the vapor pressure of dicyclopentadiene between 40.1 and 90.8°C: A = 7.925; B = −2218. At 55°C, the vapor pressure is given by

$$\log_{10} p^*(\text{mm Hg}) = -\frac{\Delta \hat{H}_{\mathrm{v}}}{RT} + A = \left(\frac{B}{T} \right) + A \tag{7.2}$$

$$p^* = 10^{\left(\frac{-2218 \, \mathrm{K}}{328 \, \mathrm{K}} \right) + 7.925} = 14.55 \, \text{mm Hg} \tag{7.3}$$

Assuming ideal gas behavior, the effective molar concentration in the vapor phase can be calculated by

$$\mathrm{C}_{vap} = \frac{n}{V} = \frac{p^*}{RT} = \left(\frac{14.55 \, \text{mm Hg}}{62.36 \, \frac{\mathrm{L \cdot mm \ Hg}}{\mathrm{mol \cdot K}} \times 328 \, \mathrm{K}} \right) = 7.11 \times 10^{-4} \, \mathrm{M} = 0.711 \, \mathrm{mM} \tag{7.4}$$

Results and Discussion

Initial attempts at the SI-ROMP of DCPD using catalyst **2** on gold substrates were conducted in neat DCPD with the observation that pDCPD films grew to 20x greater thickness for the part of the ROMP-active substrate exposed to the vapor phase than that exposed to neat liquid DCPD. The ROMP-active gold substrates exposed to neat liquid DCPD exhibited film thickness that were ≤ 30 nm. Figure 7.1 shows the PM-IRRAS of a pDCPD polymer film polymerized with monomer from the vapor phase. The IR spectrum confirms the presence of a pDCPD polymer film with

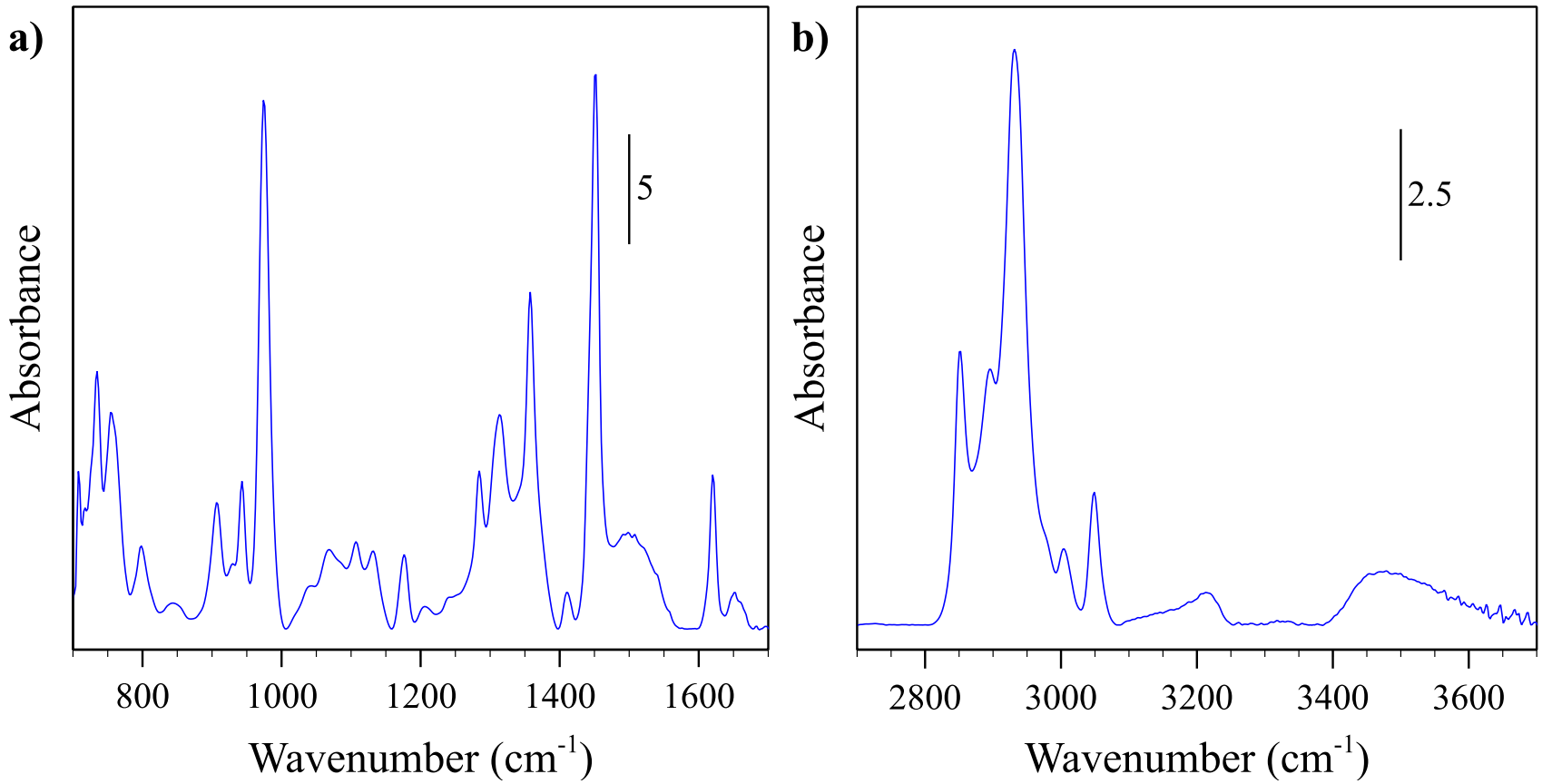

Figure 7.1: Polarization modulation-infrared reflectance-absorption spectrum of a pDCPD film polymerized using DCPD monomer from the vapor phase (see Scheme 7.1). The polymerization was conducted at 55 °C using catalyst **2** on a gold substrate for 15 min.

the same characteristic bands as that for pDCPD prepared by ROMP in solution[29] as well as polymer films prepared by SI-ROMP with monomer in the solution phase (Figure 7.2).

Figure 7.2 shows the polarization modulation-infrared reflection-absorption spectra (PM-IRRAS) of the vapor and solution pDCPD polymer films. The infrared (IR) spectra show a strong absorption band for the $C_{sp^2}-H$ stretch vibration at 3049 cm^{-1}, a weaker $C_{sp^2}-H$ stretch vibration absorption band at 3006 cm^{-1}, a strong absorption band for the methylene $C_{sp^3}-H$ asymmetric stretch vibration (ν_{as} CH_2) at 2933 cm^{-1}, a weaker absorption band for $C_{sp^3}-H$ stretch vibration (CH) at 2896 cm^{-1} and a strong absorption band for the methylene $C_{sp^3}-H$ symmetric stretch vibration (ν_s CH_2) at 2851 cm^{-1}.[29,30] The $C_{sp^2}-H$ absorption bands are smaller than the $C_{sp^3}-H$ peaks as expected from the cross-linked composition of the pDCPD polymer film.[29]

The IR spectra also show a C=C stretching absorption band at 1620 cm^{-1}, a $C_{sp^3}-H$ in-plane bending (scissoring) absorption band (δ_s CH_2) at 1453 cm^{-1}, a $C_{sp^2}-H$ in-plane bending (scissoring) absorption band (δ_s $=CH_2$) at 1408 cm^{-1}, multiple $C_{sp^3}-H$ out-of-plane bending (wagging and twisting) absorption bands (ω, τ CH_2) in the region $1350-1150$ cm^{-1}, multiple $C_{sp^2}-H$ out-of-plane bending absorption bands in the region $1000-650$ cm^{-1} and a $C_{sp^3}-H$ in-plane bending (rocking) absorption band (δ_s CH_2) at 730 cm^{-1}.[30]

Rule and Moore[31] have previously shown the *exo* isomer of DCPD to be more than an order of magnitude more reactive than the *endo* isomer for pDCPD prepared by ROMP in solution. The *endo* isomer is the majority (98%) isomer in commercially available DCPD. Monomer containing a majority (81%) of the *exo* isomer of DCPD was obtained from the *endo* isomer by following the procedure described by Nelson and Kuo.[32] There were no significant differences in pDCPD film thickness for films prepared by SI-ROMP of either *exo*-DCPD or *endo*-DCPD from the vapor phase using catalyst **2** on gold substrates.

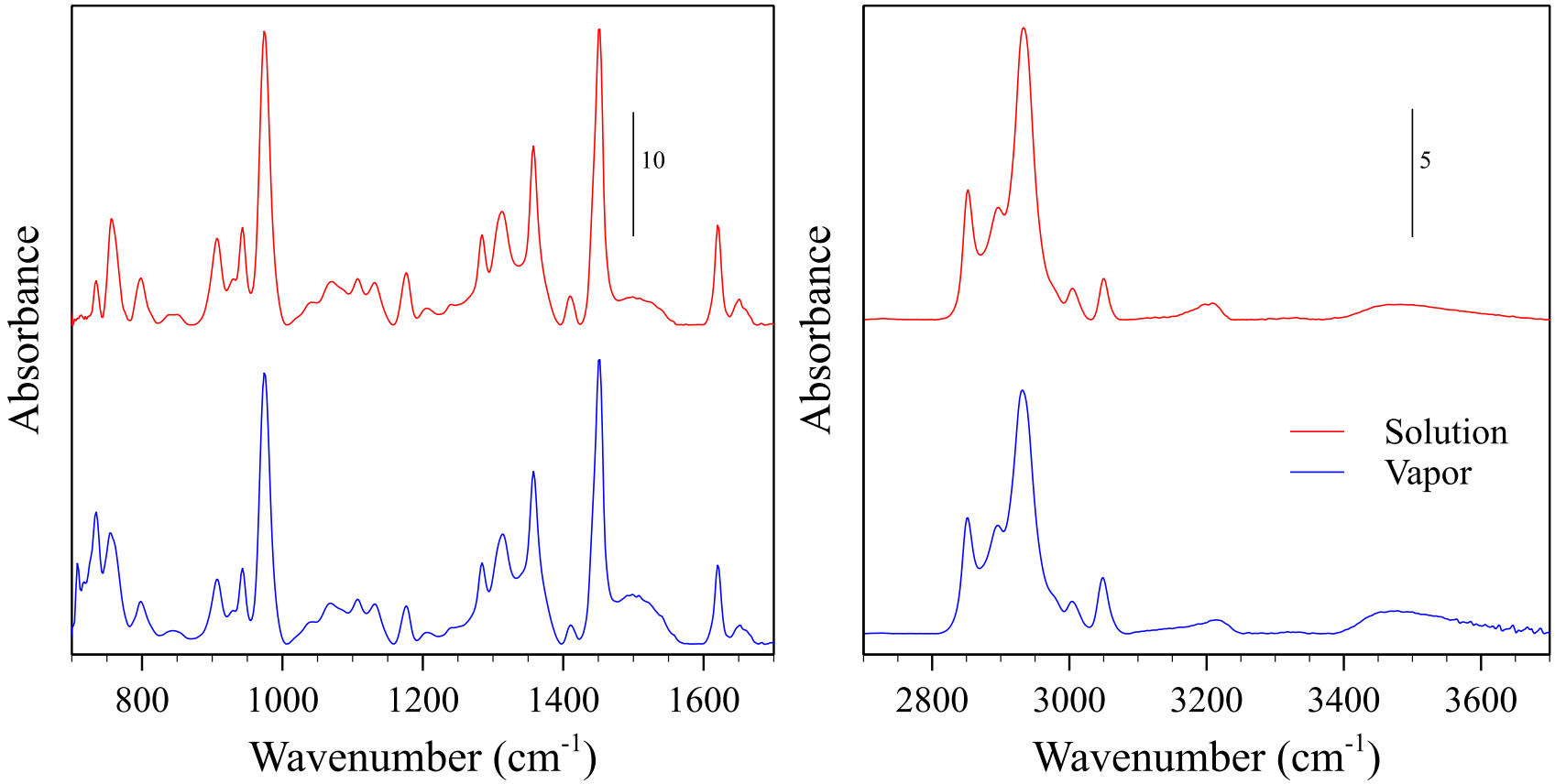

Figure 7.2: Polarization modulation-infrared reflectance-absorption spectrum of pDCPD films polymerized with monomer from the vapor phase and the solution phase. The films were polymerized using catalyst **2** on a gold substrate for 15 min. The polymer films prepared by SI-ROMP in a 0.75M DCPD in DCE solution exhibited similar thicknesses to polymer films prepared by SI-ROMP with monomer from the vapor phase

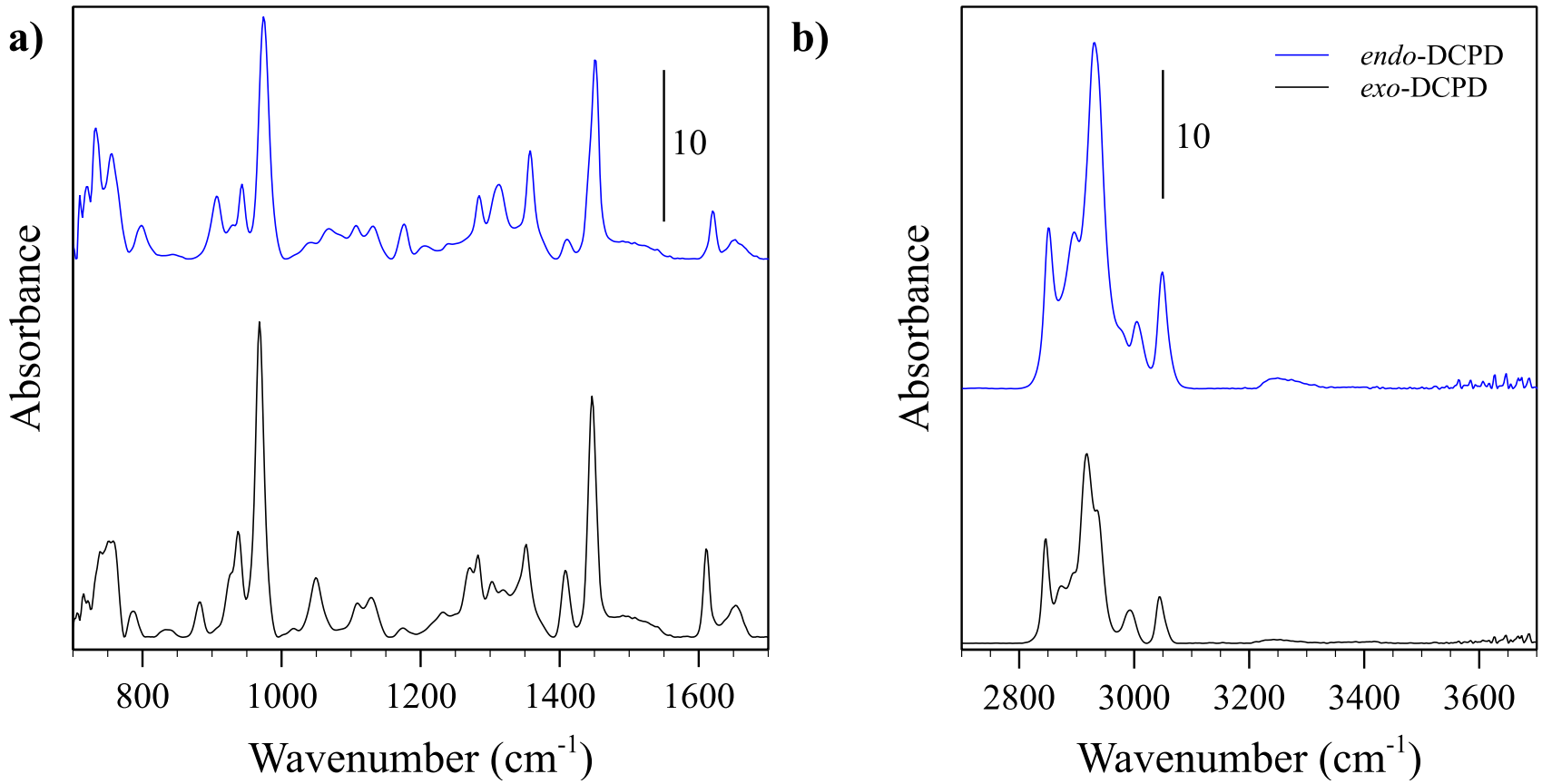

Figure 7.3: Polarization modulation-infrared reflectance-absorption spectrum of pDCPD films polymerized with monomer from the vapor phase with either the *exo* or *endo* DCPD isomer. The films were polymerized using catalyst **2** on a gold substrate for 15 min.

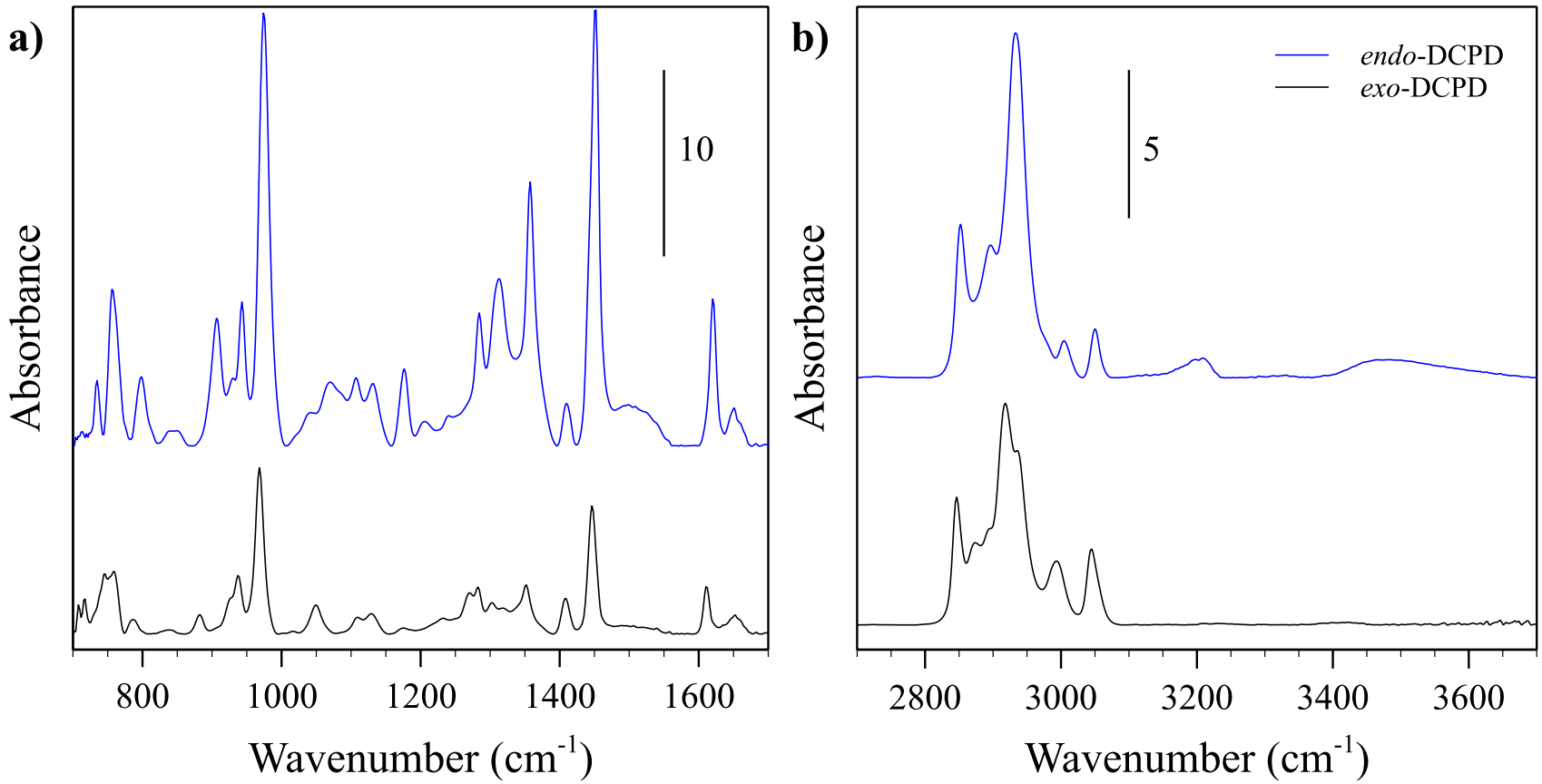

Figure 7.4: Polarization modulation-infrared reflectance-absorption spectrum of pDCPD films polymerized with monomer from the solution phase with either the *exo* or *endo* DCPD isomer. The films were polymerized using catalyst **2** on a gold substrate for 15 min.

Figure 7.3 shows the PM-IRRAS of the pDCPD polymer films polymerized with monomer in the vapor phase with either the *exo* or *endo* DCPD isomer. Figure 7.4 shows the PM-IRRAS of the pDCPD polymer films polymerized with monomer in the vapor phase with either the *exo* or *endo* DCPD Isomer. The IR spectra (Figures 7.3 and 7.4) of pDCPD polymer films polymerized from the monomer with majority *exo* isomer showed the same characteristic bands as that of pDCPD polymer films polymerized from the monomer with the majority *endo* isomer. Further investigations were conducted with the commercially obtained DCPD unless otherwise noted.

DCPD Surface-Initiated Polymerization

Film Growth Kinetics

SI-ROMP of DCPD from the vapor phase (see Scheme 7.1) using catalyst **2** on gold substrates led to pDCPD films exhibiting thicknesses $\geq$ 400 nm for polymerization times as short as 1 min with no significant change in pDCPD film thickness observed for films with greater polymerization times as shown in Figure 7.5. A kinetic model developed for the study of SI-ROMP kinetics by Harada et al.[33] and previously modified by us[5,20] was used to quantify the rate constants for propagation and termination in the growth of the pDCPD films. In the model, the change in film thickness as a function of time is given as

$$d = \left(\frac{KMm_0}{k_t\rho}\right)\left(1 - e^{-k_t t}\right) \tag{7.5}$$

where K is a rate constant that expresses both the initiation and propagation of film growth, M is the concentration of monomer in solution, k_t is the termination rate constant, m_0 is the mass of a monomer unit, and ρ is the density of the polymer. The maximum monomer concentration in the vapor phase of the polymerization vial was calculated to be 0.8 ± 0.1 mM (see Supporting Information).[27,28] The density of

Table 7.1: Propagation (K) and Termination (k_t) Rate Constants for the SI-ROMP of DCPD Utilizing Monomer in the Vapor Phase versus a 0.75 M Solution of Alumina-Filtered DCPD in DCE.

Monomer Phase	K ($m \cdot s^{-1}$)	k_t (s^{-1})
Vapor	$1.5 \times 10^{-4} \pm 0.5 \times 10^{-4}$	0.04 ± 0.01
Liquid	$4 \times 10^{-7} \pm 2 \times 10^{-7}$	0.10 ± 0.05

the polymer film was approximated to be that of the monomer ($0.98\,g \cdot cm^{-3}$).[27] The values of the rate constants obtained by a fit of the experimental data with Equation 7.5 are shown in Table 7.1.

The polymerization of neat DCPD in the liquid phase using catalyst **2** on gold substrates results in pDCPD film thicknesses of 22±3 nm as measured by ellipsometry. DCPD is known to react with air over time to form peroxides that accelerate the decomposition of metathesis catalysts and decrease the efficiency of the reaction.[34] The peroxide impurities may be removed by running the monomer solution through a column of activated, basic, Brockmann I aluminum oxide. Figure 7.6 (a) shows the concentration dependence of pDCPD thickness for films grown with both filtered and unfiltered DCPD solutions in DCE using catalyst **2** on gold substrates. Employing filtered monomer yields a dramatic increase in polymer thickness as compared to unfiltered monomer. Figure 7.6 (b) shows the growth kinetics of pDCPD grown from 0.75 M solutions of alumina-filtered DCPD in DCE at room temperature using catalyst **2** on gold substrates. The monomer exhibits rapid kinetics with no significant change in pDCPD film thickness observed for films with polymerization times greater than 30 s.

DCPD concentrations of 0.75 M in DCE were required to achieve polymer film thicknesses comparable to those obtained in the vapor phase. This level of concentra-

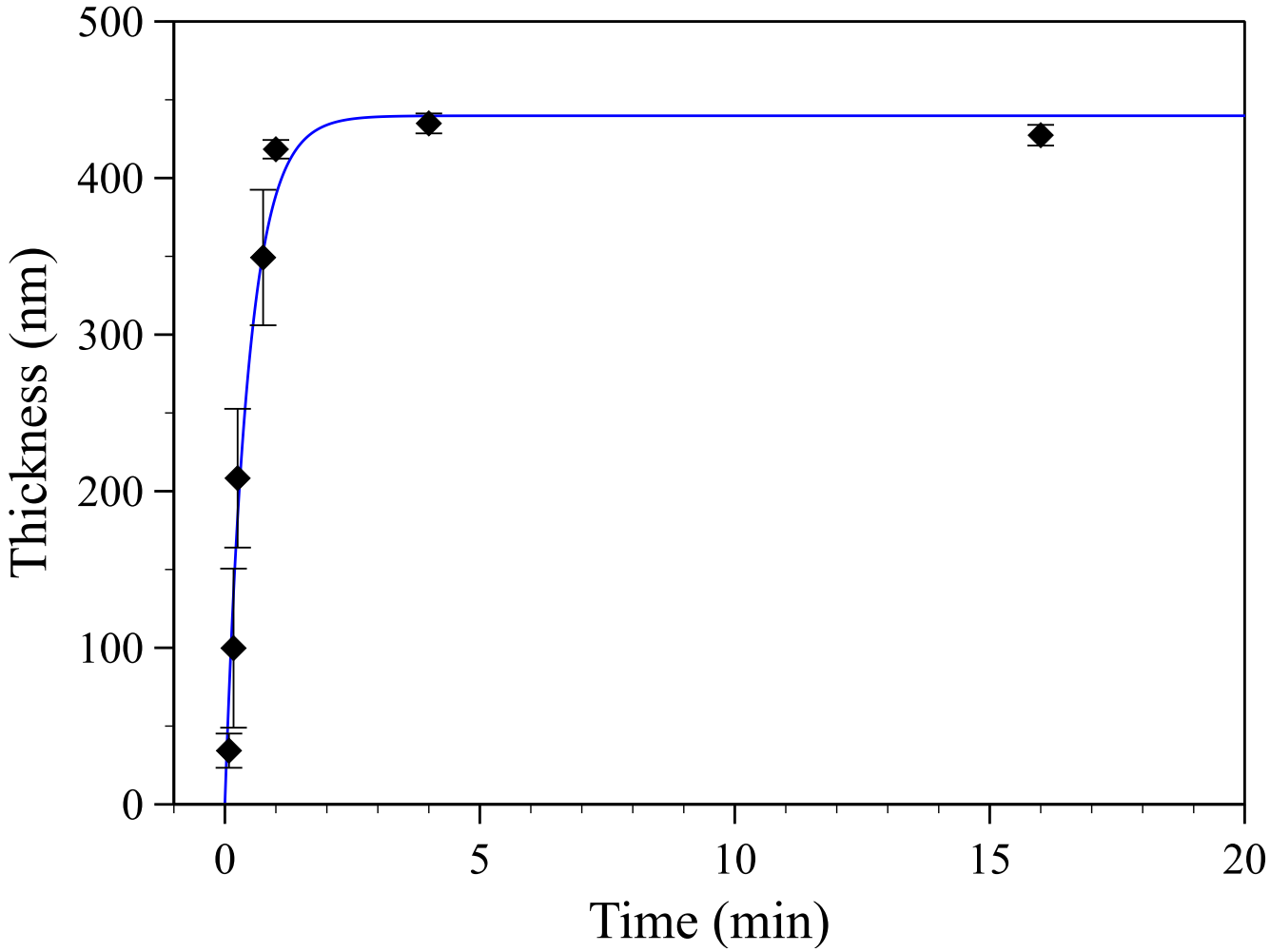

Figure 7.5: Effect of polymerization time on the profilometric thickness of pDCPD films polymerized using DCPD monomer from the vapor phase (See Scheme 7.1). The polymerizations were conducted at 55 °C using catalyst **2** on gold substrates. The solid curve represents a fit of the data with eq 7.5.

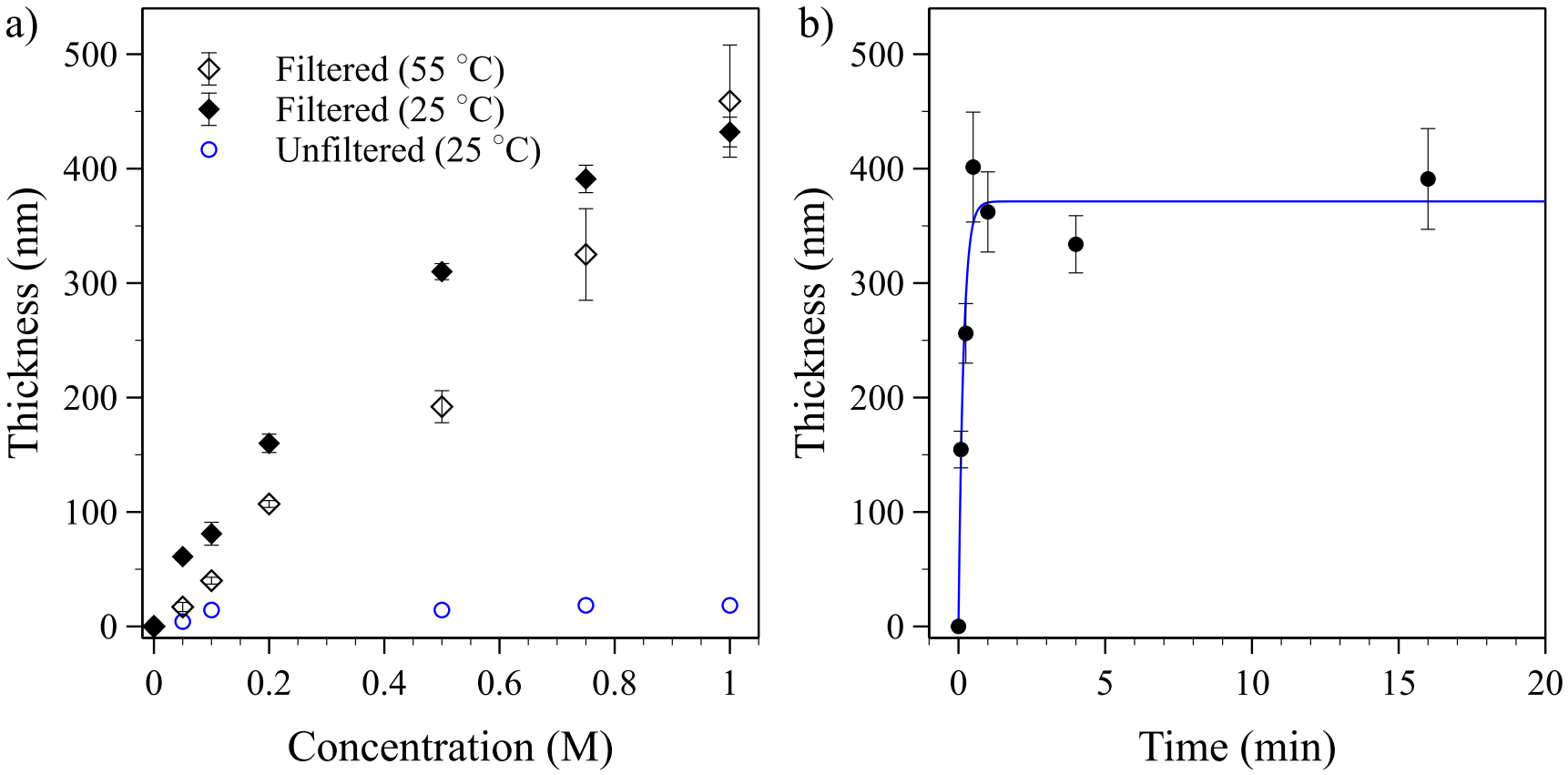

Figure 7.6: Thickness of pDCPD films grown with monomer in the solution phase. a) Concentration dependence of profilometric thickness of pDCPD films polymerized using alumina-filtered DCPD solutions, and ellipsometric thickness of pDCPD films polymerized using unfiltered DCPD solutions. The films were grown with catalyst **2** for 15 min on gold substrates. b) pDCPD film growth kinetics. The films were grown from 0.75 M solutions of alumina-filtered DCPD in DCE using catalyst **2** on gold substrates. Solid curve represents a fit of the data with eq 7.5.

tion represents a 3 order of magnitude increase over that utilized in the vapor phase as detailed above. The values of the rate constants obtained by a fit of the experimental data with Equation 7.5 are shown in Table 7.1. Polymerization of DCPD from the vapor phase exhibits K values, reflecting both the rates of initiation and propagation, that are 2.5 orders of magnitude greater than those from the liquid phase that employ filtered monomer. The former process also exhibits a rate of termination that is 2.5 times lower than that observed in the latter process. The enhanced polymerization kinetics for DCPD monomer from the vapor phase can be attributed to both an increase in the rate of propagation as well as a decreased rate of termination due to the reduction of intermolecular chain-transfer inherent in polymerizations conducted at a vapor/solid interface. To better compare the conditions for pDCPD growth in the vapor phase versus the solution phase we performed the liquid-phase polymerization at 55 °C (Figure 7.6 (a)). However, no additional benefit to the polymerization kinetics or film thickness was observed compared to polymerizations at room temperature, suggesting that the increased temperature in the vapor-phase polymerization does not lead to the enhanced rate of propagation observed.

The vapor-phase polymerization process for DCPD is robust enough to allow the utilization of monomer that contains impurities. In the vapor-phase process, the monomer is distilled and polymerized immediately, thereby avoiding the monomer purification step required in the solution-phase polymerization process. The vapor-phase process also allows for a reduction in monomer cost, since the unreacted monomer is reused in subsequent polymerizations without the worry of contamination from solution grown polymer due to secondary metathesis reactions. The vapor-phase process eliminates the need for solvent during the polymerization to enable a more environmentally conscious preparation of pDCPD films.

Film Thickness Tunability

The rapid kinetics of polymerization observed by the polymerization of DCPD from the vapor phase makes difficult the consistent preparation of surface-tethered pDCPD films that are less than 400 nm. The vapor concentration of DCPD is controllable by including an inert additive into the liquid monomer. Decane was chosen as the inert additive due to its chemical compatibility, chemical inertness, and a vapor pressure similar to the DCPD monomer. Decane was added to DCPD to control the DCPD molar concentration in the polymerization vial (see Scheme 7.1). Figure 7.7 shows the profilometric thickness of pDCPD films grown from the vapor phase for 15 min using catalyst **2** on gold substrates. The profilometric film thickness of pDCPD films grown from the vapor phase for DCPD monomer with decane shows a linear dependence on the molar fraction of DCPD in the liquid phase. The control of pDCPD film thickness afforded by the use of decane as an inert additive facilitates the employment of this process in applications that require films from tens of nanometers thick to hundreds of nanometers. This fine control in thickness adds to the versatility of the vapor-phase polymerization as a useful technique in the preparation of surface-tethered pDCPD films.

Pre-Polymerization Rinsate Solvent Film

While the polymerization of DCPD from the vapor phase allows for a reduction of intermolecular chain-transfer, we hypothesized that the presence of a thin film of solvent would enhance polymer growth by improved solvation of the propagating catalyst moiety and the growing polymer chains during SI-ROMP. I studied the effect of a rinsate solvent film at the initial stages of polymerization by rinsing the ROMP-active gold substrates with solvent prior to insertion into the polymerization vial (Table 7.2). The presence of solvent, in particular dichloromethane (DCM) and chloroform ($CHCl_3$), leads to an increase in film thickness when compared to a dry

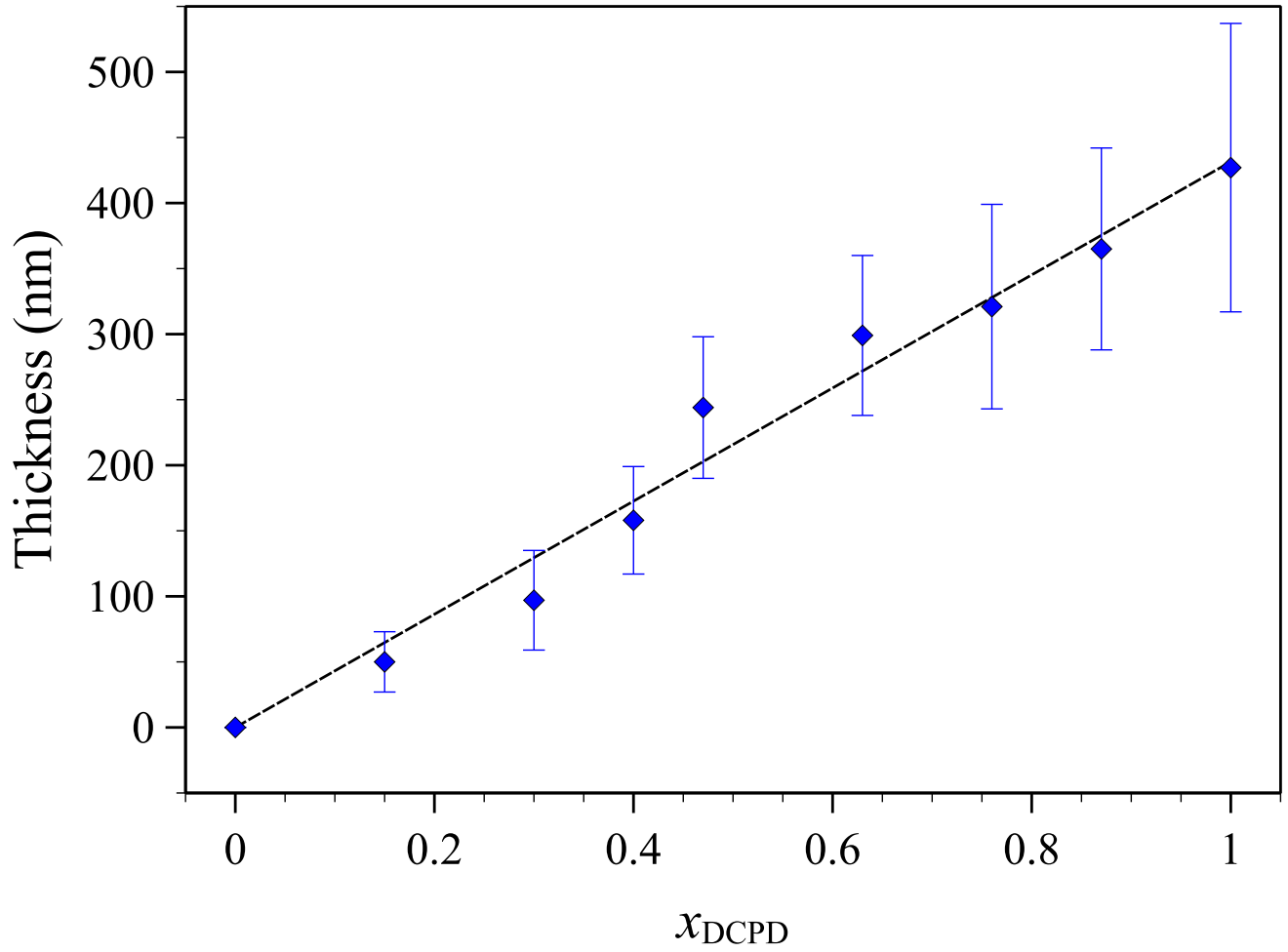

Figure 7.7: Effect of DCPD molar fraction on the profilometric thickness of pDCPD films polymerized using DCPD monomer from the vapor phase (See Scheme 7.1). The polymerizations were conducted at 55 °C using catalyst **2** on gold substrates with decane as an inert additive. The solid curve represents a linear fit of the data.

control. Bowden et al.[35] have investigated the ability of organic solvents to swell bulk pDCPD prepared by ROMP in solution. The authors employed a variety of solvents and reported the weight ratio of the swollen pDCPD slabs to their original weight after 24 h exposure to solvent. I utilized the density of the solvents to obtain the volume uptake of solvent into the pDCPD slabs from their reported ratios (Table 7.2).

$CHCl_3$ is able to swell pDCPD to a larger volume to weight ratio as compared to DCM. The improved growth observed with the $CHCl_3$ solvent film can be attributed to improved solvation of the growing polymer chains by $CHCl_3$. In addition, at the initial stages of the SI-ROMP of DCPD from the vapor phase, the solvent film evaporates from the surface while the monomer diffuses into the polymerizing film. Therefore, the presence of a less volatile solvent during polymerization should result in a smoother film. Of the solvents investigated toluene has the lowest volatility and exhibits the smoothest films albeit with no enhancement in film thickness over the dry control (Table 7.2). Sanford et al.,[36] have shown a 30% decrease in the initiation rate of catalyst **2** in toluene as compared to DCM, which explains the lack of an enhancement in pDCPD film thickness for a pre-polymerization film of toluene compared to the dry control, despite the ability of toluene to swell pDCPD to a larger extent as compared to either DCM or $CHCl_3$. Polymerization of DCPD from the vapor phase in the presence of a $CHCl_3$ film led to the thickest, smoothest films. However, the presence of solvent leads to an increased variability in film thickness and therefore, rinsing the ROMP-active gold substrates with DCM and drying in a stream of nitrogen was chosen as the preferred polymerization method due to the relatively smooth and consistent films.

The effect of performing the DCPD polymerization from the vapor phase in a nitrogen environment, with diminished moisture and oxygen concentrations was investigated (Table 7.2) due to the ability of oxygen and moisture to deactivate Catalyst

Table 7.2: Effect of a Pre-Polymerization Rinsate Solvent Film on the Profilometric Film Thickness and Roughness of pDCPD Films Polymerized With Monomer in the Vapor Phase Using Catalyst **2** on Gold Substrates.

Rinsate Solvent	pDCPD Swelling (ml/g pDCPD)[b]	Surface	Thickness (nm)	Roughness (nm)
Dichloromethane	1.85	Dry	416 ± 8	13 ± 1
Dichloromethane	1.85	Wet	531 ± 14	29 ± 14
Chloroform	2.27	Wet	613 ± 20	11 ± 2
1,2-Dichloroethane	-	Wet	408 ± 34	17 ± 9
Toluene	2.56	Wet	415 ± 12	10 ± 2
Dichloromethane [a]	1.85	Dry	377 ± 17	45 ± 29

[a]Sample polymerized in a nitrogen filled glove box. (1 Sample). [b] Ability of solvents to swell pDCPD prepared by ROMP in solution.[35]

2.[16] The catalyst attachment step utilized anhydrous DCM and the sample was dried by exposure to the nitrogen environment as opposed to drying in a stream of N_2. However, polymerization of DCPD from the vapor phase in a nitrogen environment did not confer an added advantage when compared to that performed in ambient conditions.

ROMP Catalyst

The effect of different ROMP catalysts on the polymerization of DCPD from the vapor phase was also investigated. Initiation of the ROMP catalyst occurs via the loss of a tricyclohexylphosphine ligand in the case of catalyst **1** and **2** and the loss of the bromo-pyridine ligands in the case of catalyst **3**.[17,37] Catalyst **2** has been shown to be more active than **1** for ROMP.[16] However, catalyst **2** does not initiate ROMP faster than **1** but has an improved selectivity for binding olefinic substrates in the presence of free phosphine and as such, exhibits higher ROMP activity than catalyst **1**.[11,14,37] Catalyst **3** has been shown to initiate ROMP at least six orders of magnitude faster than catalyst **2** by taking advantage of the lability of pyridine ligands.[16,17] Catalysts **2** and **3** both result in the same propagating species after initiation, thereby allowing catalyst **3** to retain the improved selectivity for binding olefinic substrates observed in catalyst **2**. Table 7.3 shows the effect of the polymerization catalyst on the pDCPD polymer film thickness and roughness for polymerizations performed using monomer from the vapor phase. Catalyst **3** produces films with greater thickness than **2**, consistent with the reported enhancement in initiation of **3** as compared to **2**. Catalyst **1** exhibits diminished pDCPD growth as compared to **2**, consistent with the superior ROMP activity of **2** compared to **1**.

The pDCPD films grown on the silicon substrate with catalyst **2** exhibit a five-fold decrease in film thickness as compared to those grown on the gold substrate. Polymerization of 5-(perfluoro-n-octyl)norbornene[5] on the silicon substrate utilizing catalyst

Table 7.3: Effect of ROMP Catalyst on the Profilometric Film Thickness and Roughness of pDCPD Films Polymerized Using Monomer in the Vapor Phase.

Substrate	Catalyst	Thickness (nm)	Roughness (nm)
Gold	**1**	40 ± 12	6 ± 4
Gold	**2**	416 ± 8	13 ± 1
Gold	**3**	576 ± 14	13 ± 4
Silicon	**2**	85 ± 6	10 ± 1
Silicon	**3**	513 ± 14	23 ± 3

2 similarly results in a five-fold decrease in film thickness compared to films grown on gold substrates. The reduction in film thickness is attributed to the differences in the catalyst tethering approach for the different substrates. For the gold substrates, the initiator/catalyst is immobilized by a surface-tethered norbornenyl group that is the acylation product of NBDAC with a hydroxyl-terminated SAM,[19] leading to a lower surface coverage of norbornene functional groups due to a less efficient two-step attachment process. In the case of the silicon substrate, a high surface coverage is achieved by the formation of a SAM from $NBSiCl_3$. Due to the high local concentration of polymer chains resulting from a high surface coverage of initiator, the effect of secondary metathesis reactions is enhanced compared to bulk polymerization.[38] Catalyst **3** is not significantly impacted by a high coverage of surface-tethered monolayers of allylic groups as evidenced by the lack of a significant change in film thickness when polymerizing on silicon versus gold substrates. I conclude that the rapid initiation kinetics of catalyst **3** allows it to exhibit similar SI-ROMP growth with both the high and low surface coverages of surface-tethered monolayers of allylic groups.

Polymer Film Properties

The polymerization of DCPD monomer from the vapor phase confers several advantages over the solvent phase polymerization in terms of a reduction in volatile organic components, reduction in reagent cost due the reusability of the unreacted monomer, tunability of the pDCPD film thickness, and the easy preparation of smoother films. In order to fully understand the advantages of the vapor-phase process, we compared the properties of pDCPD films grown from the vapor-phase with those grown from the solution phase.

Electrochemical Impedance Spectroscopy (EIS)

The barrier properties of the pDCPD films to ion transport was investigated by utilizing electrochemical impedance spectroscopy (EIS) in the presence of a 1 mM $K_3Fe(CN)_6$, 1 mM $K_4Fe(CN)_6 \cdot 3\,H_2O$, and 0.1 M Na_2SO_4 aqueous solution. Representative Bode magnitude plots for ∼400 nm pDCPD films grown from both the vapor and liquid phase on gold substrates using catalyst **2**, as well as a control film consisting of a hydroxyl-terminated SAM exposed to NBDAC, are shown in Figure 4.6. The presence of the polymer provides impedances that are 3 - 4 orders of magnitude greater than those of the control, revealing that the pDCPD films provide effective barriers to water and ion transport. The impedance spectra were fit with the equivalent circuit model shown in Scheme 3.4. The spectrum for both the vapor and solution pDCPD films shows a capacitive region at intermediate to high frequencies and a resistance against the penetration of redox species at low frequencies. The impedance at low frequency, which is due to the interfacial charge transfer resistance, improves by 3 orders of magnitude with the growth of the pDCPD films as compared to the control film. The vapor and solution pDCPD films exhibit similar capacitances of 7.9×10^{-9} F/cm^2 and 8.8×10^{-9} F/cm^2, and similar charge transfer resistances of $4.3 \times 10^6\ \Omega \cdot \text{cm}^2$ and $8.2 \times 10^6\ \Omega \cdot \text{cm}^2$, respectively. Phase angle plots of EIS spectra

Table 7.4: Advancing and Receding Water Contact Angles for pDCPD Films polymerized with Catalyst **2** for 15 min Utilizing Monomer in the Specified Phase on Gold Substrates.

	H_2O	
Monomer Phase	θ_A (°)	θ_R (°)
Vapor	86 ± 2	66 ± 3
Solution	83 ± 4	57 ± 3

corresponding to the Bode plots shown in Figure 7.8 for pDCPD films grown from either the solution or the vapor phase are shown in Figure 7.9.

Contact Angle

The surface wettability of the pDCPD films was assessed by contact angle goniometry as shown in Table 7.4. The measured advancing (θ_A) water contact angle for the vapor ($86° \pm 2°$) and solution ($83° \pm 4°$) pDCPD films are similar to the reported value of bulk pDCPD ($78° \pm 2°$).[39] The profilometric roughness for the pDCPD films polymerized from the vapor phase using catalyst **2** is 13 ± 1 nm (Table 7.2) and that for films polymerized from alumina-filtered solutions of DCPD in DCE using catalyst **2** is 33 ± 3 nm. The lower θ_A and θ_R exhibited by the solution-phase polymerized pDCPD films are attributed to the increased profilometric roughness.

PeakForce Quantitative Nanomechanical Mapping (QNM)

The mechanical properties of the pDCPD films were elucidated by utilizing PeakForce QNM to obtain the reduced Young's modulus (E_r) of the surface-tethered films as shown in Table 7.5. The accuracy of the measured material properties is highly correlated to the mechanical properties and geometry of the AFM probe cantilever and

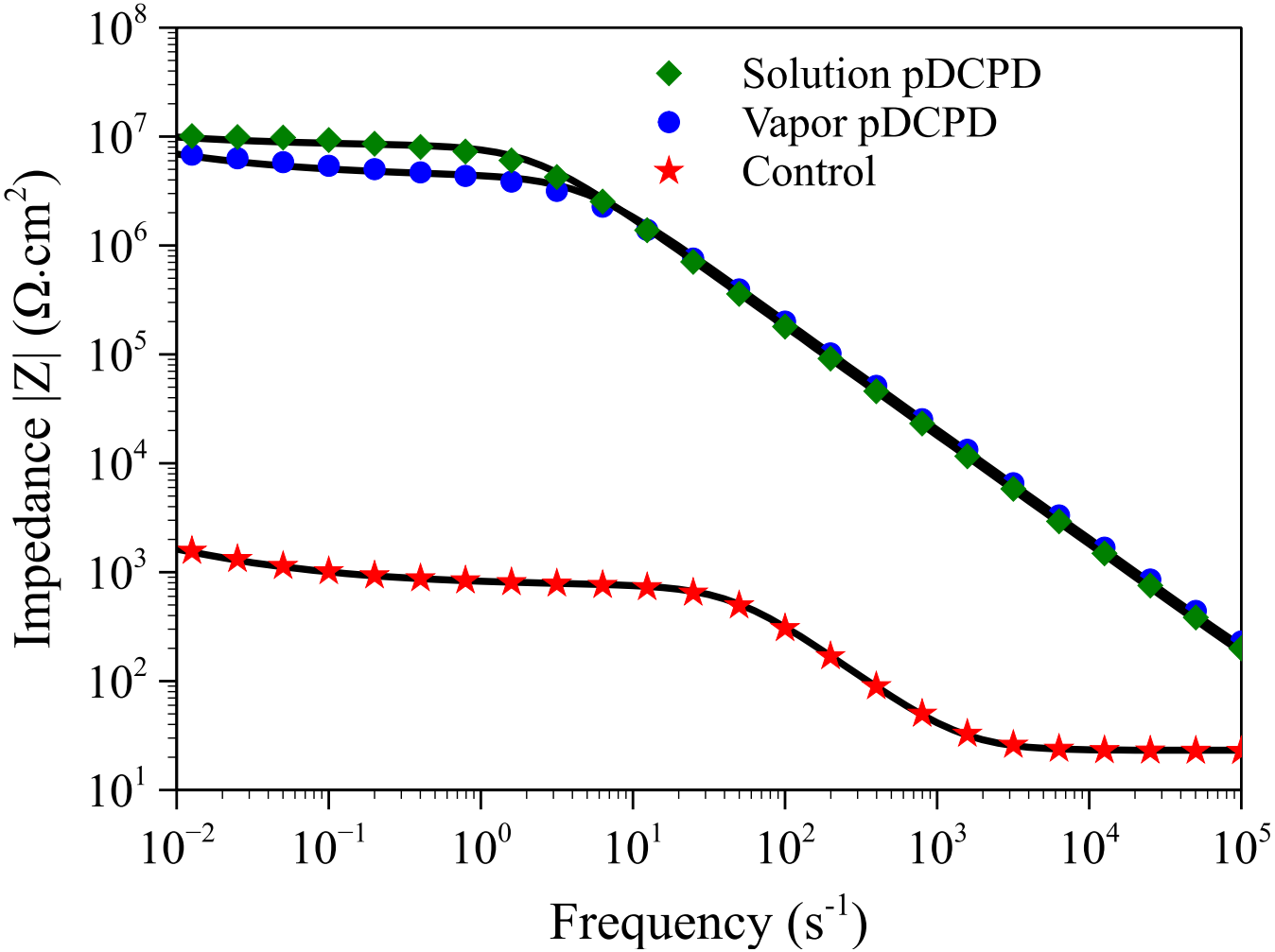

Figure 7.8: EIS of $\sim$ 400 nm pDCPD films grown from either the solution or the vapor phase, acquired in a 1 mM $K_3Fe(CN)_6$, 1 mM $K_4Fe(CN)_6 \cdot 3\,H_2O$, and 0.1 M Na_2SO_4 aqueous solution. The pDCPD films were grown with catalyst **2** for 15 min on gold substrates. The solid curve represents fits to a Randle's equivalent circuit modified with a Warburg impedance term. The charge transfer resistance obtained from a fit of the data for the solution pDCPD film is 8.2 $M\Omega \cdot cm^2$, whereas the resistance for the vapor pDCPD film is 4.3 $M\Omega \cdot cm^2$. The capacitance obtained from a fit of the data for the solution pDCPD film is 8.8 nF/cm^2, while the capacitance for the vapor pDCPD film is 7.9 nF/cm^2. The solution pDCPD film was grown from a 0.75 M alumina-filtered DCPD solution in DCE. The vapor pDCPD film was polymerized at 55 °C employing the drying method presented in Scheme 7.1.

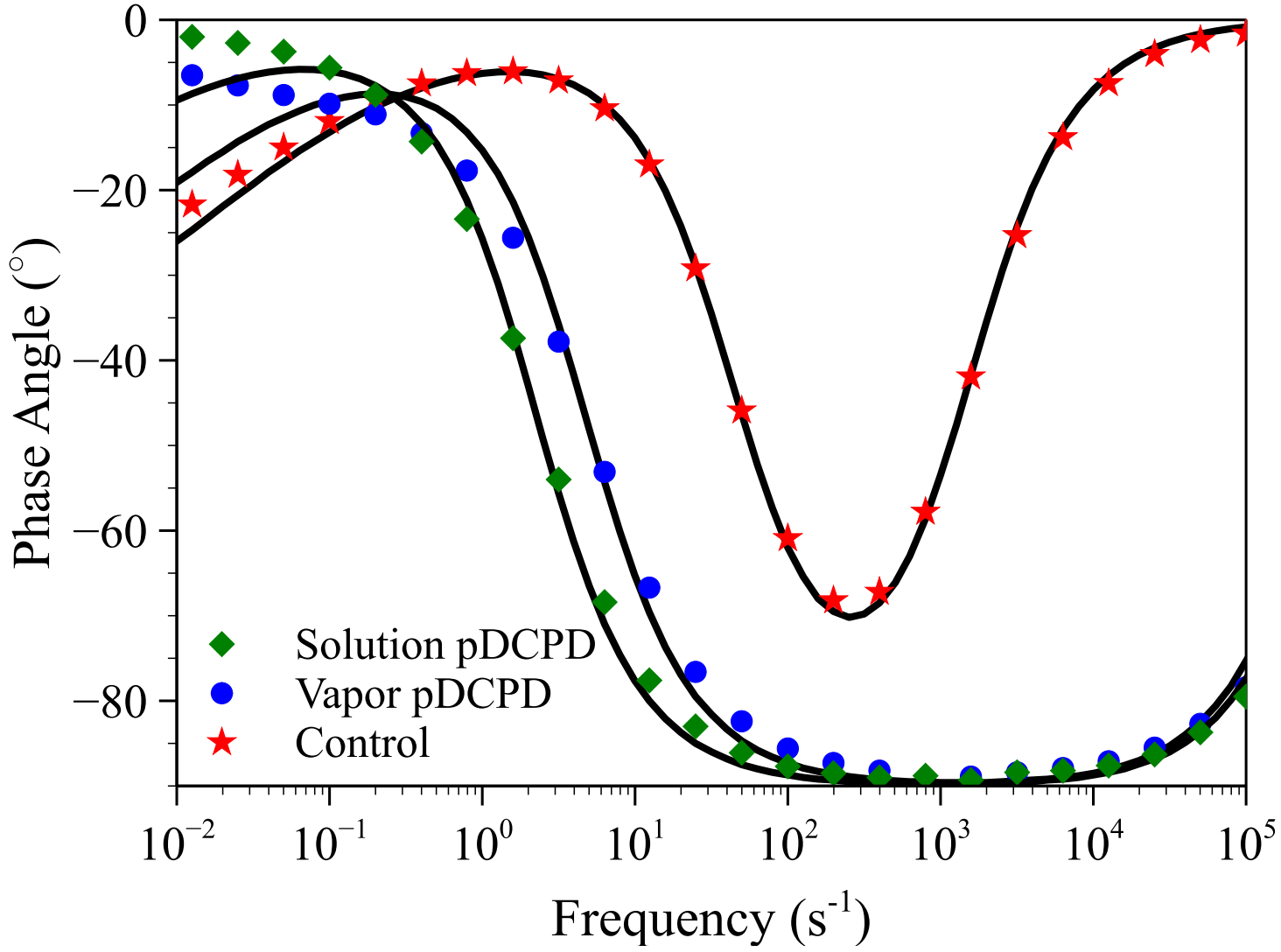

Figure 7.9: Phase angle plot of EIS of $\sim$ 400 nm pDCPD films grown from either the solution or the vapor phase, acquired in a 1 mM $K_3Fe(CN)_6$, 1 mM $K_4Fe(CN)_6 \cdot 3\,H_2O$, and 0.1 M Na_2SO_4 aqueous solution. The pDCPD films were grown with catalyst **2** for 15 min on gold substrates. The solid curve represents fits using a Randle's equivalent circuit modified with a Warburg impedance term. The solution pDCPD film was grown from a 0.75 M alumina-filtered DCPD solution in DCE. The vapor pDCPD film was polymerized at 55 °C employing the drying method presented in Scheme 7.1.

Table 7.5: Reduced Young's Modulus (E_r) of Surface-Tethered pDCPD Films Grown with Catalyst **2** for 15 min on Gold Substrates.

Sample	Nominal E (GPa)	E_r (GPa)
Polystyrene	2.7[a]	23 ± 4
pNB	0.8 [b]	6 ± 1
Vapor pDCPD	1.8 [c]	15 ± 3
Solution pDCPD	1.8 [c]	9 ± 4

[a]PeakForce QNM kit sample provided by Bruker with a reported nominal Young's modulus (E) of 2.7 GPa. [b] Bulk pNB (Avatrel^{TM}).[40] [c]Bulk pDCPD.[41]

tip, in particular, the cantilever spring constant and tip radius. The AFM tip radius can be determined by QNM from a polystyrene (PS) reference sample (PeakForce QNM Kit sample) using Equation 3.10 and the nominal Young's modulus (E) of the sample.[26] Application of this method to our PS reference sample, however, results in a large value of the tip radius (over 100 times the nominal radius), and therefore, the nominal tip radius was utilized for the data collection, resulting in values for E_r approximately 8 times greater than the E (Table 7.5). These measured values of E_r provide a direct comparison of the stiffness of the films.

The cross-linked nature of the pDCPD leads to a tougher stiffer polymer compared to a similar non cross-linked polymer such as pNB. The measured E_r for surface-tethered pDCPD films (15 GPa) in this study was approximately twice as high as that for surface-tethered pNB films (6 GPa), confirming the increased stiffness in the pDCPD films arising from the cross-linked nature of the material. Dokukin et al.[25] have shown that nanoindentation and PeakForce QNM can lead to an overestimation of polymer elastic moduli compared to bulk measurements, due to the application of stresses larger than the linearity limit for the polymers tested. I did not observe

significant differences in the E_r of vapor pDCPD (15 ± 3 GPa) and solution pDCPD (9 ± 4 GPa), which is consistent with the similar compositions observed in the IR spectra of the pDCPD films.

Conclusions

A rapid approach to the preparation of surface-anchored pDCPD films on gold and silicon substrates utilizing monomer in the vapor phase was achieved. The polymerization of DCPD monomer from the vapor phase confers several advantages over the solvent phase polymerization in regards to a reduction of volatile organic components, a reduction in reagent cost due the reusability of the unreacted monomer, and the preparation of smoother films. The solution-phase process required the purification of the DCPD monomer by filtration. Both processes exhibited rapid polymerization kinetics achieving pDCPD films exhibiting thicknesses of ∼400 nm for polymerization times as short as 1 min. The solution-phase process, however, required DCPD concentrations that were 3 orders of magnitude greater compared to those required in the vapor-phase process. The vapor-phase process also exhibited a combined rate of initiation and propagation that was 2 orders of magnitude greater and a termination rate that was ∼3 times lower than that observed in the solution-phase process. The vapor-phase process allows the easy preparation of pDCPD films with tunable thickness through the control of the vapor-phase concentration of DCPD by the presence of an inert additive, decane.

The thickness of pDCPD films prepared utilizing monomer in the vapor-phase process was enhanced by the presence of a film of a non-volatile stabilizing rinsate solvent on the ROMP-active gold substrates. Catalyst **3** led to films with greater thickness as compared to **2** for both the vapor-phase and solution-phase processes. The method for the surface attachment of the ROMP-catalyst influenced the SI-ROMP polymerization kinetics, with a lower surface coverage of the norbornene functional group

offering the best polymerization kinetics for the ROMP-catalysts considered in the study. The pDCPD films exhibited effective barrier properties and remarkable stiffness. pDCPD films prepared utilizing monomer in the vapor phase did not yield significant differences in composition, barrier properties, surface wettability and stiffness when compared to films prepared utilizing monomer in the solution phase but did yield pDCPD films that were remarkably smoother.

References

[1] Fu, D., Weng, L.-T., Du, B., Tsui, O. K. C., and Xu, B. (2002) Solventless Polymerization at the Gas-Solid Interface to Form Polymeric Thin Films. *Advanced Materials 14*, 339–343.

[2] Bielawski, C. W., and Grubbs, R. H. (2007) Living Ring-Opening Metathesis Polymerization. *Progress in Polymer Science 32*, 1–29.

[3] Bielawski, C. W., and Grubbs, R. H. (2000) Highly Efficient Ring-Opening Metathesis Polymerization (ROMP) using New Ruthenium Catalysts Containing N-heterocyclic Carbene Ligands. *Angewandte Chemie - International Edition 39*, 2903–2906.

[4] Feng, J., Stoddart, S. S., Weerakoon, K. A., and Chen, W. (2007) An Efficient Approach to Surface-Initiated Ring-Opening Metathesis Polymerization of Cyclooctadiene. *Langmuir 23*, 1004–1006.

[5] Escobar, C. A., Harl, R. R., Maxwell, K. E., Mahfuz, N. N., Rogers, B. R., and Jennings, G. K. (2013) Amplification of Surface-Initiated Ring-Opening Metathesis Polymerization of 5-(Perfluoro-n-alkyl)norbornenes by Macroinitiation. *Langmuir 29*, 12560–12571.

[6] Faulkner, C. J., Fischer, R. E., and Jennings, G. K. (2010) Surface-Initiated Polymerization of 5-(Perfluoro- n -alkyl)norbornenes from Gold Substrates. *Macromolecules 43*, 1203–1209.

[7] Gu, H., Fu, D., Weng, L. T., Xie, J., and Xu, B. (2004) Solventless Polymerization to Grow Thin Films on Solid Substrates. *Advanced Functional Materials 14*, 492–500.

[8] Lerum, M. F. Z., and Chen, W. (2011) Surface-Initiated Ring-Opening Metathesis Polymerization in the Vapor Phase: An Efficient Method for Grafting Cyclic Olefins with Low Strain Energies. *Langmuir 27*, 5403–5409.

[9] Schleyer, P. v. R., Williams, J. E., and Blanchard, K. R. (1970) Evaluation of Strain in Hydrocarbons. The Strain in Adamantane and its Origin. *Journal of the American Chemical Society 92*, 2377–2386.

[10] Gu, H., Zheng, R., Zhang, X., and Xu, B. (2004) Using Soft Lithography to Pattern Highly Oriented Polyacetylene (HOPA) Films via Solventless Polymerization. *Advanced Materials 16*, 1356–1359.

[11] Grubbs, R. H. (2004) Olefin Metathesis. *Tetrahedron 60*, 7117–7140.

[12] Trnka, T. M., and Grubbs, R. H. (2001) The Development of $L_2X_2Ru{=}CHR$ Olefin Metathesis Catalysts: An Organometallic Success Story. *Accounts of Chemical Research 34*, 18–29.

[13] P'Pool, S. J., and Schanz, H. J. (2007) Reversible Inhibition/Activation of Olefin Metathesis: A Kinetic Investigation of ROMP and RCM Reactions with Grubbs' Catalyst. *Journal of the American Chemical Society 129*, 14200–14212.

[14] Love, J. A., Sanford, M. S., Day, M. W., and Grubbs, R. H. (2003) Synthesis, Structure, and Activity of Enhanced Initiators for Olefin Metathesis. *Journal of the American Chemical Society 125*, 10103–10109.

[15] Scholl, M., Ding, S., Lee, C. W., and Grubbs, R. H. (1999) Synthesis and Activity of a New Generation of Ruthenium-Based Olefin Metathesis Catalysts Coordinated with 1,3-Dimesityl-4,5-dihydroimidazol-2-ylidene Ligands. *Organic Letters 1*, 953–956.

[16] Vougioukalakis, G. C., and Grubbs, R. H. (2010) Ruthenium-Based Heterocyclic Carbene-Coordinated Olefin Metathesis Catalysts. *Chemical Reviews 110*, 1746–1787.

[17] Love, J. A., Morgan, J. P., Trnka, T. M., and Grubbs, R. H. (2002) A Practical and Highly Active Ruthenium-Based Catalyst that Effects the Cross Metathesis of Acrylonitrile. *Angewandte Chemie International Edition 41*, 4035–4037.

[18] Simons, R., Guntari, S. N., Goh, T. K., Qiao, G. G., and Bateman, S. A. (2012) Poly(dicyclopentadiene)-Montmorillonite Nanocomposite Formation via Simultaneous Intergallery-Surface Initiation and Chain Crosslinking using ROMP. *Journal of Polymer Science Part A: Polymer Chemistry 50*, 89–97.

[19] Berron, B. J., Payne, P. A., and Jennings, G. K. (2008) Sulfonation of Surface-Initiated Polynorbornene Films. *Industrial & Engineering Chemistry Research 47*, 7707–7714.

[20] Berron, B. J., Graybill, E. P., and Jennings, G. K. (2007) Growth and Structure of Surface-Initiated Poly(n-alkylnorbornene) Films. *Langmuir 23*, 11651–11655.

[21] Brantley, E. L., Holmes, T. C., and Jennings, G. K. (2005) Blocklike Fluorocarbon and Hydrocarbon Copolymer Films via Surface-Initiated ATRP and Post-polymerization Reactions. *Macromolecules 38*, 9730–9734.

[22] Brantley, E. L., Holmes, T. C., and Jennings, G. K. (2004) Modification of ATRP Surface-Initiated Poly(hydroxyethyl methacrylate) Films with Hydrocarbon Side Chains. *The Journal of Physical Chemistry B 108*, 16077–16084.

[23] Bantz, M. R., Brantley, E. L., Weinstein, R. D., Moriarty, J., and Jennings, G. K. (2004) Effect of Fractional Fluorination on the Properties of ATRP Surface-Initiated Poly(hydroxyethyl methacrylate) Films. *The Journal of Physical Chemistry B 108*, 9787–9794.

[24] Du, B., Tsui, O. K. C., Zhang, Q., and He, T. (2001) Study of Elastic Modulus and Yield Strength of Polymer Thin Films Using Atomic Force Microscopy. *Langmuir 17*, 3286–3291.

[25] Dokukin, M. E., and Sokolov, I. (2012) Quantitative Mapping of the Elastic Modulus of Soft Materials with HarmoniX and PeakForce QNM AFM Modes. *Langmuir 28*, 16060–16071.

[26] Young, T. J., Monclus, M. A., Burnett, T. L., Broughton, W. R., Ogin, S. L., and Smith, P. A. (2011) The Use of the PeakForce Quantitative Nanomechanical Mapping AFM-based Method for High-Resolution Young's Modulus Measurement of Polymers. *Measurement Science and Technology 22*, 125703.

[27] United States Coast Guard, *Chemical Hazard Response Information System (CHRIS), COMDTINST M16565.*; 1999.

[28] Burchfield, P. E. (1942) Vapor Pressures of Indene, Styrene and Dicyclopentadiene. *Journal of the American Chemical Society 64*, 2501–2501.

[29] Perring, M., and Bowden, N. B. (2008) Assembly of Organic Monolayers on Polydicyclopentadiene. *Langmuir 24*, 10480–10487.

[30] Silverstein, R. M., Webster, F. X., and Kiemle, D. J. *Spectrometric Identification of Organic Compounds*, seventh ed.; Wiley: New York, 2005.

[31] Rule, J. D., and Moore, J. S. (2002) ROMP Reactivity of endo- and exo-Dicyclopentadiene. *Macromolecules 35*, 7878–7882.

[32] Nelson, G. L., and Kuo, C.-L. (1975) An Improved Procedure for the Preparation of exo-Dicyclopentadiene. *Synthesis 1975*, 105–106.

[33] Harada, Y., Girolami, G. S., and Nuzzo, R. G. (2003) Catalytic Amplification

of Patterning via Surface-Confined Ring-Opening Metathesis Polymerization on Mixed Primer Layers Formed by Contact Printing. *Langmuir 19*, 5104–5114.

[34] Cheung, T. T. P. *Kirk-Othmer Encyclopedia of Chemical Technology*; John Wiley & Sons, Inc., 2000.

[35] Bowden, N. B., Gupta, A., and Long, T. R. High-Density Polydicyclopentadiene. 2013; http://www.google.com/patents/US20130020262.

[36] Sanford, M. S., Love, J. A., and Grubbs, R. H. (2001) Mechanism and Activity of Ruthenium Olefin Metathesis Catalysts. *Journal of the American Chemical Society 123*, 6543–6554.

[37] Sanford, M. S., Ulman, M., and Grubbs, R. H. (2001) New Insights into the Mechanism of Ruthenium-Catalyzed Olefin Metathesis Reactions. *Journal of the American Chemical Society 123*, 749–750.

[38] Brittain, W. J., and Minko, S. (2007) A Structural Definition of Polymer Brushes. *Journal of Polymer Science Part A: Polymer Chemistry 45*, 3505–3512.

[39] Perwuelz, A., Campagne, C., and Lam, T. (1999) Caractérisation de la surface du polydicyclopentadiène (Poly-DCPD) : influence du vieillissement sur le mouillage et l'adhésion de peinture. *Journal de Chimie Physique* 904–922.

[40] Hess-Dunning, A. E., Smith, R. L., and Zorman, C. A. (2014) Development of Polynorbornene as a Structural Material for Microfluidics and Flexible BioMEMS. *Journal of Applied Polymer Science 131*, 40969.

[41] Le Gac, P. Y., Choqueuse, D., Paris, M., Recher, G., Zimmer, C., and Melot, D. (2013) Durability of Polydicyclopentadiene under High Temperature, High Pressure and Seawater (offshore oil production conditions). *Polymer Degradation and Stability 98*, 809–817.

Chapter 8

CONCLUSIONS AND FUTURE WORK

Conclusions

In this dissertation, I have prepared and characterized surface-tethered poly(ionic liquid) (PIL) films via surface-initiated ring-opening metathesis polymerization (SI-ROMP). The PIL films were prepared from monomers that coupled the polymerizable norbornene functional group with a dimethyimadazolium cation coupled to a hexafluorophosphate anion. The physical and chemical properties of the PIL films were shown to be tunable via anion exchange to easily incorporate various anions. This tunability enables surface-tethered PILs to easily and efficiently take on various properties. An increase in one of these properties, glass transition temperature (T_g), can lead to the detachment of the PIL films from gold substrates. A novel route to surface-tethered random copolymer films was achieved via the anion exchange of the PIL films with a binary mixture of anions. While surface-tethered PIL films allow you to discretely adjust film properties via anion selection, the ability to create random copolymer films offers a continuous tuning of film properties between the extremes of the two homopolymers for the PIL. Part of the dissertation presented a novel and rapid route to achieve surface-tethered poly(dicyclopentadiene) (pDCPD) films via SI-ROMP in the vapor phase and characterized the subsequent pDCPD films.

In Chapter 4, the synthesis and subsequent SI-ROMP of an IL monomer to form dynamic, anion-adaptive PIL films with thicknesses greater than 500 nm was achieved. p[N_1−dMIm][PF_6] films undergo anion exchange with traditional anions, such as ClO_4^-, FSI, and $^-NTf_2$, as well as larger anions in the form of dyes to alter properties, including ion conduction, mechanical properties, surface wettability,

and color. The p[N_1−dMIm] films behave as anionic chameleons and as such, adapt to their anionic environment where dynamic environmental response is critical. The surface wettability and viscoelastic properties, i.e. storage and loss modulus, of the p[N_1−dMIm] films are highly dependent on the film anion and are tunable via a simple anion exchange mechanism. The electrolyte cation does not impact ion conduction in p[N_1−dMIm] films when performed in aqueous electrolytes, while the film anion determines the resistance of the p[N_1−dMIm] film to ion conduction with the order, PF_6^- > $^-NTf_2$ ≫ FSI^- ≫ ClO_4^-. In particular, the film resistance to ion conduction for the p[N_1−dMIm] with the ClO_4^- anion is estimated to be orders of magnitude lower despite the film being only slightly more solvated, suggesting that the ClO_4^- anion behaves differently than the other ions investigated. The film resistance in aqueous electrolytes can be eliminated by employing an ionic liquid as the electrolyte, improving the solvation of the p[N_1−dMIm] films. The adaptability and tunability of these surface-tethered films enable their use for multiple applications.

In Chapter 5, p[N_1−dMIm][PF_6] films polymerized on gold substrates undergo anion exchange with traditional anions, such as ClO_4^-, FSI^-, and $^-NTf_2$, but are unable to incorporate smaller anions without detachment from the gold surface. This behavior is attributed to an increase in the glass transition temperature T_g, where the incorporation of disruptive anions leads to a stronger electrostatic coupling to the film backbone. This increase in T_g results in an increase in the entropic penalties for the film to remain tethered to the surface via a chemisorbed gold-thiol bond and results in the detachment of the polymer film with anion exchange. The incorporation of disruptive anions was accomplished by the preparation of p[N_1−dMIm][PF_6] films on silicon substrates and taking advantage of the covalent attachment scheme for the silicon substrates. p[N_1−dMIm][PF_6] film prepared on silicon substrates were able to incorporate disruptive anions in the form of triflate (^-OTf), which could not be incorporated for the p[N_1−dMIm][PF_6] films on gold substrates. The film thickness

of these films remained constant throughout the anion exchange process with minimal variation in the polymer carbon backbone as observed by the retention of the $C_{sp2}-H$ and $C_{sp3}-H$ infrared absorption bands.

The synthesis and subsequent SI-ROMP of an IL monomer $[N_3-dMIm][PF_6]$ exhibiting a larger repeat unit molecular volume (V_m) to form dynamic, anion-adaptive PIL films on gold substrates was achieved. An increase in V_m leads to a decrease in T_g and subsequently in the entropic penalties for a surface-tethered PIL film to remain tethered to the surface while incorporating small anions. The $p[N_3-dMIm][PF_6]$ films on gold substrates were shown to undergo anion exchange with anions, such as ClO_4^-, as well as disruptive anions in the form of ^-OTF and trifluoroacetate $CF_3CO_2^-$.

In Chapter 6, poly(ionic liquid) (PIL) random co-polymer (coPIL) films were prepared by the simple anion exchange of $p[N_1-dMIm]$ films with 0.2 M aqueous solutions consisting of the PF_6^- anion with either the ClO_4^- or the FSI^- anions. The composition of the coPIL films was determined using infrared spectroscopy (PM-IRRAS) and a linear system of equations. The $p[N_1-dMIm]$ films exhibit a thermodynamically driven selectivity, with the PF_6^- anion selective for the film for $p[N_1-dMIm][PF_6][ClO_4]$ coPIL films and the FSI^- anion selective for the film for $p[N_1-dMIm][PF_6][FSI]$ coPIL films. The surface wettability for $p[N_1-dMIm][PF_6][ClO_4]$ films is dependent on the film composition, continuously tunable with film composition, and shows that the concentration of the ClO_4^- anion on the surface is higher than that determined for the $p[N_1-dMIm][PF_6][ClO_4]$ film. The resistance of the $p[N_1-dMIm][PF_6][ClO_4]$ film to ion conduction is linearly dependent on the binary anion mole fraction of ClO_4^- in solution(x_{ClO_4}), which is thermodynamically related to the binary anion mole fraction of ClO_4^- in the film (y_{ClO_4}). In this way a key characteristic of the film, film resistance, can be continuously tuned between the extremes of the two homopolymers. The ability to easily form coPIL films that exhibit a continuum of properties between the properties of

the homopolymers greatly increases the utility of PIL films. PIL films already exhibit tremendous discrete tunability in their properties via anion exchange, which can now be extended to a continuous tunability to obtain specific properties for any desired application.

In Chapter 7, a rapid approach to the preparation of surface-anchored pDCPD films on gold and silicon substrates utilizing monomer in the vapor phase was achieved. The polymerization of DCPD monomer from the vapor phase confers several advantages over the solvent-phase polymerization in regards to a reduction of volatile organic components, a reduction in reagent cost due the reusability of the unreacted monomer, and the preparation of smoother films. The solution-phase process required the purification of the DCPD monomer by filtration. Both processes exhibited rapid polymerization kinetics achieving pDCPD films exhibiting thicknesses of $\sim$400 nm for polymerization times as short as 1 min. The solution-phase process, however, required DCPD concentrations that were 3 orders of magnitude greater compared to those required in the vapor-phase process. The vapor-phase process also exhibited a combined rate of initiation and propagation that was 2 orders of magnitude greater and a termination rate that was $\sim$3 times lower than that observed in the solution-phase process. The vapor-phase process allows the easy preparation of pDCPD films with tunable thickness through the control of the vapor-phase concentration of DCPD by the presence of an inert additive, decane.

The thickness of pDCPD films prepared utilizing monomer in the vapor-phase process was enhanced by the presence of a film of a non-volatile stabilizing rinsate solvent on the ROMP-active gold substrates. Catalyst **3** led to films with greater thickness as compared to **2** for both the vapor-phase and solution-phase processes. The method for the surface attachment of the ROMP-catalyst influenced the SI-ROMP polymerization kinetics, with a lower surface coverage of the norbornene functional group offering the best polymerization kinetics for the ROMP-catalysts considered in

the study. The pDCPD films exhibited effective barrier properties and remarkable stiffness. pDCPD films prepared utilizing monomer in the vapor phase did not yield significant differences in composition, barrier properties, surface wettability, and stiffness when compared to films prepared utilizing monomer in the solution phase but did yield pDCPD films that were remarkably smoother.

Future Work

This dissertation details the preparation and characterization of surface-tethered poly(ionic liquid) (PIL) films, of surface-tethered PIL random copolymer films, and of surface-tethered polydicyclopentadiene (pDCPD) films. In particular, the discrete tunability of PIL film properties via anion exchange, the novel and rapid preparation of copolymer films via binary anion exchange for the continuous tunability of PIL films, and the novel and rapid preparation of pDCPD films by SI-ROMP of monomer from the vapor phase were demonstrated. In order to aid in the utility and understanding of the surface-immobilized films considered, I suggest the following topics that could be addressed in the future.

Anion exchange of the resident counter ion in surface-tethered PILs is a crucial methodology in obtaining the desired material and surface properties. Results in Chapter 4 sample a small range of material properties that can be achieved by anion exchange of PIL films. However, I do not study the kinetics of anion exchange, which would be useful in the utilization of the PIL films. Understanding how anions exchange into the film and how quickly can allow one to design transient process that could take advantage of the simplicity of tuning material properties in ILs. For example, a surface-tethered PIL can be used in a bioremediation process, where the film is initially loaded with beneficial ions that are exchanged into an aqueous waste stream while the film captures unwanted anions. Understanding the kinetics of anion exchange could enable you to determine key parameters for the success of such a

system.

In Chapter 4, I studied the ionic conduction of PIL films. A natural extension of this study is to incorporate electroactive anions (Appendix A) and study the ion conduction in conjunction with redox kinetics of the PIL films. An improved ion and electron conduction can be achieved with surface-immobilized PILs, where one can take advantage of the proximity of the film to the electrode surface to achieve rapid electron transfer kinetics, while enjoying the improved ion conduction a PIL film could provide.

In Chapter 5, I detailed the preparation of PIL films with a larger repeat unit molecular volume (V_m) than those considered in Chapter 4. The larger V_m extended the utility of this PIL film on gold substrates and enabled new surface properties of the PIL film. Preparation of PIL films with even larger V_m would enable a myriad of new surface properties. Escobar et al.[1] have shown that monomers containing longer side chains enhance the polymerization kinetics of the monomer with SI-ROMP. Additionally, an increase in V_m results in a higher dielectric constant[2] as well as a greater ionic conduction.[3] The preparation of surface-tethered PIL films exhibiting higher dielectric constants as well as ion conduction could lead to the utility of the PIL films in numerous applications such as energy storage.

Friction Reduction with Surface-Tethered Poly(Ionic Liquids)

Tribology is the study of friction, wear and lubrication of interrelating surfaces in relative contact.[4] The conservation of energy, material and financial resources, the environment, as well as safety considerations, emphasize the importance of controlling friction and wear.[5] Liquid lubrication is the most common lubrication method, but is often undesirable due to environmental concerns, ensuring confinement in the contact zone, circulation, contamination, and other effects.[5] Surface engineering, where the surface properties of moving contacts are modified in a favorable manner, by depo-

sition of solid/dry lubricants or by surface treatment are often preferred in applications where traditional lubricants (liquid) fail to provide adequate performance, such as extreme environmental conditions, high contact pressures, or low ambient pressures.[5–8] Solid/dry lubricants generally have lower vapor pressures, better boundary lubrication properties, relative insensitivity to radiation effects, and less sensitivity to temperature changes.[7]

Nature has provided us with a template for systems that exhibit relatively low coefficients of friction (COFs). Synovial joints are able to achieve COFs on the range of 0.001 to 0.005 at mean pressures on the order of 100 atm and at shear rates from 0 to 10^7 s^{-1}.[9] The low coefficients of friction exhibited by synovial joints are largely due to the two-phase structure of the joint, a solid phase made up of collagen and proteoglycans with entrapped brush-like charged macromolecules, such as hyaluronic acid and lubricin in synovial fluid.[9–11] Due to the expense and incompatibility of the use of biological proteins and charged macromolecules in non-biological applications, materials systems that mimic the function and composition of synovial joints could exhibit performance that approaches or surpasses natural systems.[12]

Ishikawa et al.[13] have performed the only investigation to date of a pIL brush in tribological applications, where they showed that low sliding frictional coefficients (COF ~ 0.01) could be achieved when the substrate and probe both contained a pIL brush and a compatible IL was used as a mobile component. Ishikawa et al. were also able to demonstrate the wear characteristics of the pIL brush; while they were only able to achieve $\sim$ 50 nm thick pIL brushes over a 72 h SI-ATRP process, the pIL brushes were able to withstand up to 800 friction cycles before an increase in the COF in a dry nitrogen atmosphere.

pIL coatings and ionic liquids could replace the charged macromolecules and biological polymers inherent in synovial lubrication. Raviv et al. have shown effective friction coefficients lower than $\sim 0.0006 - 0.001$ by utilizing polyelectrolyte brushes

in water. They attribute the exceptional resistance to interpenetration displayed by the brushes in tandem with the fluidity of the hydration layers surrounding the charged, rubbing polymer segments.[14] pILs could achieve similar performance due to the structural similarities with polyelectrolyte brushes in addition to extending the utility of polyelectrolyte brushes by enabling use in environments unsuitable to aqueous systems.

Polydicyclopentadiene with Reporter Functionality

The ability of a material to detect and report localized damage prior to catastrophic failure is a pivotal feature at the intersection of structural health monitoring (SHM) and non-destructive evaluation (NDE).[15–17] The early detection of impending failure is particularly important in applications in which the material is used as a load-bearing material or in applications where catastrophic failure of the material would lead to further damage to other systems.[15,16] Polymer composites imbued with multi-functional properties are the material of choice due to the ability to design and cheaply manufacture light-weight, sustainable, thermally, mechanically, and chemically robust polymer composites.[15,18] Stimuli-responsive materials able to detect thermal, mechanical, optical, and chemical solicitation have been used to effectively develop sensors, probes, and information displays by taking advantage of organic or inorganic chromophores such as dyes with available delocalized electrons, or metal derivatives (i.e. metal nanoparticles and nanocrystalline semiconductors) since they confer a variation in the opto-electronic properties as a response to the stimulus.[18,19]

Chromogenic polymer systems able to detect through a prompt optical response (absorption and emission) to an external stimuli triggered by mechanical (shearing, grinding and pressing) stress are favored due to their quick and simple functionality and visual signaling.[18,19] Mechanochromic polymer composites, which are materials based on dye-doped polymers that are optically sensitive to mechanical stimuli, may

be obtained via two distinct routes, either the covalent bonding of highly responsive molecular species to the polymer chains, or the dispersion of responsive species within the polymer bulk.[18,19] In the latter case, the control of interphase interactions between the chemical functional species (dye) and the multiphase system (polymer composite) allows for the effective modulation of the response to stimuli.[18,19]

The bruising of skin is a natural template in reporting local damage. Bruise formation optically communicates the release of red blood cells, due to damage, into the extravascular space and the color evolution of the bruise provides information on the material state of skin.[20] Polymeric systems that could report localized damage would offer an extended performance by enabling preventative maintenance and/or replacements of systems prior to catastrophic failure. The preparation of stimuli-responsive pDCPD by the incorporation of stimuli responsive reporter molecules can enable the aforementioned responsive polymeric systems. In the design of smart materials, the combination of molecular structure and supramolecular organization of the components is considered to be the most effective route in obtaining products with versatile features.[21] Polymers are attractive and fundamental components of these complex systems due to their response to changes in their environment and their varied structural and functional properties.[21,22] Chromogenic materials composed of a functional dye physically dispersed in the pDCPD macromolecular matrix that switches its optical properties, for example absorption, emission, or refractive index, as a function of external mechanical stimuli can be developed. Organic or inorganic chromophores such as molecules with available delocalized electrons (pDA) or metal derivatives, such as metal nanoparticles (CdSe) or nanocrystalline semiconductors can constitute the basis of a sensor mechanism by conferring to the pDCPD an ability to vary the optical features in response to a mechanical stimulus.

Conjugated polymers (CPs) are compounds with alternating saturated and unsaturated bonds and this overlap results in conductivity and fluorescence when light is

absorbed.[19] Changes in the chemical nature, effective conjugation length, intramolecular conformation, and intramolecular packing can change the absorption and fluorescence properties of CPs and therefore provide mechanisms that can be implemented in sensing applications.[19] Polydiacetylene (pDA), a conjugated polymer, is an attractive molecule in the use of stimuli-responsive materials.[19] Diacetylene (DA) monomers are typically amphiphilic, enabling the molecules to self assemble into various nano/micro-shapes in the correct self-assembly environment.[19,23] The polymer is polymerized by the UV or $\gamma-$irradiation of the supra-molecularly-assembled crystalline or semicrystalline states of the DA monomer without the need for chemical initiators or catalysts.[23]

pDAs undergo a blue ($\lambda_{\max}$ 640nm) to red ($\lambda_{\max}$ 550nm) color change accompanied by the generation of fluorescence when subjected to external stimuli, such as mechanical stress (mechanochromic), heat (thermochromic), and organic solvents (solvatochromic).[19,23,24] This transition is attributed to the rotation about the C$-$C bond of the polymer backbone changing the planarity and the $\pi-$orbital overlap of the backbone causing a significant blue-shift in the absorption spectrum. The CP pDA has been used to develop solution and solid state biosensors that take advantage of the blue to red color change induced by a conformational change of the conjugated ene-yne backbone of pDA by external stimuli such as temperature change, pH change, or mechanical stress.[19,24] Incorporating pDA into pDCPD while ensuring sufficient coupling of the pDA to the bulk material would impart the mechanochromic properties of the pDA to the composite material. Mechanical stresses imparted upon the material would be transferred into the pDA activating the mechanochromic response of the pDA and optically reporting a change in the material state to an observe

Ultra-small pyrolytically synthesized CdSe nanocrystals exhibit white light emission characterized by two features (peaks) attributed to emission from energetically different midgap states.[25,26] The position of the emission features has been shown to

be sensitive to the nanocrystal size and the nanocrystal surface ligands, with the first emission feature shifting to higher wavelengths with increasing nanocrystal size and decreasing ligand length.[26] The CdSe nanocrystals have been encapsulated in polymer and have demonstrated good photostability over time.[25,27,28] The incorporation of CdSe reporter molecules in a pDCPD coating would allow the use of the emission shift of the CdSe in the sensing of localized damage within the coating.

References

[1] Escobar, C. A., Harl, R. R., Maxwell, K. E., Mahfuz, N. N., Rogers, B. R., and Jennings, G. K. (2013) Amplification of Surface-Initiated Ring-Opening Metathesis Polymerization of 5-(Perfluoro-n-alkyl)norbornenes by Macroinitiation. *Langmuir 29*, 12560–12571.

[2] Choi, U. H., Mittal, A., Price, T. L., Lee, M., Gibson, H. W., Runt, J., and Colby, R. H. (2015) Molecular Volume Effects on the Dynamics of Polymerized Ionic Liquids and their Monomers. *Electrochimica Acta 175*, 55–61.

[3] Choi, U. H., Lee, M., Wang, S., Liu, W., Winey, K. I., Gibson, H. W., and Colby, R. H. (2012) Ionic Conduction and Dielectric Response of Poly(imidazolium acrylate) Ionomers. *Macromolecules 45*, 3974–3985.

[4] Findik, F. (2014) Latest progress on tribological properties of industrial materials. *Materials and Design 57*, 218–244.

[5] Holmberg, K., Ronkainen, H., Laukkanen, A., and Wallin, K. (2007) Friction and wear of coated surfaces âĂŤ scales, modelling and simulation of tribomechanisms. *Surface and Coatings Technology 202*, 1034–1049.

[6] Bhushan, B. (2007) Nanotribology and nanomechanics of MEMS/NEMS and BioMEMS/BioNEMS materials and devices. *Microelectronic Engineering 84*, 387–412.

[7] Hilton, M., and Fleischauer, P. (1992) Applications of solid lubricant films in spacecraft. *Surface and Coatings Technology 54-55*, 435–441.

[8] Roberts, E. (1990) Thin solid lubricant films in space. *Tribology International 23*, 95–104.

[9] Seror, J., Merkher, Y., Kampf, N., Collinson, L., Day, A. J., Maroudas, A., and Klein, J. (2011) Articular cartilage proteoglycans as boundary lubricants: structure and frictional interaction of surface-attached hyaluronan and hyaluronan–aggrecan complexes. *Biomacromolecules 12*, 3432–43.

[10] Chan, S. M. T., Neu, C. P., Komvopoulos, K., and Reddi, a. H. (2011) The role of lubricant entrapment at biological interfaces: reduction of friction and adhesion in articular cartilage. *Journal of biomechanics 44*, 2015–20.

[11] Chan, S. M. T., Neu, C. P., DuRaine, G., Komvopoulos, K., and Reddi, a. H. (2012) Tribological altruism: A sacrificial layer mechanism of synovial joint lubrication in articular cartilage. *Journal of biomechanics 45*, 2426–31.

[12] Greene, G. W., Banquy, X., Lee, D. W., Lowrey, D. D., Yu, J., and Israelachvili, J. N. (2011) Adaptive mechanically controlled lubrication mechanism found in articular joints. *Proceedings of the National Academy of Sciences of the United States of America 108*, 5255–5259.

[13] Ishikawa, T., Kobayashi, M., and Takahara, A. (2010) Macroscopic Frictional Properties of Poly(1-(2-methacryloyloxy)ethyl-3-butyl Imidazolium Bis(trifluoromethanesulfonyl)-imide) Brush Surfaces in an Ionic Liquid. *ACS Applied Materials & Interfaces 2*, 1120–1128.

[14] Raviv, U., Giasson, S., Kampf, N., Gohy, J.-F., Jerome, R., and Klein, J. (2003) Lubrication by charged polymers. *Nature 425*, 163–165.

[15] Jin, X., Götz, M., Wille, S., Mishra, Y. K., Adelung, R., and Zollfrank, C. (2013) A Novel Concept for Self-Reporting Materials: Stress Sensitive Photoluminescence in ZnO Tetrapod Filled Elastomers. *Advanced Materials 25*, 1342–1347.

[16] Bruns, N., Pustelny, K., Bergeron, L. M., Whitehead, T. A., and Clark, D. S.

(2009) Mechanical Nanosensor Based on FRET within a Thermosome: Damage-Reporting Polymeric Materials. *Angewandte Chemie 121*, 5776–5779.

[17] Brubaker, C., Frecker, T., Njoroge, I., Smudde, C., Shane, D., Meyer, J., Rosenthal, S., Sanchez, F., Jennings, G., and Adams, D. Detecting and communicating material damage using embedded CdSe nanocrystals. CAMX 2015 - Composites and Advanced Materials Expo. 2015.

[18] Pucci, A., Bizzarri, R., and Ruggeri, G. (2011) Polymer composites with smart optical properties. *Soft Matter 7*, 3689–3700.

[19] Lee, K., Povlich, L. K., and Kim, J. (2010) Recent advances in fluorescent and colorimetric conjugated polymer-based biosensors. *Analyst 135*, 2179–2189.

[20] Jeney, V., Eaton, J. W., Balla, G., and Balla, J. (2013) Natural history of the bruise: Formation, elimination, and biological effects of oxidized hemoglobin. *Oxidative Medicine and Cellular Longevity 2013*.

[21] Pucci, A., and Ruggeri, G. (2011) Mechanochromic polymer blends. *J. Mater. Chem. 21*, 8282–8291.

[22] Bünsow, J., Kelby, T. S., and Huck, W. T. S. (2010) Polymer Brushes: Routes toward Mechanosensitive Surfaces. *Accounts of Chemical Research 43*, 466–474.

[23] Yoon, B., Lee, S., and Kim, J.-M. (2009) Recent conceptual and technological advances in polydiacetylene-based supramolecular chemosensors. *Chem. Soc. Rev. 38*, 1958–1968.

[24] Carpick, R. W., Sasaki, D. Y., and Burns, A. R. (2000) First Observation of Mechanochromism at the Nanometer Scale. *Langmuir 16*, 1270–1278.

[25] Bowers, M. J., McBride, J. R., and Rosenthal, S. J. (2005) White-Light Emission from Magic-Sized Cadmium Selenide Nanocrystals. *Journal of the American Chemical Society 127*, 15378–15379.

[26] McBride, J. R., Dukes III, A. D., Schreuder, M. A., and Rosenthal, S. J. (2010) On ultrasmall nanocrystals. *Chemical Physics Letters 498*, 1–9.

[27] Schreuder, M. a., Gosnell, J. D., Smith, N. J., Warnement, M. R., Weiss, S. M., and Rosenthal, S. J. (2008) Encapsulated white-light CdSe nanocrystals as nanophosphors for solid-state lighting. *Journal of Materials Chemistry 18*, 970.

[28] Gosnell, J. D., Rosenthal, S. J., and Weiss, S. M. White Light Emission Characteristics of Polymer-Encapsulated CdSe Nanocrystal Films. 2010.

Appendices

Appendix A

SURFACE-TETHERED POLY(IONIC LIQUID) FILMS WITH ELECTROACTIVE ANIONS

Introduction

In Chapter 4, I studied the ionic conduction of PIL films. Here, I incorporate electroactive anions and study the ion conduction in conjunction with redox kinetics of the PIL films. An improved ion and electron conduction can be achieved with surface-immobilized PILs, where one can take advantage of the proximity of the film to the electrode surface to achieve rapid electron transfer kinetics, while enjoying the improved ion conduction a PIL film could provide.

p[N_1−dMIm] Film Anion Exchange

Figure A.1 shows the IR spectra for a p[N_1−dMIm][PF_6] polymer film grown on a gold substrate. The dominant absorption band is the P−F stretch at 865 cm^{-1}.[1] Weaker absorption bands due to the polymer carbon backbone are also observed, in particular, a C=C stretching absorption band at 1589 cm^{-1}, a symmetric CH_2 in-plane bending (scissoring) absorption band at 1462 and 1423 cm^{-1}, an asymmetric CH_3 absorption band at 1392 cm^{-1}, a symmetric CH_3 absorption band at 1243 cm^{-1}, and a CH_3 in-plane bending (rocking) absorption band at 742 cm^{-1}.[2] Figure A.1 also shows the IR spectra for a p[N_1−dMIm][$Fe^{3+}(CN)_6$] polymer film. The spectra shows a lack of the $PF_6{}^-$ anion and retention of the absorbance bands for the polymer carbon backbone.

Figure A.2 shows the IR spectra for a p[N_1−dMIm][$Fe^{3+}(CN)_6$] polymer film grown on a gold substrate. The dominant absorption band is the C−N stretch at

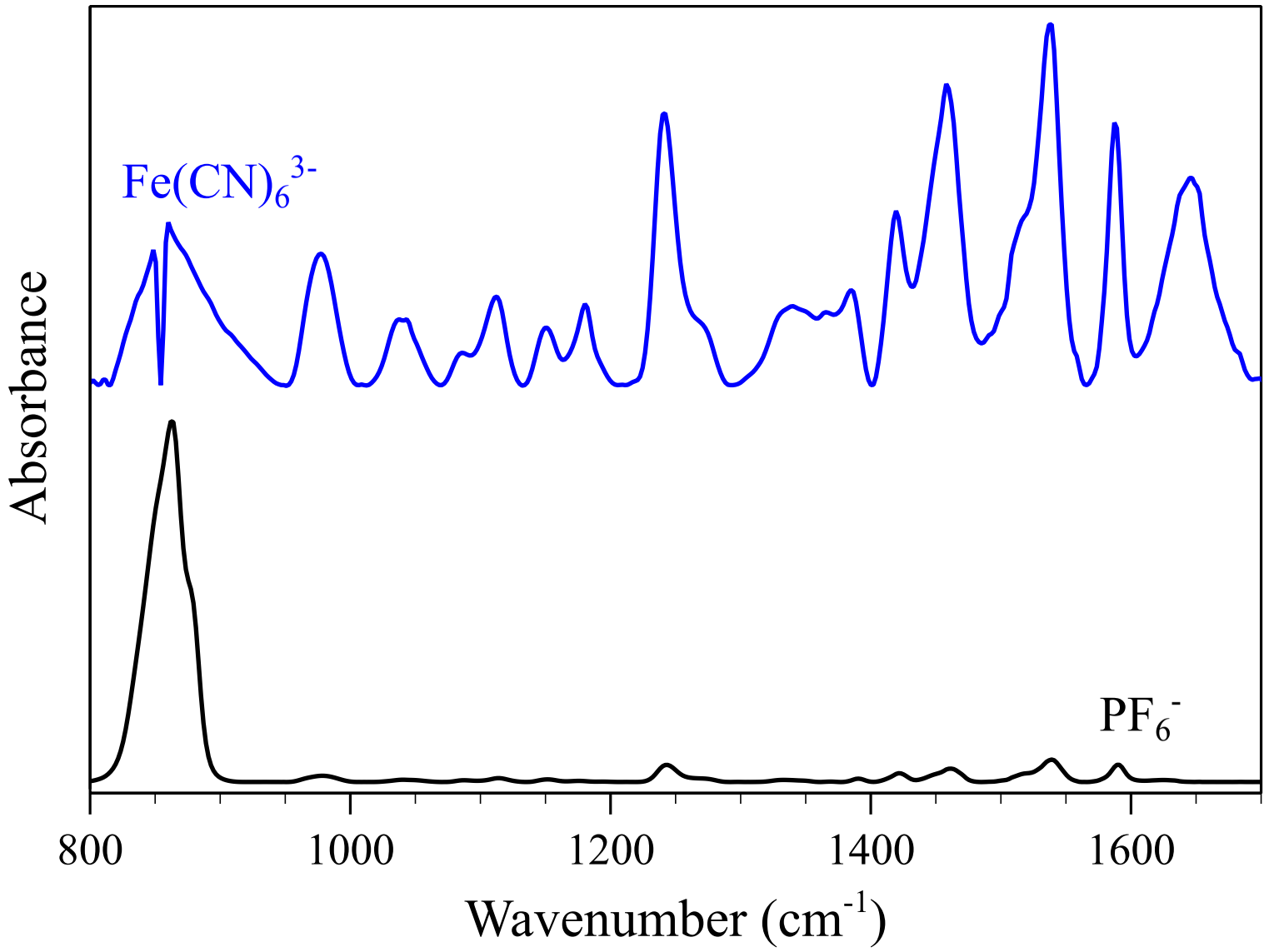

Figure A.1: Polarization modulation-infrared reflectance-absorption spectrum of p[N_1−dMIm] films on gold substrates. The p[N_1−dMIm] films were initially polymerized with the PF_6^- anion, but were successfully exchanged with the $Fe_3^+(CN)_6^{3-}$ anion.

Table A.1: Film Anion Polarization Modulation-Infrared Reflectance-Absorption Bands of p[N_1−dMIm] Films.[2,5–8]

Anion	C_{sp^3}−H Bands (cm^{-1})	C_{sp^2}−H Bands (cm^{-1})
PF_6^-	2865 (ν_s), 2942 (ν_{as})	3157, 3189
$Fe_3^+(CN)_6^{3-}$	2860 (ν_s), 2940 (ν_{as})	3148, 3186

2100 cm^{-1}.[3,4] Figure A.2 also shows the IR spectra for a p[N_1−dMIm][PF_6] polymer film, which shows a lack of the $Fe(CN)_6^{3-}$ anion.

Figure A.3 shows the IR spectra for a p[N_1−dMIm] polymer film with the PF_6^- and $Fe(CN)_6^{3-}$ anions. The major absorbance bands in the IR spectra for the PF_6^- and $Fe(CN)_6^{3-}$ anions are summarized in Table 4.2. There are minimal variations in the C_{sp^3}−H and C_{sp^2}−H stretch vibration band peak positions for the p[N_1−dMIm] polymer film with the PF_6^- and $Fe(CN)_6^{3-}$ anions as shown in Figure A.3 and Table A.1; however, the peak shapes are similar as shown in Figure A.3.

Electrochemical Impedance Spectroscopy (EIS)

Ion transport through the p[N_1−dMIm][$Fe^{3+}(CN)_6$] films was investigated by utilizing electrochemical impedance spectroscopy (EIS). The studies were conducted in the presence of a 0.1 M aqueous solution of [$K_3Fe^{3+}(CN)_6$]. A Representative Bode plot of EIS spectra for p[N_1−dMIm][$Fe^{3+}(CN)_6$] films prepared by anion exchange from a p[N_1−dMIm][PF_6] film with 0.2 M aqueous solutions $K_3Fe^{3+}(CN)_6$] as well as a control film consisting of a hydroxyl-terminated SAM on gold substrates exposed to NBDAC conducted in the presence of a 0.1 M [$K_3Fe^{3+}(CN)_6$] aqueous solution are shown in Figure A.4. The impedance spectra were fit with the equivalent circuit model shown in Scheme 3.4 to quantify the circuit parameters as shown in Tables A.2 and A.3.

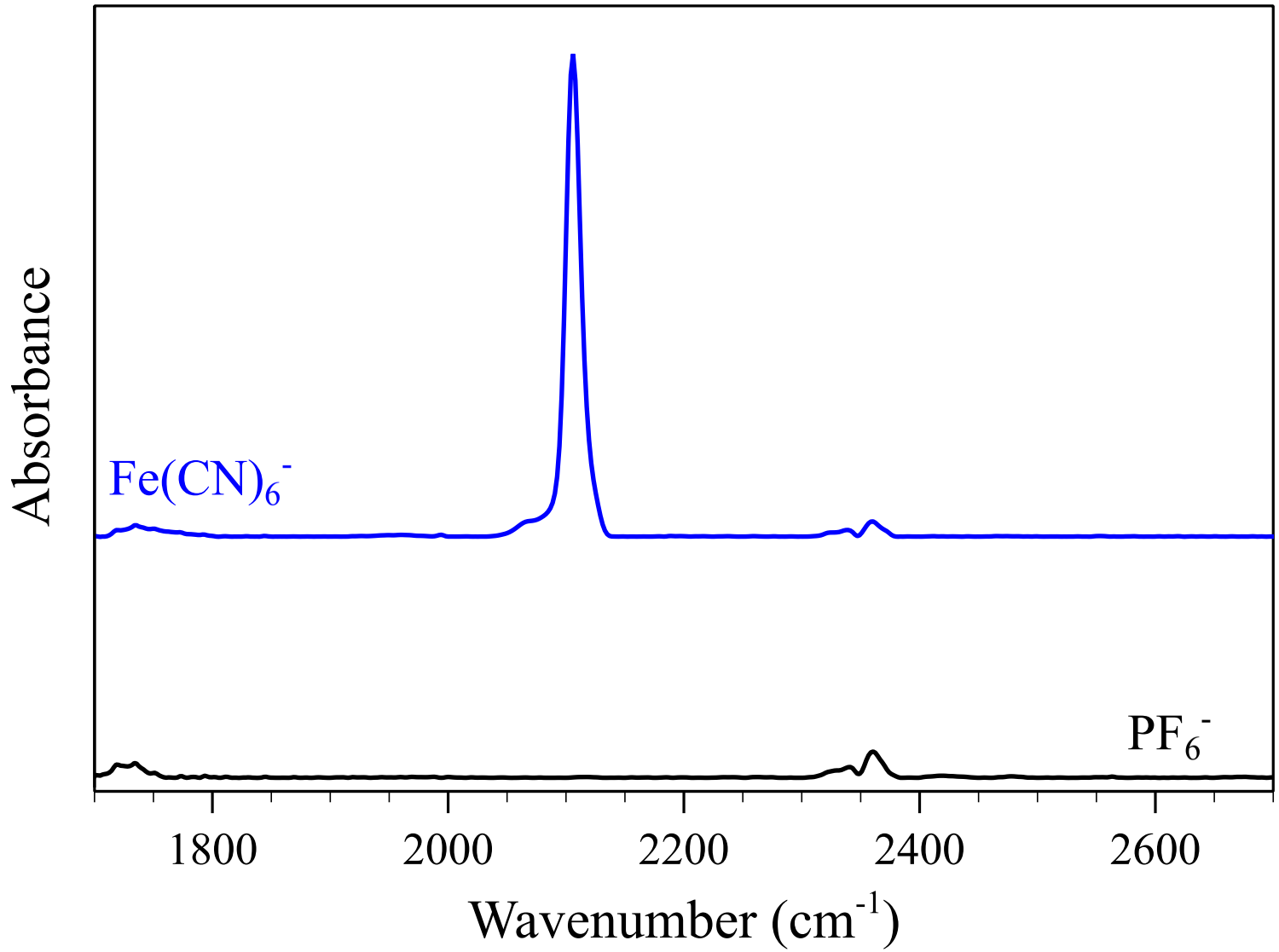

Figure A.2: Polarization modulation-infrared reflectance-absorption spectrum of p[N_1−dMIm] films on gold substrates. The p[N_1−dMIm] films were initially polymerized with the PF_6^- anion, but were successfully exchanged with the $Fe(CN)_6^{3-}$ anion.

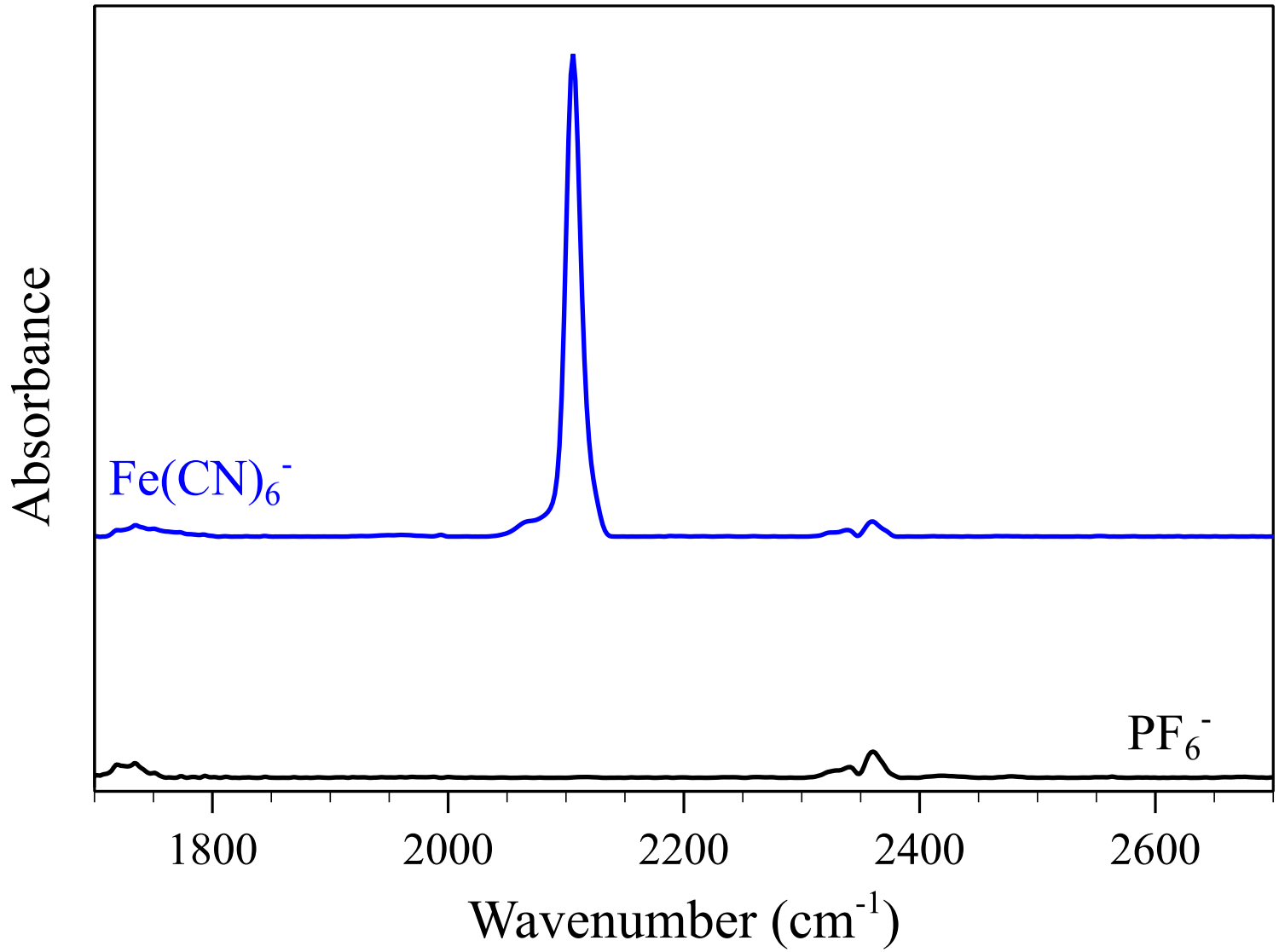

Figure A.3: Polarization modulation-infrared reflectance-absorption spectrum of p[N_1−dMIm] films on gold substrates. The p[N_1−dMIm] films were initially polymerized with the PF_6^- anion, but were successfully exchanged with the $Fe_3^+(CN)_6^{3-}$ anion.

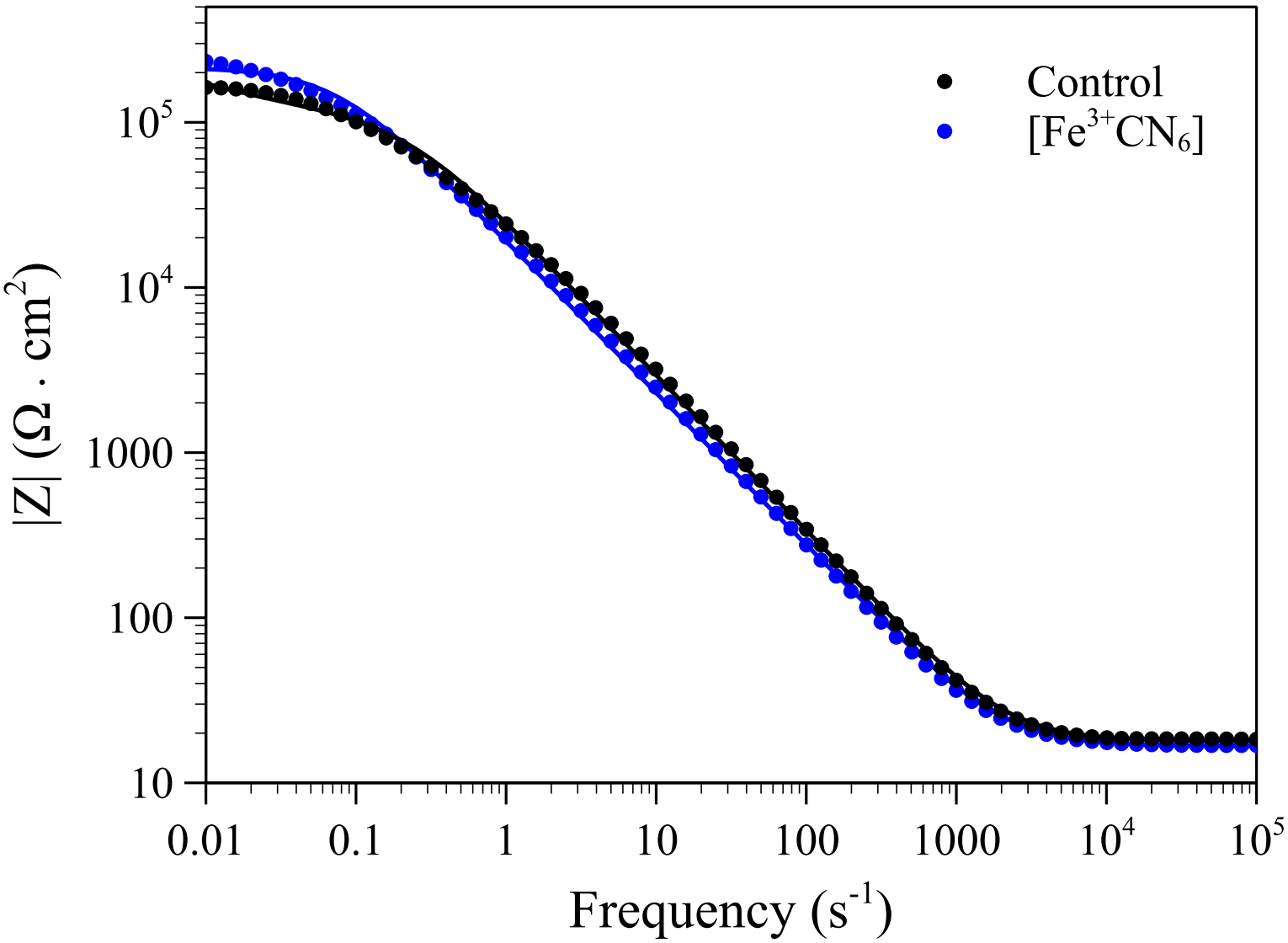

Figure A.4: Bode plot of an EIS spectrum for a p[N_1−dMIm][$Fe^{3+}(CN)_6$] film acquired in a 0.1 M aqueous solution of $K_3Fe^{3+}(CN)_6$. EIS of a film consisting of a hydroxyl-terminated SAM exposed to NBDAC acquired in a 0.1 M $K_3Fe^{3+}(CN)_6$ aqueous solution is shown as a control. Solid curves represent fits with the equivalent circuit in Scheme 3.4.

Table A.2: p[N_1−dMIm] Solution Resistance (R_s), Interfacial Resistance (R_i), and Interfacial Capacitance (C_i) Values Obtained from a Fit of the EIS Spectra in Figure A.4 with the Equivalent Circuit in Scheme 3.4.

Electrolyte	R_s ($\Omega \cdot cm^2$)	R_i ($M\Omega \cdot cm^2$)	C_i ($\mu F/cm^2$)
$K_3Fe^{3+}(CN)_6$	17 ± 0.1	0.22 ± 0.002	11.9 ± 0.1
Control[1]	18 ± 0.1	0.11 ± 0.002	8 ± 0.1

[1] The control film is a gold substrate modified with a hydroxyl-terminated SAM exposed to NBDAC with spectra acquired in a 0.1 M $K_3FeCN)_6$] aqueous Solution.

Table A.3: p[N_1−dMIm] Film Resistance (R_f), Conductivity (κ_f), and Capacitance (C_f) Values Obtained from a Fit of the EIS Spectra in Figure A.4 with the Equivalent Circuit in Scheme 3.4.

Electrolyte	R_f ($\Omega \cdot cm^2$)	κ_f ($\mu S/cm$)	C_f ($\mu F/cm^2$)
$K_3Fe^{3+}(CN)_6$[a]	$\leq 17 \pm 0.1$	$\geq 3.6 \pm 0.2$	-
Control[b]	-	-	-

[a] The film resistance for the film is theoretically lower than the R_s observed. [b] The control film is a gold substrate modified with a hydroxyl-terminated SAM exposed to NBDAC with spectra acquired in a 0.1 M $K_3Fe(CN)_6$] aqueous solution.

Phase angle plots of EIS spectra corresponding to the Bode plots of Figure A.4 for p[N_1−dMIm][$Fe^{3+}(CN)_6$] films on gold substrates, as well as a control film consisting of a hydroxyl-terminated SAM on gold substrates exposed to NBDAC, conducted in the presence of a 0.1 M $K_3Fe(CN)_6$ aqueous solution are shown in Figure A.5.

Cyclic Voltametry (CV)

Ion and electron conduction in the p[N_1−dMIm][$Fe^{3+}(CN)_6$] films was investigated by utilizing cyclic voltammetry (CV). The studies were conducted with various electrolytes and at a 20 mV/s scan rate. The current-voltage observed for the p[N_1−dMIm][$Fe^{3+}(CN)_6$] films is shown in Figure A.6. The scans with the 20 mM $K_3Fe(CN)_{6/}K_4Fe(CN)_6$ electrolyte and the 10 mM $K_3Fe(CN)_{6/}K_4Fe(CN)_6$ electrolyte produced similar curves and the largest current of the electrolytes studied. This behavior arises due to a high concentration of redox species in solution resulting in electron conduction mainly in solution. The other electrolytes studied in Figure A.6 had over an order of magnitude less in redox species concentration. However, they also included a supporting electrolyte that would exchange into the film during the collection of the CV's.

Figure A.7 shows the current-voltage observed for the p[N_1−dMIm][$Fe^{3+}(CN)_6$] films run with a 1mM concentration of redox species or without any redox species. The curves shown in Figure A.7 demonstrate both the ion and electron conduction capability of these films with peaks arising due to electron donation to redox species in the film as well as in solution. Further studies need to be conducted in order to fully elucidate the mechanisms at work in this system.

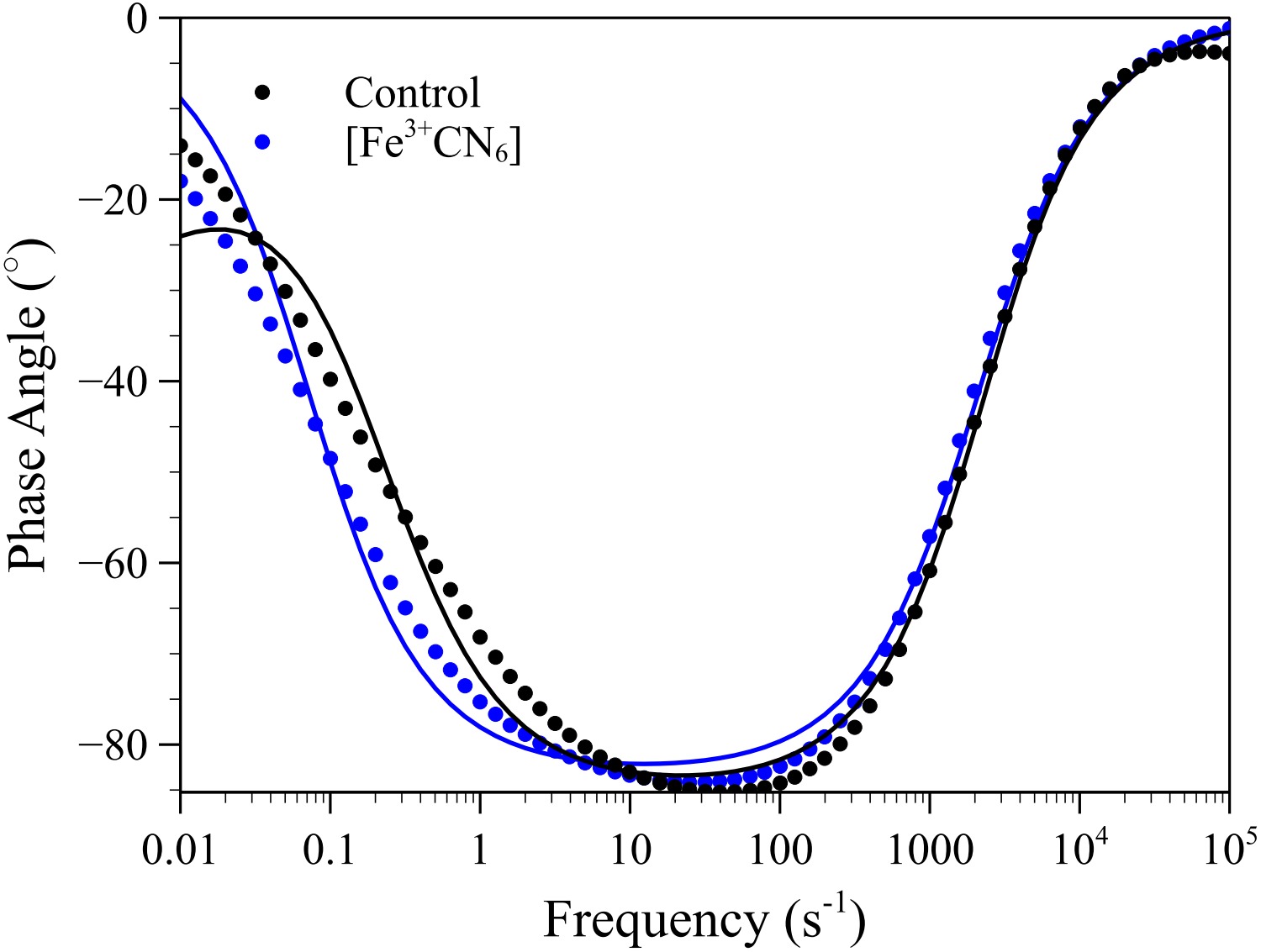

Figure A.5: Phase angle plot of an EIS spectrum for a p[N_1−dMIm][$Fe^{3+}(CN)_6$] film acquired in a 0.1 M aqueous solution of $K_3Fe(CN)_6$. EIS of a film consisting of a hydroxyl-terminated SAM exposed to NBDAC acquired in a 0.1 M $K_3Fe(CN)_6$ aqueous solution is shown as a control. Solid curves represent fits to the equivalent circuit in Scheme 3.4.

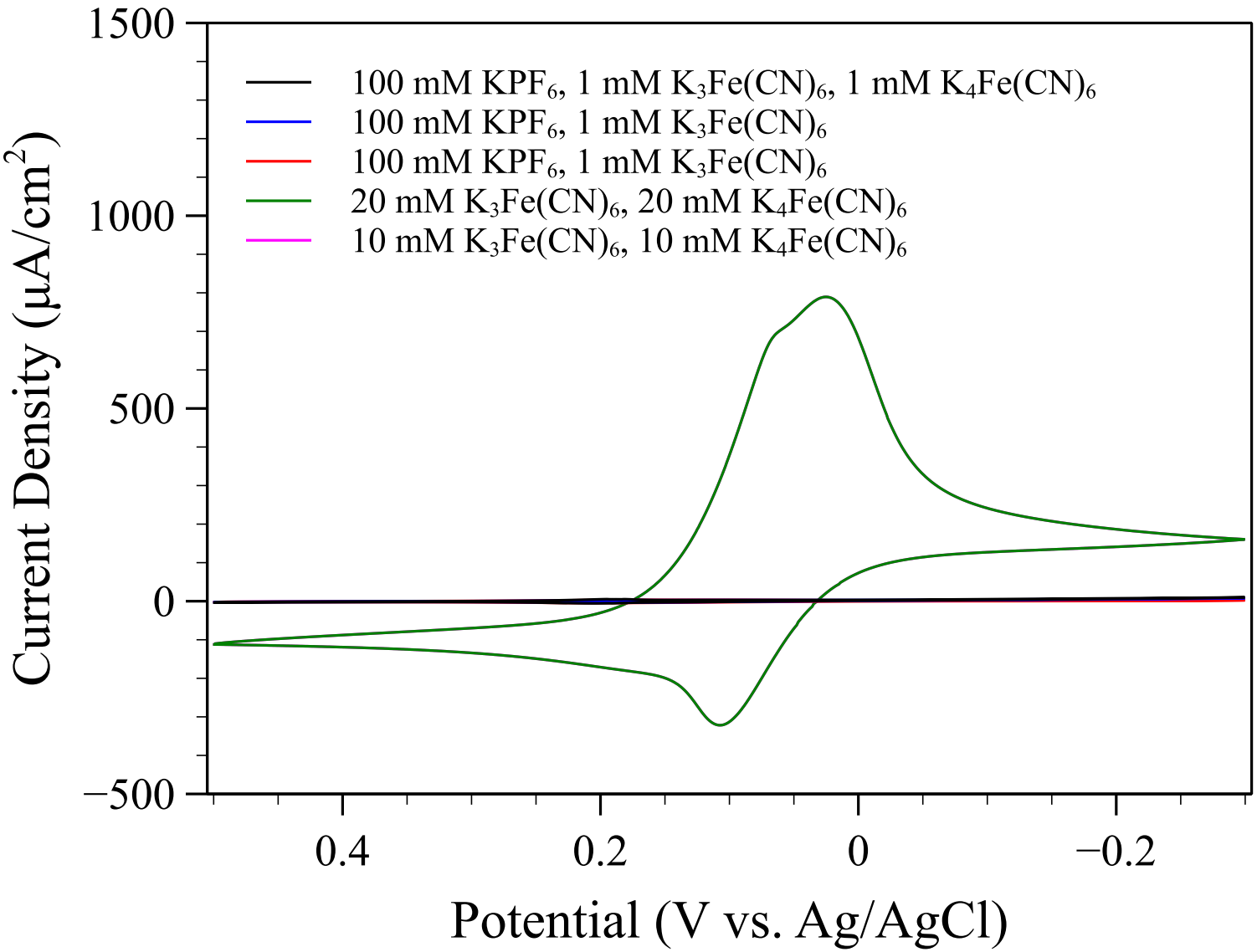

Figure A.6: Current-voltage seen for the 20th cycles of cyclic voltammetry experiment for p[N_1−dMIm][$Fe^{3+}(CN)_6$] films conducted at a 20 mV/s scan rate.

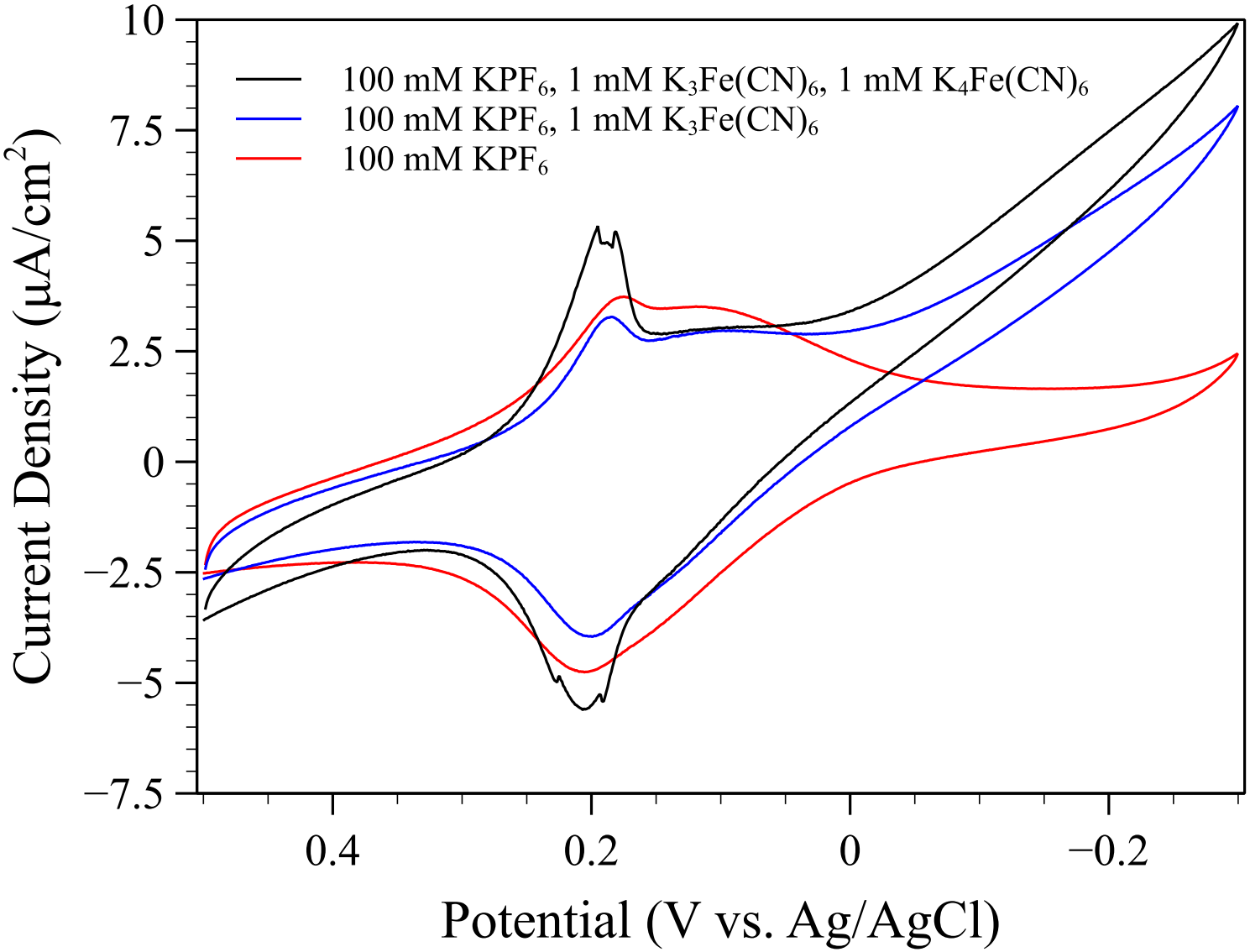

Figure A.7: Current-voltage seen for the 20th cycles of cyclic voltammetry experiment for p[N_1−dMIm][$Fe^{3+}(CN)_6$] films conducted at a 20 mV/s scan rate.

References

[1] Heyns, A., and van Schalkwyk, G. (1973) A Study of the Infrared and Raman Spectra of Ammonium Hexafluorophosphate NH4PF6 over a Wide Range of Temperatures. *Spectrochimica Acta Part A: Molecular Spectroscopy 29*, 1163–1175.

[2] Silverstein, R. M., Webster, F. X., and Kiemle, D. J. *Spectrometric Identification of Organic Compounds*, seventh ed.; Wiley: New York, 2005.

[3] Miller, F. A., and Wilkins, C. H. (1952) Infrared Spectra and Characteristic Frequencies of Inorganic Ions. *Analytical Chemistry 24*, 1253–1294.

[4] Sehgal, S. C. J., Warrier, A. V. R., and K, H. (1973) Electronic and vibrational spectra of ferricyanide ions doped in NaCl and KCl crystals. *Journal of Physics C: Solid State Physics 6*, 193.

[5] Hardwick, L. J., Saint, J. A., Lucas, I. T., Doeff, M. M., and Kostecki, R. (2009) FTIR and Raman Study of the $Li_xTi_yMn_{1-y}O_2$(y = 0, 0.11) Cathodes in Methylpropyl Pyrrolidinium Bis(fluoro-sulfonyl)imide, LiTFSI Electrolyte. *Journal of The Electrochemical Society 156*, A120–A127.

[6] Yoon, H., Best, A. S., Forsyth, M., MacFarlane, D. R., and Howlett, P. C. (2015) Physical Properties of High Li-ion Content N-propyl-N-methylpyrrolidinium Bis(fluorosulfonyl)imide Based Ionic Liquid Electrolytes. *Physical Chemistry Chemical Physics 17*, 4656–4663.

[7] Kiefer, J., Fries, J., and Leipertz, A. (2007) Experimental Vibrational Study of Imidazolium-Based Ionic Liquids: Raman and Infrared Spectra of 1-ethyl-3-methylimidazolium Bis(trifluoromethylsulfonyl)imide and 1-ethyl-3-methylimidazolium Ethylsulfate. *Applied Spectroscopy 61*, 1306–1311.

[8] Shkrob, I. A., Marin, T. W., Zhu, Y., and Abraham, D. P. (2014) Why

Bis(fluorosulfonyl)imide Is a "Magic Anion" for Electrochemistry. *The Journal of Physical Chemistry C 118*, 19661–19671.

Appendix B

EMBEDDING REPORTER MOLECULES IN SURFACE-TETHERED POLYMER FILMS

Introduction

The ability of a material to detect and report localized damage prior to catastrophic failure is a pivotal feature at the intersection of structural health monitoring (SHM) and non-destructive evaluation (NDE).[1–3] The early detection of impending failure is particularly important in applications in which the material is used as a load-bearing material or in applications where catastrophic failure of the material would lead to further damage to other systems.[1,2] Polymer composites imbued with multi-functional properties are the material of choice due to the ability to design and cheaply manufacture light-weight, sustainable, thermally, mechanically and chemically robust polymer composites.[1,4] Stimuli-responsive materials able to detect thermal, mechanical, optical and chemical solicitation have been used to effectively develop sensors, probes and information displays by taking advantage of organic or inorganic chromophores such as dyes with available delocalized electrons, or metal derivatives (i.e. metal nanoparticles and nanocrystalline semiconductors) since they confer to their embedding material a variation in the opto-electronic properties as a response to the stimulus.[4,5]

Chromogenic polymer systems able to detect through a prompt optical response (absorption and emission) to an eternal stimuli triggered by mechanical (shearing, grinding and pressing) stress are favored due to their quick and simple functionality and visual signaling.[4,5] Mechanochromic polymer composites, which are materials based on dye-doped polymers that are optically sensitive to mechanical stimuli, may

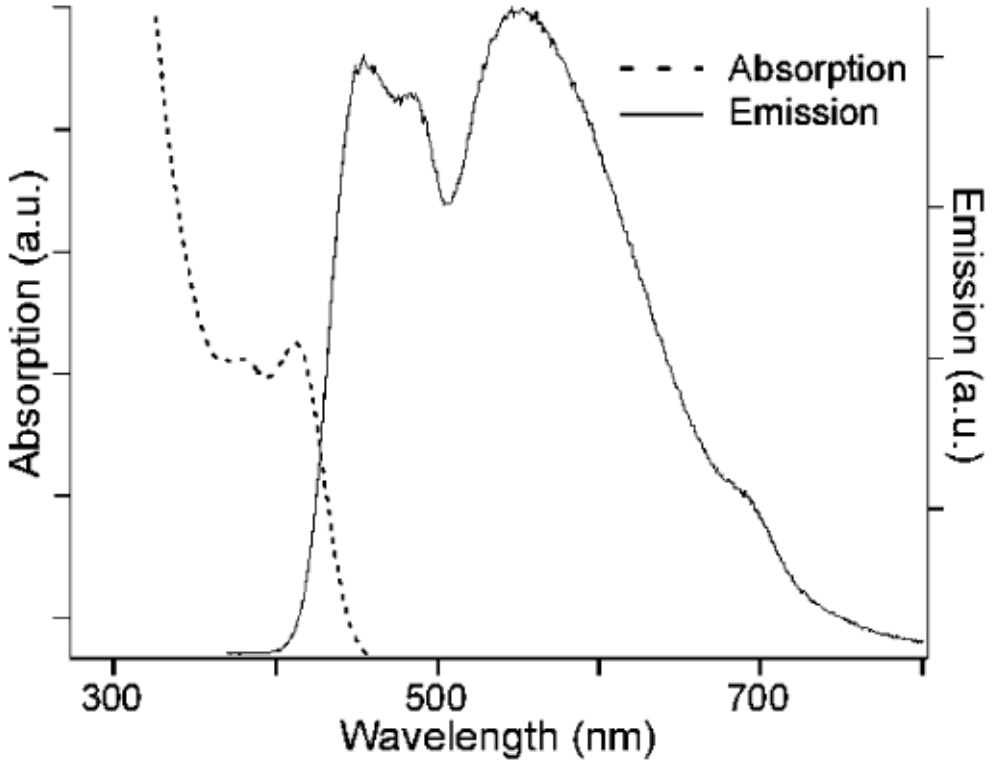

Figure B.1: Absorption and emission spectra of CdSe nanocrystals.[6]

be obtained via two distinct routes, either the covalent bonding of highly responsive molecular species to the polymer chains, or the dispersion of responsive species within the polymer bulk.[4,5] In the latter case, the control of interphase interactions between the chemical functional species (dye) and the multiphase system (polymer composite) allows for the effective modulation of the response to stimuli.[4,5]

Ultra-small pyrolytic CdSe nanocrystals exhibit white light emission characterized by two features (see Figure B.1), the first of which is sensitive to the size and the surface ligands of the nanocrystal, shifting to higher wavelengths with increasing nanocrystal size and decreasing ligand length.[6,7] Incorporation of the CdSe nanocrystals into a polymer matrix could enable the sensing of changes to the material due to external mechanical stresses.[3,8] External mechanical stresses that elicit local damage to the polymer matrix, such as micro cracks or delamination, are hypothesized to cause the detachment of CdSe surface ligands and the aggregation of the

CdSe nanocrystals leading to a change in the emission properties of the nanocrystals. The CdSe nanocrystals have been encapsulated in polymer and have demonstrated good photostability over time.[6,9,10] Here, I report the incorporation of CdSe reporter molecules into a surface-tethered polymer coating for the use of the emission shift of the CdSe in the sensing of localized damage within the coating.

Experimental Methods

Pyrolytically grown 15 Å CdSe nanocrystals with defect-ridden surfaces and citric acid surface ligands with lengths on the order of the diameter of the CdSe nanocrystals were obtained from the Rosenthal group (Chemistry).

Polymerization of pNBF8 on Glass Substrates

ROMP-active substrates of glass were prepared as described in Chapter 3. The ROMP-active substrates were quickly rinsed with DCE and immediately placed in a 0.05 M 5-(perfluoro-n-octyl)norbornene (pNBF8)[11] solution in DCM for up to 15 min. The substrates were subsequently rinsed with DCM, ethanol, water, and ethanol and dried in a stream of nitrogen.

Incorporation of CdSe Nanocrystals

The nanocrystals were suspended in chloroform ($CHCl_3$) and introduced into the surface-anchored pNBF8 polymer matrix by placing several drops of the CdSe nanocrystal solution on top of the pNBF8 substrates. The substrates were left overnight and rinsed with copious amounts of dichloromethane (DCM) to ensure the complete removal of any CdSe nanocrystals on the surface.

Emission Spectra

Emission spectra were acquired using a Labsphere SLMS-LED-1050 integrating light sphere system, coupled with a fiber optic cable to a 410 nm UV filter and CDS 600 CCD-based spectrometer and accompanying software. The light sphere is used to spatially integrate the radiant flux of the optical radiation generated by the sample. A 405 nm laser operating at 10 mW was used as the excitation source.

Results and Discussion

Figure B.2 shows the emission spectra of CdSe nanocrystals embedded in 5-(perfluoro-n-octyl)norbornene (pNBF8) grown on glass with Catalyst **3**. The spectra were recorded as a percent of the maximum saturation of the detector. Despite the use of a 410 nm cutoff UV filter, there is a large peak at 405 nm corresponding to the excitation source. The peak was confirmed to be due to the excitation source by collecting spectra with no samples in the integrating sphere (Empty Chamber), for which the peak was observed. The spectra of the CdSe nanocrystals in $CHCl_3$ exhibits the two features observed in Figure B.1 for CdSe emission spectra reported in the literature. The first peak for the CdSe emission is not present for CdSe nanocrystals embedded in pNBF8, but the second feature is present. We hypothesize that this change in the shape of the emission spectra for CdSe embedded in pNBF8 is due to the interaction of the nanocrystals with the polymer matrix. These features are more clearly seen in Figure B.3.

Figure B.4 shows the total CdSe emission for the region between 425 and 850 nm over time for CdSe nanocrystals in $CHCl_3$ as well as in pNBF8. The data shows that the CdSe nanocrystal emission remains constant when embedded in pNBF8 for over a month compared to that of the CdSe nanocrystals in $CHCl_3$. The instability of the CdSe nanocrystals in solution can been attributed to the oxidation of the nanocrystal surface as well as a loss of solvent to evaporation. Further experiments

are required to elucidate the mechanism of interaction for the CdSe nanocrystals with the polymer matrix in addition to quantifying their ability to sense material changes due to external stimuli.

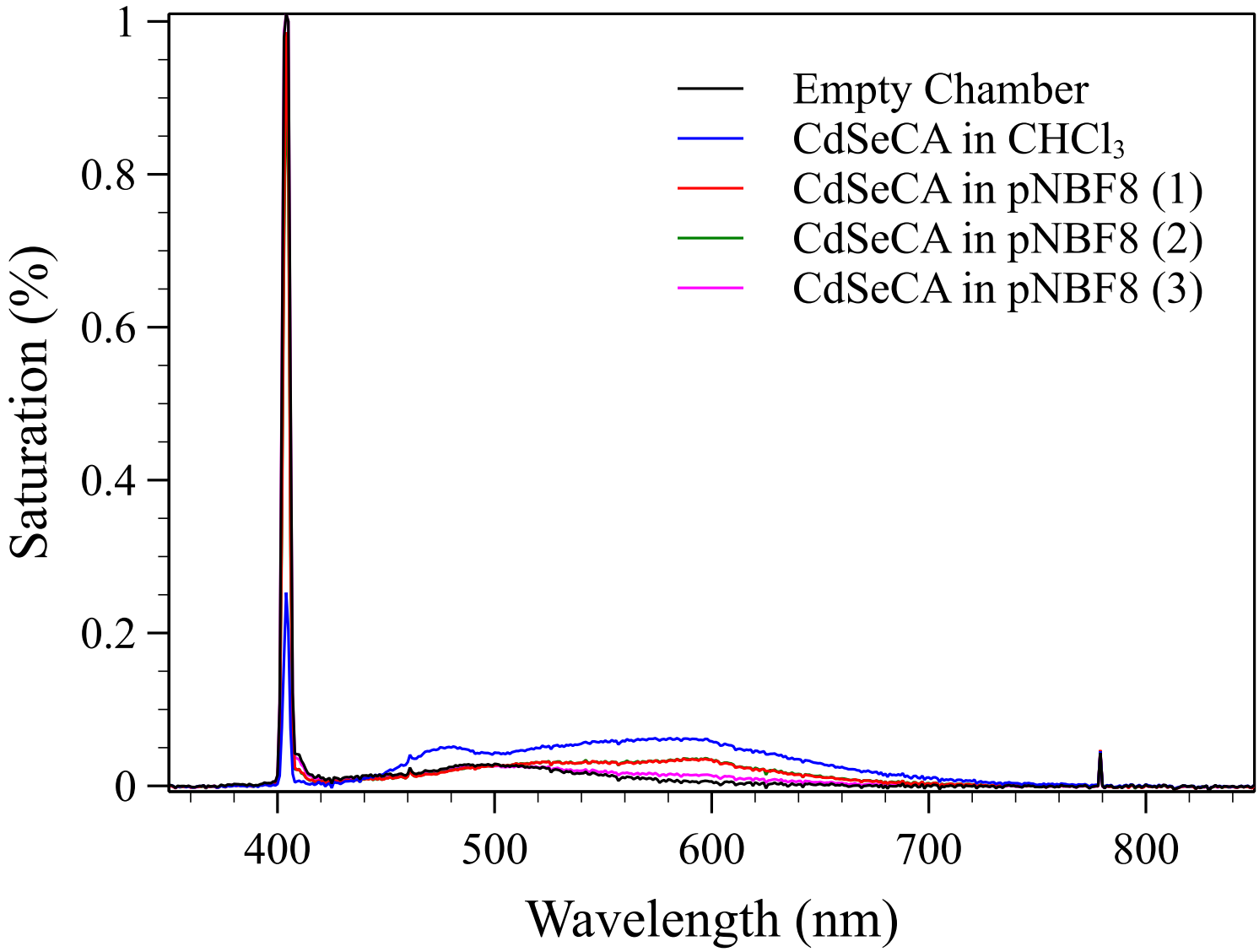

Figure B.2: Integrating sphere emission spectra of CdSe nanocrystals embedded in 5-(perfluoro-n-octyl)norbornene (pNBF8) grown on glass with Catalyst **3**, and suspended in $CHCl_3$. The CdSe nanocrystals were excited with 405 nm light.

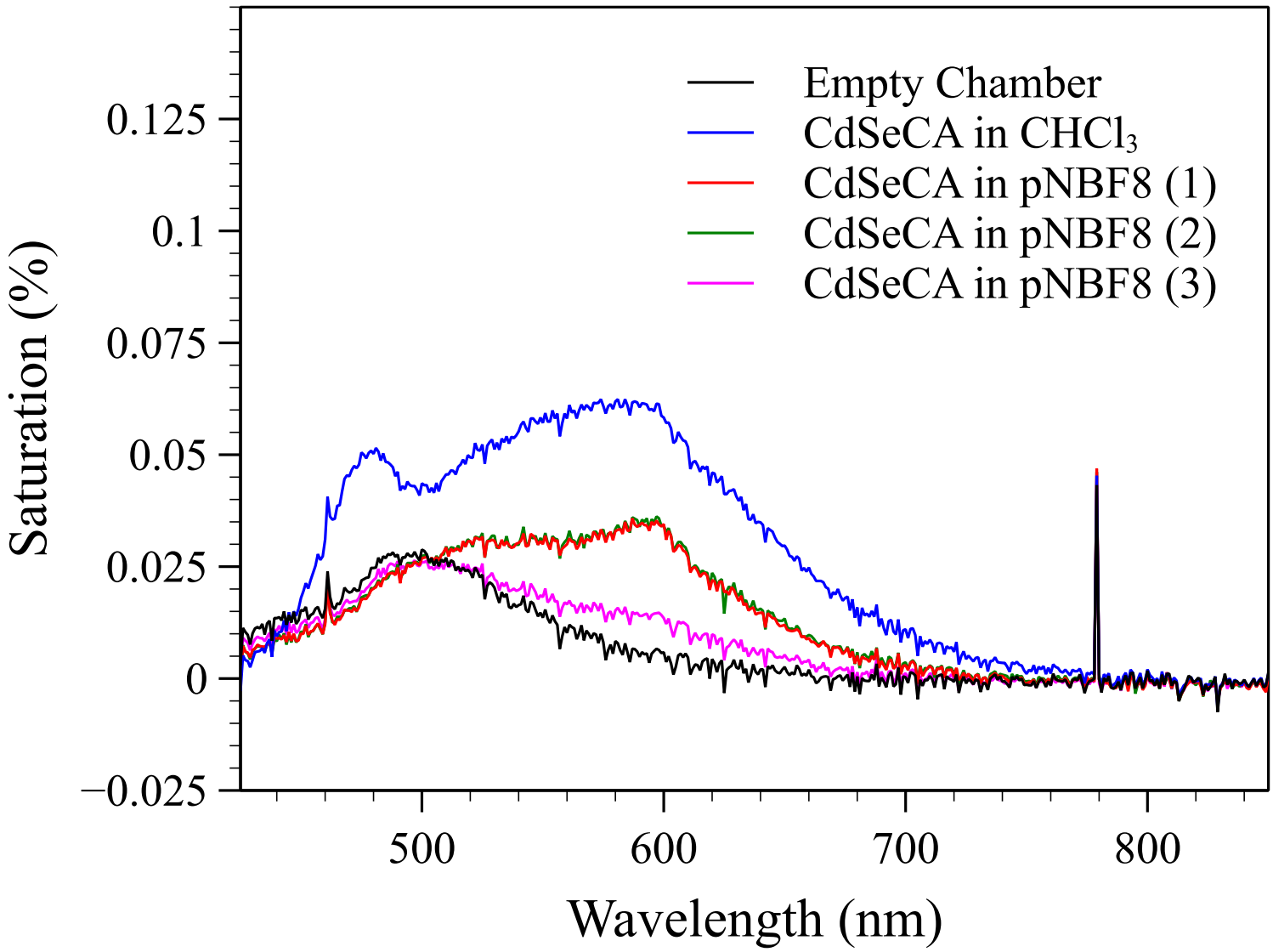

Figure B.3: Integrating sphere emission spectra of CdSe nanocrystals embedded in 5-(perfluoro-n-octyl)norbornene (pNBF8) grown on glass with Catalyst **3**, and suspended in $CHCl_3$. The CdSe nanocrystals were excited with 405 nm light.

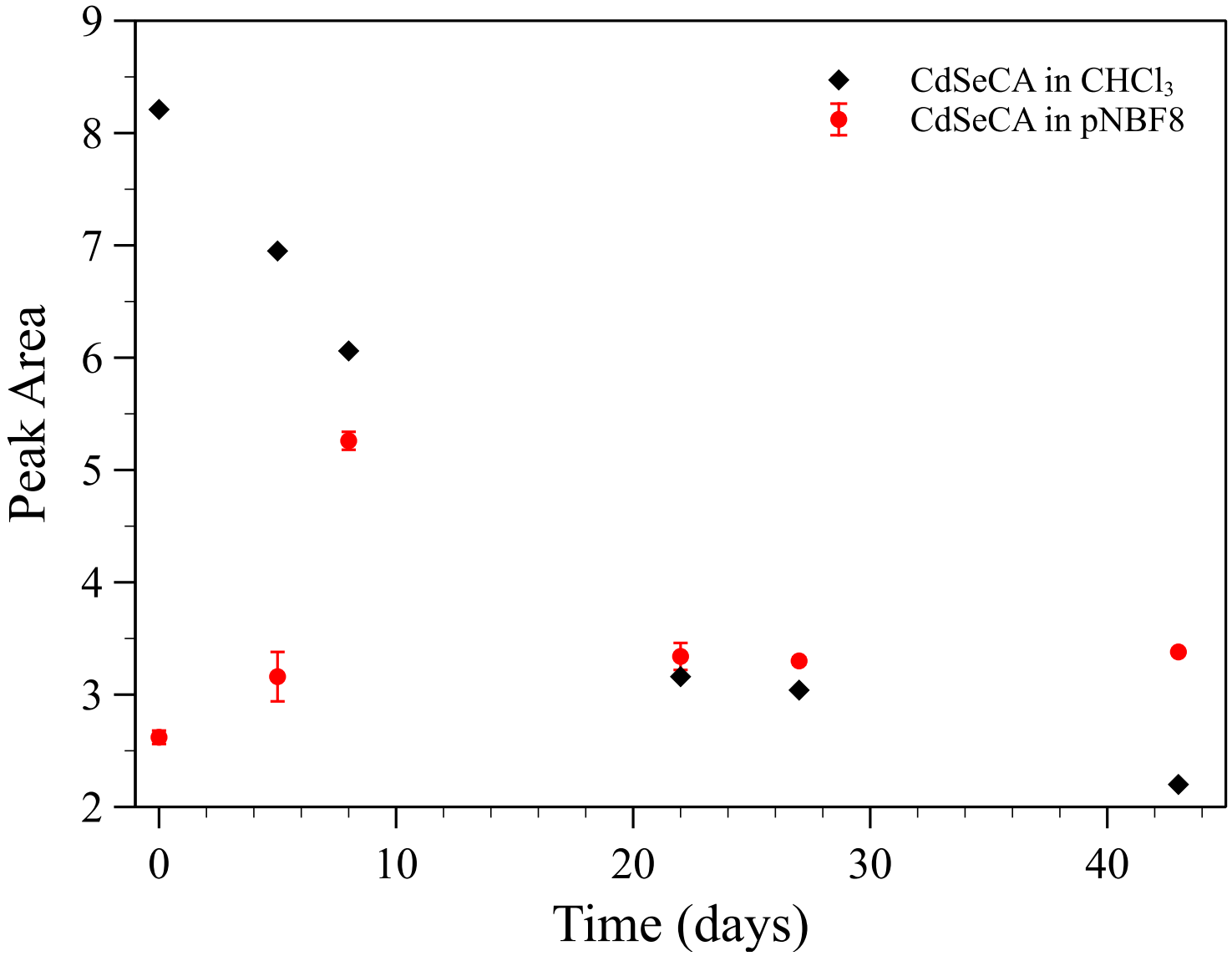

Figure B.4: CdSe nanocrystal emission as a function of time. Integrating sphere emission spectra of CdSe nanocrystals embedded in 5-(perfluoro-n-octyl)norbornene (pNBF8) grown on glass with Catalyst **3**, and suspended in $CHCl_3$ were collected for each time point. The CdSe nanocrystals were excited with 405 nm light and the emission for the region between 425 and 850 nm was integrated with subtraction of the background emission from the empty chamber to determine the area under the peak of the CdSe emission peak (Peak Area).

References

[1] Jin, X., Götz, M., Wille, S., Mishra, Y. K., Adelung, R., and Zollfrank, C. (2013) A Novel Concept for Self-Reporting Materials: Stress Sensitive Photoluminescence in ZnO Tetrapod Filled Elastomers. *Advanced Materials 25*, 1342–1347.

[2] Bruns, N., Pustelny, K., Bergeron, L. M., Whitehead, T. A., and Clark, D. S. (2009) Mechanical Nanosensor Based on FRET within a Thermosome: Damage-Reporting Polymeric Materials. *Angewandte Chemie 121*, 5776–5779.

[3] Brubaker, C., Frecker, T., Njoroge, I., Smudde, C., Shane, D., Meyer, J., Rosenthal, S., Sanchez, F., Jennings, G., and Adams, D. Detecting and communicating material damage using embedded CdSe nanocrystals. CAMX 2015 - Composites and Advanced Materials Expo. 2015.

[4] Pucci, A., Bizzarri, R., and Ruggeri, G. (2011) Polymer composites with smart optical properties. *Soft Matter 7*, 3689–3700.

[5] Lee, K., Povlich, L. K., and Kim, J. (2010) Recent advances in fluorescent and colorimetric conjugated polymer-based biosensors. *Analyst 135*, 2179–2189.

[6] Bowers, M. J., McBride, J. R., and Rosenthal, S. J. (2005) White-Light Emission from Magic-Sized Cadmium Selenide Nanocrystals. *Journal of the American Chemical Society 127*, 15378–15379.

[7] McBride, J. R., Dukes III, A. D., Schreuder, M. A., and Rosenthal, S. J. (2010) On ultrasmall nanocrystals. *Chemical Physics Letters 498*, 1–9.

[8] Brubaker, C., Frecker, T., Njoroge, I., Shane, D., Smudde, C., Rosenthal, S., Jennings, G., and Adams, D. In-situ material state monitoring using embedded CdSe quantum dots. Proceedings of SPIE - The International Society for Optical Engineering. 2016.

[9] Schreuder, M. a., Gosnell, J. D., Smith, N. J., Warnement, M. R., Weiss, S. M., and Rosenthal, S. J. (2008) Encapsulated white-light CdSe nanocrystals as nanophosphors for solid-state lighting. *Journal of Materials Chemistry 18*, 970.

[10] Gosnell, J. D., Rosenthal, S. J., and Weiss, S. M. White Light Emission Characteristics of Polymer-Encapsulated CdSe Nanocrystal Films. 2010.

[11] Escobar, C. A., Harl, R. R., Maxwell, K. E., Mahfuz, N. N., Rogers, B. R., and Jennings, G. K. (2013) Amplification of Surface-Initiated Ring-Opening Metathesis Polymerization of 5-(Perfluoro-n-alkyl)norbornenes by Macroinitiation. *Langmuir 29*, 12560–12571.